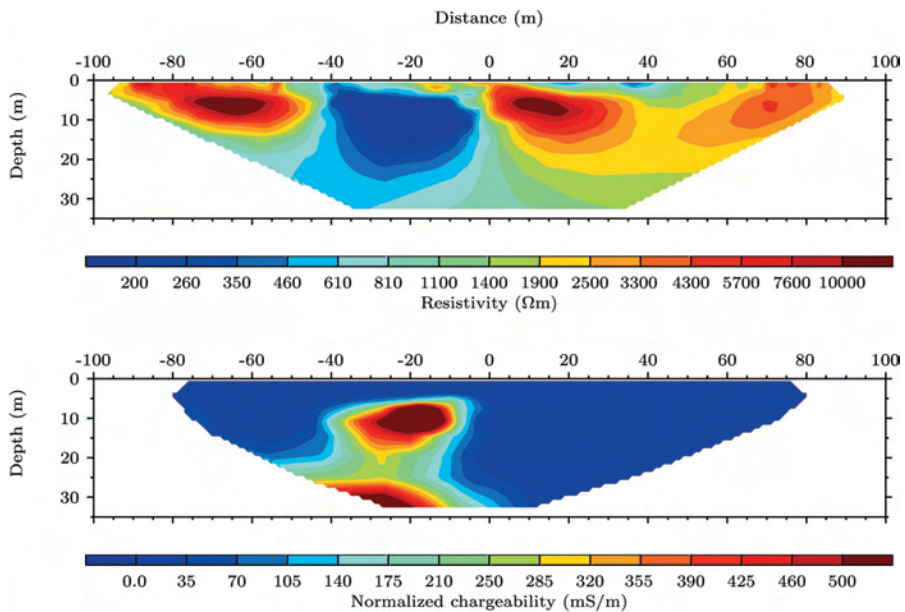


Thomas Ingeman-Nielsen

# Geophysical techniques applied to permafrost investigations in Greenland



# Geophysical techniques applied to permafrost investigations in Greenland

**Thomas Ingeman-Nielsen**

Ph.D. Thesis  
BYG•DTU R-123

Arctic Technology Centre  
Department of Civil Engineering  
Technical University of Denmark  
2005

ISSN 1602-2917  
ISBN 87-7877-192-7

## Geophysical techniques applied to permafrost investigations in Greenland

Copyright (c), Thomas Ingeman-Nielsen, 2005

Printed by Eurographic A/S, Copenhagen

Arctic Technology Centre  
Department of Civil Engineering  
Technical University of Denmark

BYG•DTU R-123  
ISSN 1602-2917  
ISBN 87-7877-192-7

Front page illustration:  
Profiles of resistivity and normalized chargeability across a talik in the Sisimiut area (profile L5).

# Preface

---

This thesis was prepared at the Arctic Technology Centre, Department of Civil Engineering (BYG), Technical University of Denmark, in partial fulfillment of the requirements for acquiring the Ph.D. degree in engineering. The project has been carried out in the period from January 2002 to October 2005, with Professor Arne Villumsen and Associate Professor François Baumgartner as supervisors, whom I wish to thank for guidance and support.

I wish to thank colleagues at the Arctic Technology Centre, especially Gheorghe Goncear for being a good companion during several months of field work in Greenland.

During this work I have spent six months at Zonge Engineering and Research Organization Inc. in Tucson, Arizona. I am grateful to Dr. Kenneth Zonge and Mr. Scott Urquhart for making their facilities available to me, and to friends and colleagues at Zonge for fruitful discussions and a pleasant stay.

The field work and external stay have been financially supported by Otto Mønstedts Fond and Inge Lehmanns Legat.

I appreciate the help of Jo Riber in proof reading this thesis, and most importantly I am grateful to Heidi for being my ever patient and loving wife.

Lyngby, October 2005



Thomas Ingeman-Nielsen



# Abstract

---

The presence and distribution of permafrost is a major concern in engineering related problems in arctic environments. The interstitial ice content of permafrozen sediments, which may even be in excess of the unfrozen pore volume, constitutes a risk of loss of strength and settling upon permafrost degradation, that may for instance be induced by construction work. Permafrost distribution also influences the flow in and recharge to aquifers and therefore determines whether aquifers may be exploited for abstraction purposes. This thesis is concerned with the application of geophysical techniques to permafrost investigations in West Greenland and consists of three main parts. The first part reports an integrated geophysical survey conducted near the town of Sisimiut. The second and third parts focus on theoretical studies and field tests of a ground based, multifrequency frequency-domain electromagnetic (FDEM) method and the complex resistivity (CR) technique, and evaluations of their applicability to permafrost investigations.

Two permafrost areas close to Sisimiut, West Greenland, have been surveyed with a range of geophysical techniques comprising DC resistivity, induced polarization (IP), VLF-R, ground penetrating radar (GPR) and seismic refraction methods. Especially the combination of resistivity, IP and GPR measurements proves powerful in determining the lateral distribution of frozen sediments and the depth to the frost table. Indications of frozen ground are high resistivity, low normalized chargeability and a strong reflector at the frost table. Area 1 is found to contain one large highly resistive frozen body, area 2 has several frozen areas separated by unfrozen areas (taliks) caused by the presence of water bodies. Although many aspects of the 2D and 3D permafrost distribution could be clarified using multi-electrode resistivity and IP profiles, borehole information shows that the estimation of the thickness of frozen sediments was grossly overestimated in area one. Furthermore areas of high ground ice contents are not uniquely identified, and other methods are therefore needed to improve reliability of such interpretations.

The ground based, small coil, multifrequency FDEM technique is a fast and lightweight surveying method, requiring no electrical contact with the ground, and is thus potentially applicable to mapping both vertical and lateral resistivity distribution year round at low cost. A theoretical study of misorientation effects in

the response of a HCP configuration over a homogeneous half-space shows that both the real and imaginary parts may be severely corrupted even at small coil axes misalignments. With few exceptions, extreme errors increase with increasing axis inclination and are highly dependent on the direction of misorientation. Six different apparent resistivity definitions are studied, but none of them are robust in all the studied situations. In general the modeling shows that currently available equipment cannot be expected to yield sufficiently accurate results to allow quantitative 1D interpretation even when applied in less hostile environments. Application of the method at the Sisimiut field site confirms that the method is not well suited for permafrost studies in Greenland due to misalignment effects and limited responses of the resistive environment.

Theory and laboratory studies indicate that the complex resistivity dispersions of geological materials may be depending on temperature and ice content. A wide frequency bandwidth CR survey has therefore been conducted at the Sisimiut field site to evaluate the applicability of the method to permafrost mapping. The results suggest that a characteristic spectral response is observed in permafrozen areas, but the collected data seem to be obscured by errors possibly relating to electromagnetic and capacitive coupling effects as well as equipment related issues. New modeling tools were developed to address these effects, and the models show that keeping electrode contact resistance low is crucial to avoiding capacitive coupling problems. Equipment tests showed that the current reference link introduces errors in the measured reference signal. Improvements have been made to the system, and a subsequent field test resulted in data that could be reasonably well fitted by geologically sensible 1D models. If the observed permafrost responses can be confirmed with the improved system, the CR technique may prove valuable in future permafrost investigations.

# Resumé

---

Forekomst og fordeling af permafrost er af afgørende betydning i ingeniørrelaterede problemstillinger i Arktis. Isindholdet i frosne sedimenter kan overstige porevolumenet af den tilsvarende ufrosne aflejring. Derfor udgør de ved optøning en fare for sætninger og tab af styrke; situationer der f.eks. kan induceres i forbindelse med bygningsarbejder. Permafrostforekomster påvirker også nedsivning til og strømme i grundvandsmagasiner og er således bestemmende for, hvorvidt disse kan udnyttes i forbindelse med vandforsyning. Denne afhandling drejer sig om anvendelsen af geofysiske metoder til kortlægning af permafrostforekomster i Vestgrønland og består af tre dele. Første del beskriver en geofysisk undersøgelse af permafrostforhold nær byen Sisimiut. Anden og tredje del omhandler teoretiske studier af og feltundersøgelser med en frekvens domæne elektromagnetisk (FDEM) metode og en metode til måling af jordens komplekse elektriske modstand (CR), samt en vurdering af disse metoders anvendelighed i forbindelse med permafrostkortlægning.

To permafrostområder nær Sisimiut i Vestgrønland er blevet undersøgt med en række geofysiske metoder omfattende geoelektriske målinger, induceret polarisation (IP), VLF-R, georadar (GPR) og seismisk refraktion. Specielt kombinationen af geoelektriske målinger, IP og georadar data viser sig særdeles anvendelig i kortlægning af den laterale fordeling af frosne sedimenter og dybde til frostspejlet. Indikationer for permafrost er høje elektriske modstande, lav normaliseret polarisabilitet (normalized chargeability) og en tydelig reflektor ved frostspejlet. I område 1 findes ét stort frossent område med høj elektrisk modstand, i område 2 findes flere frosne områder, der pga. søer og vandløb er adskilt af ufrosne områder. Selvom mange aspekter af permafrostfordelingen i to og tre dimensioner kunne kortlægges med multielektrode profileringer, viser informationer fra borehuller, at tykkelsen af de frosne sedimenter i område 1 blev stærkt overvurderet. Derudover kan områder med massive isforekomster (islinser) ikke entydigt identificeres, og andre metoder er derfor nødvendige for at forbedre pålideligheden af sådanne fortolkninger.

Den multifrekvente FDEM metode baseret på små spoler er en let og hurtig metode, som ikke kræver elektrisk kontakt med jorden og kan derfor potentielt anvendes året rundt med lave omkostninger til kortlægning af modstandsfordelingen i jorden. Et teoretisk studie af effekter af fejlorientering på målinger med en

HCP konfiguration over et homogent halvrum viser, at både den reelle og imaginære del kan være svært fejlbehæftet selv ved små fejlorienteringer af spoleakserne. Med få undtagelser er fejl-ekstremerne stigende med aksehældningen og stærkt afhængig af retningen af fejlorienteringen. Seks forskellige definitioner af tilsyneladende resistivitet undersøges, men ingen af dem er robuste i alle de modellerede situationer. Generelt viser modelberegningerne, at de instrumenter, der for tiden er tilgængelige, ikke kan forventes at give resultater af tilstrækkelig nøjagtighed til at der kan foretages kvantitative 1D fortolkninger. Anvendelse af metoden i feltområdet ved Sisimiut bekræfter, at metoden ikke er anvendelig til permafrostundersøgelser i Grønland pga. fejlorienteringseffekter og de relativt høje resistiviteter.

Teori og laboratorieundersøgelser antyder, at geologiske materialers komplekse modstand kan afhænge af temperaturen og isindholdet. Feltundersøgelser er således foretaget med CR metoden, for at bedømme dens anvendelighed i forbindelse med permafroststudier. Resultaterne antyder at permafrostforekomster er forbundet med et karakteristisk spektralt respons, men de indsamlede data synes at være behæftede med fejl, der kan relatere sig til elektromagnetisk (EM) og kapacitiv kobling, så vel som instrumentspecifikke fejl. Nye modelleringsredskaber er udviklet til behandling af disse effekter og viser, at det er yderst vigtigt at holde kontaktmodstanden lav for at undgå problemer med kapacitiv kobling. Test af det anvendte udstyr viser, at referencemålingen var fejlbehæftet. Udstyret er blevet forbedret på dette punkt, og en efterfølgende feltundersøgelse resulterer i data der kan fortolkes med geologisk fornuftige 1D modeller.

Såfremt de permafrostrelaterede spektrale egenskaber kan bekræftes med det forbedrede udstyr, kan CR metoden vise sig at blive et værdifuldt værktøj i fremtidige permafrostundersøgelser.

# Papers included in the thesis

---

- [A] Ingeman-Nielsen, T. & Baumgartner, F. (in prep): Misalignment effects in FDEM measurements. *Near Surface Geophysics*. Submitted 2005.  
Currently under revision.
- [B] Ingeman-Nielsen, T. & Baumgartner, F. (in press): Numerical modeling of complex resistivity effects on a homogeneous half-space at low frequencies. *Geophysical Prospecting*.  
Accepted for publication, October 2005.
- [C] Ingeman-Nielsen, T. & Baumgartner, F. (in press): CR1Dmod: A Matlab program to model 1D complex resistivity effects in electrical and electromagnetic surveys. *Computers & Geosciences*.  
Accepted for publication subject to minor revisions, April 2005.
- [D] Ingeman-Nielsen, T. (2005): Error sources relating to CR measurements over a wide frequency bandwidth. Technical paper.  
Not submitted.



# Table of Contents

---

<b>1</b>	<b>Introduction</b>	<b>1</b>
1.1	Background . . . . .	1
1.2	Structure of the thesis . . . . .	2
<b>2</b>	<b>The Sisimiut field location</b>	<b>5</b>
2.1	Location and climate . . . . .	5
2.2	Geological setting . . . . .	6
2.2.1	The bedrock . . . . .	6
2.2.2	Quaternary deposits . . . . .	6
2.3	Location of geophysical field sites . . . . .	7
2.4	Data acquisition and processing . . . . .	8
2.4.1	Geoelectricity and IP . . . . .	8
2.4.2	VLF and VLF-R . . . . .	10
2.4.3	Seismic refraction . . . . .	10
2.4.4	Step-frequency GPR . . . . .	11
2.4.5	Boreholes . . . . .	11
2.5	Results from area 1 . . . . .	12
2.5.1	MEP . . . . .	12
2.5.2	Wenner and VLF-R . . . . .	14
2.5.3	Vertical Electrical Sounding . . . . .	16
2.5.4	Boreholes . . . . .	17
2.5.5	Implications for the geophysical interpretation . . . . .	18
2.6	Results from area 2 . . . . .	19
2.6.1	Geoelectricity and IP . . . . .	20
2.6.2	Boreholes . . . . .	20
2.6.3	Seismic refraction . . . . .	24
2.6.4	Ground penetrating radar . . . . .	24
2.6.5	Interpretation . . . . .	28
2.7	Discussion . . . . .	28
2.8	Conclusion . . . . .	30
<b>3</b>	<b>The FDEM method</b>	<b>31</b>
3.1	Introduction . . . . .	31
3.2	Theoretical background . . . . .	32

3.3	Sensitivity to misorientation of transmitter and receiver . . . . .	34
3.3.1	Summary of results from Paper A . . . . .	34
3.3.2	The effect of independently varying inclinations . . . . .	35
3.4	Sensitivity to errors in separation distance . . . . .	38
3.5	Field test with a FDEM system in Sisimiut . . . . .	39
3.5.1	Results . . . . .	40
3.6	Discussion . . . . .	43
3.7	Conclusion . . . . .	44
<b>4</b>	<b>The CR method</b>	<b>45</b>
4.1	Introduction . . . . .	45
4.2	Background and fundamentals . . . . .	45
4.2.1	Complex resistivity of earth materials . . . . .	45
4.2.2	Origin and phenomenological models of the CR effect . . . . .	47
4.3	Justification for applying the CR method in the Greenlandic environment . . . . .	50
4.4	EM coupling in the CR method . . . . .	51
4.4.1	Summary of Paper B . . . . .	52
4.4.2	Summary of Paper C . . . . .	53
4.5	CR measurements over wide frequency ranges . . . . .	54
4.5.1	Summary of Paper D . . . . .	54
4.5.2	CR measurements in Sisimiut . . . . .	55
4.6	Discussion and outlook . . . . .	61
4.7	Conclusion . . . . .	62
<b>5</b>	<b>Discussion</b>	<b>63</b>
<b>6</b>	<b>Conclusion</b>	<b>65</b>
	<b>Appendices</b>	<b>67</b>
<b>A</b>	<b>Misalignment effects in FDEM measurements</b>	<b>69</b>
A.1	Introduction . . . . .	71
A.2	Theoretical background . . . . .	72
A.2.1	Normalization . . . . .	73
A.2.2	Response on a homogeneous half-space . . . . .	74
A.2.3	Apparent resistivity algorithms . . . . .	75
A.3	Misalignment effects . . . . .	76
A.3.1	Dipole misorientation . . . . .	76
A.3.2	Special case: The effect of topography . . . . .	78
A.3.3	The effect of misorientation on apparent resistivity . . . . .	79
A.3.4	Spacing effects . . . . .	84
A.3.5	LIN instruments . . . . .	85
A.4	Conclusion . . . . .	85

<b>B</b>	<b>Numerical modeling of complex resistivity effects on a homogeneous half-space at low frequencies</b>	<b>89</b>
B.1	Introduction . . . . .	91
B.2	Theory . . . . .	92
	B.2.1 EM coupling of grounded wires on a homogeneous half-space	92
	B.2.2 Complex resistivity . . . . .	93
	B.2.3 Complex EM coupling . . . . .	94
B.3	Pure coupling on a homogeneous half-space . . . . .	95
B.4	Half-space with complex resistivity . . . . .	96
B.5	Removal of EM coupling . . . . .	99
B.6	Application to field data . . . . .	101
B.7	Conclusion . . . . .	103
<b>C</b>	<b>CR1Dmod: A Matlab program to model 1D complex resistivity effects in electrical and electromagnetic surveys</b>	<b>109</b>
C.1	Introduction . . . . .	111
C.2	The Complex Resistivity model . . . . .	112
C.3	Theoretical basis . . . . .	113
	C.3.1 EM coupling between grounded wires . . . . .	113
	C.3.2 TEM calculations . . . . .	115
	C.3.3 FDEM calculations . . . . .	117
	C.3.4 DC geoelectrical calculations . . . . .	118
C.4	Calculation of Hankel and Cosine transforms . . . . .	118
	C.4.1 Numerical integration . . . . .	118
	C.4.2 Fast Hankel Transform filters . . . . .	119
	C.4.3 Comments on the transform routines . . . . .	119
C.5	Spline interpolation applied to dipole integrations . . . . .	120
C.6	Program structure . . . . .	120
C.7	Conclusion . . . . .	123
C.8	Acknowledgements . . . . .	124
<b>D</b>	<b>Error sources relating to CR measurements over a wide frequency bandwidth</b>	<b>127</b>
D.1	Introduction . . . . .	129
D.2	Data acquisition . . . . .	130
	D.2.1 Equipment and layout . . . . .	130
	D.2.2 Frequency domain measurements . . . . .	132
	D.2.3 System calibration . . . . .	134
D.3	Identifying unexpected effects in the collected data . . . . .	134
D.4	Causes for the observed effects . . . . .	136
	D.4.1 Deviation from 1D earth model . . . . .	136
	D.4.2 Layout effects . . . . .	137
	D.4.3 Capacitive coupling effects . . . . .	139
	D.4.4 Equipment related challenges . . . . .	145

D.4.5	Discussion of error sources . . . . .	150
D.5	Field test . . . . .	152
D.5.1	Equipment and setups applied . . . . .	152
D.5.2	Results and discussion . . . . .	153
D.6	Conclusions . . . . .	157
<b>E</b>	<b>Schematics of the isolation amplifier</b>	<b>159</b>
<b>F</b>	<b>Borehole logs</b>	<b>163</b>
F.1	Borehole 2003-4 . . . . .	164
F.2	Borehole 2003-5 . . . . .	165
F.3	Borehole 2003-6 . . . . .	165
F.4	Borehole 2003-7 . . . . .	166
	<b>Bibliography</b>	<b>167</b>
	<b>Errata</b>	<b>179</b>

# Introduction

---

## 1.1 Background

Permafrost, or perennially frozen ground, is a section of the subsurface in which the temperature is continually below  $0^{\circ}\text{C}$  for two years or more (Washburn, 1979). The definition is based exclusively on the temperature regime, and thus permafrost can exist in any type of sediment or rock. Permafrost is considered to cover approximately 26% of the land masses of the world, and is therefore of major concern.

In sediments and fractured rock the presence of permafrost often results in substantial ice content in the pore spaces, and as a result the permafrost distribution is of immediate interest to many engineering geological problems in the arctic. The presence of permafrost seriously influences flow and recharge to groundwater aquifers due to changes in the hydraulic properties of the frozen sediments (Kane & Chacho, 1990). The vertical extent of permafrost determines whether subpermafrost aquifers are at all present, and the lateral extent and continuity if recharge is possible and therefore whether aquifers may be exploited for abstraction purposes. The interstitial ice content may even be in excess of the unfrozen pore volume. In such cases, the changes in the ground thermal regime induced by construction work may cause thawing and thereby loss of strength and settling of the subsurface material.

Furthermore, the present permafrost distribution and temporal changes have long term climatic impact. Due to low temperatures, the microbial degradation in permafrozen areas is slow, and as a result arctic peat land contains enormous carbon storages. With permafrost degradation due to global warming, microbial activity in arctic areas is expected to be increasingly active in production of greenhouse gasses (Rivkina et al., 2002). Drastic increases in emissions of both methane  $\text{CH}_4$  and carbondioxide  $\text{CO}_2$  — the two most important greenhouse gasses — are expected, depending on local conditions (Gorham, 1991; Christensen et al., 2004). In either case, permafrost degradation is bound to have major impact on the carbon cycle on a global scale.

Near surface geophysical surveys have been applied in permafrost investigations for decades. Many of the physical properties mapped in such surveys depend on temperature. For instance, the electrical resistivity and compressional wave velocity of geological materials increase with decreasing temperature (Hoekstra & McNeill, 1973; King, 1984; King et al., 1988) and the permittivity decreases with temperature (Hoekstra & Delaney, 1974). Although some parameters are in fact temperature dependent in a strict sense, the most significant changes in physical parameters occur due to phase changes between water in liquid and frozen form. Therefore, when geophysical techniques are applied in mapping of permafrost, it is often ice-bonded permafrost which is mapped.

In relation to construction work, ice-bonded permafrost is precisely the main concern, as sediments with ice contents in excess of the unfrozen pore volume are connected with a risk of massive settling upon thawing. However, changes in local conditions such as shading, vegetational cover and albedo due to construction work may also cause aggradation of permafrost. Therefore, mapping of sediment types in unfrozen areas in the discontinuous permafrost zone is likewise important. In particular the distribution of fine-grained sediments is of concern, as these are more prone to development of massive ground ice than more permeable sediments (Lunardini, 1981).

Based on these considerations, an ideal combination of geophysical tools for permafrost investigations should be able to map the vertical and lateral distribution of permafrost as well as the distribution of fine-grained sediments. The ability to distinguish changes in permafrost from changes in lithology is of equal importance. In the Greenlandic environment, due to logistical considerations and the relatively small and confined survey areas involved, lightweight and rapid methods are desirable in order to minimize survey time and costs.

This thesis is concerned with the evaluation of geophysical techniques, in an attempt to establish a combination of techniques useful for permafrost investigation in West Greenland. The objective is pursued through the application of a range of conventional geophysical tools in a permafrost area near the town of Sisimiut. Furthermore, two techniques not conventionally applied in permafrost investigations have been studied and evaluated for use in the Greenlandic environment.

## 1.2 Structure of the thesis

The present chapter contains the background and motivation for the research and describes the structure of the thesis.

Chapter 2 presents a field study with conventional geophysical techniques applied to permafrost investigations near the town of Sisimiut, West Greenland.

Chapter 3 describes a study of misalignment effects in a ground based frequency

domain electromagnetic technique using small coils. The model and results presented in Paper A are summarized and additional modeling results are presented to complete the analysis. Finally, application of the technique at the Sisimiut field site is evaluated.

Chapter 4 provides an introduction to the complex resistivity method and presents the main results of Paper B and Paper C relating to the modeling of electromagnetic coupling effects based on complex resistivities. A study of error sources relating to wide frequency bandwidth complex resistivity measurements (Paper D) is summarized and application at the Sisimiut field site is evaluated.

Chapter 5 presents an overall discussion of the results and chapter 6 the main conclusions.

Appendices A through D contain the four papers of the thesis. Papers A through C have been submitted to international, peer reviewed journals, whereas Paper D, which describes a study of error sources relating to CR measurements at high frequencies, is not intended for submission in its current form.



## The Sisimiut field location

---

This chapter describes a field study in the conventional application of geophysical techniques to mapping permafrost in an area near Sisimiut, West Greenland.

### 2.1 Location and climate

Sisimiut is located on the west coast of Greenland slightly north of the Arctic Circle, around  $67^{\circ}\text{N}$  and  $54^{\circ}\text{W}$ , see Figure 2.1. The Danish Meteorological Institute (DMI, 2005) report a mean annual precipitation of 383 mm and an average annual air temperature of  $-3.9^{\circ}\text{C}$  for Sisimiut (averages for the period 1961–1990), which places the area in the zone of discontinuous permafrost (Christiansen & Humlum, 2000). Occurrence of permafrost is variable and highly dependent on local (micro) climatic conditions such as shading and vegetative cover, and the town has several textbook examples of anthropogenic changes in the ground temperature regime and the resulting permafrost distribution due to road construction and other building activities.

Figure 2.2 shows the monthly average air temperatures for the years 2001–

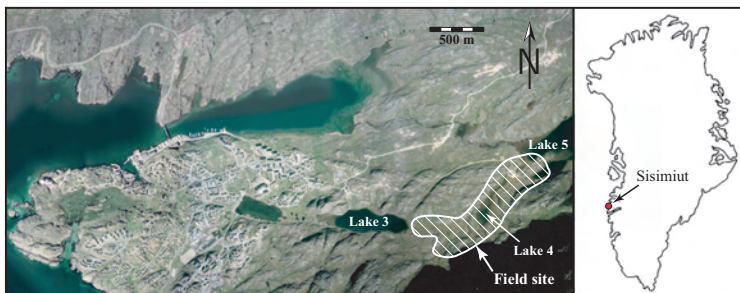


**Figure 2.1:** Location of the field site near the town of Sisimiut, West Greenland.

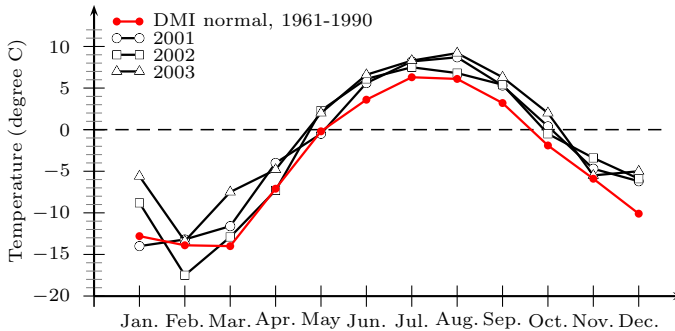


**Figure 2.2:** Monthly average air temperatures for 2001–2003 compared with the DMI normal for the years 1961–1990 (DMI, 2005).

2003, which have been slightly higher than the normal temperature for the period 1961–1990 (DMI, 2005). This is in accordance with reports that permafrost is generally degrading in the Sisimiut area (Foged & Clausen, 2003).

## 2.2 Geological setting

### 2.2.1 The bedrock

Sisimiut is located in the Nagssugtoquidian Mobile Belt, which here consists mainly of banded gneiss with amphibolitic and pegmatic veins (Foged, 1979). The gneisses are highly metamorphosed and altered, and seem to have been derived from granites, which can still be observed in areas where the deformation has been less intense (Escher et al., 1976). The gneisses often appear weathered and fractured, and have two main structural directions, ENE—WSW and E—W.

### 2.2.2 Quaternary deposits

The entire area was ice-covered during the last glacial maximum in the late Weichselian (Weidick, 1976); however, true glacial till deposits are rare in the area. The interaction of isostatic uplift and eustatic sea level rise during the retreat of the ice cover and in the post glacial period has resulted in sedimentary sequences consisting of thick glaciomarine, marine and fluvial deposits (Clausen, 2005, priv. comm.). Typically, the layer overlaying the bedrock is coarse-grained, unsorted glacial or glaciomarine sediments. This is overlain by a sequence of relatively well sorted marine deposits which may comprise clay, silt and sand, often with shell fragments. The top layer is composed of fluvial sediments deposited after the regression. This sequence may include eroded and redeposited marine sediments, and may therefore also contain shell fragments in places.

## 2.3 Location of geophysical field sites

The field location is approximately 3 km east of the town, between the two lakes presently in use for water supply, Lake 3 and Lake 5. Figure 2.3 shows a map of the area concerned. The map is based on local town coordinates, a coordinate system previously used in Greenland by public institutions, such as Nukissiorfiit (the water supply company) and Asiaq (Greenland Survey). It is a metric system with increasing coordinate values from east to west and from south to north.

The most detailed available maps of this area are in town coordinates only, and therefore all maps presented for Sisimiut are in town coordinates. Whenever specific coordinates are given in the text, both UTM and town coordinates will be given. Transformation between the two coordinate systems can be performed by means of an Excel spreadsheet (Jacobi, 2000).

The field area is divided in two parts by the smaller and shallow Lake 4 upstream of Lake 5. It consists of a glacial valley at an elevation of approximately 40–50 m above sea level. To the southeast the Kællingehætten massif rises to elevations of more than 500 m, and to the northeast the valley is bordered by outcropping bedrock with elevations up to approximately 90 m. Several smaller bedrock outcrops are also found in the valley. Typical tundra vegetation covers most of the valley floor. Furthermore, in large areas the surface is very wet during summer months, indicating poor drainage properties and possible existence of permanently frozen ground below the active layer. Between Lake 4 and Lake 5 to the northwest of the stream connecting the two, is a larger area with no vegetation. The sedimentary deposits here consist of well sorted sands of fluvial origin. In the following, the southeastern part, between Lake 3 and Lake 4 will

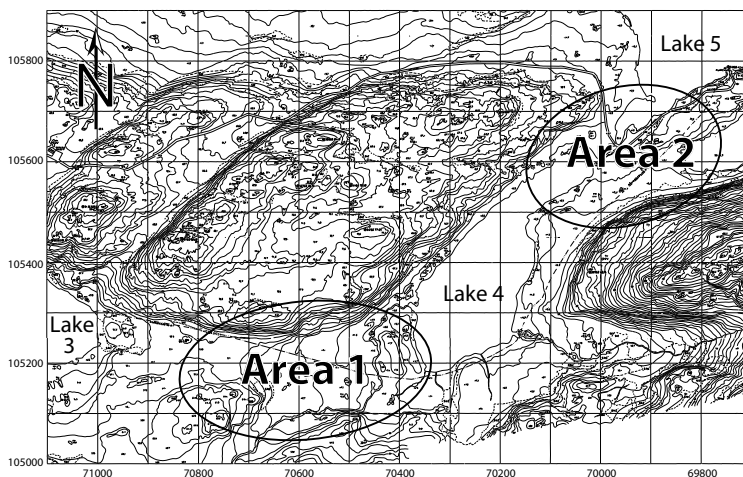


**Figure 2.3:** A map of the survey site showing the two main areas of interest located between Lake 3 and 4 and Lake 4 and 5.

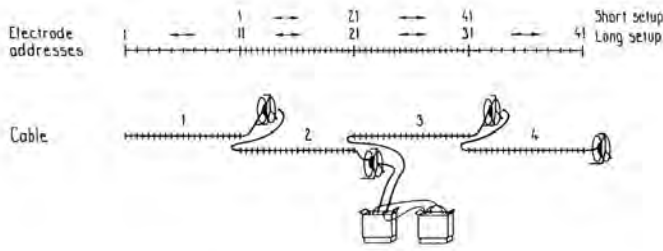


**Figure 2.4:** Measurement setup for Multi Electrode Profiling using the SAS 4000 and the LUND Imaging System (ABEM, 1999).

be referred to as area 1 and the northwestern part between Lake 4 and Lake 5 will be referred to as area 2.

## 2.4 Data acquisition and processing

The geophysical survey was performed during the two consecutive summers of 2002 and 2003. Measurements were carried out during two weeks in the end of June and three weeks in July/August both years.

The geophysical techniques applied and described in this chapter comprised geoelectrical, georadar, seismic refraction and VLF measurements. Horizontal loop frequency domain EM measurements as well as complex resistivity measurements were also collected, and will be treated separately in chapters 3 and 4.

### 2.4.1 Geoelectricity and IP

An ABEM SAS 4000 terrameter was used for all geoelectrical and induced polarization (IP) measurements. The SAS 4000, which has an input impedance of at least  $10\text{ M}\Omega$  (ABEM, 1999), was used with normal stainless steel electrodes for both current injection and potential measurements. Multi Electrode Profiles (MEP) were collected using the LUND Imaging System, in which a total of 41 electrodes are connected to the terrameter through multicore cables and an electronic switching device, see Figure 2.4. Minimum electrode separations of 2.5 and 5 m were used resulting in nominal profile lengths of 200 and 400 m, respectively. The electrode configuration was the Wenner configuration with a-spacings in the range from 1 to 12 times the minimum electrode separation. The normal layout contains a total of 277 measurements and has a high measurement density in the central part, whereas the distant parts have lower densities. After completion of one electrode layout, the setup can be extended by one quarter length at a time.

IP measurements were collected simultaneously with the resistivity data. Dahlin et al. (2002) showed that under normal site conditions, it is possible to collect IP

data using stainless steel electrodes and multicore cables and that inductive and capacitive effects are minimal.

A 50% duty-cycle square current waveform with a period of six seconds was applied, and the transmitted current amplitude was mostly in the range from 20 mA to 100 mA. A delay time of 10 ms was used, and the decay was measured over a one second integration period using ten windows of 100 ms. Four measurements were stacked at each location, and the measured values are expressed as apparent resistivity [ $\Omega\text{m}$ ] and apparent chargeability [ms].

The SAS 4000 supplies relative error estimates based on the standard deviation of the measured values. To obtain a conservative estimate of the relative error on the total chargeability, the error on the individual time windows have been summed and divided by the total chargeability.

Whereas the relative error on the resistivity data in general is very low, much higher errors of more than 20% are not uncommon for the chargeabilities. Measurements with a relative error of more than 5% on the apparent resistivity and more than 25% on the apparent chargeability were discarded. Figure 2.5 shows three examples of observed IP decay curves. Figure 2.5(a) shows the normal expected monotonous decay, with a relatively low error less than 10%. Figure 2.5(b) shows an example of a discarded noisy decay curve. A third type of decay is presented in Figure 2.5(c), where the first or the first few windows show a reduced response, which may be negative as in the presented example. At some locations the negative response was so large that the summation of the total chargeability became negative. The literature contains several examples of negative apparent chargeabilities over three-dimensional targets (Seigel, 1959; Dieter et al., 1969) and Nabighian & Elliot (1976) developed a theoretical model for negative chargeabilities over a layered half-space. However, these publications are concerned with the total apparent chargeability only, the decays are not discussed. It is speculated that the negative effects observed in the Sisimiut field data are due to inductive and capacitive effects, and possibly related to the use of multicore cables. An increase of the delay time would reduce the effects but has not been attempted. Since data points with this type of decay often exhibited large relative errors as well, all such decays have been discarded. In most profiles 10 to 20% of the IP data points were discarded.

The apparent resistivity and chargeability data sets have been inverted using the Res2Dinv software (Loke, 2000). Inversion was carried out using least-squares optimization, and resistivity and chargeability data were inverted sequentially. The chargeability data are presented terms of the inverted chargeability divided by the inverted resistivity — normalized chargeability — as defined by Keller (1959, he termed it "specific capacity") and recently shown by Slater & Lesmes (2002) to be related to the complex surface conductivity.

A short Vertical Electrical Sounding (VES) was collected in area 1. The Schlumberger electrode configuration was applied, and the collected data were inverted using the inversion modeling package SELMA24 (Christensen & Auken, 1992).

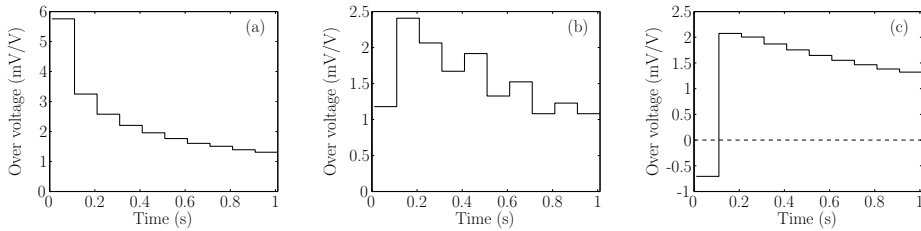


**Figure 2.5:** Three examples of observed IP decay curves. A good monotonous decay (a), a noisy decay curve (b), and an example of negative IP (c).

Furthermore, normal Wenner profiling was conducted in order to quickly delineate areas with very high resistivity. An a-spacing of 10 m was used, and stainless steel electrodes were applied for both current and potential measurements.

### 2.4.2 VLF and VLF-R

A VLF EM16 instrument from Geonics with the additional EM16R console was used for measuring apparent resistivity profiles in the Very Low Frequency (VLF) band. The VLF and VLF-R methods are lightweight methods that are convenient and easily applied in the arctic environment, since they measure the fields generated by distant transmitters positioned around the world. However, measurement profiles are limited to directions perpendicular to (VLF) and aligned with (VLF-R) the direction to the transmitter. According to charts published in Paterson & Ronka (1971) and McNeill & Labson (1991) Sisimiut is located in a zone which should be covered by several transmitters, among which are the NAA in Maine, USA, the GBR transmitter in England, and possibly FUI in France and JXZ in Norway. In practice, however, only the primary field of the GBR transmitter operating at 16 kHz was strong enough to permit measurements. And even this was weak and made the manual nulling procedure difficult at times. As the survey direction of the VLF measurements were poorly aligned with the structures of interest in the present survey area, no anomalies of interest were observed, and only the VLF-R data will be discussed.

### 2.4.3 Seismic refraction

A Terraloc Mark 6 seismograph from ABEM was used for the collection of one seismic refraction profile. A total of 24 geophones were used at a spacing of 5 m. A shotgun with blank shots was used as source. Shotpoints were located at a spacing of 20 m along the profile, starting 2.5 m before the first geophone and ending 2.5 m after the last. An additional forward and reverse off-end shot was performed 17.5 m from the start of the line and 22.5 m past the end, giving a total of 9 shotpoints.

The collected data were band-pass filtered to reduce noise, and first arrivals

were picked using the Seisimager software suite. Manual interpretation was carried out using the intercept-time method and Hagedoorns plus-minus method (Hagedoorn, 1959; Cummings, 1979) where possible. Tomographical inversion was also performed using Seisimager.

#### 2.4.4 Step-frequency GPR

Ground penetrating radar measurements were performed using a step-frequency georadar from the Norwegian Geotechnical Institute (NGI) (Kong & By, 1995). The system uses an HP8714ET network analyzer as both signal generator and receiver. The network analyzer supplies a harmonic signal at discretely stepped frequencies. A range of frequencies from 1 to 1601 MHz at 1 MHz intervals was collected. The sampling time at each frequency was 1/250 s. A separation distance of 1 m was used between the antennas, which were moved at steps of 0.5 m along the profiles.

The collected data were processed using the Matlab software SFGPR, developed at the Arctic Technology Centre by Delapierre (2003, priv. comm.). The optimum frequency range for the reflectors of interest was found to be from 45 to 501 MHz. The selected frequency spectrum was transformed to time domain using the Inverse Fast Fourier Transform technique. A gain function of the SEC type (Spherical spreading and Exponential attenuation Compensation) was applied to the data which are presented in radargrams in two-way travel time (TWT).

#### 2.4.5 Boreholes

During fieldwork in July/August 2003, four boreholes were made, three of which reached the bedrock. The location of these boreholes are given in Table 2.1 in UTM and town coordinates.

**Table 2.1:** The location of boreholes drilled in 2003 is given in UTM (zone 22) coordinates as well as the local town coordinates.

Borehole	UTM – zone 22			Town coordinates	
	Northing	Easting	Elevation	X	Y
2003–4	7426797	386543	42.5 m	70013	105614
2003–5	7426832	386568	43.3 m	69988	105649
2003–6	7426387	385954	48 m	70595	105194
2003–7	7426384	386000	47 m	70549	105192

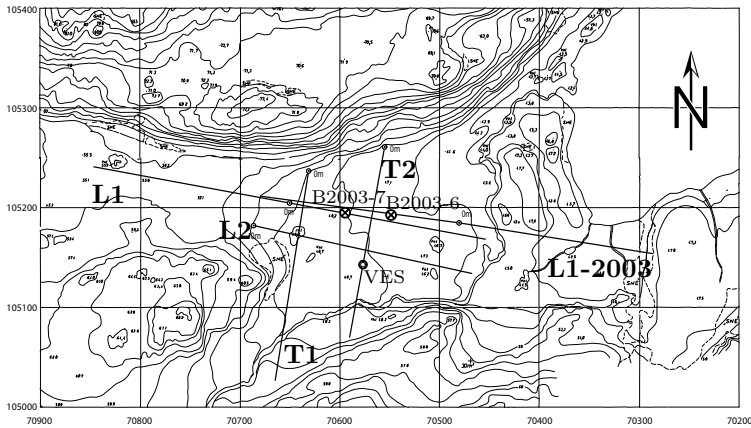


**Figure 2.6:** Map of area 1, showing the location of lines used in the survey, as well as the location of the two boreholes 2003-6 and 2003-7. Most of the surveying was done during June 2002, but the two boreholes and the MEP line L1-2003 were done during August 2003.

## 2.5 Results from area 1

Most of the measurements in area 1 were collected during June 2002. One MEP data set was collected along line L1 (refer to Figure 2.6), and normal Wenner profiling was conducted along line L1, L2, T1 and T2, with an a-spacing of 10 m. VLF-R data were collected along line L1 and L2. An additional MEP line was collected in August 2003 (L1-2003), prior to drilling of the two boreholes 2003-6 and 2003-7.

### 2.5.1 MEP

The MEP data were collected with the intention of estimating the thickness of permafrost in the area as well as the depth to the bedrock. A MEP survey had been performed the previous year by a student group (Andersen et al., 2001), and previous knowledge was therefore available concerning the presence of a highly resistive body of possibly frozen ground. Figure 2.7 presents the inverted model resistivity sections. The profile collected by Andersen et al. (2001) has been re-processed with parameters identical to those used for the other sections and is presented in the figure for reference (but is not shown on the map). From its most westerly point until its center, the 2001 profile is in-line with L1. The remaining 200 m of the profile is in-line with line L1-2003. The maximum separation perpendicular to the 2002 profile is 10 m at the easternmost point of the 2001 profile.

Differences between the three profiles occur mainly in the near surface part, which appears more resistive on the 2002 profile. This profile was collected in June, where the active layer is not yet fully thawed. In fact snow cover was still

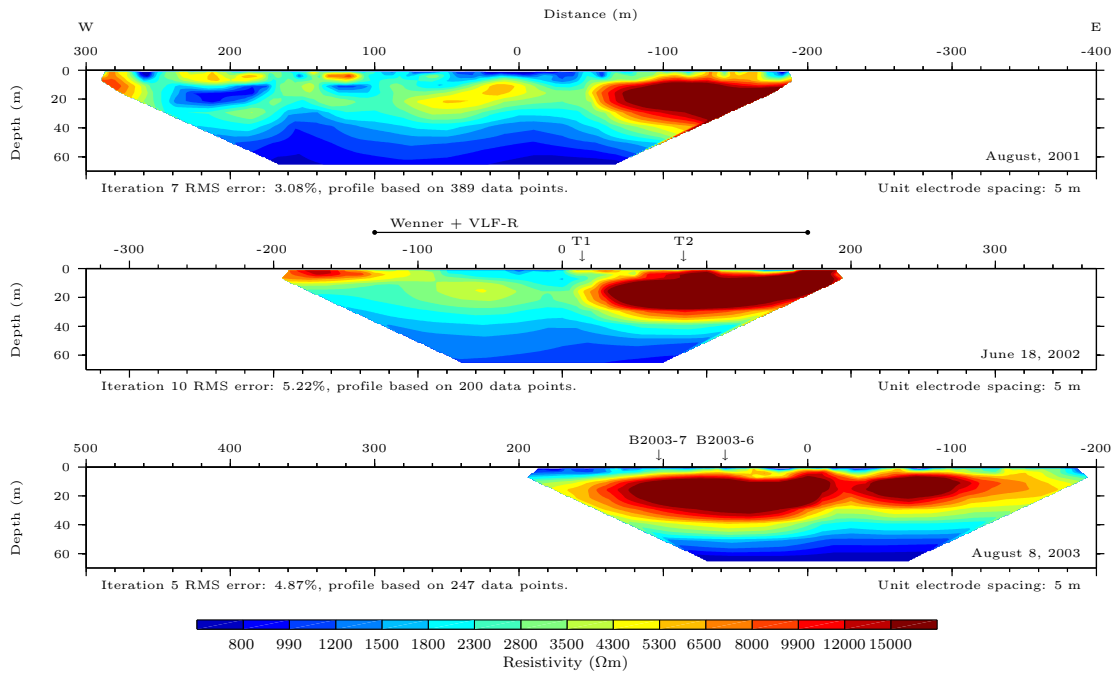


**Figure 2.7:** The L1 MEP line. Data are shown for three different years. The data from 2001 (top) were collected by Andersen et al. (2001).

present several places in the area. The profile collected in August 2003, on the other hand, shows relatively low resistivity at the surface, as does the 2001 profile. The changes in near-surface resistivity thus seem to be related to freezing and thawing of the active layer.

A highly resistive body is found well-aligned on all three profiles in the eastern end of the area. The inverted resistivity of the body is above 15 k $\Omega$ m, and peaks at resistivities close to 50 k $\Omega$ m. These very high resistivities indicate highly frozen sediments possibly with a large ice content. The area was observed to have palsalike properties of upheaval and a rounded form, which is also apparent from the elevation contours in Figure 2.6. On the 2003 profile, a decrease in the resistivity is observed around location -35 m. This is aligned with a small stream crossing the area. The running water causes a larger heat conduction into the ground, resulting in quicker and deeper thawing of the active layer, and possibly higher temperatures in the permafrozen layer as well.

High subsurface resistivities (up to 5.5 k $\Omega$ m) are observed further west on the 2001 and 2002 profiles as well, indicating the presence of frozen ground over most of the length of L1. The bedrock is of relatively low resistivity, 800  $\Omega$ m or less. Assuming that the bedrock interface is coinciding with the lower boundary of the highly resistive body, the depth to the bedrock appears to be between 30 and 40 m, decreasing towards west.

A likely interpretation based on the MEP data alone would be a depth between 30 and 40 m, decreasing to the west.

### 2.5.2 Wenner and VLF-R

Figure 2.8 shows a comparison of normal Wenner profiling data with VLF-R data along L1. The location of this profile is marked in Figure 2.7 above the 2002 resistivity model.

The Wenner profiling data is similar to one sequence of the apparent resistivity data collected with the MEP technique. However, it is not possible to quantitatively interpret Wenner data for a single a-spacing, and all conclusions must be made based on the measured apparent resistivity data. In this case they are seen to be very stable around 3 k $\Omega$ m until after position +20 m, where a drastic increase occurs, and the measurements become more oscillating. The apparent resistivity data from the VLF-R method presented in the lower part of the figure shows a similar tendency. However, the overall apparent resistivity values are lower. The penetration of EM fields can be described by the skin-depth, which is defined as the depth at which the field-amplitude is reduced by 1/e or approximately 37%. Using a bedrock resistivity of 800  $\Omega$ m and a frequency of 16.0 kHz, the skin-depth of the field from the GBR transmitter is given by (Telford et al., 1990):

$$\delta = \sqrt{\frac{2\rho}{\omega\mu_0}} \approx \sqrt{\frac{800\Omega\text{m}}{4\pi^2 \cdot 10^{-7} \cdot 16\text{kHz}}} \approx 113\text{m} \quad (2.1)$$

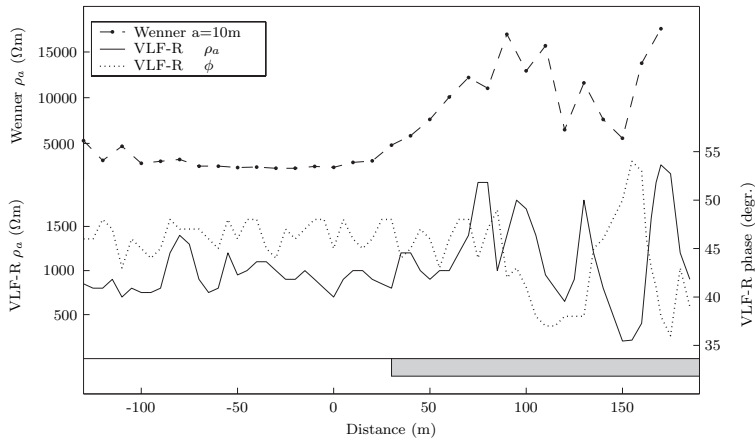


**Figure 2.8:** Comparison of Wenner profile and VLF-R data from the L1 line. The grey box in the lower part of the figure indicates the location of the highly resistive anomaly on the MEP line from June 2002.

where  $\mu_0$  is the magnetic permeability of free space and  $\omega$  is the angular frequency. Thus the investigated volume with the VLF-R method is large, and the bedrock resistivity has a large influence on the measured apparent resistivity, resulting in lower values than those obtained through Wenner profiling.

The phase angle of the VLF-R measurement can be used to anticipate the subsurface layering. A phase angle of approximately  $45^\circ$  indicates homogeneous conditions, whereas the phase angle will generally increase when a lower more conductive layer is present and decrease when a lower more resistive layer is present (Geonics, 1979).

The phase angle in the first part of the profile is slightly above  $45^\circ$  on average, indicating a high over low environment. In the westernmost part of the profile, both phase and apparent resistivity oscillate drastically, indicating resistivity changes in the bedrock. These changes may be what is also seen to a lesser extent in the oscillating Wenner measurements.

The highly resistive body observed on the MEP section, the location of which is indicated in Figure 2.8 by a grey rectangle, is well aligned with the anomalous changes in both VLF-R and Wenner data.

Based on the Wenner profiling and VLF-R data, as well as information from the MEP sections of 2002 and 2003, a map of the extent of the high resistivity area has been produced, see Figure 2.9. On the map, the approximate location of the anomalous bedrock zone observed on the VLF-R profiles is also shown. Effects of this anomaly were identified on the T2 Wenner profile and in the long a-spacing apparent resistivity data from two of the MEP profiles. The anomaly could not be established with certainty on the T1 profile. The direction of this zone is

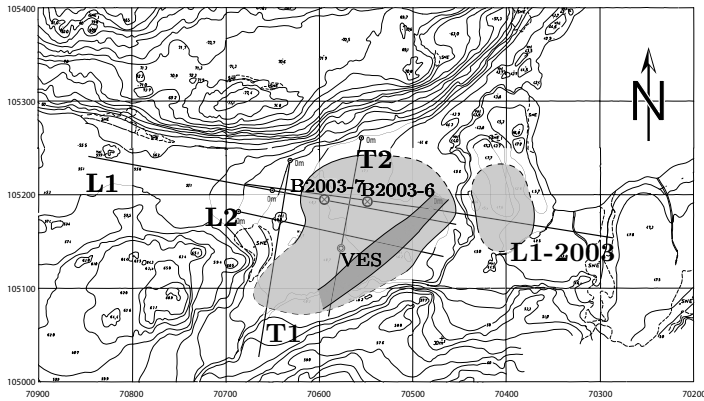


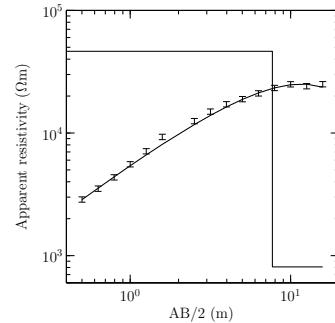
**Figure 2.9:** Map showing the extent of the highly resistive area (light grey) as interpreted from Wenner profiles, MEP, and VLF-R data. The anomalous low resistivity bedrock zone is also included (dark grey).

**Figure 2.10:** Fit of the inverted model to the field data for the VES collected on T2 (right).

**Table 2.2:** Inverted model for the vertical electrical sounding collected on T2.

	$\rho$	sdev	Thickn.	sdev
Layer 1	606 $\Omega\text{m}$	und.	0.1m	und.
Layer 2	46.4 $\text{k}\Omega\text{m}$	0.22	7.6m	0.31
Layer 3	809 $\Omega\text{m}$	0.50	-	-

und.: undetermined



approximately NE-SW, which corresponds well with main structural elements in the area.

### 2.5.3 Vertical Electrical Sounding

A short Vertical Electrical Sounding (VES) was collected centered at location +120 m on the T2 profile. The largest current electrode separation applied was 31.7 m. The ground was observed to be frozen hard very close to the surface, and it was difficult to plant the electrodes. A three layer inversion was carried out with initial parameters based on resistivities and layer thicknesses interpreted from the MEP profile. Only the basement resistivity was loosely bound at 800  $\Omega\text{m}$ . The parameters of the inverted model (refer to Table 2.2) were poorly determined, but nevertheless of great interest. The thickness of the highly resistive layer is interpreted here as being much less than what was found from the MEP.

**Table 2.3:** Depth, frozen bulk density ( $\rho_{bf}$ ), porosity ( $\varphi$ ), and percent ice volume for selected samples from B2003-6 and B2003-7, based on raw data from Mortensen (2004).

Sample	Depth [m]	$\rho_{bf}$ [g/cm <sup>3</sup> ]	$\varphi$	Ice vol. [%]
<b>B2003-6</b>				
P6	2.5	2.13	0.335	31.2
P7	3.0	1.58	0.640	63.4
P9	4.0	2.01	0.408	40.3
P10	4.5	1.11	0.868	80.7
P15	7.0	1.51	0.655	60.4
<b>B2003-7</b>				
P6	3.0	1.74	0.524	46.18
P12	6.0	1.66	0.590	57.32
P15	8.0	1.69	0.573	55.18
P20	10.5	1.96	0.434	42.64

## 2.5.4 Boreholes

Two boreholes were drilled in August 2003. Borehole logs and lithological descriptions have been compiled by Clausen (2005, priv. comm.) and are included in Appendices F.3 and F.4. Both boreholes were terminated after reaching the bedrock at depths of 9.7 m and 13.0 m for boreholes 2003-6 and 2003-7 respectively. The two boreholes show similar sequences starting with coarse-grained glacial sediments of marine origin at the bottom. On top is a thick sequence of marine clays of postglacial origin with varying silt and sand content, but with a coarsening tendency towards the top. The top of the sequence is composed of sands and silts of marine or fluvial origin. Both boreholes show the entire sedimentary sequence expected for this area.

The depth to frozen ground was 0.6 m and 0.15 m for boreholes 2003-6 and 2003-7 respectively. The entire sedimentary sequence had a high interstitial ice content and several horizons of massive ice were penetrated at both locations. The thickness of such ice lenses were mostly between 0.5 to 1.5 cm, but occasionally larger lenses of up to 10 cm in thickness were observed.

Table 2.3 summarizes some physical properties of the cores, which were collected, transported and stored in frozen condition, and studied in the laboratory by Mortensen (2004).

No temperature observations are available from the borehole, and thus the permafrost distribution in the bedrock is unknown. Nevertheless, since the sediments penetrated immediately above the bedrock interface were frozen with a high ice content, it is likely that the bedrock is at subzero temperatures to a considerable depth.

## 2.5.5 Implications for the geophysical interpretation

The depth to the bedrock is grossly overestimated when using only information from the MEP interpretation. This is partially due to poor depth resolution of the electrode layout, but the horizontally layered macroanisotropy due to the ice content may also result in equivalency problems. As described by Maillet (1947) such a vertical sequence can be described by a constant transverse conductance,  $T = h \cdot \rho$ , and thus the thickness and effective resistivity can be varied (within limits) without significant changes in the measured apparent resistivity. The interpretation of the layer properties may be further complicated by sandwiching between two more conductive layers.

To illustrate the problem, a simplified 2-D section of the encountered three layer permafrost situation has been studied. The apparent resistivity section, corresponding to the measurements made with the MEP equipment, has been forward modelled using the Res2Dmod software (Loke, 1999), and subsequently inverted with the same parameters as the measured field sections. The result is presented in Figure 2.11. It is clear that the thickness of the highly resistive body is overestimated, whereas the thickness of the less resistive part of layer two is better resolved. Additional modeling has shown that the problem of overestimating thickness could have been somewhat reduced — although not eliminated — by choosing a smaller electrode separation of i.e. 2.5 m.

Another interesting observation is that a substantial part of the sedimentary sequence is composed of clays, and yet very high resistivities are observed. Hoekstra et al. (1975) presented results showing a linear relationship between the volume percentage ice content and the resistivity of a Fairbanks silt deposit. In-situ resistivity information sufficiently accurate to allow correlation to the measured ice contents is not available in this case. Nevertheless, it can be safely established that the resistivities indicated by both MEP and VES are substantially higher than those reported by Hoekstra et al. for similar ice volumes ( $\sim 50\text{-}60\%$ ).

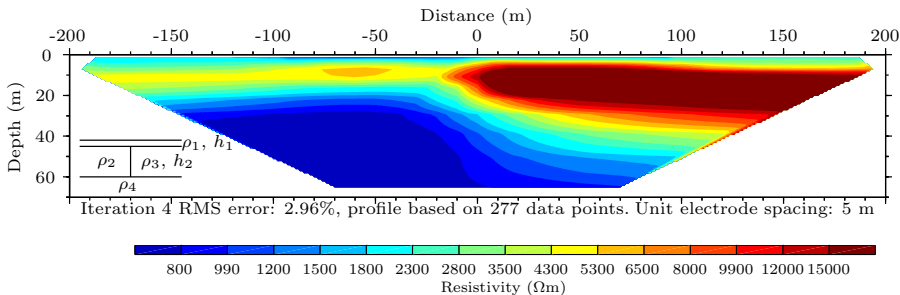


**Figure 2.11:** Model of permafrost section. A 0.5 m thick unfrozen active layer,  $\rho_1 = 600 \Omega\text{m}$ , overlies a 12.5 m thick frozen zone of varying resistivity,  $\rho_2 = 5 \text{ k}\Omega\text{m}$  and  $\rho_3 = 50 \text{ k}\Omega\text{m}$ . The basement resistivity ( $\rho_4$ ) is  $800 \Omega\text{m}$ . The model apparent resistivity has been calculated for the same electrode configuration and layout as applied in the field using RES2Dmod, and subsequently inverted with RES2Dinv.

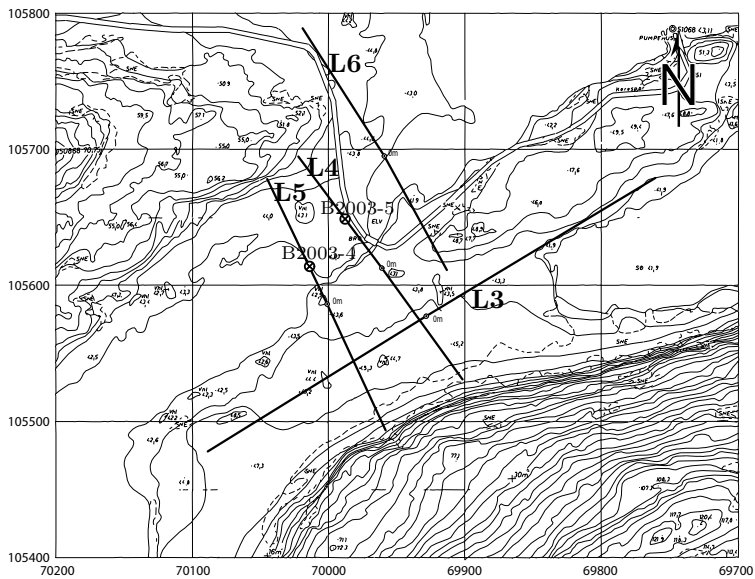


**Figure 2.12:** Map of area 2 showing the location of lines used in the survey, as well as the location of the two boreholes 2003-4 and 2003-5. Surveying conducted during July/August 2002, and June and July/August 2003.

Apart from the ice content, the high resistivity of the clay deposits may also relate to the mineralogy. In studies of quaternary deposits from the Sisimiut area, Foged (1979) found that the material in the clay fraction, did indeed poses clay-like properties for swelling, and x-ray diffraction analyses indicated Illite-like structure. These findings are still disputed, and other scientists argue that even the clay fraction has not been significantly chemically altered, and thus reflect the mineralogy of the basement (Clausen, 2005, priv. comm.). If so, the frozen clay deposits of the area may not have the good surface conduction properties normally attributed to clays.

## 2.6 Results from area 2

This area was surveyed during field campaigns in July/August 2002 and again in June and July/August 2003. Four main profiles were defined, L3 to L6, see Figure 2.12. Profiles L3, L4 and L5 were surveyed with MEP during each of the three field campaigns, to study the temporal variation of resistivity and IP effects. During the second field campaign of 2003, a seismic refraction profile was measured on L4, and GPR data were collected along L4 and L5.

### 2.6.1 Geoelectricity and IP

Figure 2.13 shows the inverted resistivity profiles collected along L4 for all three field campaigns. Most of the profile is dominated by high resistivity interpreted as being related to permanently frozen sediments extending to depths of approximately 20 m. Yet a narrow area centered around pos. -20 m shows very low resistivities, a resistivity contrast of approximately 200:1. Temporal changes are apparent between the early summer and late summer measurements in the upper part of the profiles corresponding to frozen and unfrozen active layers.

Induced polarization data from the same profile are presented in Figure 2.14. Areas with high values of normalized chargeability are correlated with areas interpreted as unfrozen, and the sections further indicate a division of the anomaly in an upper part related to the sedimentary deposits, and a lower part possibly related to bedrock chargeability.

Similar results were obtained on line L5 (Figures 2.15 and 2.16). Here the low resistive anomaly has increased in size and the high resistive areas have diminished drastically in size. This is interpreted to be due to the proximity to Lake 4, the heat capacity of the water body influencing the distribution of massive permafrost. Temporal changes are very pronounced on this profile, with the active layer showing important changes in resistivity over the course of only six weeks.

The division of the normalized chargeability anomaly is here more pronounced than on the L4 profile. The low resistive areas in the near-surface layers observed in the late summer profiles, are correlated with areas of increased normalized chargeability which are not distinguishable with the applied contour intervals. It should be noted that the amplitude of the June anomaly is in fact the same as that observed in July/August on profile L4. The contour values of the two plots are not comparable, due to the excessively high normalized chargeabilities observed in the late summer on L5.

The L4 and L5 resistivity models leave the impression that the basement is more conductive north of the anomaly than south of it. A 400 m profile collected along L3 (which is approximately perpendicular to L4 and L5, to the south of the anomaly) in June 2003, shows that this is not the case (refer to Figure 2.17). Normalized chargeability data (not shown) also show a large response for the basement below L3.

### 2.6.2 Boreholes

Boreholes 2003-4 and 2003-5 were drilled in August 2003 on profile L5 and L4, respectively. The logs are included in Appendices F.1 and F.2 and show that frozen ground was encountered at a depth of 1.6 m in 2003-5, but not in 2003-4. The latter reached the bedrock at a depth of just over 19 m. This depth correlates well with the expected depth based on the MEP profiles.

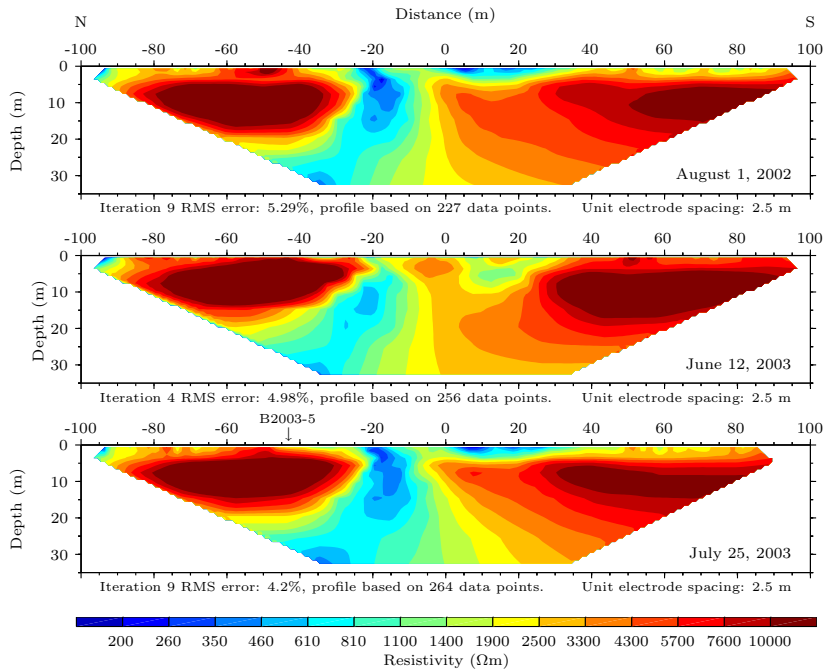


Figure 2.13: Inverted resistivity sections from the L4 line.

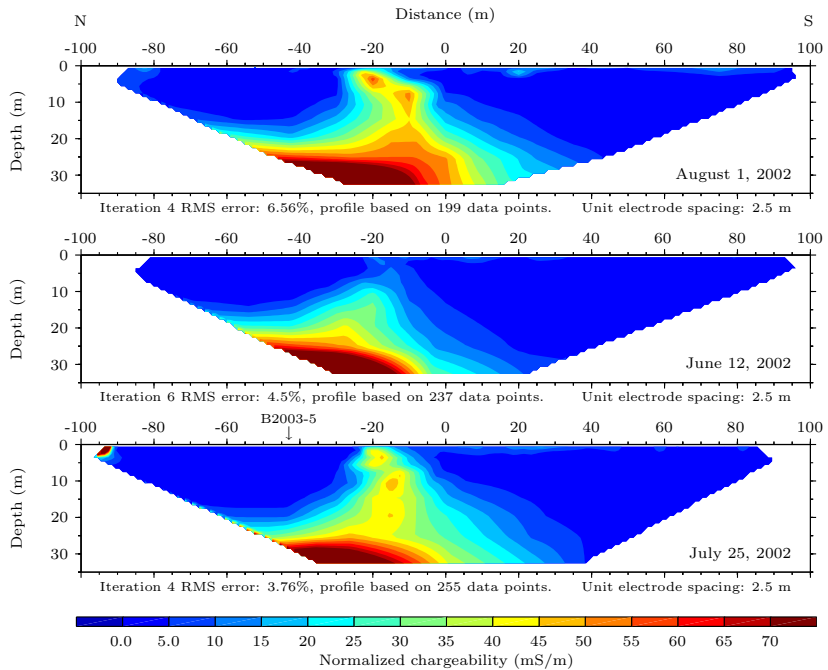


Figure 2.14: Inverted normalized chargeability sections from the L4 line.

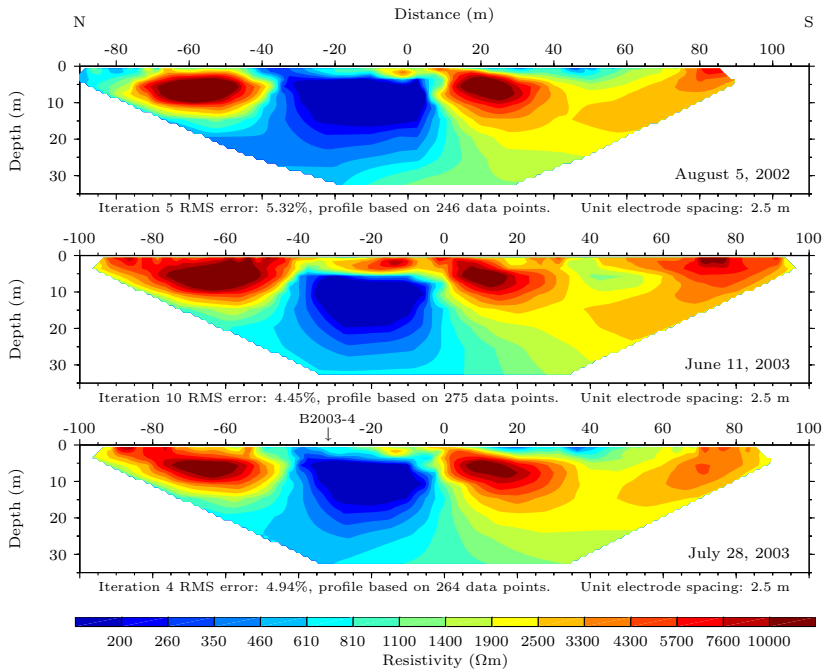


Figure 2.15: Inverted resistivity sections from the L5 line.

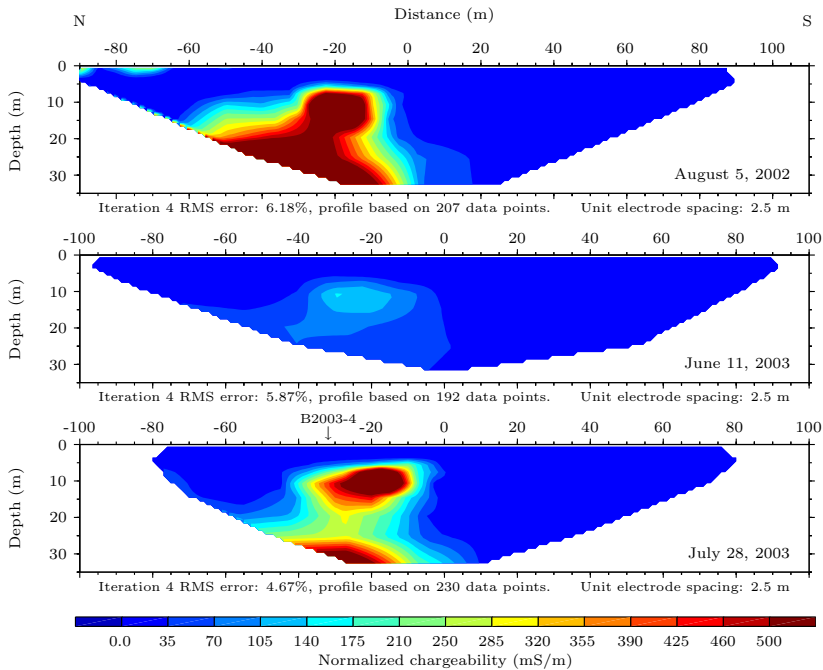
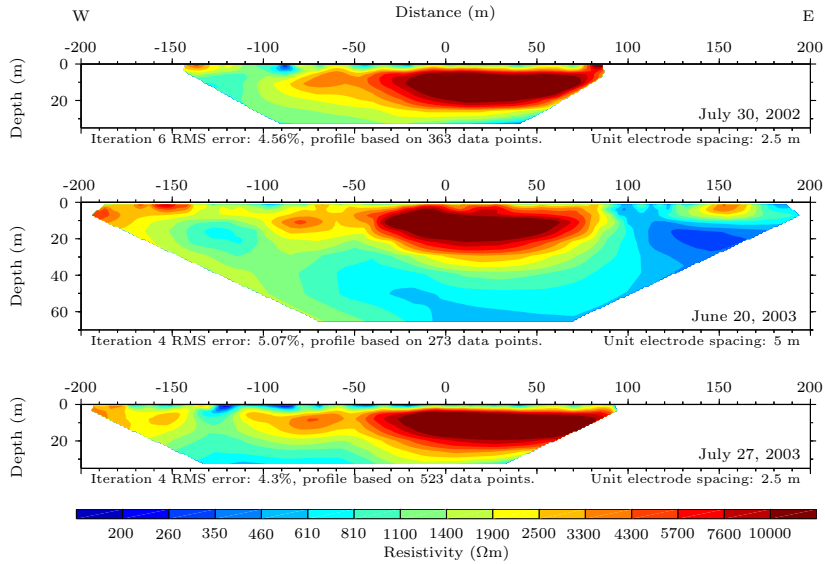
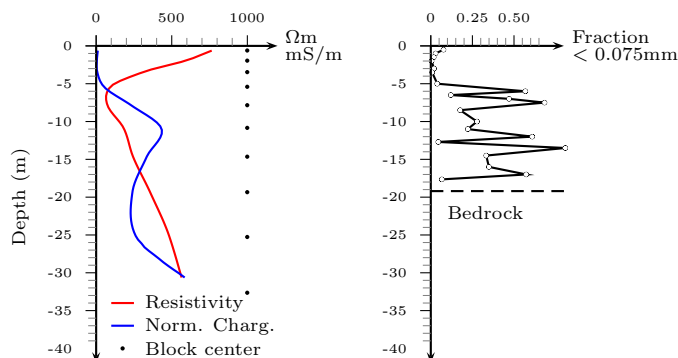


Figure 2.16: Inverted normalized chargeability sections from the L5 line.

Part of the marine and meltwater sequences, from a depth of approximately 6 m, has a high fraction of fines. Figure 2.18 shows relatively good correlation of these sequences with the normalized chargeability parameter, which is in concordance with the suggestions of Slater & Lesmes (2002) that the parameter is related to surface conductivity. The parameter should be valuable in mapping the unfrozen fines of this area, but is not useful when sediments are frozen.



**Figure 2.17:** Inverted resistivity sections for the L3 line.



**Figure 2.18:** Comparison of the inverted resistivity and normalized chargeability with the fraction of fines ( $\phi < 0.075\text{mm}$ ) observed in B2003-4. The inverted parameters are interpolated, and the depths to the centers of the model blocks used in the interpolation are indicated.

### 2.6.3 Seismic refraction

Traveltime curves for the seismic refraction profile collected along L4 are shown in Figure 2.19. The three controls formulated by Leung (2003) to identify problems with incompatible traveltime data have been applied to the data set. Several shot combinations have incompatible reciprocal times, especially when the data spans position -20 m of the profile. Some occurrences of incompatible slopes were also observed. This indicates that subsurface layering is not homogenous, and that standard interpretation methods may not be applicable over the entire profile length.

Apparent directly from the traveltime curves is a change in near-surface velocity around location -20 m, as well as indications of a discontinuity between location -20 m and 0 m.

Hagedoorns plus-minus method was applied to the data set and was successful at estimating depths to the first reflection in the northern end of the profile. The rugged appearance of the traveltime data in the southern end made precise layer assignment difficult, and Hagedoorns method was thus unsuccessful. Estimates of the depth and velocities in this area and around shotpoint -20 m have been calculated based on averages of observed velocities and the corresponding intercept times. A schematic representation of the manually interpreted velocity model of the shallow subsurface is given in Figure 2.20.

The shallow refractor is interpreted as being the boundary between the active layer and the permafrost. The calculated depth is somewhat shallower than the depth of 1.6 m observed in borehole 2003-5, but the velocity contrast is within the expected range (Roethlisberger, 1961; Timur, 1968; Scott & Hunter, 1977; King, 1984). Part of the discrepancy may be attributed to the large spacing between geophones compared to the depth of the refractor. The layout was dimensioned to give a depth to the bedrock, yet only uncertain estimates amounting to approximately 6 km/s were obtained from the extreme ends of the profile.

The anomalous zone around -20 m is aligned with the stream connecting the two lakes, and the increase in velocity is due to the saturated, unfrozen sediments.

The results of the tomographic inversion (Figure 2.21) gives an estimate of the depth to the bedrock of 15–20 m in the northern part of the profile, and apparently somewhat shallower to the south. The possible location of a discontinuity in the bedrock surface is indicated around -10 m. The inverted velocity of the bedrock was highly dependent on the maximum bounds on velocity, indicating a poor determination on both velocity and depth. Also distinguishing between frozen sediments and bedrock is difficult due small resistivity contrasts.

### 2.6.4 Ground penetrating radar

Very good resolution of the near surface sedimentary deposits has been obtained with the ground penetrating radar technique. Figure 2.23 shows the profiles collected along L4 and parts of L5. One strong clear reflector, related to the

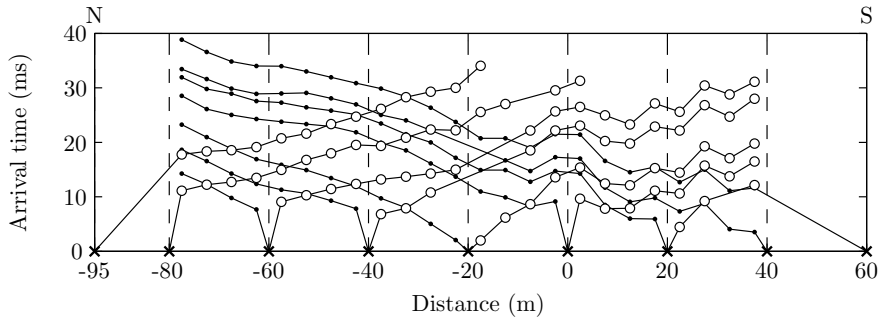


**Figure 2.19:** Shotpoints and traveltimes plots for the seismic refraction data obtained on profile L4.

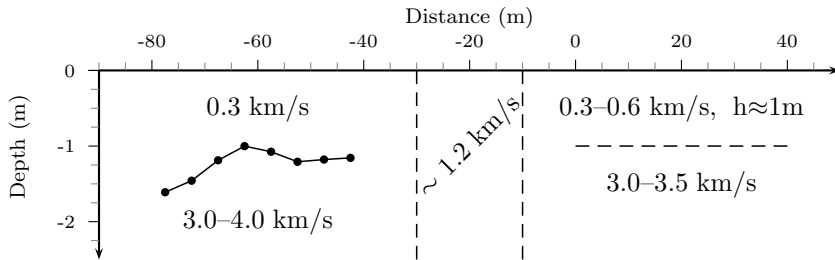


**Figure 2.20:** Schematic representation of velocities and thicknesses interpreted through Hagedoorns plus-minus method (left) and intercept times for the collected seismic data.

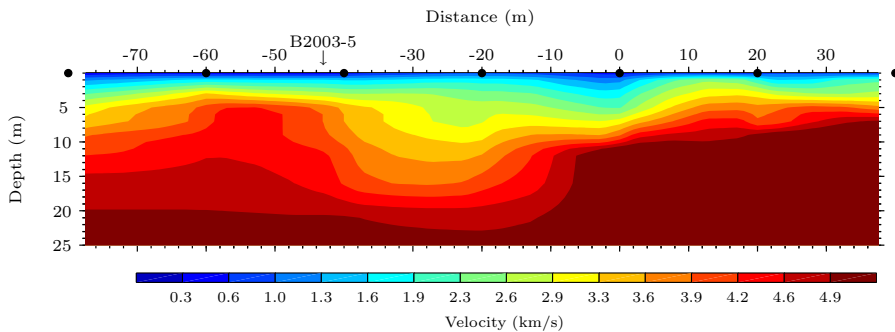


**Figure 2.21:** The result of the tomographic inversion of seismic refraction data collected along profile 4. Shot points are indicated with a point at the ground surface.

active layer to permafrost interface, is visible over most parts of the profiles.

A Common Mid-Point (CMP) data set was collected at position -43 m on L4, before drilling was commenced. In a CMP sounding, the two antennas are moved successively farther away from a common mid-point in opposite directions. As described by Annan & Davis (1976) the resulting data can be used to establish both the depth to relatively planar reflecting interfaces and the propagation velocities above them. Figure 2.22 shows the sounding and interpreted direct air and ground waves, as well as two identified reflectors, and Table 2.4 lists the inferred ground and propagation properties. The reflector depths and relative permittivities are in concordance with the available borehole information. The high relative permittivity of the second layer is due to the water saturation of the sediments immediately above the permafrost.

Interpretation of the depth to the top of the permafrost based on the GPR profile L4 is in good agreement with interpretation of the seismic refraction data. Between position -80 m and -40 m, the overall shape of the boundary is identical, although the depths identified with the two methods are not in absolute agreement. In the southern end, both methods indicate a more shallow depth to the interface around one meter.

Due to the shallow depth of the reflector, it is necessary when calculating depths to take into account the antenna separation and include the offset of zero time due to the traveltime of the direct wave in the air. A depth scale based on a ground velocity of 0.12 m/ns is included in Figure 2.23.

On the profile along L5 the same reflector is visible, but it is abruptly terminated at location -87 m and -53 m. The part of the profile where the interface is visible is correlated with the area of high ground resistivity on the MEP profile (refer to Figure 2.15). The southern termination correlates with the area of low resistivity, causing quick attenuation of the radar waves. It is also likely that changes in the coupling between the antennas and the ground influence the re-

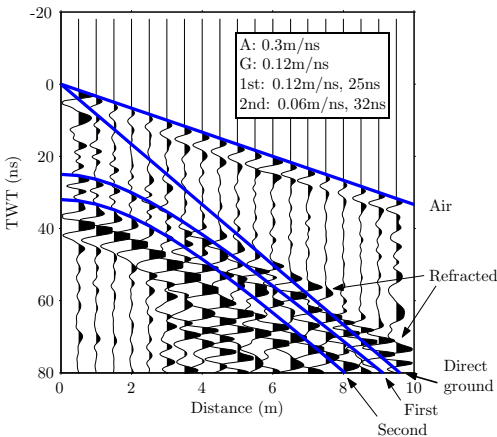


**Figure 2.22:** CMP sounding on L4 at position -43m (left).

**Table 2.4:** Summary of layer velocities, relative permittivities and reflector depths as inferred from the CMP sounding.

Layer	Velocity (m/ns)	$\epsilon_r$	$t_0$ (ns)	Depth (m)
Air	0.3	1	0	-
First	0.12	6.25	25	1.50
Second	0.06	25	32	1.76

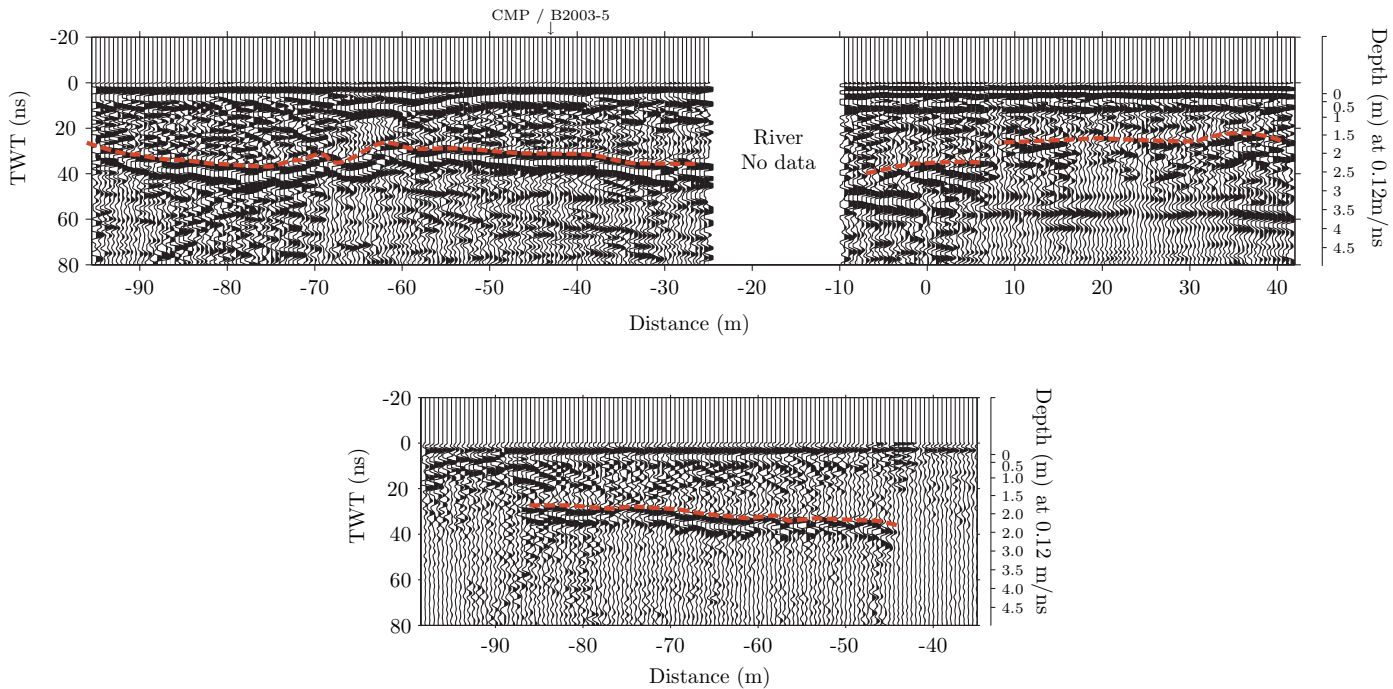


**Figure 2.23:** SFGPR profiles obtained on line L4 and L5. The dashed red line indicates the interpreted depth of the interface between active layer and permafrost. The metric depth scale is an indication only. It is based on a propagation velocity of 0.12 m/ns corresponding to the value in the top layer in B2003-5.

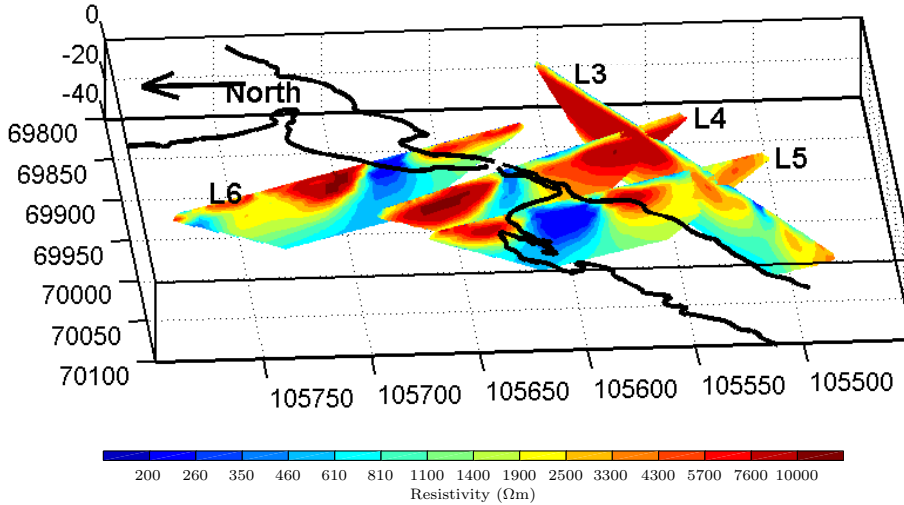


**Figure 2.24:** Illustration of the resistivity distribution in area 2, and the alignment of the low-resistive anomaly with the water bodies.

sults, as changes in the topsoil properties (such as water saturation) were observed due to the vicinity of the lake. The northern termination is not well understood, but may also relate to changes in the subsurface resistivity.

### 2.6.5 Interpretation

In Figure 2.24 four of the collected resistivity profiles have been oriented in three dimensions, in order to give a better impression of the resistivity distribution in the subsurface. The shoreline of Lake 4, Lake 5 and the connecting stream are shown as well. A striking correlation is seen between the location of the low resistive anomaly and the water bodies.

All available information supports the interpretation that the anomaly is due to unfrozen sediments, a talik, due to the presence of the water bodies. This is interesting because the water flow in the stream connecting the two lakes is small, except for times of peak runoff in the early summer months. Apparently the flow is adequate to keep the ground unfrozen in the affected areas (except for the active layer), and indicates that the permafrost in the area is indeed vulnerable.

## 2.7 Discussion

For the two areas studied, it was possible to determine important features of the permafrost distribution using conventional geophysical methods. In area 1, a highly resistive body was delineated using geoelectric and VLF-R measure-

ments. Borehole information confirmed the presence of frozen ground with a high ice-content coinciding with the mapped structure. In area 2, a combination of resistivity, IP and georadar measurements proved useful in the prediction of lateral distribution of frozen ground and thickness of the unfrozen active layer. The interpretation was in concordance with information from two boreholes, one intercepting frozen ground, the other one not. The geophysical manifestations of permafrost in this area are high resistivities combined with low normalized chargeability and a strong GPR reflection from the boundary between active layer and permafrost.

Furthermore, the IP measurements expressed in normalized chargeabilities proved interesting in the distinction between unfrozen sand and finer sediments. This parameter and its relation to the geology should be studied in detail and could become a useful tool in the evaluation of the risk of upheaval and massive ground ice formation upon permafrost aggradation.

On the other hand, serious problems were encountered when trying to establish the thickness of the permafrost as well as in distinguishing between different sediment types in frozen condition. As the IP response was low in frozen areas and the georadar did not reveal much deep information, only resistivity information is available to support such interpretations. However, the resistivity contrasts between frozen and unfrozen sediments are unexpectedly large in the study area. Especially the frozen clay and silt deposits show maximum resistivities that are one to two orders of magnitude higher than those reported in the review by (Scott et al., 1990). Other studies in Greenland show results in agreement with the those of Scott et al. Geoelectrical measurements on the Disko Island, which were accompanied by borehole information, showed frozen clay deposits with resistivities on the order of a few hundred  $\Omega\text{m}$  (Ingeman-Nielsen, 2001). Similar results were obtained in Kangerlussuaq in August 2005 (unpublished data), and data from Qaanaaq also show low resistivities in an area expected to be permafrozen, although no borehole information was available (Baumgartner, 2003, priv. comm.). Thus, if geophysical studies are not accompanied by borehole information, interpretation of lithology in frozen areas is difficult and unreliable. In some cases, the presence of frozen ground may even be misinterpreted due to low resistivities.

If the normalized chargeability of frozen sediments proves to be always low, independent of sediment type, this parameter may constitute the additional information needed to ensure correct interpretation of the presence of frozen ground. For distinguishing between frozen sediment types or determining the presence of massive ground ice and estimating ice content, other methods are needed.

Seismic refraction surveys have proved useful in a number of similar permafrost related surveys (Roethlisberger, 1961; Scott & Hunter, 1977; Wescott, 1982), but Scott et al. (1990) concludes that the method is mostly useful in determining thickness of and variations in the active layer. The results presented here are in concordance with this latter position. The relatively complicated situation encountered in survey area 2, combined with what seems to be a relatively small velocity contrast between frozen sediments and bedrock, has in this

case rendered the depth to bedrock poorly determined at best. Nevertheless the method has supplied some information on the relative changes in bedrock topography, which have been neither confirmed nor contradicted by other methods. It is possible that the method would have been more successful had it been applied in the more simple environment found in area 1.

On the basis of the presented results it seems necessary to study the use of other geophysical methods not previously used in permafrost mapping in the Greenlandic environment. Preliminary tests have been performed with gravimetric equipment, but the soft, water-rich and irregular surface soils made precise alignment and manual reading very difficult. It is therefore suggested that such measurements be undertaken in late spring or early winter, when the ground is frozen. The method should be capable of supplying a better determination of the bedrock topography, and has been reported to give information on the distribution of ground ice (Kawasaki et al., 1982).

The application of a small coil frequency domain electromagnetic method and complex resistivity measurements have been addressed in this study. The first was chosen because it is a light-weight, non-grounded method which is easily and rapidly applied and thus cost effective. The latter method is more cumbersome but has theoretical potential in discrimination between sediment types and delineation of permafrost. The results of this research is presented in chapters 3 and 4.

## 2.8 Conclusion

A field study of two permafrost locations in the vicinity of the town of Sisimiut, West Greenland has been presented. The combination of resistivity and IP measurements with georadar data proved powerful in determining the lateral extents of permanently frozen sediments, as well as the depth to the top of the permafrost. Indications of frozen ground at the Sisimiut field site were high resistivity, low normalized chargeability and a strong reflector at the top of the permafrost. Temporal variations in the resistivity structure of the subsurface were recorded, indicating that multielectrode profiling may be useful in studying the growth or degradation of permafrost. The use of IP data to distinguish unfrozen segments with a high content of fine-grained sediments seems promising, but may be more useful in areas where permafrost is less pronounced.

Despite these interesting results, traditional methods face severe problems when it comes to the important problem of distinguishing frozen sediment types and detecting the presence of massive ground ice. Although some aspects of the vertical permafrost distribution could be clarified, the applied methods also had difficulties determining the transition from sediments to bedrock. Other techniques are needed to improve interpretations of such features.

# The FDEM method

---

## 3.1 Introduction

The FDEM technique comprises a number of different individual techniques. The discussion here is limited to the ground based, near-field technique based on small coils, which will be referred to simply as the FDEM technique. This method has the advantage of being a fast and light-weight surveying method, which requires no electrical contact with the ground. In theory it can therefore be used year round at low cost. In terms of data handling, inversion and modeling, the method is further advantageous, as both transmitter and receiver can be treated as magnetic dipoles, thereby simplifying the involved equations.

The FDEM technique has previously been applied in arctic environments for permafrost studies. It has been used to map the lateral extent of permafrost and the presence of massive ground ice (Hoekstra, 1978; Osterkamp et al., 1980; Kay & Duckworth, 1983), and has also been used to study the growth of permafrost after draining of a lake (Sinha & Stephens, 1983b). Studies of frazil ice that may cause damming of channel flow in rivers have also been undertaken (Arcone et al., 1987). All of this work has been done with Low Induction Number (LIN) instruments (or ground conductivity meters) that operate at sufficiently low frequencies that the ground conductivity can be assumed to be proportional to the imaginary part of the measured response. The general result is that although lateral variations may be detected, the vertical distribution of permafrost and distinction between changes in permafrost or changes in lithology is seldom possible, unless previous geological information is available from boreholes. A few studies of permafrost situations using multifrequency instruments have also been published (Daniels et al., 1976; Sinha & Stephens, 1983a; Palacky & Stephens, 1992) and report more optimistic results in relation to clarifying vertical permafrost distribution.

Yet, in the Greenlandic environment the multifrequency FDEM technique faces problems. Rugged topography and loss of line of sight makes proper alignment and positioning of the coils difficult. This chapter describes a study of some relevant aspects of the sensitivity of the FDEM method to different types

of misalignment of transmitter and receiver. A test of an APEX MaxMin system at the field site near Sisimiut (area 2) is also presented.

### 3.2 Theoretical background

The fields of a loop source of current can be approximated by the fields arising from a magnetic dipole source with the magnetic moment  $m = IS$ , where  $I$  is the current flowing in the loop and  $S$  is the effective area of the loop. The approximation is valid as long as the distance to the observation point is large compared to the loop radius (Wait, 1955).

The orientation of a magnetic dipole can be fully described by the two angles  $(\theta, \phi)$ , see Figure 3.1, where  $\theta$  is the inclination of the dipole axis from vertical, and  $\phi$  is the angle of rotation around the  $z$ -axis. Both receiver and transmitter can be treated as a superposition of three orthogonal dipoles directed along the axes of the coordinate-system. Thus, the field from a magnetic dipole transmitter, as observed by a magnetic dipole receiver is given by the relation:

$$\begin{aligned} H_r = & \sin \theta_r \cos \phi_r (\sin \theta_t \cos \phi_t H_{xx} - \cos \theta_t H_{zx}) \\ & + \sin \theta_r \sin \phi_r (\sin \theta_t \sin \phi_t H_{yy}) \\ & - \cos \theta_r (\sin \theta_t \cos \phi_t H_{xz} - \cos \theta_t H_{zz}) \end{aligned} \quad (3.1)$$

where subscript  $t$  denotes the transmitter, subscript  $r$  denotes the receiver, and  $H_{ij}$  is the field-component from an  $i$ -directed transmitter as observed by a  $j$ -directed receiver dipole. Equation 3.1 is a simplification which is valid over a layered half-space, the general solution is given in Paper A.

The three configurations most often used in FDEM prospecting are the Vertical Coaxial (VCA), the Vertical Coplanar (VCP) and the Horizontal Coplanar (HCP) configurations, referring to the coil planes (vertical/horizontal) and axes. In terms of the field components of equation 3.1, the measured field of the VCA, VCP and HCP configurations correspond to the  $xx$  ( $\theta_{t,r} = \frac{\pi}{2}$ ,  $\phi_{t,r} = 0$ ),  $yy$  ( $\theta_{t,r} = \frac{\pi}{2}$ ,  $\phi_{t,r} = \frac{\pi}{2}$ ) and  $zz$  ( $\theta_{t,r} = 0$ ,  $\phi_{t,r} = 0$ ) components, respectively. Analytical expressions exist in the case of dipoles at the surface of a homogeneous half-space under the quasi-static approximation and with the assumption that the magnetic permeability of the subsurface equals that of free space (Wait, 1952; Keller & Frischknecht, 1966; Ward & Hohmann, 1988). They are functions of the location of the receiver relative to the transmitter and the conductivity of the ground, and are listed in Paper A.

FDEM field measurements are measurements of the combined effect of the free-space (primary) field,  $H^P$ , and the secondary field,  $H^S$ , caused by currents induced in the ground by the primary field. Data are usually normalized by the primary field, yielding the mutual coupling ratio:

$$\frac{H^P + H^S}{H^P} = \frac{H^S}{H^P} + 1 = \frac{Z}{Z_0} \quad (3.2)$$

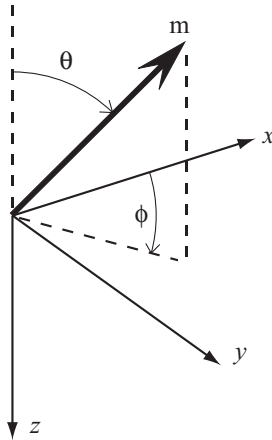


**Figure 3.1:** The direction of the dipole moment is defined in terms of the angle from vertical,  $\theta$ , and the angle from the  $x$ -axis,  $\phi$ . The coordinate system is defined with the  $z$ -axis positive down.

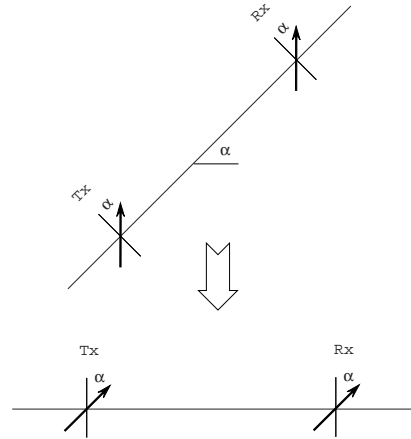


**Figure 3.2:** Vertical dipoles on a linear topography can be treated as angled dipoles on a half-space.

This operation is generally carried out in the instrument, assuming a certain configuration and dipole spacing. The primary fields of the three configurations mentioned above are given by (Keller & Frischknecht, 1966)

$$H_{xx}^P = \frac{m}{2\pi r^3} \quad , \quad H_{yy}^P = -\frac{m}{4\pi r^3} \quad , \quad H_{zz}^P = -\frac{m}{4\pi r^3} \quad (3.3)$$

where  $r$  is the distance between the magnetic dipoles, and assuming the transmitter dipole is located at the origin and the receiver dipole on the  $x$ -axis.

Modeling results are often presented as a function of a normalized frequency parameter, the induction number

$$B = \sqrt{\frac{\sigma \mu_0 \omega}{2}} \cdot r \quad (3.4)$$

where  $\sigma$  is the conductivity of the subsurface,  $\mu_0$  is the magnetic permeability of free-space, and  $\omega$  the angular frequency ( $2\pi f$ ). This greatly simplifies the presentation as only one data set is needed to describe the behavior of a specific dipole configuration for any combination of  $\sigma$ ,  $f$  and  $r$ , as long as the assumptions are valid.

### 3.3 Sensitivity to misorientation of transmitter and receiver

For a given measurement configuration, i.e. the HCP configuration, misalignment of the coils corresponds to changes in the directional angles ( $\theta$ ,  $\phi$ ) with respect to the nominal values. As described by equation 3.1, the resulting response in the misaligned situation is affected by several components, and interpretation of the data based on the nominal configuration will be in error.

In the case of a linear topography, the effect of the topographical relief can be treated as misorientation of the dipoles. Figure 3.2 illustrates this for a HCP configuration used in-line, that is with the axis connecting the dipoles parallel to the topographical gradient.

#### 3.3.1 Summary of results from Paper A

In Paper A the effects of variations in  $\phi_t$  and  $\phi_r$  for a small misalignment of  $5^\circ$  in both  $\theta_t$  and  $\theta_r$  were studied for the HCP configuration. The resulting errors were found to change in a complex and non-monotonic way as a function of both induction number and dipole orientations. However, global extremes were observed for specific combinations of rotation angles of multiples of  $\pi$ , corresponding to the situations when the dipole axes are located in the vertical plane connecting the two dipoles. This general observation has few exceptions over narrow ranges of induction numbers, connected to the migration of the extrema between locations that observe the general rule.

In the vertical plane connecting the dipole axes, these can either be tilted away from each other (A), towards each other (T) or to the same side (S). It was concluded, that in situation S (corresponding to the application of the system in-line on a linear topography) identical errors were observed irrespective to which side the dipoles were tilted. Severe effects are observed on the real part of the ratio of the secondary field to the primary field (the parameter generally used in interpretation), especially at low induction numbers, and even at small inclinations. The imaginary part is not significantly influenced by this type of misalignment.

The concept of apparent resistivity is often used in interpretation of geophysical measurements. In relation to FDEM measurements it suffers from the existence of many different definitions of apparent resistivity, based on different components of the field response. In Paper A six different apparent resistivity definitions were tested for values of  $\theta_t = \theta_r \leq 10^\circ$  in the situations T, A and S.

An apparent resistivity definition based on an automated curve matching algorithm involving both real and imaginary parts as proposed by Van der Kruk et al. (2000) was applied (type 5). Inspired by Wilt & Stark (1982) the same algorithm was modified to calculate apparent resistivities based on amplitude, phase, real and imaginary parts independently (types 1-4). Finally, inspired by

recent developments in helicopter borne EM data handling (Beamish, 2002), a least-squares inversion technique with the system elevation as additional free parameter was also tested (type 6).

In situations T and A, definition 5 (based on both real and imaginary part) gave results closest to the nominal half-space resistivity, although errors reached 30% at low induction numbers. In situation S, definitions 2 and 4, based on the phase and imaginary part respectively, gave results very close to the nominal resistivity. Yet none of the definitions were optimal in all three situations, and thus none of them can be declared superior to the others.

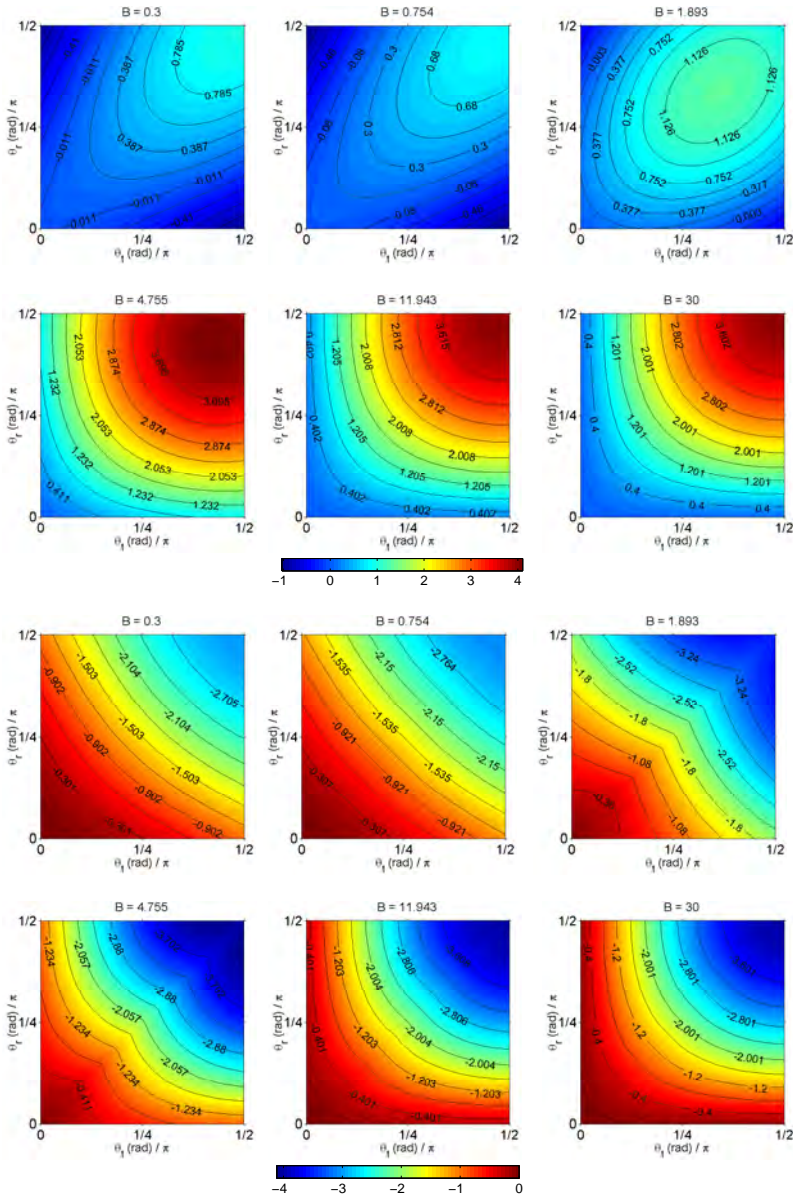
A subset of FDEM instruments, the so called Low Induction Number (LIN) instruments or Ground Conductivity Meters, operate in the LIN approximation, under which the apparent conductivity is directly proportional to the imaginary part of the response. These instruments are thus not significantly affected by topography (S) when operated over a homogeneous half-space, however, situations T and A result in extreme errors of approximately 19% at inclinations of only 5°. LIN instruments fixed on a rigid boom, like the Geonics EM-31 or GEM-2 by Geophex, are only affected by rotation around the boom axis, if operated parallel to the ground surface. Over a homogeneous half-space, the change due to such rotation is insignificant.

### 3.3.2 The effect of independently varying inclinations

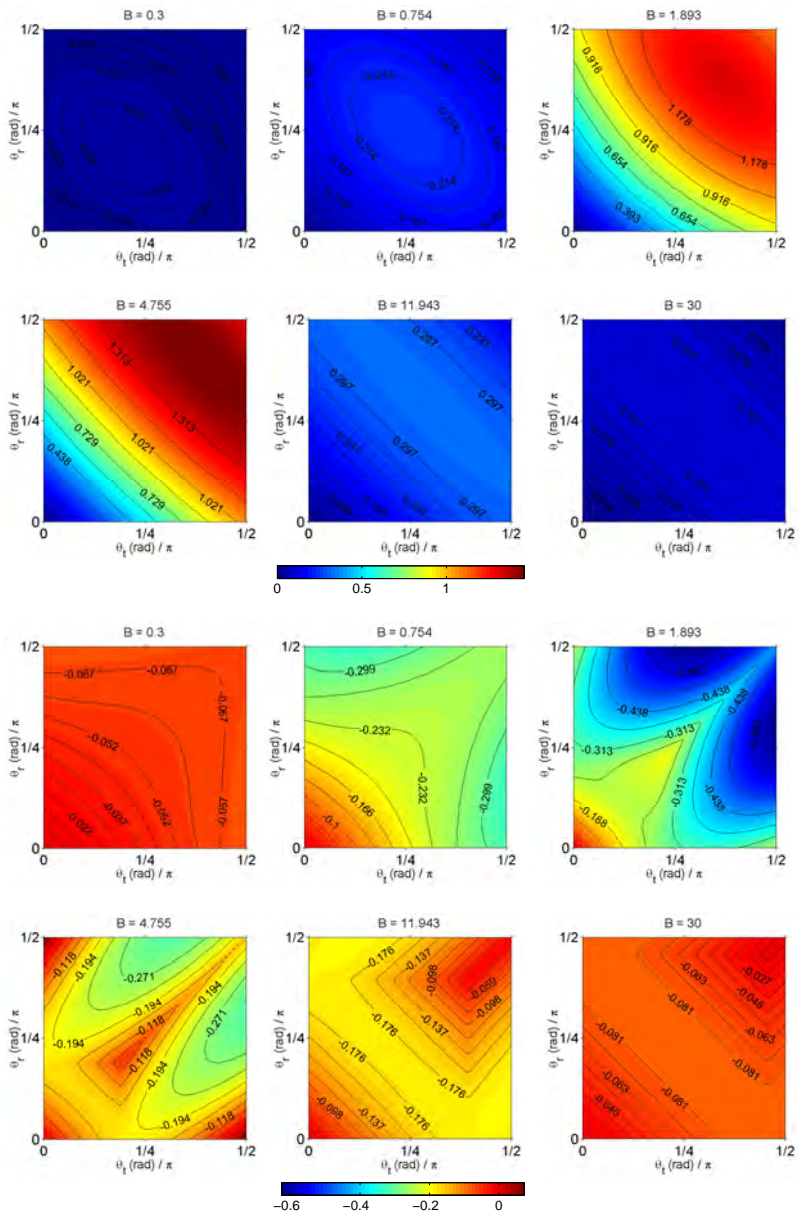
To complete the analysis, the effect of independent changes in the angle  $\theta$  for the transmitter and receiver has also been studied. The main challenge in this analysis is to choose meaningful values of the rotation angles for the two dipoles. This is problematic because the analysis in Paper A showed that the maximum and minimum errors change differently with respect to the rotational angles, and furthermore the changes are different for the real and imaginary parts of the response.

Figure 3.3 presents contour plots of the real part of the observed error as a function of both transmitter and receiver inclination for six different induction numbers. For every combination of axes inclinations ( $\theta_t, \theta_r$ ) and induction number, the values of the rotational angles are chosen to give the maximum error (top) and the minimum error (bottom). Thus the combination ( $\phi_t, \phi_r$ ) may change within each plot and between the plots. Similarly, Figure 3.4 shows the imaginary part of the observed errors. Rotational angles are here chosen such as to maximize the errors on the imaginary part, and thus differ from the choices made in Figure 3.3. The presented plots all have zero error at the lower left hand corner, corresponding to inclinations of 0°.

The extreme errors increase monotonously with increasing transmitter and receiver inclination when the approximate relation  $\theta_t + \theta_r \leq 40^\circ$  is fulfilled. The only exception is the maximum error on the real part at the three lowest induction numbers, which is negative when the inclination of one of the dipoles is much larger than that of the other. This component of the error is also positive and



**Figure 3.3:** Real part of the difference between the misaligned and nominal mutual coupling ratios for the HCP configuration,  $\left(\frac{Z}{Z_0}{}_{mis} - \frac{Z}{Z_0}{}_{nom}\right)$  for different values of axes inclinations  $(\theta_t, \theta_r)$ . The rotational angles  $(\phi_t, \phi_r)$  are chosen to give the extreme maximum error (top) and the extreme minimum error (bottom).



**Figure 3.4:** Imaginary part of the difference between the misaligned and nominal mutual coupling ratios for the HCP configuration,  $\left(\frac{Z}{Z_0}_{mis} - \frac{Z}{Z_0}_{nom}\right)$  for different values of axes inclinations  $(\phi_t, \phi_r)$ . The rotational angles  $(\phi_t, \phi_r)$  are chosen to give the extreme maximum error (top) and the extreme minimum error (bottom).

monotonously increasing with inclination when  $\theta_t = \theta_r$ , as described in Paper A.

The errors in the imaginary part are generally smaller (closer to zero) than the errors in the real part.

The extension of the analysis presented here calls for a few extensions to the conclusions made in the paper. The observed migration of the minimum error on the real part from situations S towards situation A and back to the respective S situation, is observed for inclinations up to  $30^\circ$  only. When the inclinations of the two dipoles are allowed to differ, distinction must be made between the situation where  $\phi_{t,r} = (0, 0)$  and  $\phi_{t,r} = (\pi, \pi)$  (referred to as  $S_0$  and  $S_\pi$ ). The minimum error on the real part is located at  $S_0$  for  $\theta_t < \theta_r$  and at  $S_\pi$  for  $\theta_t > \theta_r$ , outside the range of induction numbers where the migration occurs. The two S situations are identical only for  $\theta_t = \theta_r$ .

### 3.4 Sensitivity to errors in separation distance

One of the disadvantages of the FDEM method is that the response of the sub-surface, the secondary field, is measured in presence of the primary field. In order to obtain the pure ground response, the primary field must be subtracted from the measured response. This is usually done in the instrument simultaneously with the acquisition of the measurement. The instrument assumes a specific separation distance between transmitter and receiver in order to compensate for the primary field. In practice the compensation is often done by feeding a compensation voltage (equal but opposite to the induced primary voltage at the assumed separation) into the receiver circuitry so that only the secondary response is measured. In a field situation it is seldom possible to keep the separation distance exact, and therefore errors may be introduced into the measured data.

As described by Frischknecht et al. (1991) it is possible to correct these errors. The formula for correcting data from the HCP or VCP configurations is

$$\left[ \frac{Z}{Z_0} - 1 \right]_{\text{corr}} = \left[ \left[ \frac{Z}{Z_0} - 1 \right]_{\text{obs}} + \left( 1 - \left( \frac{r}{r'} \right)^3 \right) \right] \cdot \left( \frac{r'}{r} \right)^3 \quad (3.5)$$

where  $r$  is the separation distance assumed by the instrument in the compensation and  $r'$  is the actual separation. The corrected value is the value the instrument would have read, had it used the actual separation in the compensation.

Manual interpretation would be easier if measurements could be corrected to the assumed spacing. In practice this is of course not possible, as the correction would apply to the response of the ground, the composition of which is not known prior to the interpretation. However, it is possible to take the actual separation distance into account in computer modeling and inversion of the data.

In actual field operation the measurement of transmitter and receiver locations are always subject to uncertainty, depending on the accuracy of the procedure and the equipment used to obtain the coordinates or distances. As an example, Figure 3.5 presents the effects that small variations in the separation distance have

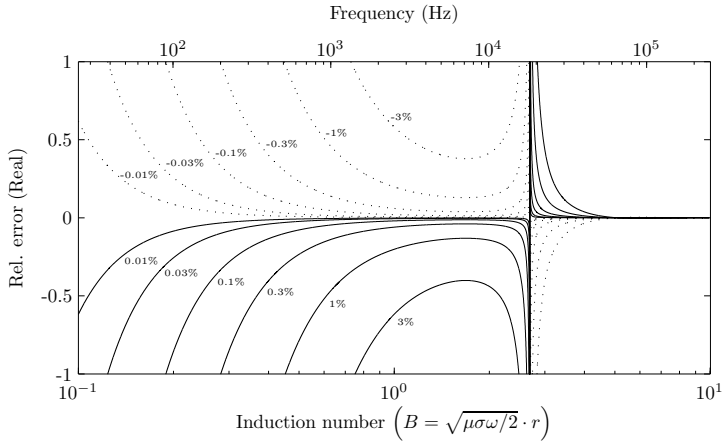


**Figure 3.5:** The relative error in the real part of the measurement caused by small changes in the separation distance presented as functions of the induction number. A frequency scale is given in the top of the plot, for a separation distance of 100 m and a ground resistivity of 100  $\Omega\text{m}$ .

on the observed response for a HCP configuration over a homogeneous half-space. It is evident that even small errors adversely affect the real part of the measured response. The relative error on the imaginary part amounts to approximately three times the error on the separation at any frequency, i.e. an error of 3% in the separation results in a relative error of approximately 9% on the imaginary part.

### 3.5 Field test with a FDEM system in Sisimiut

A MaxMin II system from APEX was applied in survey area 2 in Sisimiut along profiles L4 and L5. The system was operated in the HCP configuration with an intercoil spacing of 50 m. Data were collected at the five available frequencies, 222, 444, 888, 1777 and 3555 Hz.

Although the equipment manual specifies a drift-free zero, tests on a granitic outcrop of 6000  $\Omega\text{m}$  resistivity indicated poor zeroing of the instrument. This problem was corrected by subtracting the difference between the observed response and the theoretical response using a 6000  $\Omega\text{m}$  half-space model at a separation of 100 m. The instrument specifications promises a scale readability between  $\pm 0.005$  and  $\pm 0.01$  depending on frequency and noise conditions. After zero correction, the real and imaginary parts of the responses were all within these limits at both 50 and 100 m separations.

The scaling factor for the real part was tested as described in Frischknecht et al. (1991) by changing the intercoil spacing from the nominal value. This should result in a change in the real part as  $(r/r')^3$ , where  $r$  is the nominal spacing and  $r'$  is the actual spacing. The real part of the measured response at

90 m separation was 0.02–0.05 larger than expected, indicating slight problems. It is possible that the scaling and zero problems are related.

### 3.5.1 Results

During surveying the reference cable was used to determine the intercoil separation, and the actual coil locations were marked to allow subsequent measurement of the actual spacing for each measurement. This practice has resulted in deviations from the nominal spacing of 50 m. The actual separation and the vertical elevation difference between the coils is shown in Figure 3.6(a) for the profile along L4. The real part of the measured response (b) is highly correlated with the separation distance. As expected from the theoretical considerations, a separation distance shorter than the nominal results in an increase in the response (i.e. the first point of the profile), whereas a larger separation results in a reduced response. When the normalization of the measurements is corrected based on the actual separation, most of this correlation disappears (c). It is apparent that a vertical elevation difference between the coils also results in large decreases in the real part of the measured responses. This effect is visible especially in the first part of the profile, and is coherent with the modeling results presented in Paper A.

The two measurements at -40 and -30 m, for which the elevation differences are approximately 0 m, have negative real parts even after the spacing correction is applied. Under normal conditions, and over a homogeneous half-space, the real part of the response would be expected to be small and positive. The discrepancy is possibly related to the zeroing of the instrument or the observed errors in the scaling factor for the real part, but an effect of deeper seated structures in the bedrock cannot be ruled out.

The imaginary part is not significantly affected by the spacing errors and is presented in Figure 3.6(d) only in the corrected form. Although the responses are generally very small, an anomaly is observed in the imaginary data for the frequencies 1777 and 3555 Hz. The anomaly is centered around -20 m and is aligned with the low resistive anomaly observed in the L4 MEP profile from 2002.

The Toronto Plate program (Farquharson, 2002, priv. comm.) has been used to manually fit the response of a vertical conductive plate in a non-conducting half-space to the measured imaginary data. The closest fit to the data at 1777 Hz was obtained using a plate with a strike length of 600 m, a depth extent of 120 m and a conductance of 0.3, located 5 m below the coil configuration, see Figure 3.7. The forward model resulted in real parts of less than  $\pm 0.0025$ , and thus explains that an anomaly was not observed in the real part of the measured response.

The conductance of the modeled plate is very large compared to what would be expected based on the MEP profiles. Using a thickness of 15 m for the low-resistive zone as observed on the MEP, the resulting resistivity should be 50  $\Omega\text{m}$ , which is less than what was observed. The depth extent of the plate is also much

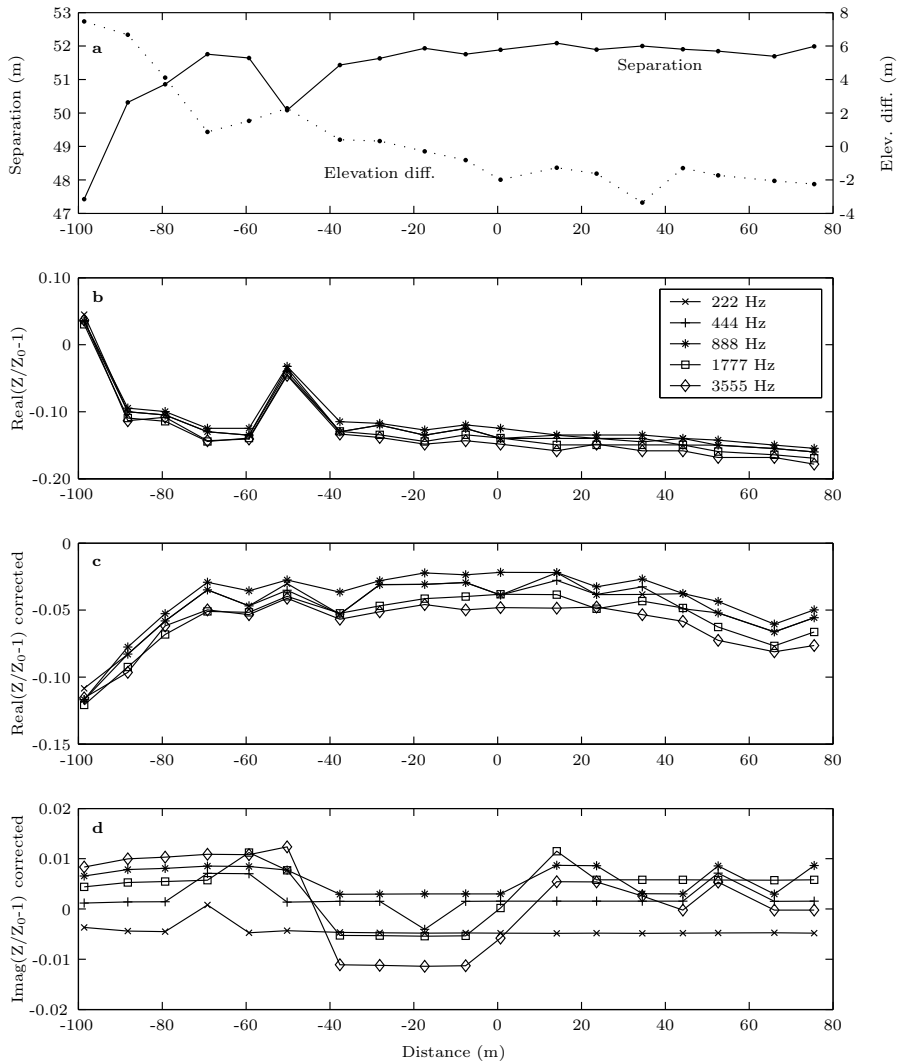


**Figure 3.6:** FDEM data measured with the APEX MaxMin II system along L4 at the Sisimiut field location (area 2). The four graphs show the separation distance and elevation difference of the two coils (a), the real part of the measured response (b), and the real and imaginary parts of the measured response corrected for normalization errors due to the separation distance (c and d).

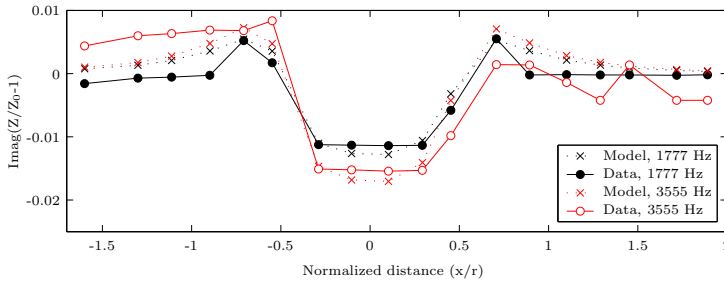


**Figure 3.7:** Vertical conductive plate model of the anomaly in the imaginary part of the response measured along L4 at 1777 and 3555 Hz. The modeled plate has a strike length of 600 m and a depth extent of 120 m. The conductance of the plate ( $\sigma t$ ) is 0.3 at 1777 Hz and 0.2 at 3555 Hz. The profile is located 5 m above the upper edge of the plate and the host medium is assumed to be non-conductive. Small constant offsets have been subtracted from the observed data to align them with the model data.

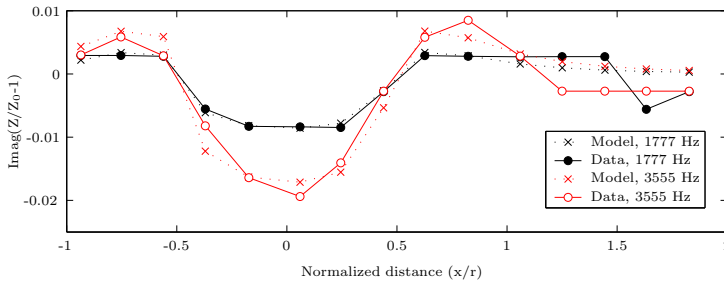


**Figure 3.8:** Vertical conductive plate model of the anomaly in the imaginary part of the response measured along L5 at 1777 and 3555 Hz. The modeled plate is identical to that in Figure 3.7 except for the conductance, which in this case is 0.2. Small constant offsets have been subtracted from the observed data to align them with the model data.

greater than expected.

Due to the presence of the two lakes, Lake 4 and Lake 5, the unfrozen zone (and thus the low resistive anomaly) becomes wider to the northeast and southwest of the measured profile. It is plausible that this could necessitate a greater depth extent and conductance of the plate in order to fit the data, than would be expected from the size of the resistivity anomaly on the MEP profile along L4. The lower resistivity of the bedrock may also affect the response and may be the cause of the offset observed between the imaginary parts at different frequencies.

The anomaly observed in the 3555 Hz data is more noisy, but in spite of a poor fit the resulting model indicates a lower conductance ( $\sigma t = 0.2$ ) and thus a closer resemblance to the observations from the MEP profile.

Measurements obtained on the L5 profile have been treated in a similar way. The real parts are again negative and a strong correlation with separation distance

is apparent even after correction. An anomaly centered around position -13 m is observed in the imaginary part and can be fitted well with the vertical plate model using a conductance of 0.2 (Figure 3.8). The anomaly is well aligned with the low-resistive anomaly observed on MEP L5 in 2002. The modeled conductance corresponds to a resistivity of approximately 200  $\Omega\text{m}$  when the width of the plate is set to 40 m as indicated from the MEP. This resistivity is close to the one observed in the MEP profile.

## 3.6 Discussion

The area in which the presented field data were collected had only little topographic variation and was therefore close to ideal in relation to misorientation effects. Still, the real part of the measurements was corrupt and noisy, and correlation with the separation distance could not be completely removed. The imaginary part was much less affected and proved useful for obtaining quantitative models in terms of vertical conductive plates.

The field site has resistivity contrasts of up to 1:200; contrasts considered to be among the largest that could be expected in sedimentary deposits in a Greenlandic environment. Nevertheless, the observed anomalies were very small and close to the detection limit of the instrument, which is why interpretations could only be obtained based on the higher frequencies. This is a grave limitation of the method when applied in resistive environments.

Based on the presented theoretical considerations and practical results it must therefore be concluded that the multifrequency dipole-dipole FDEM technique is not well suited for this type of application in the Greenlandic environment. It cannot be expected to give reliable results for vertical nor lateral distribution of permafrost unless great care is taken in positioning the coils. Even then, the real part of the response will probably be useless and the imaginary part only of limited use. The available studies suggesting different conclusions (Daniels et al., 1976; Sinha & Stephens, 1983a; Palacky & Stephens, 1992) have all been conducted in environments with much lower resistivities, and are therefore not directly comparable. In these studies problems are also reported relating to topographical variation (Sinha & Stephens, 1983a) and repeatability of the measurements (Palacky & Stephens, 1992).

The presented results clearly favor the use of LIN-instruments. Because such instruments utilize only the imaginary part of the response at low induction numbers, they are less affected by errors in separation distance and misorientation of the coils. Especially such instruments that have the two coils fixed on a rigid boom clearly will not suffer from changes in separation and misorientation of the coils relative to each other. The drawback of these instruments is the limited penetration depth, which is often less than 10 m. Thus, in practice they will not be applicable to investigations of the vertical resistivity distribution in permafrost areas in Greenland.

### 3.7 Conclusion

An equation describing the response observed in dipole-dipole FDEM measurements due to misorientation of the dipole axes has been formulated. The equation has been applied in an exhaustive study of the effects of misorientation in the case of a HCP configuration on the surface of a homogenous half-space. The analyses show that both the real and imaginary parts may be severely corrupted even at small misalignments. In the special case of the HCP configuration used inline on a linear topography, the imaginary part is much less affected than the real part. It is of special interest that extreme errors are observed for specific combinations of coil axes rotations of multiples of  $\pi$  over most of the range of induction numbers studied. With few exceptions the extreme errors are increasing with increasing axis inclination for small values of the inclination.

A study of six different apparent resistivity definitions in three special cases involving misorientation of the coil axes in the vertical plane connecting the coils showed that quantitative interpretation of multifrequency dipole-dipole FDEM measurements is difficult at best. None of the definitions gave acceptable results in all cases, but definitions based on the phase or imaginary parts of the response were superior for a system used in-line with linear topographical variation.

A field test performed in an area with only little topographical variation confirms that the real part is easily corrupted and cannot be relied upon for quantitative interpretation. The imaginary part proved useful in the interpretation but showed only small anomalies in spite of large resistivity contrasts.

It is concluded that the multifrequency dipole-dipole FDEM technique is not well suited for permafrost studies in the Greenlandic environment. Instead LIN instruments may be applied to map the lateral resistivity variations in areas of discontinuous permafrost.

# The CR method

---

## 4.1 Introduction

The CR method was originally developed for use in mineral exploration, and was mainly applied to the detection of sulfide deposits. Such deposits result in large responses that are recognizable even at the relatively few and low frequencies applied in the beginning. As the method developed so did an interest in discriminating different sources of the observed responses, and the frequency bandwidth of the measurements was increased to include sampling of frequencies up to approximately 100 Hz.

Recently a renewed interest in the CR method has appeared in relation to environmental investigations, and a number of laboratory studies have been published dealing with the effect of organic contaminants on CR measurements (Olhoeft, 1985; Vanhala & Peltoniemi, 1992; Börner et al., 1993; Vanhala, 1997). These studies have shown that wider ranges of frequencies are necessary in order to develop proper model descriptions of the observed dispersions. The trend is towards wider frequency ranges with denser sampling of frequencies. In spite of this interest in CR effects over wide frequency ranges, only few data sets from real field situations have been published.

This chapter gives an introduction to the background CR method and its possible application to permafrost investigations. Paper B, Paper C and Paper D, relating to modeling of EM coupling in CR measurements and investigations of error sources in wide frequency bandwidth measurements, are summarized. Finally a field study with the CR technique at the Sisimiut field site is presented.

## 4.2 Background and fundamentals

### 4.2.1 Complex resistivity of earth materials

The fact that the resistivities of geological materials are complex-valued and vary with frequency is well-established. Over the years, a multitude of models have

been suggested for the description of observed complex resistivities, and good summaries have been published by Pelton et al. (1983), Saloheimo (1990) and Dias (2000).

The Cole-Cole model has been subject to special interest. It was introduced in geophysical prospecting by Pelton et al. (1978), but was originally developed by Cole & Cole (1941) to describe complex dielectrical behavior. The Cole-Cole resistivity dispersion is usually written as

$$\rho^* = \rho_0 \left( 1 - m \left( 1 - \frac{1}{1 + (i\omega \tau)^c} \right) \right) \quad (4.1)$$

where  $\rho_0$  is the resistivity in the DC limit,  $m$  is the chargeability,  $\tau$  is the time constant, and  $c$  is referred to as the frequency dependence. Pelton et al. (1978) showed that interpretation based on this model could be used to discriminate different types of mineralizations as well as the grain size of mineralized inclusions.

Figure 4.1 shows the two representations of CR data normally used: the magnitude and phase plots of apparent resistivity and an Argand plot of the measured impedance. Magnitudes are generally plotted on a logarithmic scale and phases on a linear scale. The Argand plot is a complex plane plot, where the real and imaginary parts are usually normalized by the real part of the measurement at the lowest frequency. Conventionally, phases and imaginary parts are plotted with the sign reversed yielding a positive phase peak.

Traditionally CR measurements may also be reported as Percent Frequency Effect (PFE) or Metal Factor (MF) defined as (Madden & Cantwell, 1967)

$$\text{PFE} = \frac{\rho_{\text{dc}} - \rho_{\text{ac}}}{\rho_{\text{ac}}} \cdot 100 \quad \text{and} \quad \text{MF} = \frac{\rho_{\text{dc}} - \rho_{\text{ac}}}{\rho_{\text{dc}} \cdot \rho_{\text{ac}}} \cdot 2\pi \cdot 10^5$$

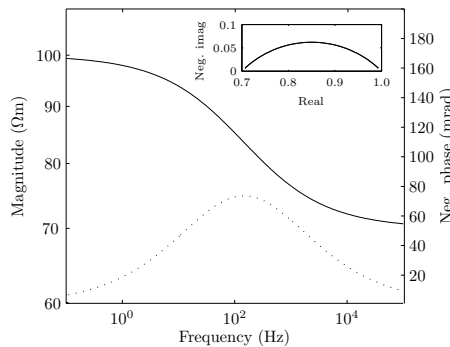


**Figure 4.1:** A plot of the magnitude (solid) and phase (dots) of a Cole-Cole dispersion with the parameters  $\rho_0 = 100\Omega\text{m}$ ,  $m = 0.3$ ,  $\tau = 0.01$  and  $c = 0.5$ . The insert shows a complex plane plot, an Argand plot, of the same dispersion. Convention is to plot the phase values and imaginary parts with the sign reversed. For field data, the real and imaginary parts plotted in the Argand plot are generally normalized by the resistivity at the lowest frequency.

where  $\rho_{dc}$  is the DC or low frequency resistivity (typically at 0.125 Hz), and  $\rho_{ac}$  is the resistivity at a higher frequency, typically at 1 Hz.

### 4.2.2 Origin and phenomenological models of the CR effect

Despite of decades of research, the exact origin of CR effects is not fully understood. However, the electrode effect and the membrane effect are generally accepted as the two main causes of polarization phenomena in the ground at low frequencies.

#### The electrode effect

The electrode effect is related to processes taking place at interfaces between an electrolyte and a metal or metallic mineral grains. When a metal is brought in contact with water, positive metal ions will dissolve, leaving the electrons in the bulk metal. Dissolution would occur until the chemical potential in the solution and the metal were at equilibrium, were it not for the electrical potential which builds up due to the charge separation. Thus, the positively charged ions in solution are attracted to the negatively charged metal surface, and a so-called double layer is formed. Ions must cross this potential barrier in order to pass into solution, and thus the double layer tends to prevent further dissolution.

Due to the existence of a hydration shell around ions in solution, there is a lower limit to the approach to the metal surface. Hence, the ions in solution are separated from the metal surface by a layer of solvent molecules, which is generally in the order of a few Ångström (Rubinstein, 1995). The size of the ions is such that their charge cannot necessarily balance the charge on the metal surface. The remaining charge is held with increasing disorder, due to thermal motion, in what is known as the diffuse part of the double-layer. The thickness of this part is analogous to the Debye-Hückel theory of the size of the ionic atmosphere around an ion in solution and is given by (Grahame, 1947):

$$\kappa^{-1} = \left( \frac{\epsilon k T}{2 n e^2 \nu^2} \right)^{1/2} \quad (4.2)$$

where  $\epsilon$  is the permittivity of the fluid,  $k$  is Boltzman's constant,  $T$  is the absolute temperature,  $n$  is the normal ion concentration of the electrolyte,  $e$  is the elementary charge, and  $\nu$  is the valence of the normal ions. The calculated thickness is the distance over which the potential in the diffuse part of the double layer is reduced by an exponential factor (to approximately 37%). Due to the charge separation, the interface has a capacitance attached to it, but faradaic charge transfer is also possible through electrochemical reactions, and the double layer can therefore be treated as a complex-valued electrical impedance,  $Z$ .

Metallic mineral-electrolyte interfaces have been intensely studied (Marshall & Madden, 1959; Scheider, 1975; Angoran & Madden, 1977; Olhoeft, 1982; Klein

et al., 1984), and most seem to fit the empirical relationship (Saloheimo, 1990):

$$Z(\omega) = \frac{Z_b}{(i\omega)^b} \quad (4.3)$$

where  $Z_b$  is a constant and the exponent  $b$  varies between 0.25 and 0.8 for different electrode materials. The most common value of  $b$  is approximately 0.5, a behavior referred to as the Warburg impedance. The empirical relation in eq. 4.3 has been developed theoretically by Saloheimo (1990) for a planar electrode surface where a simple redox-reaction takes place.

### The membrane effect

Rocks that do not have an apparent metallic mineral content may also show complex resistivity effects. This effect is usually called the membrane or background effect, regardless of the origin.

The primary driving forces for ionic movement in an electrolyte are the chemical and electrical potential gradients. The current flowing in such a system can be divided into current due to anion and cation movement. Marshall & Madden (1959) proposed that the pores in a geological material could be viewed as a series of zones with different ion transfer properties. Some zones are taken to be cation selective, i.e. the mobility and diffusion coefficients of cations are larger than those of anions. When an electrical potential is applied, most of the current will be carried by cations in these zones. A concentration gradient will build up between the ends of such a zone, until a steady state is reached. When the external field is removed, the electrolyte will return to equilibrium thereby generating current flow.

The Marshall & Madden model was used to describe the effects observed in clay containing sediments. Clay particles most often possess a static negative surface charge. When in contact with an electrolyte a double layer will form to balance the charge (Mitchel, 1993), analogously to the electrode process described earlier.

Through physical reasoning, rather than actual experimental evidence, it is hypothesized that the diffuse part of the double layer may act similar to a cationic selective membrane. It will allow the migration of cations but restrict anion movement (Ward & Fraser, 1967). Thus, when a clay particle partially blocks a pore path polarization effects may occur (Figure 4.2). Based on this model, Anderson & Keller (1964) show that an optimum clay-content (depending on the clay type) resulting in a maximum polarization effect exists.

It has also been suggested that simply a decrease in the diameter of a pore may cause similar effects (Keller & Frischknecht, 1966; Zonge, 1972). Layers of water molecules are usually attached to the walls of a pore, and in very narrow pores the viscosity of the water increases due to the forces that bind the water molecules to the walls. This may give rise to the necessary changes in mobility.

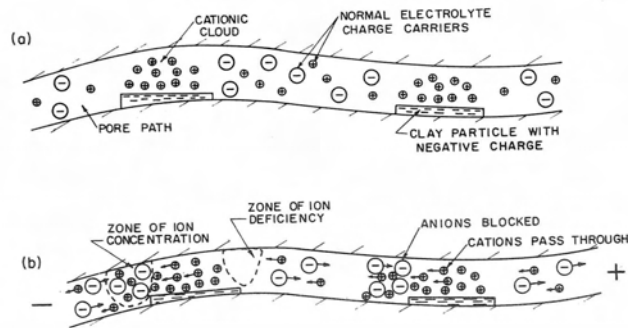


**Figure 4.2:** Model of how clay particles partially blocking a pore path may cause polarization phenomena (Ward & Fraser, 1967).

### Effective media approaches

Even though the electrode and membrane theories explain that polarization effects are observed in geological materials, they are microscopic theories and do not themselves result in useful macroscopic descriptions of complex resistivity.

The common way to obtain such relations is through mixing rules, where the average medium properties depend on the actual properties of the different inclusions and their size and distribution. Wait (1982) generalized the Maxwell-Garnett mixing rule for spherical inclusions (Garnett, 1904) to allow for an impedance at the surface of the particles. He also showed that the effective resistivity can be rewritten in the form of a Cole-Cole dispersion, when the material contains small volume fractions of perfectly conducting particles and the form of interfacial impedance given in equation 4.3 is adopted. The formula can be extended to describe coated (Wait, 1982) and elongated inclusions (Wait, 1989). Similar expressions exist for inclusions of different properties and larger volume fractions (Van Voorhis et al., 1973; Sihvola, 1999). Other authors have applied effective media approaches to explain the membrane effects as well (Chew & Sen, 1982; Lima & Sharma, 1990, 1992).

More complicated electrochemical models, taking into account specific processes taking place at the interface, have been developed (Wong, 1979; Wong & Strangway, 1981; Saloheimo, 1990). Yet these models have not found a general usage in the geophysical community, due to their complexity and dependence on parameters, which often are unknown in field experiments.

### 4.3 Justification for applying the CR method in the Greenlandic environment

At present no theory describing the effect of permafrost on CR responses has been presented. However, there are several indications that temperature influences the response. Theoretically, the thickness and potential drop over the diffuse part of the double layer depends on the temperature (eq. 4.2). So do the ionic activities and mobilities (Murrmann, 1973), which are important factors in electrochemical models. Also the reaction speed of chemical reactions is generally temperature dependent, and therefore faradaic charge transfer processes are affected. The type of membrane effect suggested to be related to pore size could be expected to show variation with temperature as well, due to the temperature dependence of the viscosity water.

Temperature could also be expected to have indirect influence on CR effects. It is well established that even at relatively low subzero temperatures there may still be considerable amounts of unfrozen water in certain soil types (Anderson et al., 1973; Anderson & Morgenstern, 1973). As ions and solutes tend to be rejected from the growing ice lattice on freezing, they are excluded and concentrated in the remaining unfrozen phase (Anderson & Morgenstern, 1973; Stähli & Stadler, 1997). Changes in ionic concentration has been shown by Keevil & Ward (1962) and Vinegar & Waxman (1984) to have significant effect on resistivity dispersions of different geological materials. Furthermore, when the ice content is significant, it may alter the pore sizes and shapes thereby affecting conduction paths.

A number of authors have studied temperature effects on resistivity dispersions. Collett (1959) studied polarization effects in time domain as function of temperature and found an increase with decreasing temperature for samples dominated by electrode polarization and a decrease for membrane polarization. However, the results were later doubted by Keevil & Ward (1962) who pointed out that electrolyte activity may have been the dominating parameter. Saint-Amant & Strangway (1970) studied the variation in complex permittivity of geological materials at both high and low temperatures and showed that there is in fact a temperature effect on the dispersions. They also studied the effect of moisture content at subzero temperatures and found that Debye type dispersions were observed above a critical water content. Olhoeft (1977) studied permafrozen clay samples in their natural state, and showed some variation with temperature. He also showed a strong frequency dependence of the complex resistivity. Kay & Duckworth (1983) studied the effect of permafrost on CR effects of mineralized rock and in consistency with Collett (1959) found an increase in chargeability with a decrease of temperature. In contradiction to these results, Vinegar & Waxman (1984) concluded that their two samples showed no or very little effect of temperature.

Although there is no consensus on the effect of temperature variation, most

authors agree that an effect may be observable. Application of the CR method in areas with permafrost, and the acquisition of high quality field data over a wide range of frequencies may have great impact on the understanding of the physical and chemical basis of the technique.

## 4.4 EM coupling in the CR method

The CR method has evolved from induced polarization and resistivity methods, which are normally explained in terms of static theory. The CR method is therefore also generally treated in a static approximation. Although this approach has proved useful at sufficiently low frequencies, it is not the case in general, and as measurements at higher frequencies are collected, the method must be considered an electromagnetic (EM) method.

CR measurements are usually conducted using grounded wires for both transmitter and receiver in a collinear dipole-dipole configuration, see Figure 4.3. In addition to the potential differences observed due to injection of current into the ground, CR measurements are also, as any other EM method, affected by inductive coupling between the transmitter, the receiver and the ground.

The approximative solution first published for EM fields of a dipole-dipole array on a homogeneous half-space was that of West (1943) for a dipole spacing of  $N=1$ . Wait (1951) presented an analytical solution for a dipole-dipole configuration over a homogeneous half-space, a solution which contained several errors and was later corrected by Wait & Gruszka (1986b). Millett (1967) is therefore often credited with the first general solution for calculating the response of any collinear dipole-dipole configuration over a homogeneous half-space. Dey & Morrison (1973) were the first to publish the theoretical background for the multi-layer problem. Several other studies have addressed the inductive coupling problem through forward modeling (Hohmann, 1973; Hallof, 1974; Hohmann, 1975; Wynn & Zonge, 1975; Nair & Sanyal, 1980).

As described by Sunde (1968) the electromagnetic coupling between two grounded wires in an arbitrary configuration on the surface of the earth can be calculated as an integration of mutual impedances of virtual electrical dipoles

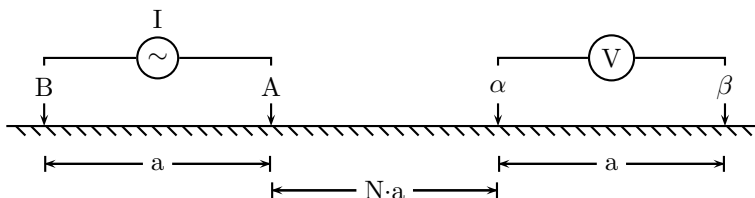


**Figure 4.3:** The general collinear dipole-dipole electrode configuration.  $N$  is the dipole separation factor called the  $N$ -spacing, and  $a$  is the dipole size in meters.

along the paths of the wires:

$$Z = \int_A^B \int_\alpha^\beta \left[ P(r) \cos \xi + \frac{\partial^2 Q(r)}{\partial S \partial s} \right] ds dS \quad (4.4)$$

where  $dS$  and  $ds$  represent infinitesimal elements of the transmitter and receiver wires, respectively, and  $r$  and  $\xi$  are the distance and angle between them.  $P$  and  $Q$  are complex functions that depend on the composition of the ground.

By analogy with DC theory, a so-called apparent complex resistivity is obtained by multiplying the mutual impedance with a geometric factor (Wait & Gruszka, 1986b). When inductive coupling is negligible this approach gives correct results. However, in general the true apparent complex resistivity should be obtained by inverting the coupling equation using a homogeneous half-space model, as practice is in other EM methods.

In fact, the DC based apparent resistivity formulation deteriorates gradually for commonly applied dipole sizes, even over the relatively low frequencies generally used in CR prospecting. Therefore, much effort has been put into developing decoupling schemes to separate the EM coupling response from the intrinsic CR response of the subsurface.

The most commonly used decoupling method is purely empirical and consists of the fitting of a linear or quadratic equation to the phase measurements at two or three low frequencies (Hallof, 1974; Coggon, 1984; Song, 1984). Extrapolation to zero frequency results in the so-called three point decoupled phase value. An obvious drawback of this method is that the spectral behavior of the resistivity cannot be assessed. Another widely used empirical decoupling method was introduced by Pelton et al. (1978) who suggested a multiplication of two Cole-Cole models, where one is used to fit the low frequency dispersion and the other the EM coupling. Major & Silic (1981) pointed out that an addition of the two models is theoretically preferable.

#### 4.4.1 Summary of Paper B

Paper B is concerned with the interaction of CR effects and EM coupling. The calculational considerations are discussed for a collinear dipole-dipole configuration on a homogeneous half-space, and the main decoupling schemes are reviewed.

In spite of obvious importance, the EM coupling response based on a complex resistivity has not been studied much. The paper illustrates how a Cole-Cole type resistivity dispersion affects the EM coupling response, and the independent effect of the real and imaginary parts of the dispersion on the coupling response is studied. It is observed that the imaginary part of the resistivity dispersion has only little influence on the real part of the coupling, whereas both real and imaginary parts of the dispersion influences the imaginary part of the coupling response.

Two data sets are presented in the paper. One contains measurements at frequencies up to 10 kHz, the other was collected using long dipoles and a large

N-spacing over the normal frequency range (0.1 to 100 Hz). Both are affected by EM coupling. The two data sets were interpreted using a manually fitted CR based homogeneous half-space EM coupling model and an additive double Cole-Cole model. It is shown that the CR based EM coupling is capable of fitting both data sets reasonably well. As predicted by Major & Silic (1981) the double Cole-Cole model is not able to fit the high frequency data set with a realistic model. Furthermore, a comparison of the interpreted low frequency dispersions for the large dipole data set shows large deviations in the Cole-Cole parameters obtained by the two approaches. It is concluded that the CR based EM function fits the data equally well or better than the double Cole-Cole model in the two simple cases presented.

The paper clearly shows, that whereas the common decoupling schemes certainly have proved their usefulness in practical surveys relating to mineral exploration, they may not be appropriate in applications where differences are more subtle. Also, when it comes to understanding the physical and chemical processes involved in CR effects, the decoupling schemes probably corrupts the data to an extent where in depth interpretation is not possible. Instead, more focus should be put on using the actual EM coupling equations and studying the effect of complex resistivity dispersions on the EM coupling response.

#### 4.4.2 Summary of Paper C

Paper C presents a one dimensional modeling software package, CR1Dmod, dedicated to calculating EM responses in the presence of CR effects. The software handles frequency domain coupling for grounded wires as well as small coils in the horizontal coplanar configuration (HCP or HLEM). In time domain, CR1Dmod is capable of calculating the response of the central loop TEM configuration. For completeness, DC responses of the most common electrode configurations can also be calculated.

In the case of grounded wires, which is of interest in CR prospecting, the wires may be divided into any number of arbitrarily oriented linear segments, provided that the receiver and transmitter wires do not intersect.

The Hankel transforms involved in the calculations are often slowly convergent or may in some cases not be convergent at all. However, under the quasi-static approximation, assuming also a non-magnetic subsurface, analytical solutions to the homogeneous half-space expressions can be obtained (Wait, 1951). The usual practice is therefore to calculate a half-space response analytically based on the properties of the first layer and add to this a correction term, which accounts for the summed effect of the additional layering (Ryu et al., 1970). The correction term consists of a Hankel transform, which has better convergence properties than the full solution and thus evaluate faster.

As a new contribution, analytical solutions for the Hankel transforms in the  $P$ -function of the grounded wire response and the central loop response are presented for non-magnetic homogeneous half-spaces. These formulations, which

were inspired by a similar formulation by Wait (1952) for the HCP FDEM configuration, allow fast evaluation of responses where permittivities in all media are taken into account. In CR1Dmod, calculations can be performed using the full solutions, the new non-magnetic approximation and the traditional quasistatic or low frequency approximation.

The code is found to be in agreement with other authors (Kauahikaua & Anderson, 1979; Anderson, 1981; Christensen & Auken, 1992; Auken et al., 2001), although the computation time is not as efficient as other routines. On the other hand, CR1Dmod seems to handle some situations better, especially when high frequencies are involved. Furthermore, the code handles complex resistivities as well as permittivities and magnetic permeabilities, options that are not commonly available in similar software.

## 4.5 CR measurements over wide frequency ranges

### 4.5.1 Summary of Paper D

A number CR measurements have been collected in relation to this study, all containing frequencies up to 9216 Hz. Most of these data sets contain effects that cannot be explained by traditional models of natural polarization phenomena in the ground. The normal 1D EM coupling calculations likewise fail to explain the observed responses. Paper D presents a study of some important error sources relating to high frequency CR measurements. Some of these error sources are general, others relate specifically to the instrumentation used for the study.

For this study CR equipment manufactured by Zonge Engineering and Research Organization has been used. It consists of a GDP 32<sup>II</sup> geophysical receiver and a GGT3 transmitter. Paper D describes the system in detail and provides general information on practical aspects of the measurement technique.

Model studies of two general error sources are presented: Effects of the practical layout of electrodes and cables and effects of capacitive coupling between wires and ground.

Effects of offsetting electrodes and wires from their ideal collinear configurations were studied using the CR1Dmod software. In practical surveying several receiver dipoles are connected simultaneously to speed up data acquisition. Similarly several transmitter dipoles are connected to the transmitter through a switch box to avoid moving the transmitter too often. In practice the two sets of dipoles are therefore offset. The model studies, which are based on homogeneous half-space responses, show that the phase effects are minimal and amount to no more than approximately 6 mrad for the configurations considered.

Two models were developed to describe capacitive coupling effects for the receiver and transmitter dipoles. For the receiver dipole, capacitive coupling proved to be strongly dependent on the electrode contact resistance, and may severely affect the measurements for high contact resistances. For small phase errors, the

model suggests that the decrease in the negative phase angles is proportional to the product of the dipole size ( $a$ , [km]), the frequency ( $f$ , [kHz]) and the contact resistance ( $R_c$ , [ $k\Omega$ ]):

$$\Delta\phi \approx K \cdot a \cdot f \cdot R_c \quad (4.5)$$

where  $K$  is the proportionality constant, which takes the values 38.6, 36.3 and 35.9 for N-spacings 1, 3 and 5.

A simple model was also suggested for the transmitter dipole based on transmission line theory. The model approximates the ground by a distributed resistance per unit length. Determination of this parameter is the main challenge in application of the model. It predicts phase effects that increase with increasing ground resistance and are of opposite sign than those predicted by the receiver dipole model. The model needs improvement to be of practical use.

Both the transmitter and receiver are capable of operating at frequencies up to 9216 Hz. However, the studies presented in Paper D show that the current reference measurement constitutes a weak link in the system at high frequencies. The isolation amplifier used to galvanically isolate the current reference signal, and the signal cable passing the reference signal to the receiver, proved to have residual responses that were not effectively calibrated out at high frequencies. Furthermore, the error was shown to be depending on the shunt resistor used as well as the type of load connected to the transmitter. Comparison was made with a Hall device current reference, which proved more accurate in some situations. In order to reduce the effects, changes were made to the design of the low-pass filters in the isolation amplifier, and the signal cable was reduced to the minimum length required.

A subsequent field test showed that measurements collected with the modified instrumentation applied in the nominal collinear dipole-dipole configuration resulted in data that could be fitted reasonably well by geologically sensible 1D models. However, discrepancies are still observed at high frequencies, and development of a better current reference system should be undertaken to ensure optimal data quality.

### 4.5.2 CR measurements in Sisimiut

Complex resistivity measurements were collected at the Sisimiut field site in area 2 along profiles L3, L4 and L5 in August 2003. Dipole spacings of 10 and 20 m and N-spacings from 1 to 8 were used, and measurements were collected at frequencies from 0.125 Hz to 9216 Hz. The applied equipment was manufactured by Zonge, and is described in detail in Paper D. The data were collected with the original system in the original configuration and thus the described changes to the system do not affect the data presented here. In fact, the observations made from the Sisimiut data constituted the main incentive to study the different error sources presented in Paper D.

The high frequency phase excursions observed in the Sisimiut data are es-

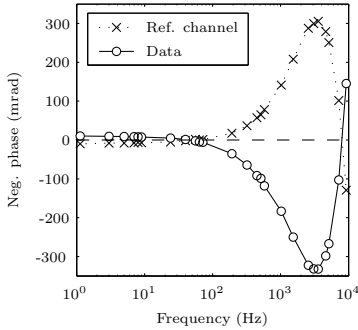


**Figure 4.4:** A data set where the data and reference phases are similar but opposite in sign at high frequencies (position -10m, N-spacing 4, on profile L4 with A-spacing 10m, profile not shown).

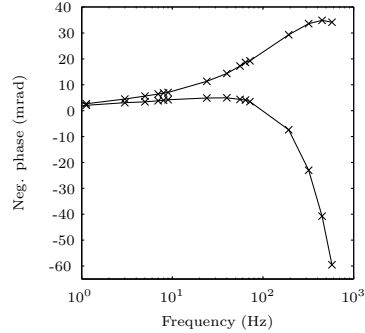


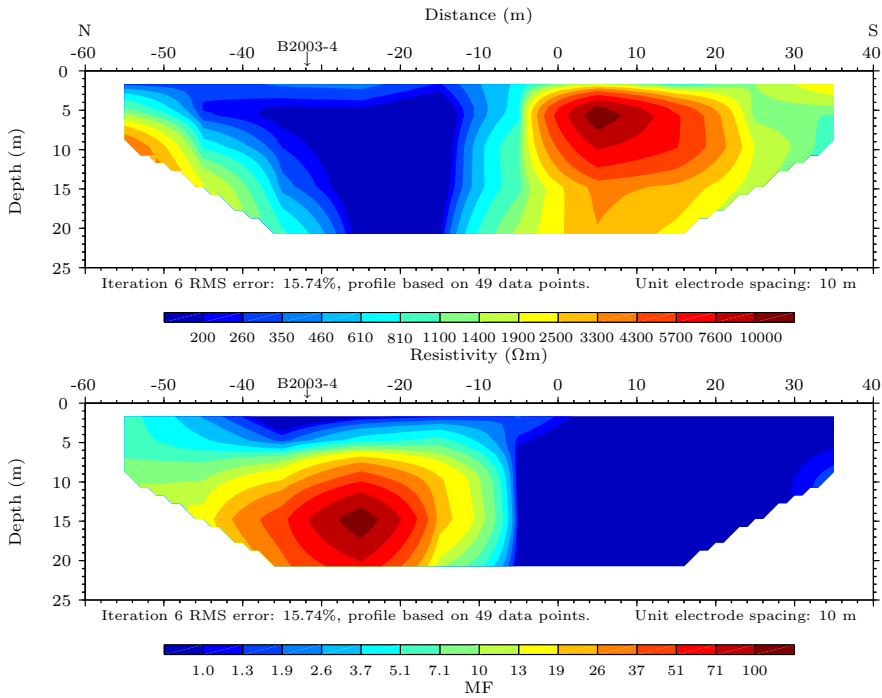
**Figure 4.5:** Example of two measurements at the same location but with transmitter and receiver interchanged (position -10m, N-spacing 2, on profile L5 with A-spacing 10m, see figure 4.7).

pecially larger than expected. Often the measured phase data show similar but opposite frequency dependence compared to the reference channel, see Figure 4.4. The figure is at the same time an example of the large positive phases (plotted negative due to the plotting convention) that are unexpectedly observed in many of the measurements. Where measurements of two adjacent spreads overlap, differences are observed between the two data sets, see Figure 4.5. In the ideal theoretical case, such measurements should be identical due to reciprocity.

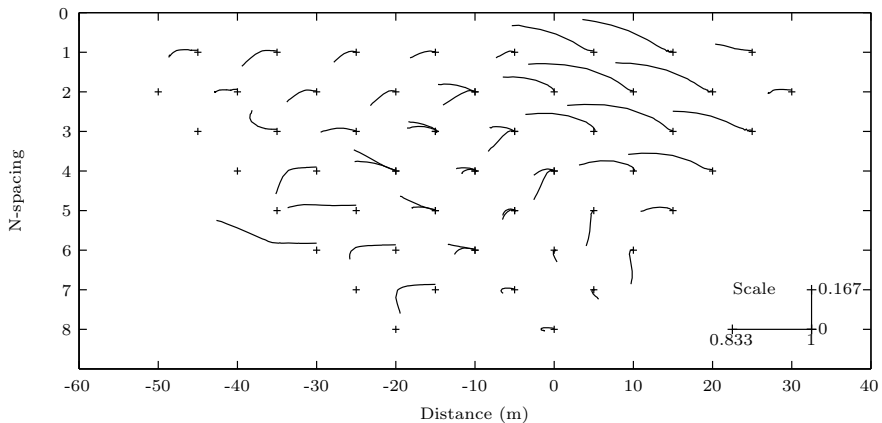
Due to the observed high frequency effects and based on the results described in Paper D the discussion of the field data is limited to frequencies up to 576 Hz (the 9<sup>th</sup> harmonic of the 64 Hz fundamental), and even in this range interpretation must be cautious.

Figure 4.6 shows inverted sections of 0.125 Hz resistivity and metal factor based on 0.125 and 1 Hz measurements for the L5 profile. The resistivity distribution is coherent with the one obtained from the MEP data, and the metal factor anomaly correlates well with the normalized time domain chargeability anomaly on the same profile (refer to section 2.6.1). This is coherent with the discussion by Slater & Lesmes (2002) on the relation between different chargeability parameters in frequency and time domain.

Figure 4.7 shows a spectral pseudosection of the L5 profile, where each measurement is represented by an Argand plot. Nine locations at the center of the profile have been measured on both spreads, and the differences in the Argand plots are clearly visible. Measured contact resistances were observed to increase drastically in the northern part of the profile, where the surface layer consisted of dry sand without vegetational cover. Despite attempts to reduce contact resistance by placing several electrodes in parallel, exceedingly high contact resis-



**Figure 4.6:** 0.125 Hz resistivity and MF based on 0.125 and 1 Hz from profile L5 inverted using RES2DINV.



**Figure 4.7:** Spectral pseudosection of the L5 profile showing Argand type plots for each measurement from 0.125 to 576 Hz. The scale refers to the real (horizontal) and negative imaginary part (vertical) of the Argand plots. The dipole spacing was 10 m.

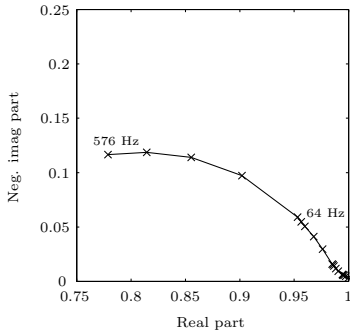


**Figure 4.8:** Argand plot of the characteristic response observed in highly resistive areas interpreted as permafrost (position 20m and N-spacing 2, on profile L5 with A-spacing 10m, see figure 4.7).

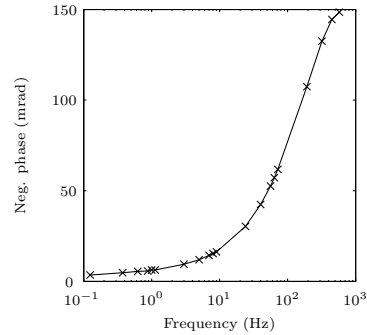


**Figure 4.9:** The characteristic phase response observed over highly resistive areas interpreted as permafrost (position 20m and N-spacing 2, on profile L5 with A-spacing 10m, see figure 4.7).

tances were observed, reaching 40 k $\Omega$  at the northernmost potential electrodes. All data obtained from this dipole except one were noisy and are not reproduced in the profile. At the overlapping locations, differences in contact resistance of up to 3 k $\Omega$  were observed. The measurements of contact resistance are two electrode measurements, and naturally include the resistance of the current path in the ground in addition to the actual electrode contact resistance. It is therefore interesting that measured resistances are lower over the permafrozen area than over the low resistive anomaly, which must be attributed to a conductive current path in the wet and vegetated active layer above the permafrost.

Although the overall impression of the profile may be one of disorder, each individual data set is generally continuous and have low standard deviations over the presented frequency spectrum. One particular observation is of significant interest. The area of high resistivity in the inverted profile seems to be correlated with a certain spectral behavior. The Argand plots of measurements in this area all show large responses and have a characteristic concave shape in the high frequency part, see Figure 4.8. The phase response is characterized by low values (<10 mrad) at low frequencies and a large phase peak at very high frequencies, most often located above 500 Hz (Figure 4.9).

The L4 profile was measured using both 10 and 20 m dipoles. Figures 4.10 and 4.11 show the resistivity and metal factor sections of the combined data sets. Good correlation is found with the MEP profiles, except in the deep parts of the sections where the CR measurements indicate lower bedrock resistivity to the south rather than the north of the anomaly. In the spectral pseudosection, which is shown for the 20 m dipole size, areas of high resistivity correlate with

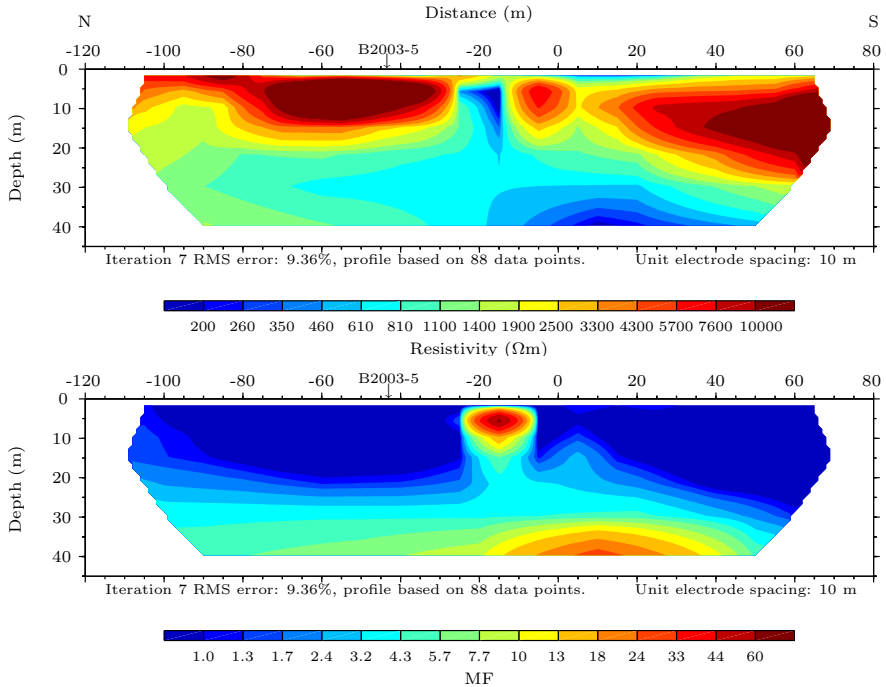


**Figure 4.10:** 0.125 Hz resistivity and MF based on 0.125 and 1 Hz from profile L4 inverted using RES2DINV. The inverted sections include data obtained using 10 m and 20 m dipole spacings.

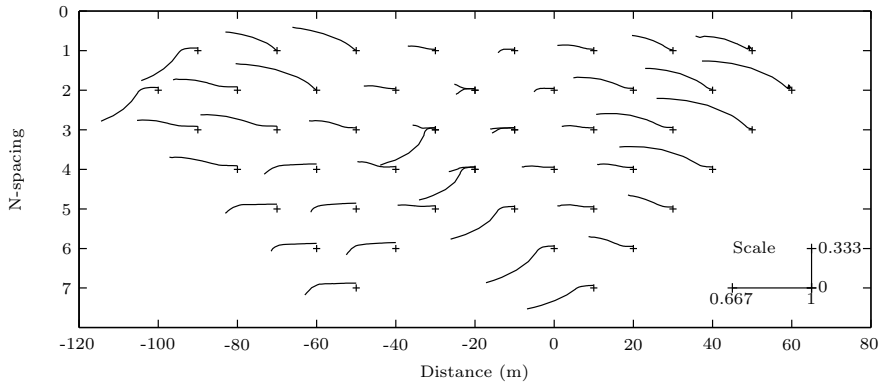


**Figure 4.11:** Spectral pseudosection of the L4 profile showing Argand type plots for each measurement from 0.125 to 576 Hz. The scale refers to the real (horizontal) and negative imaginary part (vertical) of the Argand plots. The dipole spacing was 20 m.

characteristic Argand plots similar to those observed on L5. Such results were obtained for the 10 m profile also. Another characteristic curve shape stands out on this profile and is characterized by large positive imaginary parts resulting in down-bending of the Argand curve. This shape is recognizable in seven measurements all collected using the same transmitter dipole. It is likely that this effect is caused by poor grounding or other errors relating only to this particular transmitter dipole.

The low frequency imaginary parts are generally observed to increase with N-spacing on this profile, indicating that the bedrock may be polarizable.

A series of 1D models have been calculated using CR1Dmod (Paper C) in an attempt to explain the observed phase effects as EM coupling. High phase responses as those observed in areas considered to be permafrost could only be obtained using very low resistivities. Although phase reversals (i.e. Figure 4.5) can be obtained by EM coupling in a high over low resistivity environment, the reversal occurs at higher frequencies, and only after a normal phase peak. The directly plunging phase behavior observed in these data sets could not be modelled. As the effect is mostly observed close to the low resistive anomaly, and since 3D effects on EM coupling in CR surveys have not been studied at higher frequencies, it cannot be excluded that EM coupling may play a role. However, based on the moderate resistivities observed in the area, EM coupling is not likely to completely explain the observed responses.

As discussed in Paper D, the presented responses are actually a division of the measured input channel waveform by the reference channel waveform, corresponding to subtracting the reference phase from the input channel phase and dividing the amplitudes. It is therefore unlikely that responses like the one presented in Figure 4.4 are due to phenomena in the ground. It rather indicates problems with the reference signal. Such problems were studied in Paper D, and were found to be significant at frequencies above 1000 Hz. The Sisimiut data indicate problems at much lower frequencies. The discrepancies may possibly be attributed to the fact that a low voltage transmitter was applied for the study in Paper D in place of the field transmitter, due to power and receiver input voltage considerations and common-mode problems.

Capacitive coupling could play a role in the differences observed at overlapping locations, since large differences in contact resistance have been measured. However, the approximate relation obtained in Paper D fails to predict the large phase effects observed, based on the relatively short dipoles and low frequencies involved. It is therefore likely that a large part of the response is due to reference channel problems. In the study of the reference measurement method it was observed that high frequency errors depended on what type of load the transmitter was transmitting across. This effect could possibly explain the observations.

The characteristic responses observed in permafrozen areas cannot be fitted by a single Cole-Cole model, although the high frequency part in many cases have the correct behavior. Saint-Amant & Strangway (1970) observed dispersion in

the same frequency range for very cold basaltic rock samples due to a small water content. The dispersions observed here are larger, and are probably caused by a combination of effects, but the correlation with high resistive frozen areas deserves thorough investigation when the equipment is perfected for high frequency measurements as discussed in Paper D. It should be noted that the previously discussed reference channel problems do not seem to be the cause of the responses observed in permafrost areas.

Phases of up to  $-50$  mrad were observed at the lowest frequency in the western part of profile L3, in an area with low resistivities which is probably unfrozen. The phase responses had dispersive characteristics most often with indications of a phase peak at frequencies lower than 0.125 Hz. Since no phase peaks are available and the phase spectra are affected by increases at higher frequencies that cannot be explained by available EM coupling models, further interpretation has not been successful. It is suggested that laboratory tests be made to establish the nature of these low frequency dispersions, and their possible relation to the fine-grained sediments of the area.

## 4.6 Discussion and outlook

The presented field data indicates that a characteristic and easily recognizable spectral behavior is correlated with high resistive areas interpreted to be permanently frozen. If this can be confirmed in additional studies, and if it can be shown that unfrozen sediments with a high resistivity do not exhibit the same behavior, the CR method may prove to be a valuable tool in permafrost investigations.

Nevertheless, the study has also shown that the technique and instrumentation still suffers from significant error sources, which render high frequency measurements virtually uninterpretable, and may even affect the low frequency data traditionally used. The equipment changes suggested and tested at a field site in Denmark have minimized the effects in the high frequency range, although some discrepancies are still observed and should be addressed in future work.

The capacitive coupling models, although purely theoretical, provide valuable information about the importance of electrode contact resistance. The model of the transmitter dipole must be refined and the important question of selecting a reasonable ground resistance must be addressed. Extension of the model to include electrode contact resistance would be a logical and important improvement. The model for the receiver dipole should be of immediate interest to the CR community once it has been confirmed by field tests.

With the current progress in wide frequency bandwidth CR measurements the traditional view of the EM coupling as an annoying side effect must be modified. The decoupling schemes have been shown to deteriorate with increasing frequency, and therefore interpretation must be based on the full EM coupling expressions. The development of the CR1Dmod modeling code presented in Paper C has proved very useful in both interpretation of field data and modeling of possible

error sources. A logical next step would be to extend the forward modeling code with inversion capability.

In terms of EM coupling, the Sisimiut data have shown that there is also an urgent need for knowledge about 3D effects in high frequency CR measurements. The work of Hohmann (1975) concerning 3D modeling using integral equations is thus of great interest, and could be advantageously applied to CR problems.

## 4.7 Conclusion

A new forward modeling tool, CR1Dmod, has been developed. It handles layered earth models with complex resistivity for several frequently used electromagnetic methods. The software has been applied to modeling of layout related errors in CR surveys, and the results show that errors due to the common practice of offsetting the dipoles from their ideal collinear locations are of minor importance.

Two capacitive coupling models have been developed as extensions to the CR1Dmod code for grounded dipoles. They show that capacitive coupling may be appreciative in surveys with moderate to long dipoles and that keeping electrode contact resistance low is of crucial importance.

A wide frequency bandwidth CR survey has been conducted at the Sisimiut field site. Although the data are affected by large errors possibly related to non-1D EM and capacitive coupling as well as equipment related issues, a characteristic and easily recognizable spectral behavior was observed in areas with permafrost. If equipment can be improved and the effects confirmed in future studies, the CR method may prove a valuable tool in distinguishing changes in permafrost distribution from changes in lithology.

Based on the results from Sisimiut and subsequent testing of the equipment applied, it has been shown that the current reference link introduces errors in the measured reference signal. The system has been improved by changing the low pass filters in the isolation amplifier and by removing excess reference cable. A subsequent field test resulted in data that could be fitted reasonably well by geologically sensible 1D models. Minor discrepancies are still observed and further improvement of the current reference method is advisable.

# Discussion

During the course of this study, a number of different geophysical methods have been applied to permafrost investigations in sedimentary deposits at the Sisimiut field site. Table 5.1 summarizes the applicability of each method to the determination of six aspects of the permafrost distribution and other significant properties at the field site. VLF-R measurements were of little use due to poor reception and were more affected by bedrock properties than permafrost distribution. Seismic refraction data provided some information on the lateral distribution of frozen ground and active layer thickness, but only indications of bedrock topography and depth were obtained. On the other hand, the combination of DC resistivity, induced polarization and ground penetrating radar measurements supplied very good information on several aspects, and is suggested as the basis for future geophysical permafrost investigations in Greenland.

The vertical distribution of permafrost and the depth to bedrock are aspects

**Table 5.1:** Summary of the applicability of the evaluated geophysical methods to different aspects of the permafrost investigations conducted at Sisimiut.

Method	Active layer thickness	Lateral permafr. distrib.	Vertical permafr. distrib.	Discrim. unfrozen fines	Discrim. frozen fines	Depth to bedrock
DC resistivity	✓	✓✓	✓	✓	%	✓
IP	✓	✓	✓	✓✓	%	%
VLF/VLF-R	%	✓	%	%	%	%
GPR	✓✓	✓	%	%	%	%
Seismic refraction	✓	✓	%	%	%	(✓)
Multifrequency FDEM	%	(✓)	%	%	%	%
LIN FDEM (theoretical)	?	✓✓	?	?	?	%
Complex resistivity	?	✓✓	✓	✓✓	?	✓

✓✓	Good information obtained	%	Not useful
✓	Some useful information obtained	?	Uncertain or not evaluated
(✓)	Indications only		

that are not sufficiently well clarified using the suggested combination of methods. Neither is discrimination of frozen fine-grained sediments in the present study, and high resistivities is the only indication of the presence of massive ground ice and the resulting risk of settling upon thawing. Although resistivity variations may be effectively mapped using DC resistivity, CR or LIN FDEM techniques, the resistivity, as most other physical parameters, is not uniquely related to the lithology or presence of frozen ground and massive ground ice. Therefore combinations of methods are generally needed to obtain proper models of the subsurface. Even so, a priori geological information is required to calibrate and thereby increase the reliability of geophysical interpretations. The overestimation of the thickness of the sedimentary sequence in area 1 of the Sisimiut field site based on the inversion of resistivity profiles is an illustrative example. The a priori information can be obtained from boreholes or local scale geological mapping; unfortunately both sources are scarce in most parts of Greenland, and the drilling of boreholes is difficult and very expensive due to the logistics involved. The challenge is therefore to choose geophysical methods that reduce the need for such information or provide the best possible basis for choosing borehole locations.

When applied conventionally using low frequencies, complex resistivity measurements were observed to yield information similar to what is obtained with the combined DC resistivity and IP methods. CR measurements could therefore possibly substitute these in a survey combination with the GPR method. However, the acquisition of CR data is slower and more cumbersome than modern multielectrode profiling methods used in DC and IP surveys. Nevertheless, the high frequency responses observed in CR measurements over permafrost may — if confirmed — supply additional information not available in DC and IP data, and may thus help overcome some of the ambiguity of DC resistivity distributions.

In the assessment of settling risks upon permafrost degradation, methods that directly measure the subsurface ice content would be preferable. Density variations in areas with massive ground ice may in some cases be detected by gravity methods (Kawasaki et al., 1982), which could also possibly supply better determinations of bedrock depths. The nuclear magnetic resonance (NMR) method, measuring the spin echo of hydrogen atoms, is of great interest, since water molecules are the most abundant source of hydrogen in the near surface geological environments in Greenland. In a recent study by Kleinberg & Griffin (2005) NMR was used to study the unfrozen water content of drill cores of permafrozen sediments, but the method have not been widely used in permafrost investigations. Were it possible to modify the system used by Kleinberg & Griffin to be sensitive to hydrogen contained in ice formations, such equipment would provide a more direct way of studying permafrost distribution.

## Conclusion

---

This thesis has been concerned with the evaluation of geophysical tools applied to permafrost mapping in Greenland. At a field site near the town of Sisimiut, a combination of resistivity, induced polarization and ground penetrating radar measurements proved powerful in determining the lateral extents of permanently frozen sediments, as well as the depth to the top of the permafrost. Indications of frozen ground were high resistivity, low normalized chargeability and a strong reflector at the permafrost table. Furthermore, the IP method seems capable of distinguishing fine-grained sediments in this area, and may therefore be useful in determining the risk of massive ground ice development in case of permafrost aggradation.

The horizontal loop electromagnetic method (HLEM), a ground based multifrequency FDEM method, was studied theoretically and in a field test at the Sisimiut site, but was found inappropriate for application in the Greenlandic environment. A thorough theoretical study of misalignment effects show that the measurements are severely corrupted even by small errors in coil alignment. The field test confirmed that the real part of the measurements is useless in quantitative interpretation, whereas the imaginary part may be the basis of semi-quantitative indications in some cases. Generally, currently available equipment cannot be expected to yield sufficiently accurate results to allow quantitative 1D interpretation even when applied in less hostile environments. The theoretical studies favor the use of ground conductivity meters, which are not as severely affected by misalignment and better suited to study moderate to high resistivities.

A wide frequency bandwidth complex resistivity survey at the Sisimiut field site resulted in measurements, which were affected by large errors possibly related to EM and capacitive coupling as well as equipment related problems. Based on model calculations using the CR1Dmod software, developed as part of this research, it was concluded that the modelled layout related errors were of minor importance, whereas capacitive coupling is a major concern when moderate to long dipoles are applied. Keeping contact resistance low is crucial to avoiding capacitive coupling. Laboratory tests of the CR equipment showed that the current

reference link introduces errors in the measured reference signal. The system has been improved by changing the low pass filters in the isolation amplifier and by removing excess reference cable.

Despite the problems encountered, the Sisimiut CR survey suggests that a characteristic spectral behavior is observed in areas with permafrozen sediments. If this effect is confirmed in studies with the improved equipment, the CR method may be a valuable tool in future permafrost investigations, and could possibly substitute DC resistivity and IP measurements in a survey combination with the GPR method.

# Appendices



APPENDIX A

# Misalignment effects in FDEM measurements

---

Submitted to *Near Surface Geophysics*.

Reviewers have recommended publication subject to moderate revisions.



# Misalignment effects in FDEM measurements.

Thomas Ingeman-Nielsen<sup>1,\*</sup> and François Baumgartner<sup>1,2</sup>

<sup>1</sup> Arctic Technology Centre, BYG•DTU, Technical University of Denmark, DK-2800 Kgs. Lyngby, Denmark.

<sup>2</sup> Institute of Geophysics, Faculty of Earth Sciences and Environment, University of Lausanne, CH-1015 Lausanne, Switzerland.

\* Corresponding author: Phone: (+45) 45252251, Fax: (+45) 45885935, E-mail address: tin@byg.dtu.dk.

---

## Abstract

The objective of this study is to develop an understanding of the 3D misorientation and alignment errors liable to occur in dipole-dipole electromagnetic measurements with the horizontal coplanar loop configuration. Development of geometric formulae for the fields of an arbitrarily directed transmitter dipole as observed by an arbitrarily directed receiver dipole over a homogeneous half-space allow us to model the response in different misalignment situations. Over most of the frequency spectrum, we find that extreme values of the error occur, when the two dipole axes are both located in the vertical plane connecting the centers. By applying six different apparent resistivity definitions we study the effect of these errors. In the case where the dipole axes are oriented away from or towards each other, an algorithm based on both the real and imaginary parts of the response gives the best results, although errors of up to 30% are still observed at axes inclinations of only 5° from vertical. When the dipole axes are oriented in the same direction, equivalent to using the system in-line on a linear topography, apparent resistivity definitions based on the phase or the imaginary part alone are relatively undisturbed. From the analysis, it is in general not possible to declare one definition superior to the others, as none of them perform well in all situations. The results highlight the advantage of the type of low induction number instruments where transmitter and receiver are fixed relative to each other. For other systems, quantitative interpretation of data from areas with topography seems doomed to failure, and even on level ground utmost care must be taken in measuring separation and coil orientations at great accuracy, thereby increasing surveying time and cost.

*Keywords:* Frequency-domain ground EM, homogeneous half-space model, misorientation effect, topographic effects, apparent resistivity.

---

## A.1 Introduction

In connection with groundwater research in Greenland, the Arctic Technology Center has considered the frequency-domain electromagnetic (FDEM) method, because it is a fast and light-weight surveying method, which requires no electrical contact with the ground. Therefore it can theoretically be used year round at low cost.

In areas of rugged topography and loss of line of sight, perfect alignment of the coils is seldom possible. Therefore an evaluation of the errors due to misalignment of the coils and the effect of topography is of great interest.

There has been previously some interest in evaluating the effect of some simple cases of coil misalignment. Verma (1973) studied the effect of linear topography on the mutual coupling ratios of four different commonly used coil systems over a homogeneous half-space. Sinha (1980) studied the errors observed by a specially designed multi-axis coil system due to topographical relief and misorientation of the axis of the transmitter loop. Recently there has been a renewed interest in misalignment effects within the field of frequency-domain helicopter electromagnetic (HEM) surveys (Fitterman & Yin, 2004; Yin & Fraser, 2004), in which case the transmitter and receiver coils are fixed relative to each other inside the bird.

Here we are interested in the errors occurring due to 3D misorientation of both transmitter and receiver coil axes, as well as in obtaining a deeper understanding of the effect of linear topographical relief, in dipole-dipole measurements made at the surface of the earth. In this article we are mainly concerned with frequency soundings using the horizontal coplanar loop configuration, although many of the presented equations are generally applicable.

As an apparent resistivity transformation is commonly applied in interpretation of EM data we further investigate the effect of misalignment on different apparent resistivity definitions.

## A.2 Theoretical background

In electromagnetic theory, the fields of a loop source of current can be approximated by the fields arising from a magnetic dipole source of moment  $m = IS$ , where  $I$  is the current flowing in the loop and  $S$  is the effective area of the loop (turns-area product). This assumption is fulfilled as long as the distance to the observation point is large compared to the loop radius (Wait, 1955). Throughout this article we operate under this assumption, and hence refer to magnetic dipoles and dipole axes rather than coils and coil axes.

The dipole moment,  $m$ , of an arbitrarily directed magnetic dipole transmitter can be treated as a superposition of three orthogonal dipoles in the  $x$ -,  $y$ -, and  $z$ - directions. We label these three components  $m_x$ ,  $m_y$  and  $m_z$ . If the direction of the transmitter dipole moment is defined in terms of  $(\theta_t, \phi_t)$  as shown in Figure A.1, then the relative sizes of the orthogonal components are defined as:

$$m_x = m \sin \theta_t \cos \phi_t , \quad (\text{A.1})$$

$$m_y = m \sin \theta_t \sin \phi_t , \quad \text{and} \quad (\text{A.2})$$

$$m_z = -m \cos \theta_t . \quad (\text{A.3})$$

Because the resultant field from each dipole may again be split into  $x$ -,  $y$ -, and  $z$ -components, a total of nine terms are needed to describe the resultant field.

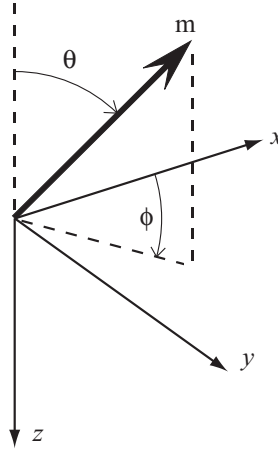


**Figure A.1:** The direction of the dipole moment is defined in terms of the angle from vertical,  $\theta$ , and the angle from the  $x$ -axis,  $\phi$ . The coordinate system is defined with the  $z$ -axis positive down.

If we consider a dipole receiver in an H-field, the magnitude of the observed field intensity is a projection of the  $x$ -,  $y$ -, and  $z$ -components of the field on the axis of the receiver. Thus the magnitude of the observed field is found by the relation

$$H_r = H_x \sin \theta_r \cos \phi_r + H_y \sin \theta_r \sin \phi_r - H_z \cos \theta_r, \quad (\text{A.4})$$

where  $(\theta_r, \phi_r)$  define the direction of the dipole receiver. Because the field of a magnetic dipole is proportional to the dipole moment we write for the field from an arbitrarily directed dipole transmitter measured by an arbitrarily directed dipole receiver

$$\begin{aligned} H_r = & \sin \theta_r \cos \phi_r (\sin \theta_t \cos \phi_t H_{xx} + \sin \theta_t \sin \phi_t H_{yx} - \cos \theta_t H_{zx}) \\ & + \sin \theta_r \sin \phi_r (\sin \theta_t \cos \phi_t H_{xy} + \sin \theta_t \sin \phi_t H_{yy} - \cos \theta_t H_{zy}) \\ & - \cos \theta_r (\sin \theta_t \cos \phi_t H_{xz} + \sin \theta_t \sin \phi_t H_{yz} - \cos \theta_t H_{zz}), \end{aligned} \quad (\text{A.5})$$

where  $H_{ij}$  is the field-intensity from an  $i$ -directed transmitter as observed by a  $j$ -directed receiver dipole.

### A.2.1 Normalization

Field measurements are measurements of the combined effect of the free-space (primary) field,  $H^P$ , and secondary field,  $H^S$ , which is a measure of the perturbation of the primary field due to the presence of the half-space. In order to reduce the range of responses, data are usually normalized with respect to the primary

field of the configuration under consideration, which yields the mutual coupling ratio

$$\frac{H^P + H^S}{H^P} = \frac{H^S}{H^P} + 1 = \frac{Z}{Z_0}. \quad (\text{A.6})$$

This operation is usually carried out in the instrument, assuming a certain configuration and dipole spacing. Only three combinations of dipole orientations have non-zero primary fields (Keller & Frischknecht, 1966)

$$H_{xx}^P = \frac{m}{2\pi r^3}, \quad (\text{A.7})$$

$$H_{yy}^P = -\frac{m}{4\pi r^3}, \quad \text{and} \quad (\text{A.8})$$

$$H_{zz}^P = -\frac{m}{4\pi r^3}. \quad (\text{A.9})$$

where  $r$  is the distance between the magnetic dipoles. In these equations it is assumed that the transmitter dipole is located in the origin and the receiver dipole on the  $x$ -axis. The three configurations are named the Vertical Coaxial (VCA), the Vertical Coplanar (VCP) and the Horizontal Coplanar (HCP) configurations, respectively, referring to the orientation of the coil planes (vertical/horizontal) and axes. For configurations with zero primary field, the primary field for the HCP configuration ( $H_{zz}^P$ ) is generally assumed in the normalization.

### A.2.2 Response on a homogeneous half-space

In the case of measurements on the surface of a homogeneous half-space with the transmitter at the origin, in the quasistatic approximation and with the assumption that the magnetic permeability of the half-space is equal to that of free-space ( $\mu_1 = \mu_0$ ), the field-components can be calculated analytically (Wait, 1952; Keller & Frischknecht, 1966; Ward & Hohmann, 1988):

$$H_{xx} = -\frac{m}{4\pi r^3} \left[ y^2 \Phi + x^2 r \frac{\partial \Phi}{\partial r} \right] \quad (\text{A.10})$$

$$H_{xy} = H_{yx} = \frac{m}{4\pi r^3} \left[ xy \Phi + xyr \frac{\partial \Phi}{\partial r} \right] \quad (\text{A.11})$$

$$\begin{aligned} H_{xz} &= \frac{mk^2 x}{4\pi r^2} \left[ I_1 \left( \frac{ikr}{2} \right) K_1 \left( \frac{ikr}{2} \right) - I_2 \left( \frac{ikr}{2} \right) K_2 \left( \frac{ikr}{2} \right) \right] \\ &= -H_{zx} \end{aligned} \quad (\text{A.12})$$

$$H_{yy} = -\frac{m}{4\pi r^3} \left[ x^2 \Phi + y^2 r \frac{\partial \Phi}{\partial r} \right] \quad (\text{A.13})$$

$$\begin{aligned} H_{yz} &= \frac{mk^2 y}{4\pi r^2} \left[ I_1 \left( \frac{ikr}{2} \right) K_1 \left( \frac{ikr}{2} \right) - I_2 \left( \frac{ikr}{2} \right) K_2 \left( \frac{ikr}{2} \right) \right] \\ &= -H_{zy} \end{aligned} \quad (\text{A.14})$$

$$H_{zz} = \frac{m}{2\pi k^2 r^5} \left[ 9 - (9 + ikr - 4k^2 r^2 - ik^3 r^3) e^{-ikr} \right], \quad (\text{A.15})$$

where  $I_n$  and  $K_n$  are the modified Bessel functions of order  $n$ ,  $k$  is the propagation constant  $k = \sqrt{-i\omega\mu_0\sigma}$ , the imaginary unit  $i = \sqrt{-1}$ , and

$$\Phi = \frac{2}{k^2 r^4} [3 + k^2 r^2 - (3 + 3ikr - k^2 r^2) e^{-ikr}] \quad (\text{A.16})$$

$$\frac{\partial\Phi}{\partial r} = \frac{2}{k^2 r^5} [-2k^2 r^2 - 12 + (-ik^3 r^3 - 5k^2 r^2 + 12ikr + 12) e^{-ikr}] \quad (\text{A.17})$$

The  $H_{ij}$  fields are total fields which include the primary field and the secondary field.

If the  $x$ -axis is aligned with the dipole-dipole axis,  $H_{xy}$ ,  $H_{yx}$ ,  $H_{zy}$  and  $H_{yz}$  are identically zero, that is, neither a primary field nor a secondary field is measured in these configurations. This type of configuration is usually referred to as a NULL or null-coupled configuration.

Thus for the response on a homogeneous half-space, equation (A.5) is reduced to

$$\begin{aligned} H_r = \sin\theta_r \cos\phi_r (\sin\theta_t \cos\phi_t H_{xx} - \cos\theta_t H_{zx}) \\ + \sin\theta_r \sin\phi_r (\sin\theta_t \sin\phi_t H_{yy}) \\ - \cos\theta_r (\sin\theta_t \cos\phi_t H_{xz} - \cos\theta_t H_{zz}) . \end{aligned} \quad (\text{A.18})$$

Because  $H_{xz}$  and  $H_{zx}$  are numerically identical but differ in sign, it is observed, that these components cancel when  $\theta_t = \theta_r$  and  $\phi_t = \phi_r$ .

### A.2.3 Apparent resistivity algorithms

The concept of apparent resistivity is commonly applied in geophysical exploration as a useful procedure for normalizing the measured response for measurement specific variables (such as transmitted current, source-receiver separation), and for parameterizing the measured response in units of an intrinsic rock property, the resistivity (Spies & Eggers, 1986). It is usually defined as the resistivity of a homogeneous half-space, which yields an identical measurement when the same geophysical system and setup is applied.

The apparent resistivity of electromagnetic exploration can be defined in a number of ways. Wilt & Stark (1982) introduce the concept of finding the apparent resistivity by graphically matching any component of dipole-dipole electromagnetic measurements to a corresponding theoretical response curve. However, this definition leads to non-unique results, necessitating a high degree of user intervention in the data processing. To overcome this problem, Das (1995, 1997) introduced a definition based on a combination of measurements with different source-receiver configurations and field components. For this definition to give reliable results, a wide frequency band must be applied, adversely affecting the surveying time and cost. Van der Kruk et al. (2000) suggested projecting the measured complex mutual coupling ratio onto the nearest homogeneous half-space Argand curve, thereby deducing the resistivity of the half-space. In practice they

minimize the cost function

$$E(\rho) = \left| \frac{Z}{Z_{0 \text{ data}}} (f, r) - \frac{Z}{Z_{0 \text{ model}}} (f, r, \rho) \right|^2, \quad (\text{A.19})$$

where  $f$  is the frequency,  $r$  is the coil separation, and  $\rho$  is the half-space resistivity. This definition can be used with any dipole configuration.

In recent years, several other definitions related to HEM measurements have emerged (Siemon, 2001; Huang & Fraser, 2002), and we would like to draw attention to the fact that in these definitions, the sensor height is often incorporated as a free parameter. Thus, using real and imaginary parts of the response as input, both the resistivity and sensor height can be deduced either by table look-up (curve matching) or a least-squares inversion technique (Beard, 2000). Beamish (2002) proved these apparent resistivity definitions to be stable and robust in the presence of cultural features, as these influences were observed to affect mostly the sensor height determination. We therefore suggest applying the same process of inversion to ground based EM data in the expectation that the resulting apparent resistivity may prove more stable with regard to misorientation effects.

## A.3 Misalignment effects

### A.3.1 Dipole misorientation

Figure A.2 gives an analysis of the effect of misorientation of the two dipoles in a HCP loop configuration. Both the transmitter and receiver dipole axes are assumed to have an angle of  $\theta = 5^\circ$  with vertical, and each plot contains information on all possible combinations of orientations ( $\phi$ ) of the misalignment of the two dipoles. Plots are given for the real and imaginary parts of the difference between the misaligned and nominal mutual coupling ratios for six induction numbers ( $B = \sqrt{\sigma\mu\omega/2} \cdot r$ ). Thus the plotted values are the absolute errors due to the misalignment.

The errors change in a complex and non-monotonic way as a function of both induction number and dipole orientations. It is worth noting that global extremes are found for various combinations of dipole axis rotations of multiples of pi, that is when the axes are located in the vertical plane connecting the two dipoles. Three different types of dipole orientations are possible in this plane: dipole axes tilted towards each other (T), dipole axes tilted away from each other (A), and dipole axes tilted to the same side (S). The latter situation corresponds to the locations at the center and four corners of each plot, and it is observed that these locations always take the same value. Hence, to which side the dipoles are tilted is unimportant.

For the imaginary part, T and A give extreme errors over most of the spectrum. Around induction numbers of approximately 3, they interchange signs, such that T, which gives maximum reduced response at low induction numbers,

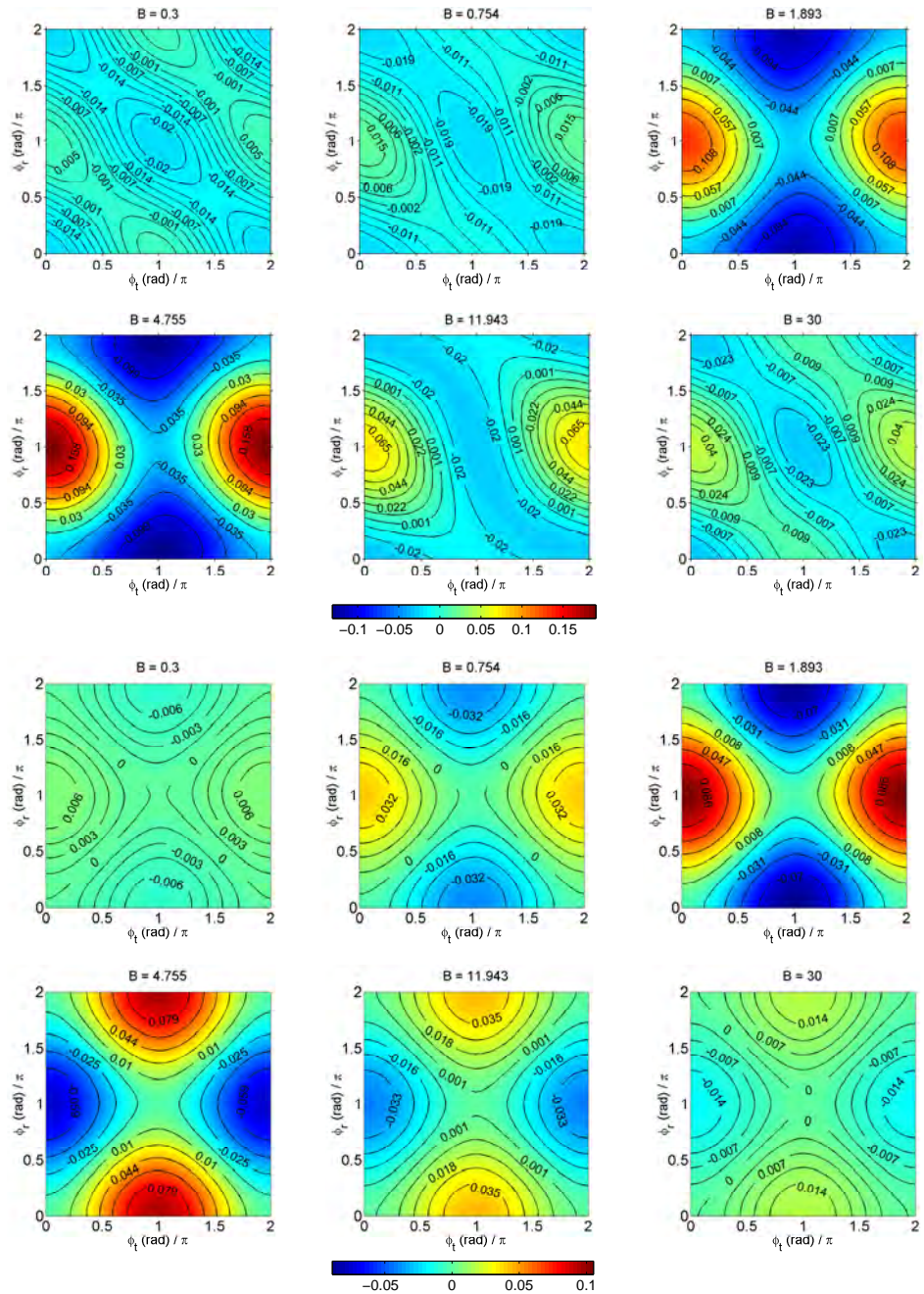


**Figure A.2:** Real (top) and imaginary parts (bottom) of the difference between the misaligned and nominal mutual coupling ratios for the HCP configuration,  $\left(\frac{Z}{Z_0}_{mis} - \frac{Z}{Z_0}_{nom}\right)$ . The misorientation of the dipole axes are  $5^\circ$  from vertical.

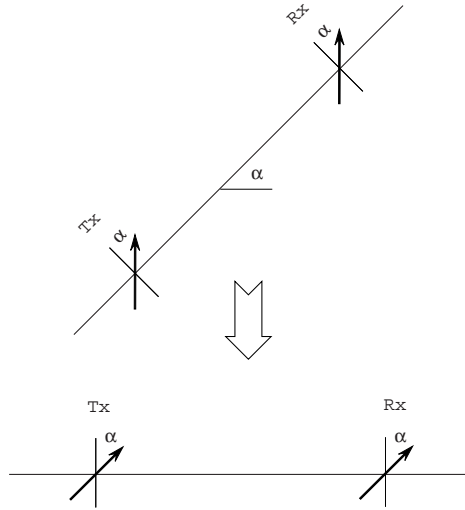


**Figure A.3:** Vertical dipoles on a linear topography can be calculated as angled dipoles on a half-space.

gives maximum increased response at high induction numbers, and vice versa. What cannot be seen from the figure is that in the transition zone, the location of the minimum migrates first from A to S and then from S to T. This transition zone becomes more pronounced with an increase in the angle between the dipole axes and vertical.

The real part shows a more complex progression. T always results in a maximum increase in the response. However, at very low and very high induction numbers, A gives the same response as T. In these situations, S gives the location of the maximum decrease. At induction numbers in the middle of the range, the maximum decrease in response migrates towards the A dipole orientation, and the absolute value of the error increases.

### A.3.2 Special case: The effect of topography

If a magnetic dipole-dipole configuration is applied in-line on a linear topography and the dipole axes are vertical, then the configuration can be computationally considered as shown in Figure A.3 (for a HCP configuration), where  $\alpha$  is the topographical inclination. For both the HCP and VCA configurations, the dipole axes will be located in the  $x$ - $z$  plane, and hence  $\phi_r = \phi_t = n\pi$ , where  $n = [0, 1, 2]$ . In these cases, equation A.18 reduces to

$$H_r = \sin^2(\alpha + \theta) H_{xx} + \cos^2(\alpha + \theta) H_{zz} , \quad (\text{A.20})$$

where  $\theta = 0$  for the HCP configuration and  $\theta = \pi/2$  for the VCA configuration. It can be easily realized that there is no effect on a VCP configuration.

The orientation of the dipoles over a linear topography corresponds to the four corners of the plots in Figure A.2, when  $\alpha$  is positive, and the center point when  $\alpha$  is negative. As previously noted, these five locations always have identical values, and the effect of topographic relief can be found by observing these points for varying inclination of the dipole axes.

Figure A.4 shows the relative errors in the response of a HCP configuration arising from different topographical gradients as a function of the induction number. On level ground, the normalized responses are, of course, identically one for all induction numbers. As topography becomes steeper, the influence from the VCA response increases, and the real part of the normalized response (at low induction numbers) decreases, with a change in sign at a topographical inclination of approximately  $35^\circ$  (Figure A.4, top). Thus at this inclination, the error in the measurement (at low induction numbers) is so large that it totally balances the nominal response. The imaginary part of the normalized response also shows a decrease, although it is much less severe (Figure A.4, middle).

For interpretation purposes we are concerned mostly with the secondary field, and usually it is the ratio of the secondary to the primary field that is used. However, when misalignment is a factor, the subtraction of the nominal primary field is erroneous, because a wrong magnitude is assumed for the primary field and the result is

$$\frac{Z}{Z_0} - 1 = \frac{H_r^P + H_r^S - H_{zz}^P}{H_{zz}^P} = \frac{H_r^S + \Delta^P}{H_{zz}^P}, \quad (\text{A.21})$$

where  $\Delta^P$  represents the error due to the VCA component of the primary field, and is therefore purely real. The magnitude of  $\Delta^P$  is increasing with the topographic angle and has a sign opposite of the measured secondary field at low induction numbers.

The ratio of the real part of  $H_r^S + \Delta^P$  to  $H_{zz}^S$ , which gives the relative error in the real value actually used in interpretation, is also plotted in Figure A.4 (bottom). Severe effects are observed, especially at low induction numbers, and even for small topographical inclinations.

The singularities occurring in the real and imaginary parts of the normalized responses arise from zero-crossings in the nominal response used in the normalization, which is given in Figure A.5 for reference. It is seen that for this special case, the real part of the response is most severely affected by topography at low induction numbers, whereas the imaginary part is much less affected.

### A.3.3 The effect of misorientation on apparent resistivity

In our analysis, we have chosen to apply the apparent resistivity algorithm of Van der Kruk et al. (2000) (type 5 in Table A.1). We modify it to use the individual parameters, real part, imaginary part, amplitude, and phase (type

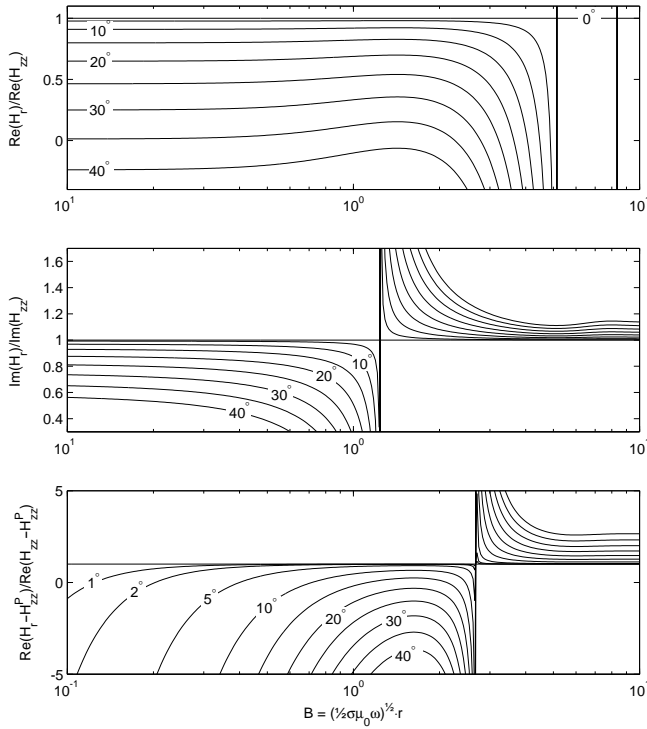


**Figure A.4:** The response due to a linear topography of inclination  $\alpha$  normalized with respect to the real and imaginary parts of the nominal HCP response. Clearly the imaginary part of the response is much less affected by topographic inclination.

1-4) as optimization parameters, thus obtaining automated versions of the curve-matching algorithm of Wilt & Stark (1982). Finally, inspired by the interpretation techniques of HEM data, we invert the real and imaginary data with both half-space resistivity and sensor height as free parameters (type 6). The inversion package SELMA (Christensen & Auken, 1992) was used for this part of the analysis for a two layer earth model, keeping the resistivity of the top layer fixed to 100k $\Omega$ m to simulate free space.

Figure A.6 shows the apparent resistivity obtained by applying the six different definitions, with the dipole axes misaligned towards and away from each other in the vertical plane connecting the two dipoles (situations T and A). All six definitions show severe effects even at small misalignment angles.

As mentioned by Wilt & Stark (1982), the type 1-4 definitions, which are based on only one part of the measured response, result in non-unique apparent resistivities. This non-uniqueness was handled by choosing the result closest to the nominal half-space resistivity, thereby obtaining the best possible solution. In

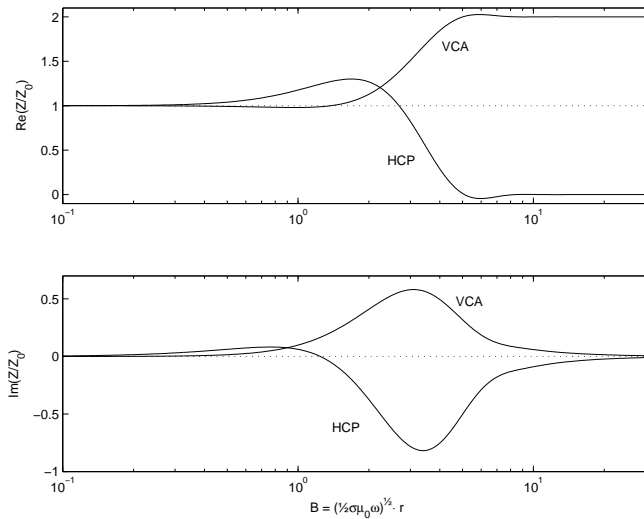


**Figure A.5:** Mutual coupling ratios for the HCP and VCA configurations over a homogeneous half-space.

practice, the choice between two solutions would have to be based on the results obtained at frequencies above or below the actual frequency at the same location and results at the same frequency at stations in the immediate vicinity.

The type 5 definition, which is based on both real and imaginary data, gives unique results, and the apparent resistivity is continuous as a function of frequency. Among all the definitions applied, this one gives results closest to the nominal half-space response. Nevertheless, the observed errors in the calculated apparent resistivity may reach 30% at low induction numbers for a misalignment of  $5^\circ$  in the T situation. The error is slightly smaller for the A situation.

The type 6 inversion algorithm results in a more noisy and discontinuous apparent resistivity profile. The calculated heights range from close to 0m to more than 20m in a complex and discontinuous pattern. However, it was found that the error in the resistivity and height was correlated, so that at frequencies in the middle and high end of the spectrum, where the apparent resistivity is close to the nominal resistivity, the calculated instrument height was close to 0m.

For the case of linear topography, we present apparent resistivity curves for topographical inclinations of  $2.5^\circ$ ,  $5^\circ$ ,  $7^\circ$  and  $10^\circ$  in Figure A.7. The large relative errors in the real part at low induction numbers previously described, result in very large errors in the apparent resistivities obtained using the type 1, 3 and 5 definitions.

As could be expected, the type 4 definition, which is based solely on the imaginary part, results in apparent resistivities very close to the nominal half-space

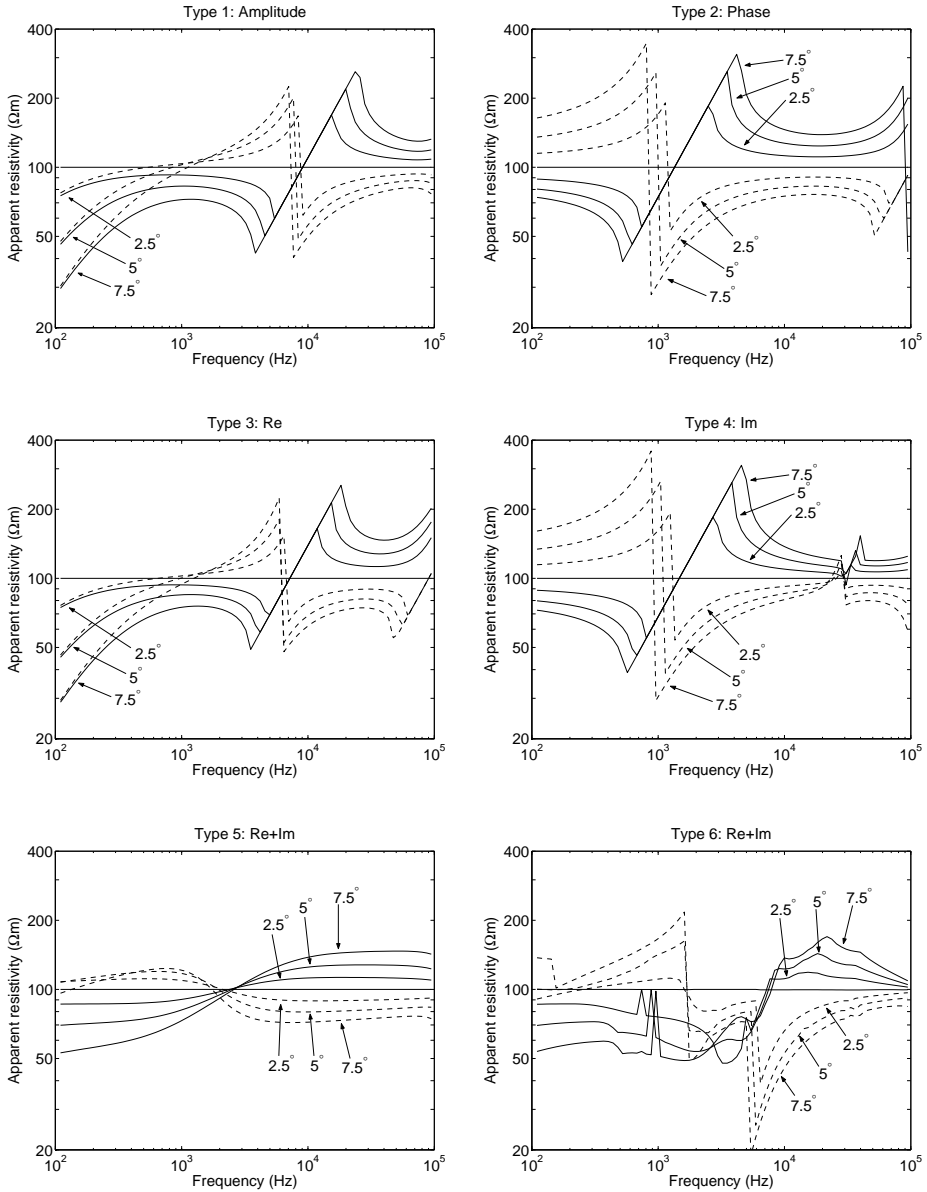


**Figure A.6:** The effect of misorientation of the dipole axes away from (dashed) or towards each other (solid) in the vertical plane connecting them is shown in terms of the six apparent resistivity definitions for three different inclinations of the axes, 2.5°, 5° and 7°.

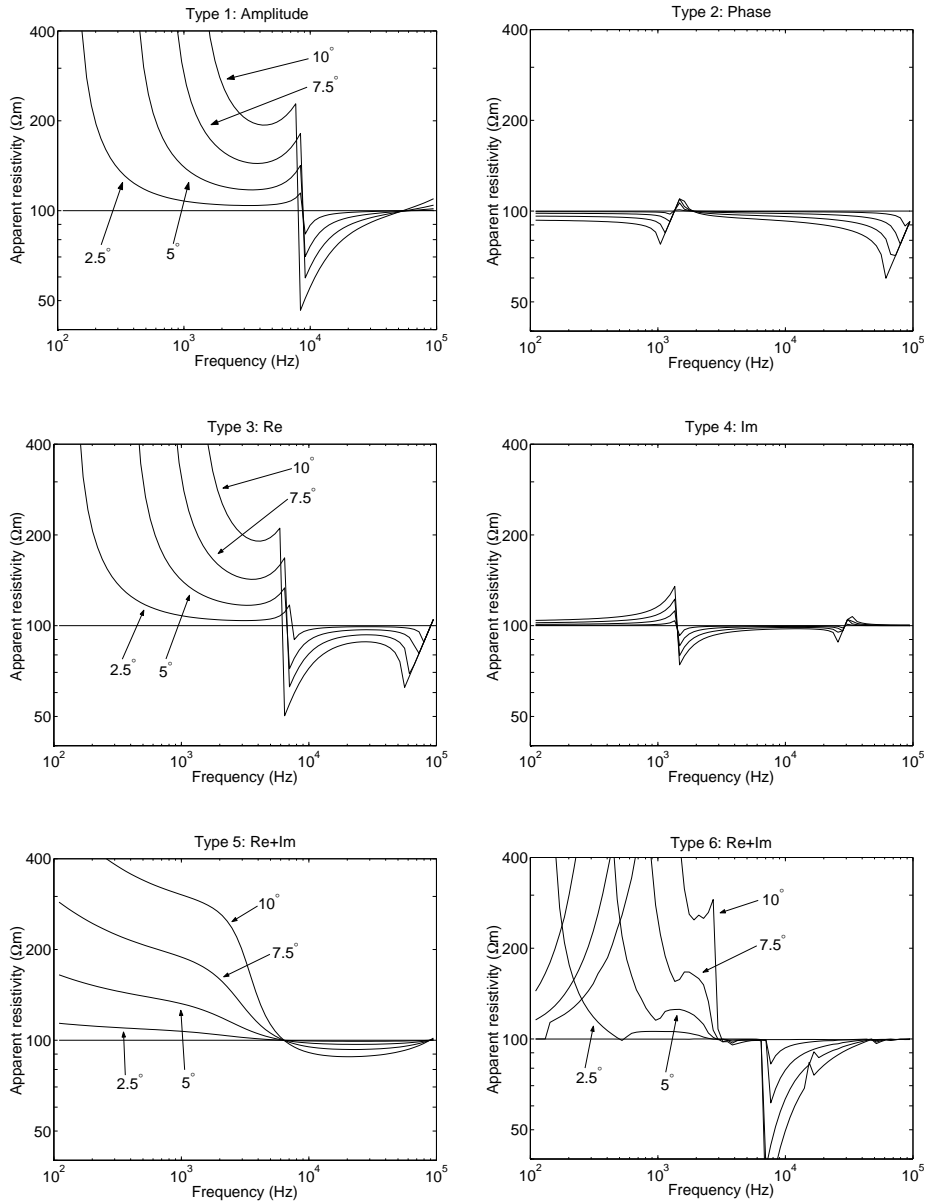


**Figure A.7:** The effect of topographic relief is shown in terms of the six apparent resistivity definitions for four different topographic gradients, 2.5°, 5°, 7° and 10°.

Type	Input	Output	Method
1	A	$\rho_a(f)$	Auto curve matching
2	$\phi$	$\rho_a(f)$	Auto curve matching
3	Re	$\rho_a(f)$	Auto curve matching
4	Im	$\rho_a(f)$	Auto curve matching
5	Re+Im	$\rho_a(f)$	Auto curve matching
6	Re+Im	$\rho_a(f), h(f)$	Inversion

**Table A.1:** Seven different apparent resistivity definitions are considered with respect to the effects of misalignment. The input parameters Re, Im, A and  $\phi$  refer to the real part, the imaginary part, the amplitude ( $\sqrt{\text{Re}^2 + \text{Im}^2}$ ) and the phase ( $\tan^{-1}(\text{Im}/\text{Re})$ ) of the mutual coupling ratio.

resistivity over the entire frequency spectrum. So does definition 2, although the phase angle includes information from the real part. The results from the type 6 inversion response are noisy with large errors in the apparent resistivity, but in contrast to the type 5 results, the nominal half-space resistivity is approached at very low frequencies.

We have compared the results of the type 3 and 4 definitions to inversions based on the real and imaginary parts using the SELMA package. Using an uncertainty of infinity for one of the components, we effectively obtain an inversion based on the other component. In all three dipole orientation situations, we found agreement between the inversion result and the automated curve-matching. We did observe differences in the location of major discontinuities, corresponding to a choice between two solutions. This was expected, due to the way the automated curve-matching algorithm was applied.

From the present analysis we conclude that in the case of misaligned dipoles on the surface of a homogeneous half-space inversion with the resistivity and measurement height as free parameters does not constitute an improvement to the automated curve-matching algorithms. Furthermore, it is not possible to declare one algorithm superior to all others.

### A.3.4 Spacing effects

Another type of misalignment error in FDEM surveys is the effect of errors in the dipole spacing. This is ultimately a normalization error, as a certain nominal dipole separation is assumed in the normalization. Because it is a normalization error, the data can be corrected, if the correct coil separation is known, as described in Frischknecht et al. (1991). That is, the data can be corrected to the actual spacing, since the normalization can be removed and reapplied using the correct spacing. This is a problem in manual curve matching type interpretations, as master curves must be available for all imaginable separation distances, whereas in computerized inversion the actual spacing can be easily taken into

account.

Spacing errors mainly affects the real part of FDEM measurements, resulting in large errors at low frequencies that decrease towards higher frequencies. The imaginary part is not significantly affected over a homogeneous half-space.

### A.3.5 LIN instruments

A popular subset of frequency domain electromagnetic instruments, known as or Ground Conductivity Meters (GCM), operate under the Low Induction Number (LIN) approximation. When the induction number is sufficiently low, the equations describing the homogeneous half-space response may be significantly simplified and an approximate apparent conductivity formulation obtained based on the imaginary part of the measured response (McNeill, 1980)

$$\sigma_a = \frac{4}{\omega\mu_0 r^2} \cdot \text{Im} \left( \frac{Z}{Z_0} - 1 \right), \quad (\text{A.22})$$

where  $\sigma_a$  is the apparent conductivity (the inverse of  $\rho_a$ ). This relation is valid for the HCP and VCP configurations. A noticeable advantage of this formulation is that the apparent conductivity is directly proportional to the measured response. The approximation errors at  $B = 0.02$ , amount to 2% for the HCP configuration and 1% for the VCP configuration.

It was previously shown that a linear topographical gradient does not influence the imaginary part of the response significantly, and thus LIN measurements are not seriously corrupted by topography. However, other types of misorientation do influence the response. As seen in Figure A.2, at low induction numbers, the T and A situations result in extreme errors in the imaginary part. Figure A.8 shows the error bounds as a function of dipole axes inclination. At  $5^\circ$  the maximum error amounts to approximately 19%.

Some LIN instruments are fixed on a rigid boom, like the EM-31 from Geonics Limited or the GEM-2 by Geophex. The advantages of such instruments in relation to misalignment effects is evident, as the coils cannot move relative to each other. If operated parallel to the ground surface, these instruments are only affected by rotation about the boom axis. Over a homogeneous half-space, the change due to the rotation angle is insignificant, but in the case of inhomogeneities or layering, differences are observed due to the different sensitivity functions of the HCP and VCP configurations.

## A.4 Conclusion

We have shown that misalignment of the coils in frequency-domain electromagnetic dipole-dipole measurements over a homogeneous half-space results in rather large changes in the response, even for relatively small misalignments. In the situation where the dipole axes of a HCP configuration are located at the correct

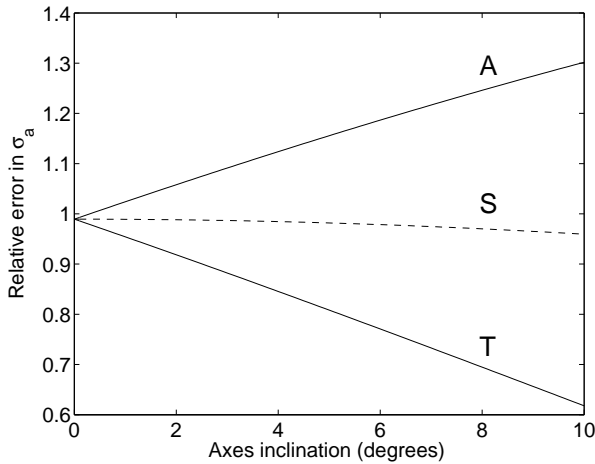


**Figure A.8:** The relative extreme errors in the apparent conductivity as calculated using the LIN-approximation is shown for the HCP configuration as a function of the dipole axes inclination for the induction number  $B = 0.01$  (solid, situations A and T). The initial error visible at  $0^\circ$  is the error arising from the LIN approximation itself. The error due to topographical relief is also shown (dashed, situation S).

separation but misoriented with respect to the vertical, the maximum errors occur, over most of the frequency spectrum, when the coil axes are misoriented in the vertical plane connecting the dipoles.

The special case of dipoles applied in-line on a linear topography results in large errors on the real part, especially at low induction numbers. The imaginary part is much less affected. Similar results were observed in the analysis of the different apparent resistivity algorithms, where the definitions based on the phase or the imaginary part of the response gave values close to the nominal half-space value.

When dipole axes are misaligned in opposite directions, the curve-matching algorithm based on both real and imaginary parts gave results closest to the half-space resistivity. But large errors of up to 30% were observed over large parts of the spectrum for a  $5^\circ$  misalignment of the dipole axes from vertical.

We conclude that the definition based on inversion with both resistivity and instrument height as free parameters does not constitute an improvement compared to other algorithms. Generally, it is not possible to declare one algorithm superior to the others, as none of them perform well in all situations.

On the basis of the presented results, it seems that quantitative interpretation of measurements made in areas with topography is doomed to failure. Even on level ground, utmost care must be taken in setting up the system at each station and measuring separation and three axis coil orientations with great precision, thereby increasing both surveying time and expenses.

## Acknowledgement

We would like to thank Associate Professor Niels B. Christensen for discussions and his helpful suggestions, all very valuable in the preparation of the paper. We are likewise grateful for the access to the inversion package SELMA24.

## References

- Beamish, D. (2002). An assessment of inversion methods for AEM data applied to environmental studies. *Journal of Applied Geophysics*, 51:75–96.
- Beard, L. P. (2000). Comparison of methods for estimating earth resistivity from airborne electromagnetic measurements. *Journal of Applied Geophysics*, 45:239–259.
- Christensen, N. B. and Auken, N. B. (1992). SELMA - simultaneous electromagnetic layered modeling and analysis. In: *Proceedings of Interdisciplinary Inversion Workshop 1 Aarhus 1992, Methodology and Applications within Geophysics, Astronomy, and Geodesy* (ed. B. H. Jacobsen), volume 41 of *Geoskrifter*, pages 49–56. Aarhus University.
- Das, U. C. (1995). Apparent resistivity curves in controlled-source electromagnetic sounding directly reflecting true resistivities in a layered earth. *Geophysics*, 60:53–60.
- Das, U. C. (1997). Multiseparation, multisystem electromagnetic depth sounding - an extension for unification. *Geophysics*, 62(1):56–62.
- Fitterman, D. V. and Yin, C. (2004). Effect of bird maneuver on frequency-domain helicopter EM response. *Geophysics*, 69(5):1203–1215.
- Frischknecht, F. C., Labson, V. F., Spies, B. R., and Anderson, W. L. (1991). Profiling Methods Using Small Sources. In: *Electromagnetic Methods in Applied Geophysics* (ed. M. N. Nabighian), volume 2, chapter 3, pages 105–270. Society of Exploration Geophysicists.
- Huang, H. and Fraser, D. C. (2002). The use of quad-quad resistivity in helicopter electromagnetic mapping. *Geophysics*, 67(2):459–467.
- Keller, G. V. and Frisknecht, F. C. (1966). *Electrical Methods in Geophysical Prospecting*. Pergamon Press, Oxford.
- McNeill, J. D. (1980). *Electromagnetic terrain conductivity measurement at low induction numbers*. Technical Note TN-6, Geonics Limited.
- Simon, B. (2001). Improved and new resistivity-depth profiles for helicopter electromagnetic data. *Journal of Applied Geophysics*, 46:65–76.
- Sinha, A. K. (1980). A study of topographic and misorientation effects in multifrequency electromagnetic soundings. *Geoexploration*, 18:111–133.
- Spies, B. R. and Eggers, D. E. (1986). The use and misuse of apparent resistivity in electromagnetic methods. *Geophysics*, 51(7):1462–1471.
- Van der Kruk, J., Meekes, J. A. C., Van Den Berg, P. M., and Fokkema, J. T. (2000).

An apparent-resistivity concept for low-frequency electromagnetic sounding techniques. *Geophysical Prospecting*, 48:1033–1052.

Verma, R. K. (1973). Topographic effects on electromagnetic depth sounding systems. *Geophysical Prospecting*, 21(1):1–25.

Wait, J. R. (1952). Current-carrying wire loops in a simple inhomogeneous region. *Journal of Applied Physics*, 23(4):497–498.

Wait, J. R. (1955). Mutual electromagnetic coupling of loops over a homogeneous ground. *Geophysics*, 20(3):630–637.

Ward, S. H. and Hohmann, G. W. (1988). Electromagnetic Theory for Geophysical Applications. In: *Electromagnetic Methods in Applied Geophysics* (ed. M. N. Nabighian), volume 1, chapter 4, pages 131–311. Society of Exploration Geophysicists.

Wilt, M. and Stark, M. (1982). A simple method for calculating apparent resistivity from electromagnetic sounding data. *Geophysics*, 47(7):1100–1105.

Yin, C. and Fraser, D. C. (2004). Attitude corrections of helicopter EM data using a superposed dipole model. *Geophysics*, 69(2):431–439.

APPENDIX B

**Numerical modeling of complex resistivity effects on a homogeneous half-space at low frequencies**

---

Accepted for publication in *Geophysical Prospecting*, October 2005.



# Numerical modeling of complex resistivity effects on a homogeneous half-space at low frequencies.

Thomas Ingeman-Nielsen<sup>1,\*</sup> and François Baumgartner<sup>1,2</sup>

<sup>1</sup> Arctic Technology Centre, BYG•DTU, Technical University of Denmark, DK-2800 Kgs. Lyngby, Denmark.

<sup>2</sup> Institute of Geophysics, Faculty of Earth Sciences and Environment, University of Lausanne, CH-1015 Lausanne, Switzerland.

\* Corresponding author: Phone: (+45) 45252251, Fax: (+45) 45885935, E-mail address: tin@byg.dtu.dk.

---

## Abstract

The many different existing models describing the spectral behavior of the resistivity of geological materials at low frequency, combined with the lack of available field data, render the interpretation of complex resistivity (CR) data very difficult. With a recent interest in CR measurements for environmental applications and thanks to technological progress, the use of wide band frequency equipment seems promising, and it is expected to shed light on the different results among the published solutions to the electromagnetic (EM) coupling problem. We review the theory of EM coupling over a homogeneous half-space with CR effects and study some aspects of the complex coupling function. We advocate the use of the CR based coupling function in the interpretation process, in order to obtain a better understanding of the physical processes involved in CR effects. Application of the model to real field data show systematic good agreement in two simple cases, even over wide ranges of frequencies. Interpretation with a double Cole-Cole model is applied for comparison, and in spite of good fits to the data, large differences are observed in the interpreted low frequency dispersion. We conclude that the use of a second Cole-Cole model to describe EM coupling may corrupt the interpretation of the low frequency dispersion, even when only the normal range of frequencies (<100 Hz) is considered, and that the use of the actual EM coupling expression is essential when the goal is a better understanding of interaction between CR effects and EM coupling.

*Keywords:* Complex resistivity, Electromagnetic coupling, Decoupling, Homogeneous half-space model.

---

## B.1 Introduction

It is a well established fact that the resistivity (or electrical impedance) of geological materials is complex-valued and varies with the frequency of the current used to obtain the measurements. The amplitude and phase spectra of the complex resistivity (CR) function have been used as a tool in discriminating between different mineralizations in mining exploration for decades (Pelton et al., 1978), and has more recently also found application within the field of environmen-

tal geophysics, i.e. in detection of organic contaminants (Vanhala et al., 1992). With the advances in modern technology and applications of the CR method to mineral discrimination and environmental applications, the phase spectrum is of increasing interest as a means of discriminating between different sources and their distribution within the probed media. The trend goes towards a dense sampling of frequencies in a wide frequency band.

Since the CR method employs alternating fields, it should be characterized as an electromagnetic (EM) method, and as such is affected by electromagnetic induction phenomena. These phenomena show a functional behavior which at low frequency (less than 10 kHz), is somewhat similar to that of CR effects. Therefore, an understanding of the EM induction phenomena is critical in the interpretation of CR data.

In this paper we review the theory of EM coupling between grounded wires on the surface of a homogeneous half-space, and study some aspects of the coupling response when the ground is polarizable. We advocate the calculation of coupling responses based on a complex resistivity function in such cases, and show this method to be superior to other commonly used decoupling schemes in two simple cases.

## B.2 Theory

### B.2.1 EM coupling of grounded wires on a homogeneous half-space

Consider a horizontal electric dipole ( $dS$ ) located on the surface of the earth, in the origin and directed along the  $x$ -axis of an ordinary lefthanded coordinate system. The electric field of such a dipole, as observed by another horizontal electric dipole located at point  $(x, y, 0)$  is given by Sunde (1968):

$$E = IdS \left[ -P(r) \cos \xi + \frac{\partial^2 Q(r)}{\partial^2 x} + \frac{\partial^2 Q(r)}{\partial x \partial y} \right] \quad (\text{B.1})$$

where  $\xi$  is the angle between the dipoles and  $r = \sqrt{x^2 + y^2}$  the distance between them. The  $P$  and  $Q$  functions are given by Dey & Morrison (1973):

$$P(r) = \frac{i\omega\mu_0}{4\pi} \int_0^\infty \left[ \frac{\lambda}{u_0} + \frac{\lambda}{u_0} R^{TE}(\lambda) \right] J_0(\lambda r) d\lambda \quad (\text{B.2})$$

$$Q(r) = \frac{-i\omega\mu_0}{4\pi k_0^2} \int_0^\infty \left[ \frac{\lambda}{u_0} \{1 + R^{TE}(\lambda)\} - \frac{u_0}{\lambda} \{R^{TE}(\lambda) + R^{TM}(\lambda)\} \right] J_0(\lambda r) d\lambda \quad (\text{B.3})$$

$$u_0 = \sqrt{\lambda^2 - k_0^2}$$

$$k_0^2 = \omega^2 \mu_0 \epsilon_0$$

Here,  $\omega$  is the angular frequency,  $\mu_0$  and  $\epsilon_0$  are the magnetic permeability and permittivity of free space, and  $k_0$  is the propagation constant of free space.  $J_0$  is the Bessel function of order 0 and  $\lambda$  is the variable of integration.  $R^{TE}$  and  $R^{TM}$  are reflection coefficients for the transverse electric and transverse magnetic modes. These depend on the layering of the subsurface and the electromagnetic properties of each layer.

The commonly used configurations in CR prospecting employ two wires of finite length. The mutual impedance  $Z = V/I$  between the wires must therefore be calculated as an integration of mutual impedances of virtual dipoles along the paths of the wires (Sunde, 1968):

$$Z_{EM} = - \int_A^B \int_\alpha^\beta \left[ P(r) \cos \xi + \frac{\partial^2 Q(r)}{\partial S \partial s} \right] ds dS \quad (\text{B.4})$$

where  $A, B$  and  $\alpha, \beta$  are the endpoints of the transmitter and receiver wires, and  $ds$  and  $dS$  are infinitesimal elements of the two wires. When the wires are parallel, as is commonly the case,  $\cos \xi$  becomes unity. The negative sign has been added to preserve the usual sign convention.

In the case of a homogeneous half-space, when the magnetic permeability of the subsurface equals that of free space ( $\mu_1 = \mu_0$ ), and when all significant distances are small in comparison with the free space wavelength, so that displacement currents in the air can be neglected ( $k_0 \rightarrow 0$ ), the  $P$ - and  $Q$ -functions reduce to the following analytical expressions (Dey & Morrison, 1973):

$$P(r) = \frac{-i\omega\mu_0}{2\pi k_1^2 r^3} [1 - (1 + ik_1 r) e^{-ik_1 r}] \quad (\text{B.5})$$

$$Q(r) = \frac{-i\omega\mu_0}{2\pi k_1^2 r} \quad (\text{B.6})$$

$$k_1^2 = -i\omega\mu_0(\sigma + i\omega\epsilon) \quad (\text{B.7})$$

where  $k_1$  is the propagation constant of the homogeneous half space. Usually, when dealing with EM coupling, the conductivity is considered constant and real and the permittivity is most often neglected. With these assumptions on a homogeneous half-space, the  $Q$ -function is real, constant (frequency independent), and only depending on the position of the grounding points of the wires. It is therefore often referred to as the grounding function. The  $P$ -function, although it too contains a purely resistive term, is referred to as the coupling function.

## B.2.2 Complex resistivity

The last term in eq. (B.7) originates from Ampere-Maxwells law, which relates the magnetic field,  $H$ , to the total current density,  $J_T$ , in the general case:

$$\nabla \times H = J_T = J_c + \frac{\partial D}{\partial t} \quad (\text{B.8})$$

The conduction current density,  $J_c$ , and the dielectric displacement,  $D$ , are related to the electric field intensity,  $E$ , through the constitutive relations:

$$\begin{aligned} J_c &= \sigma E \\ D &= \epsilon_0 E + P = \epsilon_0(1 + \chi(\omega))E \end{aligned} \quad (\text{B.9})$$

Here,  $\sigma$  and  $\epsilon_0$  are the conductivity of the medium and the permittivity of free space.  $P$  is the polarization of the media, which is related to the electric field by the electric susceptibility,  $\chi$ . The relation between  $D$  and  $E$  is in general complex-valued and frequency dependent. Since in electrical measurements, we are limited to measuring  $J_T$  and  $E$ , it is not possible at low, non-zero frequencies to distinguish between conduction and dielectric phenomena. Therefore, the relation is often described by either a complex permittivity or a complex conductivity and a constant permittivity. We choose here the latter, assume harmonic time variation, and in order to conform with geophysical literature in general, we write:

$$J_T = \left( \frac{1}{\rho^*} + i\omega\epsilon_r\epsilon_0 \right) E \quad (\text{B.10})$$

where  $\epsilon_0$  is the permittivity of free space,  $\epsilon_r$  is the relative dielectric constant, and  $\rho^*$  is the complex resistivity. The formulation in eq. (B.10) is in agreement with the theoretical results of Fuller & Ward (1970). Note, that resistivity in this definition is the inverse of the conductivity as suggested by Shuey & Johnson (1973), which is not the case for the definitions given by Olhoeft (1974) and Wait (1989).

Many different models have been proposed for the description of the dispersive behavior of the complex resistivity (Marshall & Madden, 1959; Zonge, 1972; Wong, 1979), but the most widely used seem to be the Cole-Cole model, which was originally developed by Cole & Cole (1941) to describe dielectric dispersion. It was shown by Pelton et al. (1978) to accurately describe the resistivity dispersion observed in field data from areas with metallic mineral content. The Cole-Cole model is given by:

$$\rho^* = \rho_0 \left( 1 - m \left( 1 - \frac{1}{1 + (i\omega\tau)^c} \right) \right) \quad (\text{B.11})$$

where  $\rho_0$  is the resistivity in the DC limit,  $m$  is the chargeability,  $\tau$  is the time constant and  $c$  is the frequency dependence.

### B.2.3 Complex EM coupling

Based on these considerations, the propagation constant of the subsurface can in general be written as:

$$k_1^2 = -i\omega\mu_1 \left( \frac{1}{\rho^*} + i\omega\epsilon_r\epsilon_0 \right) \quad (\text{B.12})$$

At sufficiently low frequencies, when the application of the quasi-static approximation is justified, the second term inside the parenthesis of eq. (B.12) can be neglected. Under these conditions, and in the case of a homogeneous and non-magnetic half-space ( $\mu_1 = \mu_0$ ), the mutual impedance for a collinear dipole-dipole configuration takes the relatively simple form given by Wait & Gruszka (1986b):

$$Z_{EM} = \frac{\gamma \rho^*}{4\pi} \left( \frac{2}{a(N+2)(N+1)N\gamma} - 2G(\gamma(N+1)a) + G(\gamma(N+2)a) + G(\gamma Na) \right) \quad (\text{B.13})$$

where  $\gamma = ik_1 = \sqrt{i\omega\mu_0/\rho^*}$ ,  $a$  is the dipole length (see Figure B.1),  $N$  is the dipole spacing factor and

$$G(z) = e^{-z} \left( \frac{1}{z} - 1 \right) + z Ei(z)$$

In the expression for  $G$ , the function  $Ei(z)$  is the exponential integral defined as:

$$Ei(z) = \int_z^\infty \frac{e^{-v}}{v} dv \quad (\text{B.14})$$

The low frequency limit is of special interest in the CR prospecting method. In this limit, the  $G$  function goes to  $1/z - 2$  and the resulting impedance is:

$$Z_0 = \frac{\rho_0}{\pi a(N+2)(N+1)N} \quad (\text{B.15})$$

which is equivalent to the well known apparent resistivity formulation from DC prospecting, an observation that leads Wait & Gruszka (1986b) to the definition of an apparent complex resistivity given by:

$$\rho_a(\omega) = Z(\omega) (\pi a(N+2)(N+1)N) \quad (\text{B.16})$$

where  $Z(\omega)$  is the measured complex impedance.

## B.3 Pure coupling on a homogeneous half-space

We have implemented a numerical integration solution for the EM coupling on a homogeneous half-space according to eq. (B.4), and use that to calculate the complex coupling responses presented in this paper. We have tested our algorithm against the pure coupling responses published by West (1943), Millett (1967), Dey & Morrison (1973) and the analytical solution of Wait & Gruszka (1986b, eq. (B.13) of this paper). Our data were in agreement the analytical solution and the tables of Millett (1967), as amended by Brown (1984).

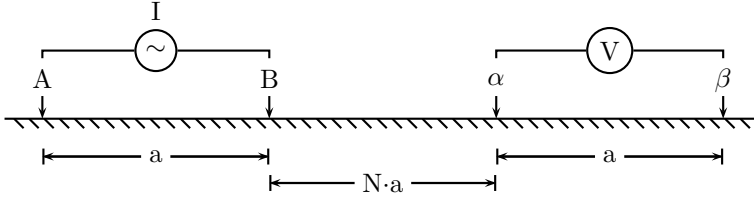


**Figure B.1:** The dipole-dipole configuration for electrical measurements.  $N$  is the dipole spacing factor and  $a$  is the length of the dipoles.

In Figure B.2 we present the phase responses of our calculations for  $N$ -spacings of 1 to 5, together with those published by Dey & Morrison (1973) and West (1943, only available for  $N=1$ ). The figure shows deviations amounting in some cases to more than 150 mrad. The deviations are most pronounced for large values of the induction parameter  $a^2 f / \rho$  and small values of  $N$ . Small differences between the values of Millett (1967) and Dey & Morrison (1973) were previously pointed out by Brown (1985), However, the differences were apparently so small that no further notice was taken.

Our model is based on the expression given by Dey & Morrison, and thus it seems that the observed deviations are due merely to the calculation and graphing capabilities available to them at the time of their publication.

## B.4 Half-space with complex resistivity

The coupling behavior based on a complex resistivity function does not seem to have been studied much, in spite of the obvious importance. In the following we present the results of forward modeling of the EM coupling response of a homogeneous half-space with four different resistivity functions:

1.  $\rho = \rho_0$
2.  $\rho = \rho^*(\omega)$
3.  $\rho = \text{Real}(\rho^*) = \rho(\omega)$
4.  $\rho = \rho_0 + i \cdot \text{Imag}(\rho^*) = \rho_0 + i\Phi(\omega)$

Functions 1 and 2 are respectively the constant DC-resistivity and the complex frequency dependent resistivity based on the Cole-Cole model. Functions 3 and 4 are included in order to show the effect of the real and the imaginary parts of the resistivity function on the real and imaginary parts of the EM coupling.

Figure B.3 shows the EM coupling response for a dipole size of 200 m and  $N$ -spacings 1 and 5. The parameters for the Cole-Cole model are  $\rho_0 = 100 \Omega m$ ,  $m =$

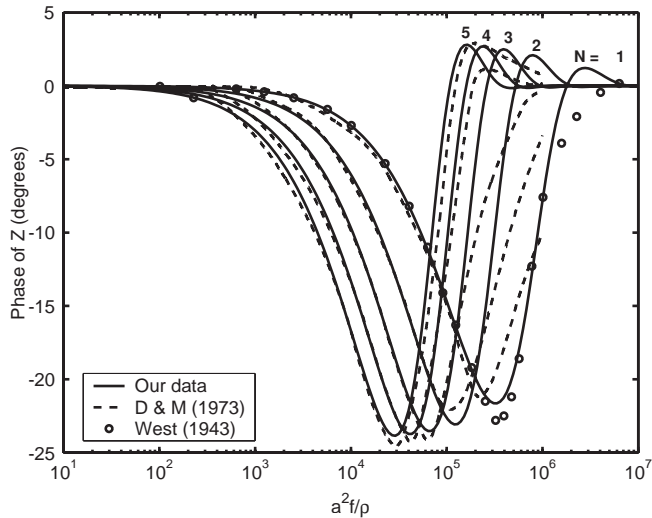


**Figure B.2:** Comparison of our calculated phase data (solid lines) with those of Dey & Morrison (1973) (dashed) and West (1943) (circles). A drastic change in the functional behavior is observed at higher values of  $a^2 f / \rho$ .

0.2,  $\tau = 0.1$ , and  $c = 0.3$ , a small to moderate response in mineral exploration context. As expected, the use of a complex resistivity function (function 2.) results in a real component that is reduced in comparison with the EM response based on the constant resistivity,  $\rho_0$ . For  $\omega \rightarrow 0$  the real component goes to  $\rho_0$ , and for  $\omega \rightarrow \infty$  the real component goes to  $\frac{1}{2}(1-m)\rho_0$ . For the imaginary part of the coupling response, the complex resistivity function also results in a reduction of the response at low frequencies. However, the amplitude of the oscillations in the response is reduced, causing two cross-overs between the complex coupling and the constant coupling responses. At high and low frequencies the imaginary part asymptotes to 0, resulting in purely resistive coupling in the two limits. This is in agreement with the observations of Wait (1951).

The resistivity function 3. ( $\text{Real}(\rho^*)$ ) results in a real part which is indistinguishable from the coupling based on the complex resistivity function. This shows that the imaginary part of the resistivity function has little effect on the real part of the coupling response. For the imaginary part of the coupling, this type of resistivity function results in coupling that asymptotes to the DC-resistivity based EM coupling at high and low frequencies. However, at intermediate frequencies, in the oscillations, it behaves like the complex-coupling function.

The response of the last resistivity function ( $R_0 + i \cdot \text{Imag}(\rho^*)$ ) is opposite. The real part of the coupling is indistinguishable from the DC-resistivity based coupling, while the imaginary part asymptotes to the complex resistivity coupling

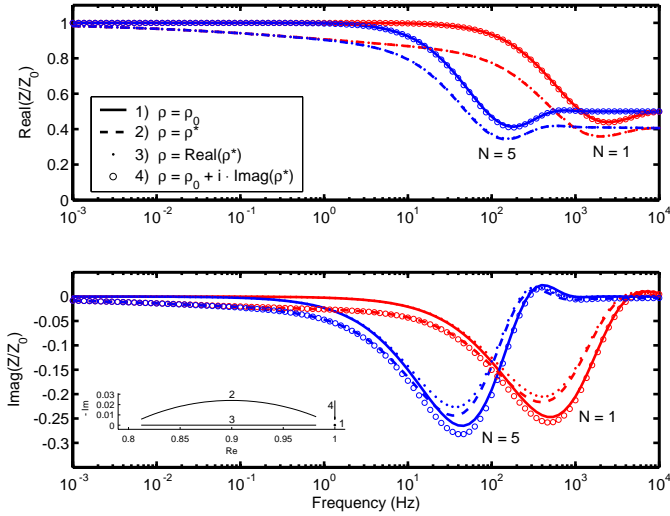


**Figure B.3:** EM coupling on a homogeneous half-space for  $a = 200$  m and N-spacings of 1 (red) and 5 (blue), for the four resistivity functions, which are shown in the Argand diagram insets (normalized by  $\rho_0$ ). The parameters of the Cole-Cole resistivity model are  $\rho_0 = 100 \Omega m$ ,  $m = 0.2$ ,  $\tau = 0.1$ ,  $c = 0.3$ .

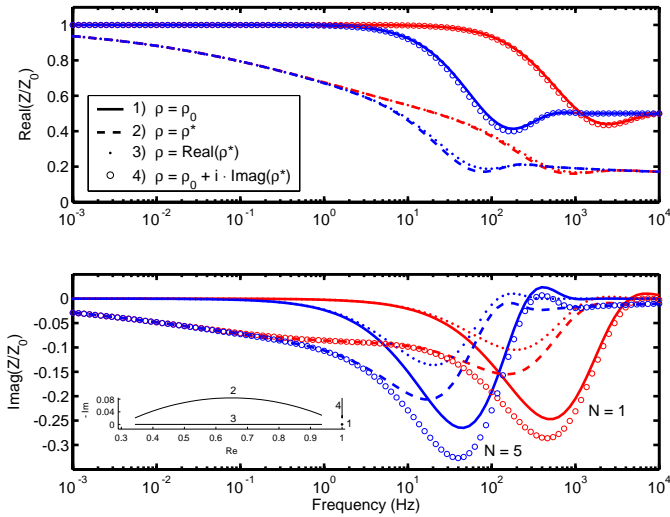


**Figure B.4:** EM coupling on a homogeneous half-space for  $a = 200$  m and N-spacings of 1 (red) and 5 (blue), for the four resistivity functions, which are shown in the Argand diagram insets (normalized by  $\rho_0$ ). The parameters of the Cole-Cole resistivity model are  $\rho_0 = 100 \Omega m$ ,  $m = 0.7$ ,  $\tau = 0.1$ ,  $c = 0.3$ .

curve at low and high frequencies, and behaves like the DC-coupling function in the oscillations.

Figure B.4 shows the coupling for a Cole-Cole model with a chargeability of  $m = 0.7$ . The high chargeability has a drastic effect on both real and imaginary parts of the complex resistivity coupling. Aside from the expected change in amplitude of the real part of the coupling at low and high frequencies, the difference between the coupling at N-spacings 1 and 5 has diminished for both real and imaginary parts. In fact, the amplitude of the oscillations in the imaginary part is much smaller as an effect of the increased chargeability. It is observed from the real part of the coupling that at high chargeabilities, there is a distinguishable contribution from the imaginary part of the complex resistivity function. This contribution was observed to increase with increasing chargeability and decreasing resistivity. However, even at resistivities below  $10 \Omega m$  and high chargeabilities, the contribution was of minor importance.

## B.5 Removal of EM coupling

Much effort has been put into the development of algorithms to separate the inductive coupling response from the observed CR data. The presented algorithms can be described as empirical or physics based approaches.

One of the empirical methods consists of the fitting of a linear or quadratic equation to the measurements at two or three low frequencies (Hallof, 1974; Coggon, 1984). The value obtained at extrapolation to zero frequency is accepted as a "DC" phase, which can be used in interpretation. Another empirical approach is to fit the phase spectrum with a multiplication (Pelton et al., 1978) or addition (Major & Silic, 1981) of two Cole-Cole dispersions. The time constant of the dispersion describing the EM coupling is smaller than that of the resistivity dispersion, and the frequency dependence close to 1. Major & Silic also showed that only the low frequency part of the coupling could be fitted by the model.

The physics based approaches use the actual EM equations to calculate coupling responses based on an assumption of the resistivity structure. An additive approach was described by Wait & Gruszka (1986b), who interpreted the observed data as an addition of the intrinsic complex resistivity dispersion and the DC-resistivity based EM coupling response. They showed that the method is a good approximation on a homogeneous half-space at low frequencies, but fails when the propagation term becomes significant in comparison with the grounding term.

Another physics based approach was published by Routh & Oldenburg (2000b, 2001), who suggested that the observed response could be approximately described by the infinite frequency conductivity ( $\sigma_\infty$ ) based EM coupling multiplied by a complex and frequency dependent function describing the complex resistivity dispersion (hence the multiplicative approach). It follows, that the phase of this function is equal to the calculated EM phase subtracted from the observed

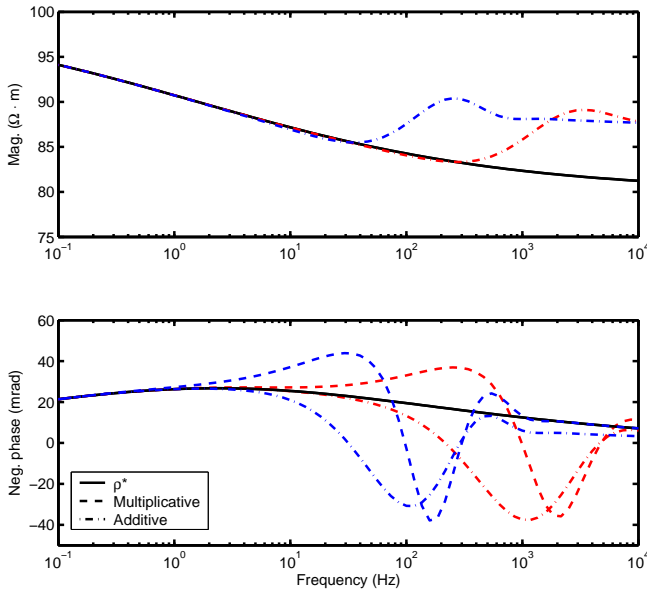


**Figure B.5:** Comparison of the additive (dots) and multiplicative (dashed) approach to decoupling for  $a = 200$  m and an N-spacing of 1 (red) and 5 (blue). The complex resistivity model (solid) is the same as used in Figure B.3. The absolute value of the complex resistivity at 0.1 Hz was used to calculate the EM coupling. The phases are plotted negative to conform with the common plotting conventions.

phase. In practice they suggest to use the conductivity structure obtained at the lowest frequency collected in calculating the EM response.

Figure B.5 shows a comparison of the additive and multiplicative approaches to decoupling at N-spacings of 1 and 5. The multiplicative approach is only considered in the phase plot, as it does not allow decoupling of the magnitude. The EM response used in the decoupling was calculated based on the absolute value of the complex resistivity at 0.1 Hz, in correspondence with common field practice. The figure shows, that for a homogeneous half-space, the additive approach gives a closer fit to the true data than does the multiplicative approach. Furthermore, the deviation of the additive approach at intermediate frequencies is opposite that of the expected resistivity phase-spectrum, while that of the multiplicative approach is in the same direction. This could, if only a limited frequency interval is available and care is not taken, lead to misinterpretations of the decoupled spectrum. With the specific model used, the additive decoupling approach is a good approximation to the true spectrum for frequencies up to 50-100 Hz at an N-spacing of 1. For larger N-spacings, the applicability of the method is reduced accordingly.

These plots show, that at higher frequencies or large N-spacings, these decoupling schemes fails to be sufficiently accurate. They are both based on the assumption that the two effects (intrinsic complex resistivity and EM coupling) are independent and separable. While this may be a good approximation at sufficiently low frequencies, it should not be the case in general. We therefore suggest, in line with Wait & Gruszka (1986b) and Routh & Oldenburg (2000a), that the CR method be treated as an EM method, when serious coupling effects are observed in the data. This implies calculating the forward EM coupling responses based on the complex resistivity distribution assumed for the location.

## B.6 Application to field data

Published field data showing the frequency variation of EM coupling effects as well as complex resistivity are limited to a few cases given by Pelton et al. (1978), and only the phase spectrum is given. We feel there is a strong need for high quality data sets of wide frequency band and many combinations of a- and N-spacings in order to verify the applicability of different decoupling schemes. Here we demonstrate the presented decoupling schemes by application to two data sets.

The first data sets was collected in Denmark over a thick sequence of clayey till deposits. The data set comprises 30 frequencies in the spectrum from 0.125 Hz to 9216 Hz, and was collected with 30 m dipoles and an N-spacing of 3. The equipment was the GDP 32<sup>II</sup> geophysical receiver from Zonge Engineering and Research Organization Inc (Zonge), with a GGT-3 transmitter. The data, which are presented in Figure B.6, suggest the presence of only a small CR effect. The two last points show an unnatural behavior in the phase. We expect this to be due to an error on the measurements, and these points have not been included in the following analysis.

We have manually fitted an EM coupling response, based on a Cole-Cole resistivity dispersion, to the data set. The parameters and RMS-error statistics are given in Table B.1. The model fits the data satisfactorily to a frequency of 1536 Hz, after which it slightly over estimates both magnitude and phase. Nevertheless, it is observed that this simple CR based EM model is capable of reproducing the trend of the data, even at high frequencies. The observed discrepancy could be due to the simplicity of the model or equipment related issues and is currently under investigation.

We have also fitted the data set with a double Cole-Cole model using the CCINV program from Zonge (MacInnes, 2000). This model fits the magnitude data better than the combined EM CR model, but it fails to fit the low frequency part of the phase data, resulting in poor RMS error statistics (Table B.1). In the present case the steep up-slope of the EM coupling forces the inversion routine to use both dispersions to fit the coupling effect, and thus the low frequency CR effect remains undetermined.

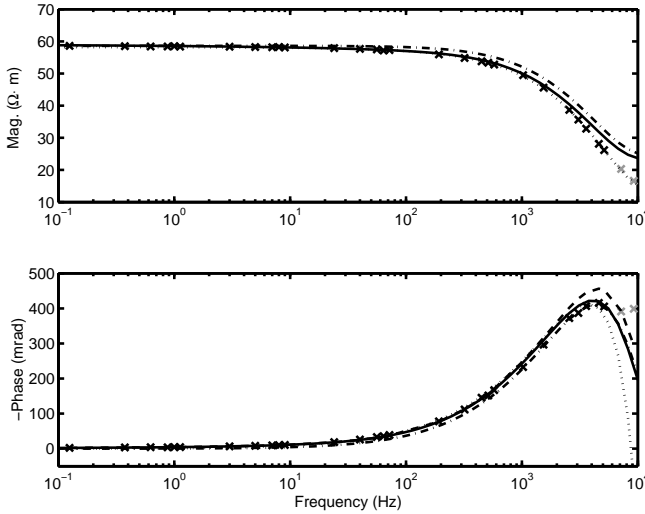


**Figure B.6:** CR data set obtained over a thick clayey till deposit with 30m dipoles and an N-spacing of 3. The figure shows the EM coupling based on the first point (dash-dot) as well as the EM coupling based on a Cole-Cole model (solid). The double Cole-Cole model data (dots) and the un-decoupled data calculated using the additive approach with the single Cole-Cole model (dashed) are also shown.

**Table B.1:** Model parameters and RMS error statistics for the Cole-Cole models fitted to the clayey till data set (Figure B.6).

	$EM_{CR}$	Additive	Multipl.	Double C-C	
				LF	HF
$\rho_0$	59			58.21	
$m$	0.07			1.0	-20.1378
$\tau$	$5 \cdot 10^{-4}$			$4.1874 \cdot 10^{-5}$	$2.5975 \cdot 10^{-7}$
$c$	0.35			0.78	0.99
$\rho_{RMS}$	0.044806	0.045393	-	0.003743	
$\phi_{RMS}$	0.045664	0.062036	0.045475	0.369349	

For illustrative purposes, we have used the manually fitted Cole-Cole model to calculate undecoupled data based on the additive and multiplicative approaches. RMS error statistics of these models are included in Table B.1. Both models show fair agreement with the collected data, although the additive approach fits the high frequency part of the data worse than the other models.

The second data set contain of 15 frequencies over the standard frequency band from 0.125 to 72 Hz, and was kindly supplied by Zonge. The dipole size was 152.4 m and the N-spacing 7. This data set was processed similarly, and the results are presented in Table B.2 and Figure B.7. Both the CR based EM coupling and the double Cole-Cole models fit the data well.

For both of the presented data sets we observe a marked difference between the low-frequency dispersions obtained when fitting a CR based EM coupling response or a double Cole-Cole model to the data. The CR based coupling fitted the data equally well or better than the double Cole-Cole model. The implication of these observations is that results obtained using the two decoupling schemes are not directly comparable, and even at low frequencies the approximation of the EM coupling with a Cole-Cole model corrupts the interpretation of the resistivity dispersion.

Although the CR based EM coupling model proved superior in the two simple cases presented here, it should be kept in mind that a necessary condition for applying this model is that the ground can be approximated by a homogeneous half-space. In order to accentuate this point, we present a data set collected in Sisimiut, Greenland, in an area containing three dimensional structures with DC resistivity contrasts of up to 1:200 with the background (Figure B.8). The data were collected with a dipole size of 20m and an N-spacing of 3 for frequencies from 0.016 to 9216 Hz. The severe effects present in this case could not be modelled or decoupled by any of the simple methods described.

## B.7 Conclusion

In this paper we advocate the use of the CR based coupling equations in calculating the EM coupling on homogeneous half-spaces with a complex resistivity dispersion, and we show some aspects of the behavior of the complex coupling function. We have presented two data sets affected by EM coupling, both of which can be approximately described as homogeneous half-spaces.

The use of the CR based coupling function resulted in better fits to the presented data than other frequently used decoupling and interpretation schemes. However, some of the other schemes also gave acceptable results. The two simple situations presented show that the empirical method of using a second Cole-Cole model to approximate the EM coupling may corrupt the interpretation of the low-frequency dispersion, even when only frequencies in the normal range (<100 Hz) are considered, and in spite of a good fit to the observed data. We therefore venture to bring doubts on the validity of the use of double Cole-Cole models when

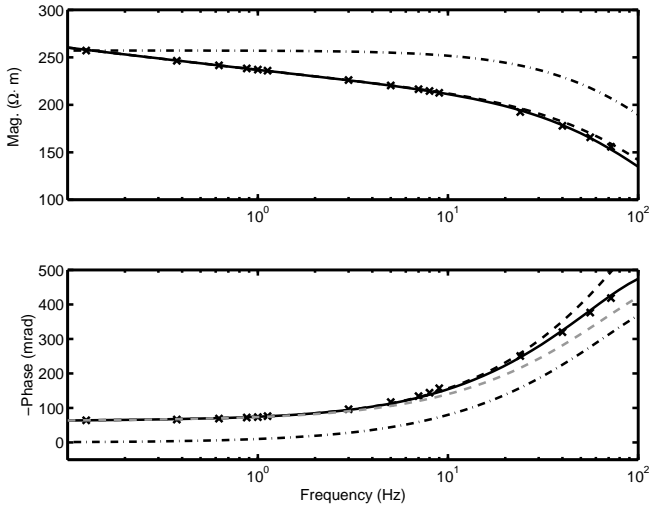


**Figure B.7:** An EM coupling curve (solid) based on a Cole-Cole resistivity dispersion fitted to the Zonge data set. Coupling curves based on the additive approach (dashed black) and the multiplicative approach (dashed gray) are shown as well, together with the pure EM coupling (dash dot) based on the first data point. The double Cole-Cole model is not shown in the figure as it is overlapping with the CR based EM coupling curves.

**Table B.2:** Model parameters and RMS error statistics for the Cole-Cole models fitted to the Zonge data set (Figure B.7).

	$EM_{CR}$	Additive	Multipl.	Double C-C	
				LF	HF
$\rho_0$	394			343.9	
$m$	0.62			0.3764	0.5816
$\tau$	5			8.5319	$1.4243 \cdot 10^{-3}$
$c$	0.17			0.32	0.70
$\rho_{RMS}$	0.003019	0.009010	-	0.004297	
$\phi_{RMS}$	0.029181	0.037092	0.085405	0.010245	

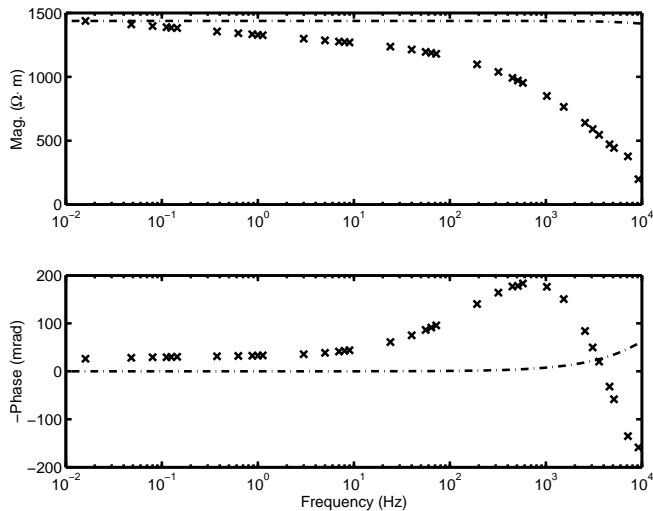


**Figure B.8:** Data from an area with a three dimensional resistivity distribution. None of the applied models were able to fit the data. The homogeneous half-space EM coupling based on the resistivity of the first point (dash-dot) is included in the figure for illustration.

the goal is source discrimination and understanding of the physical processes.

Indeed, more wide-bandwidth data sets are needed in order to give conclusive evidence as to which model is the more appropriate, and to supply a better understanding of the interaction between complex resistivity and EM coupling.

## References

- Brown, R. J. (1984). Corrections to Millett's table of electromagnetic coupling phase angles. *Geophysics*, 49(9):1554–1555.
- Brown, R. J. (1985). EM coupling in multifrequency IP and a generalization of the Cole-Cole impedance model. *Geophysical Prospecting*, 33(2):282–302.
- Coggon, J. H. (1984). New three-point formulas for inductive coupling removal in induced polarization. *Geophysics*, 49(3):307–309. See erratum: *Geophysics* (1984) Vol. 49, p. 1395.
- Cole, K. S. and Cole, R. H. (1941). Dispersion and absorption in dielectrics, I. Alternating current fields. *The Journal of Chemical Physics*, 9(4):341–351.
- Dey, A. and Morrison, F. (1973). Electromagnetic coupling in frequency and time-domain induced-polarization surveys over a multilayered earth. *Geophysics*, 38(2):380–405.

- Fuller, B. D. and Ward, S. H. (1970). Linear system description of the electrical parameters of rocks. *IEEE Transactions on Geoscience Electronics*, GE-8(1):7–18.
- Hallof, P. G. (1974). The IP phase measurement and inductive coupling. *Geophysics*, 39(5):650–665.
- MacInnes, S. (2000). *CCINV - CR to Cole-Cole Inversion Program*. Zonge Engineering and Research Organization Inc., Tucson, Arizona.
- Major, J. and Silic, J. (1981). Restrictions on the use of cole-cole dispersion models in complex resistivity interpretation. *Geophysics*, 41(6):916–931.
- Marshall, D. J. and Madden, T. R. (1959). Induced polarization, a study of its causes. *Geophysics*, 24(4):790–816.
- Millett, F. B., Jr. (1967). Electromagnetic coupling of collinear dipoles on a uniform half-space. In *Mining Geophysics*, vol. 2: The Society of Exploration Geophysicists, pages 401–419.
- Olhoeft, G. R. (1974). Electrical properties of rocks. In Strens, R. G. J., editor, *Physics and Chemistry of Minerals and Rocks*, pages 261–278. Wiley, London.
- Pelton, S. H., Ward, S. H., Hallof, P. G., Sill, W. R., and Nelson, P. H. (1978). Mineral discrimination and removal of inductive coupling with multifrequency IP. *Geophysics*, 43:588–609.
- Routh, P. S. and Oldenburg, D. W. (2000a). Complex conductivity inversion from EM coupling contaminated frequency domain IP data. 70<sup>th</sup> SEG meeting, Expanded Abstracts, 1089–1092.
- Routh, P. S. and Oldenburg, D. W. (2000b). Electromagnetic coupling in frequency-domain induced polarization data: A method for removal. 70<sup>th</sup> SEG Meeting, Expanded Abstracts, 1081–1084.
- Routh, P. S. and Oldenburg, D. W. (2001). Electromagnetic coupling in frequency-domain induced polarization data: a method for removal. *Geophysical Journal International*, 145(1):59–76.
- Shuey, R. T. and Johnson, M. (1973). On the phenomenology of electrical relaxation in rocks. *Geophysics*, 38(1):37–48.
- Sunde, E. D. (1968). *Earth Conduction Effects in Transmission Systems*. Dover, New York.
- Vanhala, H., Soininen, H., and Kukkonen, I. (1992). Detecting organic chemical contaminants by spectral-induced polarization method in glacial till environment. *Geophysics*, 57(8):1014–1017.
- Wait, J. R. (1951). *Basis of Electrical Prospecting Methods Employing Time Varying Fields*. PhD thesis, University of Toronto.
- Wait, J. R. (1989). Complex resistivity of the earth. In Kong, J. A., editor, *Progress in Electromagnetics Research I*. Elsevier, pages 1–173.
- Wait, J. R. and Gruszka, T. P. (1986). On electromagnetic coupling removal from

induced polarization surveys. *Geoexploration*, 24(1):21–27.

West, S. S. (1943). The mutual impedance of collinear grounded wires. *Geophysics*, 8(2):157–164.

Wong, J. (1979). An electrochemical model of the induced-polarization phenomenon in disseminated sulfide ores. *Geophysics*, 44(7):1245–1265.

Zonge, K. L. (1972). *Electrical Properties of Rocks as Applied to Geophysical Prospecting*. PhD thesis, The University of Arizona.



APPENDIX C

**CR1Dmod: A Matlab program to  
model 1D complex resistivity  
effects in electrical and  
electromagnetic surveys**

---

Accepted for publication in *Computers & Geosciences* subject to minor revisions,  
April 2005.



# CR1Dmod: A Matlab program to model 1D complex resistivity effects in electrical and electromagnetic surveys.

Thomas Ingeman-Nielsen<sup>1,\*</sup> and François Baumgartner<sup>1,2</sup>

<sup>1</sup> Arctic Technology Centre, BYG•DTU, Technical University of Denmark, DK-2800 Kgs. Lyngby, Denmark.

<sup>2</sup> Institute of Geophysics, Faculty of Earth Sciences and Environment, University of Lausanne, CH-1015 Lausanne, Switzerland.

\* Corresponding author: Phone: (+45) 45252251, Fax: (+45) 45885935, E-mail address: tin@byg.dtu.dk.

---

## Abstract

We have constructed a forward modeling code in Matlab, capable of handling several commonly used electrical and electromagnetic methods in a 1D environment. We review the implemented electromagnetic field equations for grounded wires, frequency and transient soundings and present new solutions in the case of a non-magnetic first layer. The CR1Dmod code evaluates the Hankel transforms occurring in the field equations using either the Fast Hankel Transform based on digital filter theory, or a numerical integration scheme applied between the zeros of the Bessel function. A graphical user interface allows easy construction of 1D models and control of the parameters. Modeling results are in agreement with other authors, but the time of computation is less efficient than other available codes. Nevertheless, the CR1Dmod routine handles complex resistivities and offers solutions based on the full EM equations as well as the quasi-static approximation. Thus, modeling of effects based on changes in the magnetic permeability and the permittivity is also possible.

*Keywords:* Complex Resistivity, Forward modeling, Terrestrial Resistivity, EM coupling, Geophysical Prospecting.

---

## C.1 Introduction

Lately, the Arctic Technology Center has had an interest in evaluating the application of the Complex Resistivity (CR) method to groundwater prospecting and permafrost mapping in Greenland. During the course of our research it became apparent that the availability of free, easy to use forward modeling software with the ability to take into account CR effects is very scarce.

The US Geological Survey has published reports of modeling codes written in FORTRAN for several electrical and electromagnetic methods<sup>1</sup>, of which the

---

<sup>1</sup>Bankey, V., Anderson, W. L., 1995. A bibliography of some geophysical computer programs, databases, and maps from the U.S. Geological Survey, 1971-1994. Open-File report 95-77, U.S. Geological Survey, available at: <http://pubs.usgs.gov/of/1995/ofr-95-0077/of-95-77.html>

EMCUPL dipole-dipole modeling routine (Kauahikaua & Anderson, 1979) is one of the few available codes to incorporate CR effects.

Modeling and field data from a loop-loop system over a polarizable, layered half-space in the frequency domain were reported by Hohmann et al. (1970), and Descloitres et al. (2000) report modification of a TEM forward modeling routine to accommodate CR effects and its application to the interpretation of negative transients in a volcanic environment. None of these codes has been made available to the scientific community in an organized manner.

We therefore decided to implement the CR1Dmod code, which would handle some of the most commonly encountered 1D forward modeling problems with complex resistivity. The Matlab environment was chosen for the development of the code. Although computationally slower than similar implementations in FORTRAN or C, the Matlab environment offers structure and easily programmable GUI's. Furthermore, with Matlab widely used in educational activities at many universities, it will be fairly easy for researchers, teachers and students to modify the configurations or algorithms of the CR1Dmod to accommodate specific needs or to implement new ones altogether.

## C.2 The Complex Resistivity model

That resistivity (or electrical impedance) measurements of geological materials are complex and vary with the frequency of the applied current is a well established fact. Over the years, several models have been proposed for the description of the dispersive behavior of the complex resistivity (Marshall & Madden, 1959; Zonge, 1972; Wong, 1979), but the most widely used seem to be the Cole-Cole model, which was originally developed by Cole & Cole (1941) to describe dielectric dispersion. Pelton et al. (1978) showed that this model would accurately describe the resistivity dispersion observed in field data obtained at low frequencies from areas with metallic mineral content. It has later been shown to also fit the spectra obtained from laboratory measurements on sedimentary samples polluted with organic solutions (Vanhala et al., 1992).

The Cole-Cole model is the resistivity model chosen for implementation in the CR1Dmod code and is given by:

$$\rho^* = \rho_0 \left( 1 - m \left( 1 - \frac{1}{1 + (i\omega \tau)^c} \right) \right) \quad (\text{C.1})$$

where  $\rho^*$  is the complex resistivity,  $\rho_0$  is the resistivity in the direct current (DC) limit [ $\Omega\text{m}$ ],  $m$  is the chargeability (no unit),  $\tau$  is the time constant [s] and  $c$  is the frequency dependence (no unit). In practice, electromagnetic theory calls for the use of conductivities rather than resistivities. In our definition of complex earth properties, the complex conductivity is simply the inverse of the complex resistivity.

## C.3 Theoretical basis

The traditional way of measuring the complex resistivity of the ground is by measuring the complex impedance in the frequency domain between two grounded wires in the co-linear dipole configuration. However, as the complex properties of the ground may potentially manifest themselves in any electromagnetic measurement, a range of different methods and configurations have been implemented in CR1Dmod. The following sections summarize the theoretical background and some practical considerations of the implemented algorithms.

### C.3.1 EM coupling between grounded wires

According to Sunde (1968), the electromagnetic coupling between two grounded wires in an arbitrary configuration on the surface of the earth can be calculated as an integration of mutual impedances of virtual dipoles along the paths of the wires:

$$\begin{aligned} Z &= \int_A^B \int_\alpha^\beta \left[ P(r) \cos \xi + \frac{\partial^2 Q(r)}{\partial s \partial S} \right] ds dS \\ &= \int_A^B \int_\alpha^\beta P(r) \cos \xi ds dS \\ &\quad + Q(|A\alpha|) - Q(|B\alpha|) - Q(|A\beta|) + Q(|B\beta|) \end{aligned} \quad (\text{C.2})$$

where A,B and  $\alpha,\beta$  are the end points of the transmitter and receiver wires (the grounding points),  $dS$  and  $ds$  are infinitesimal elements of the two wires (the virtual dipoles),  $\xi$  is the angle between the wire elements, and  $r$  is the distance between them. The  $P$  and  $Q$  functions are given by (Ward & Hohmann, 1988):

$$P(r) = \frac{\hat{z}_0}{4\pi} \int_0^\infty [1 + R_0^{\text{TE}}] \frac{\lambda}{u_0} J_0(\lambda r) d\lambda \quad (\text{C.3})$$

$$Q(r) = \frac{1}{4\pi} \int_0^\infty \left[ (1 - R_0^{\text{TM}}) \frac{u_0}{\hat{y}_0} - (1 + R_0^{\text{TE}}) \frac{\hat{z}_0}{u_0} \right] \frac{1}{\lambda} J_0(\lambda r) d\lambda \quad (\text{C.4})$$

Here,  $J_0$  is the Bessel function of order 0 and  $\lambda$  is the variable of integration.  $R_n^{\text{TE}}$  and  $R_n^{\text{TM}}$  are the generalized reflection coefficients for the transverse electric and transverse magnetic modes looking into layer  $n+1$  (Fig. C.1). These depend on the layering of the subsurface and the electromagnetic properties of each layer and are given by the recursive relations:

$$R_n^{\text{TM}} = \frac{R_{n+1}^{\text{TM}} + \psi_{n+1}^{\text{TM}}}{R_{n+1}^{\text{TM}} \psi_{n+1}^{\text{TM}} + 1} e^{-2u_n h_n} \quad , \quad \psi_{n+1}^{\text{TM}} = \frac{\frac{u_n}{\hat{y}_n} - \frac{u_{n+1}}{\hat{y}_{n+1}}}{\frac{u_n}{\hat{y}_n} + \frac{u_{n+1}}{\hat{y}_{n+1}}} \quad (\text{C.5})$$

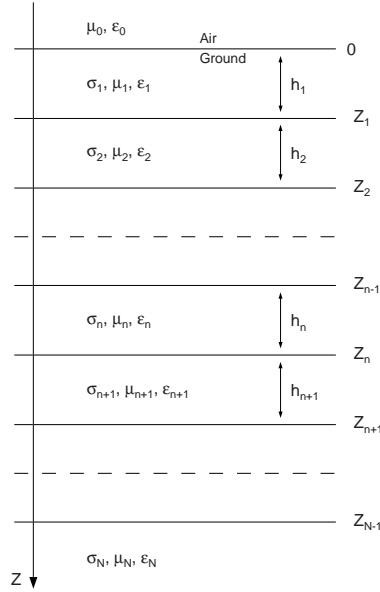


**Figure C.1:** The basis of the model is a horizontally stratified medium of  $N$  layers.

where  $h_n$  is the thickness of layer  $n$  ( $h_0 = 0$ ), and:

$$\begin{aligned}\hat{y}_n &= \sigma_n + i\omega\epsilon_n & , & \quad \hat{y}_0 = i\omega\epsilon_0 \\ \hat{z}_n &= i\omega\mu_n \\ k_n^2 &= -\hat{z}_n\hat{y}_n = \omega^2\epsilon_n\mu_n - i\omega\mu_n\sigma_n \\ u_n &= \sqrt{\lambda^2 - k_n^2}\end{aligned}$$

Here,  $\mu_n$  is the magnetic permeability of layer  $n$  [ $\text{Hm}^{-1}$ ] and  $\epsilon_n$  is the permittivity [ $\text{Fm}^{-1}$ ]. The recursion is started with  $R_N^{TM} = 0$ . The relations for  $R_n^{TE}$  and  $\psi_n^{TE}$  are obtained when  $\hat{z}_n$  is exchanged for  $\hat{y}_n$  in  $\psi_n^{TM}$ .

A few special cases exist for which simplifications of the general equations can be obtained. In the case of a non-magnetic half-space ( $\mu_1 = \mu_0$ ), the  $P$  function can be evaluated analytically. If a layered model has a non-magnetic top layer, the homogeneous half-space term, based on the properties of the first layer, can be subtracted from the kernel function and the corresponding analytical expression is added outside the transform:

$$\begin{aligned}P(r) &= \frac{\hat{z}_0}{4\pi} \left[ \int_0^\infty \frac{4R_1^{TE}u_1}{R_1^{TE}(k_1^2 - k_0^2) + (u_0 + u_1)^2} \lambda J_0(\lambda r) d\lambda \right. \\ &\quad \left. + \frac{2}{(k_1^2 - k_0^2)r^3} \left( (ik_1r + 1)e^{-ik_1r} - (ik_0r + 1)e^{-ik_0r} \right) \right] \quad (\text{C.6})\end{aligned}$$

In this formulation, the Hankel transform is a correction term to the homogeneous half-space solution, corresponding to the summed effect of the additional layers.

If, in addition to the above assumption, frequencies are sufficiently low that distances involved in the problem are much shorter than the free-space wave length, so that the dielectric properties in the air can be neglected ( $\hat{y}_0 \approx 0$ ,  $k_0 \approx 0$ ), both the  $P$ - and  $Q$ -functions can be further simplified:

$$P(r) = \frac{\hat{z}_0}{4\pi} \left[ \int_0^\infty \frac{4R_1^{\text{TE}}u_1}{R_1^{\text{TE}}k_1^2 + (\lambda + u_1)^2} \lambda J_0(\lambda r) d\lambda + \frac{2}{k_1^2 r^3} \left( (ik_1 r + 1) e^{-ik_1 r} - 1 \right) \right] \quad (\text{C.7})$$

$$Q(r) = -\frac{1}{4\pi} \left[ \int_0^\infty \left[ \frac{R_1^{\text{TE}}\hat{z}_0}{R_1^{\text{TE}}k_1^2 + (\lambda + u_1)^2} + \frac{R_1^{\text{TM}}}{(R_1^{\text{TM}} + 1)\hat{y}_1} \right] \frac{4u_1}{\lambda} J_0(\lambda r) d\lambda + \frac{2\hat{z}_0}{k_1^2 r} \right] \quad (\text{C.8})$$

### C.3.2 TEM calculations

CR1Dmod includes a functionality to model transient soundings (TEM soundings) in the central loop configuration. The implemented algorithm is based on that of Ryu et al. (1970) and Anderson (1981), in which the vertical field at the center of a circular transmitting loop is calculated in the frequency domain and transformed to time domain by means of an inverse cosine or sine transform. For consistency we have rewritten the equations using the same notation as for the case of the grounded dipoles. The frequency domain field calculation is given by:

$$\begin{aligned} H_z(\omega) &= I a \int_0^\infty \left( (1 + R_0^{\text{TE}}) \frac{\lambda}{2u_0} - \frac{1}{2} \right) \lambda J_1(\lambda a) d\lambda + \frac{I}{2a} \\ &= I a \int_0^\infty \left( \frac{(R_1^{\text{TE}} + 1) \left( u_0 + \frac{\hat{z}_0}{\hat{z}_1} u_1 \right)^{-1}}{R_1^{\text{TE}} \psi_1^{\text{TE}} + 1} - \frac{1}{2} \right) \lambda J_1(\lambda a) d\lambda + \frac{I}{2a} \end{aligned} \quad (\text{C.9})$$

Here  $a$  is the radius of the transmitter loop, and the term  $\lambda/2$  which is subtracted in the Hankel transform kernel in Eq. (C.9) corresponds to the static field in the DC limit. The term can be integrated analytically, and the resulting expression is added outside the Hankel transform. This operation ensures definite convergence of the integrand (Ryu et al., 1970).

Analogous to the grounded wire case, the kernel function of the  $H_z(\omega)$  function can be simplified in the case of a non-magnetic first layer ( $\mu_1 = \mu_0$ ), by subtracting a homogeneous half-space term from the kernel function and adding

the analytic expression outside the transform, giving:

$$\begin{aligned}
 H_z(\omega) = & I a \int_0^\infty \left( \frac{2R_1^{\text{TE}} u_1 \lambda}{R_1^{\text{TE}}(k_1^2 - k_0^2) + (u_0 + u_1)^2} - \frac{1}{2} \right) \lambda J_1(\lambda a) d\lambda + \frac{I}{2a} \\
 & + \frac{I}{(k_1^2 - k_0^2) a^3} \left( (k_0^2 a^2 - 3i k_0 a - 3) e^{-i k_0 a} \right. \\
 & \left. - (k_1^2 a^2 - 3i k_1 a - 3) e^{-i k_1 a} \right)
 \end{aligned} \tag{C.10}$$

At sufficiently low frequencies ( $k_0 \approx 0$ ), the expression further simplifies to:

$$\begin{aligned}
 H_z(\omega) = & I a \int_0^\infty \left( \frac{2R_1^{\text{TE}} u_1 \lambda}{R_1^{\text{TE}} k_1^2 + (\lambda + u_1)^2} - \frac{1}{2} \right) \lambda J_1(\lambda a) d\lambda + \frac{I}{2a} \\
 & - \frac{I}{k_1^2 a^3} \left( 3 + (k_1^2 a^2 - 3i k_1 a - 3) e^{-i k_1 a} \right)
 \end{aligned} \tag{C.11}$$

The implemented calculation routine also has the capability of modeling the response from a square loop as observed by a dipole receiver. This functionality uses integration of the  $H_z$ -field from virtual dipoles along the transmitter loop, in a way similar to the one described for the electric field of the grounded dipoles (however without grounding points). Access to this type of calculation has not yet been included in the graphical user interface, but is planned for a future version.

### C.3.2.1 Time-domain calculations

Since the transient response is a causal function ( $h_z(t) = 0$  for  $t \leq 0$ ), the transformation of the frequency response to the time domain can be obtained by means of a sine or cosine transform, and following Anderson (1974, 1981):

$$h_z(t) = -\frac{2}{\pi} \int_0^\infty \frac{1}{\omega} \text{Im} [H_z(\omega)] \cos(\omega t) d\omega \tag{C.12}$$

In Eq. (C.12) step-current excitation has been assumed. Assuming that the field does not vary over the area of the receiver loop, the relation between the vertical field and the induced voltage is given by:

$$v(t) = -\mu_0 n \pi b^2 \frac{dh_z(t)}{dt} \tag{C.13}$$

where  $b$  is the radius of the receiver loop and  $n$  is the number of turns. After making suitable substitutions, the resulting mutual impedance can be expressed as:

$$Z(\tau) = -\frac{2nb^2}{\sigma_1 a^3} \int_0^\infty \text{Im} \left[ H_z \left( \frac{2g}{\sigma_1 \mu_0 a^2} \right) \frac{2a}{I} \right] \sin(g\tau) dg \tag{C.14}$$

Here  $\tau = 2t \cdot (\sigma_1 \mu_0 a^2)^{-1}$  and  $g = \frac{1}{2} \sigma_1 \mu_0 \omega a^2$ , where  $\sigma_1$  is the DC conductivity of the first layer.

### C.3.3 FDEM calculations

The Horizontal Co-Planar loop system (HCP), also called a HLEM system, is popular in near-surface electromagnetic prospecting. Theoretically, the coils of the system are usually treated as vertical magnetic dipoles. The general expression for the  $z$ -component of the magnetic field, generated by such a system placed on the surface of a layered half-space, is given by Ward & Hohmann (1988):

$$H_z = \frac{m}{4\pi} \int_0^\infty [1 + R_0^{\text{TE}}] \frac{\lambda^3}{u_0} J_0(\lambda r) d\lambda \quad (\text{C.15})$$

where  $m$  is the magnetic moment of the transmitter, and all other parameters are as previously defined. Wait (1952) pointed out that for the case of a nonmagnetic half-space, Eq. (C.15) can be solved analytically. Thus, similarly to the case of the  $P$ -term of the grounded dipoles and the TEM central loop expression, the homogeneous half-space term can be subtracted from the kernel function and the analytical expression added outside the transform:

$$\begin{aligned} H_z = \frac{m}{4\pi} \left[ \int_0^\infty \frac{4R_1^{\text{TE}}u_1}{R_1^{\text{TE}}(k_1^2 - k_0^2) + (u_0 + u_1)^2} \lambda^3 J_0(\lambda r) d\lambda \right. \\ \left. + \frac{2}{(k_1^2 - k_0^2)r^5} \left( (9 + 9ik_0r - 4k_0^2r^2 - ik_0^3r^3) e^{-ik_0r} \right. \right. \\ \left. \left. - (9 + 9ik_1r - 4k_1^2r^2 - ik_1^3r^3) e^{-ik_1r} \right) \right] \quad (\text{C.16}) \end{aligned}$$

The expression further simplifies at sufficiently low frequencies ( $k_0 \approx 0$ ):

$$\begin{aligned} H_z = \frac{m}{4\pi} \left[ \int_0^\infty \frac{4R_1^{\text{TE}}u_1}{R_1^{\text{TE}}k_1^2 + (\lambda + u_1)^2} \lambda^3 J_0(\lambda r) d\lambda \right. \\ \left. + \frac{2}{k_1^2r^5} \left( 9 - (9 + 9ik_1r - 4k_1^2r^2 - ik_1^3r^3) e^{-ik_1r} \right) \right] \quad (\text{C.17}) \end{aligned}$$

Typically, data from magnetic dipole-dipole measurements are given as mutual coupling ratios, defined as the measured impedance normalized by the theoretical impedance of the system in free-space. The mutual coupling ratio can be calculated by dividing the expression for  $H_z$  at the position of the receiver by the corresponding primary field, the field that would be measured in free-space. For the HCP configuration the primary field is given by (Ward & Hohmann, 1988):

$$H_z^P = \frac{m}{4\pi r^3} e^{-ik_0r} (k_0^2 r^2 - ik_0r - 1) \quad (\text{C.18})$$

In case of quasi-static conditions, this expression simplifies to:

$$H_z^P = -\frac{m}{4\pi r^3} \quad (\text{C.19})$$

### C.3.4 DC geoelectrical calculations

Forward modeling capability of DC geoelectrical soundings has been included for completeness. The algorithm used to calculate the DC resistance is given by Koefoed (1979):

$$R = Q(|A\alpha|) - Q(|B\alpha|) - Q(|A\beta|) + Q(|B\beta|) \quad (\text{C.20})$$

with

$$Q(r) = \frac{\rho_1}{2\pi} \int_0^\infty K_1(\lambda) J_0(\lambda r) d\lambda \quad , \text{ where} \quad (\text{C.21})$$

$$K_n(\lambda) = \frac{K_{n+1} + \frac{\sigma_{n+1}}{\sigma_i} \tanh(\lambda h_n)}{\frac{\sigma_{n+1}}{\sigma_n} + K_{n+1} \tanh(\lambda h_n)} \quad , K_N = 1$$

Computational efficiency of Eq. (C.21) is usually increased by subtracting the homogeneous half-space response from the kernel and adding it outside the Hankel transform:

$$Q(r) = \frac{\rho_1}{2\pi} \left( \int_0^\infty (K_1(\lambda) - 1) J_0(\lambda r) d\lambda + \frac{1}{r} \right) \quad (\text{C.22})$$

## C.4 Calculation of Hankel and Cosine transforms

The general form of the Hankel transform, which occurs in all the presented EM field equations, can be written:

$$f(r, \Phi) = \int_0^\infty K(\lambda, \Phi) J_n(\lambda r) d\lambda \quad (\text{C.23})$$

where  $K$  is the kernel function,  $J_n$  is the Bessel function of order  $n$ ,  $\Phi$  represents the model parameters (here the layer properties) and  $r$  is the calculation distance. The inverse fourier transform, in the form of cosine or sine transform, which is used in the time domain calculations, is obtained by exchanging  $J_n$  with the cos or sin functions.

Two different approaches exist for the calculation of Hankel and harmonic transforms: numerical integration and digital filtering. CR1Dmod includes implementations of both approaches.

### C.4.1 Numerical integration

Numerical integration of Hankel transforms have been reported by a number of authors (Frischknecht, 1967; Dey & Ward, 1970; Hohmann et al., 1970). The general approach is to evaluate the integral in segments between the zeros of the Bessel function. Usually the first few segments, where the kernel function shows the largest variations, are computed using an adaptive quadrature rule, and the remainder of the integral, usually limited to a fixed number of segments,

is calculated using a non-adaptive gaussian quadrature rule. If the kernel function is well behaved, an alternating convergent series is eventually obtained, to which some sort of convergence improvement scheme (Itoh, 1989; Chave, 1983) can be applied to speed up the rate of convergence and minimize computation time. Several methods have been suggested but the most widely used in geophysical literature is the Euler method.

The NHT routine of CR1Dmod uses Matlabs built-in adaptive Simpsons quadrature rule (QUAD) to evaluate the first few segments. The remaining segments are evaluated using the built-in adaptive Lobatto quadrature rule (QUADL). The Euler method of convergence improvement, in the form presented by Press et al. (1986), is applied to the series. The integration is terminated when the last term added to the series is less than a tolerance specified by the user, or when a predefined number of segments have been calculated.

The routine uses precalculated locations of the first 300 zeros of  $J_n$  ( $n = 0, 1$ ). If more than 300 segments are required for the calculations, further zeros are approximated by adding multiples of  $\pi$ . However, usually 300 segments are more than adequate to obtain the desired accuracy.

### C.4.2 Fast Hankel Transform filters

The main disadvantage of the numerical integration scheme is the time of computation. Many evaluations of the kernel function are needed in order to obtain a reasonable precision. The development of the Fast Hankel Transform technique (Gosh, 1971; Johansen & Sørensen, 1979; Anderson, 1979; Christensen, 1990), based on digital filtering theory, has resulted in a much faster way to calculate Hankel transforms. By choosing appropriate substitutions, the Hankel transform can be converted to a convolution integral, which is evaluated in the fourier domain as a simple multiplication of a set of precalculated filter coefficients and calculated values of the kernel function.

This approach result in a great increase in speed, but also puts a restraint on the maximum accuracy obtainable with a given set of filter coefficients.

The function implemented in CR1Dmod is based on a Fortran routine originally written by N. B. Christensen (pers. comm., 2004) and the filter values of Christensen (1990).

### C.4.3 Comments on the transform routines

CR1Dmod contains independent routines to calculate NHT and FHT (also capable of cosine and sine transforms). They have intentionally been kept separate from the remaining code, so that they can be used in other applications. A separate driver program for a vertical magnetic dipole configuration over a homogeneous half-space is included with CR1Dmod to show the efficiency and precision of the FHT versus the NHT routine. This program also serves to demonstrate the use FHT and NHT routines for other applications.

## C.5 Spline interpolation applied to dipole integrations

In order to increase the speed of computations in CR1Dmod, spline interpolation schemes have been implemented for two situations.

EM calculations of certain wire configurations comprise integration over virtual electrical dipoles along the wires. Such integrations often result in a very large number of evaluations of the field equations. In CR1Dmod the user can choose to use cubic spline interpolation to significantly reduce the number of calculations.

The FHT method offers an easy and quick way of calculating transforms of multiple  $r$  distances. However, the calculated distances are logarithmically spaced at the sampling interval of the filter coefficients used. For maximum flexibility, but at the cost of computation speed, we have chosen to let the user set the number of evaluations per decade of distance, and calculate these individually.

The interval of  $r$  distances  $[R_1; R_2]$  on which the spline is based, is determined automatically based on the configuration, such that  $R_1$  is the second largest regular distance smaller than the smallest distance needed for the calculation. Similarly,  $R_2$  is the second smallest regular distance larger than the greatest distance needed.

For the inverse fourier transform (implemented as a sine transform) used in the time domain calculations, CR1Dmod allows for cubic spline interpolation of the frequency domain response in a similar way.

As the frequency interval needed for the transform is not known a priori, CR1Dmod lets the user specify the limits in terms of an induction number range. The induction number is taken to be  $B = \sqrt{\frac{1}{2}\omega\mu_0\sigma_1} \cdot a$ , where  $\sigma_1$  is the DC conductivity of the first layer and  $a$  the radius of the transmitter loop. After the calculations have completed, the evaluations of the frequency domain expressions can be plotted together with the cubic spline evaluations, to check that the specified range and sampling interval were appropriate.

## C.6 Program structure

CR1Dmod consists of two main windows, one that controls the model parameters and configuration of the measurement, and one that controls the calculation specific parameters.

The left hand side of the model window features an interactive plot of the half-space model (Fig. C.2). By clicking the mouse in the plot, the user can insert layer boundaries and drag these to the desired position. In the right hand side of the window, the lower section gives input fields for the layer parameters, including Cole-Cole model parameters, relative permittivity ( $\epsilon_r = \epsilon/\epsilon_0$ ) and magnetic susceptibility ( $\chi = \mu/\mu_0 - 1$ ), and allows for adding and deleting layers

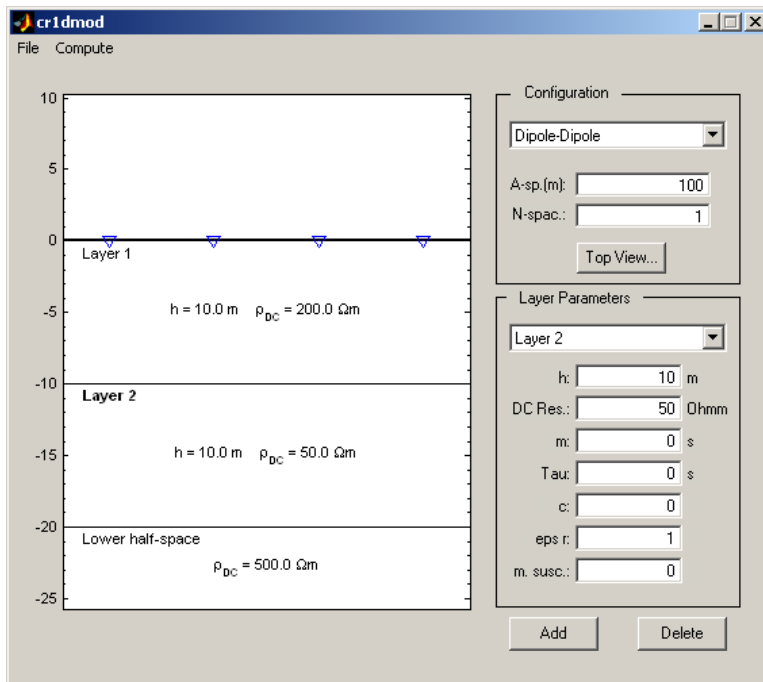


**Figure C.2:** The main model window of CR1Dmod features a graphical representation of the model, in which the user can add or delete layers and move boundaries. The right hand side of the window gives control of the configuration and layer parameters of the model.

in the model. The upper right hand section of the window gives control of the measurement configurations. Table C.1 lists the available configurations and the type of calculation available for each configuration.

The General Surface Array (GSA) allows for arbitrary location of receiver and transmitter electrodes on the surface of the layered half-space. A special window is called up by pressing the "topview" button. This window allows the user to place the electrodes, either by dragging them with the mouse, or by entering new coordinates in the input fields. The topview window also lets the user add and move segments of the receiver and transmitter wires. Thus, the influence caused by the placement of the wires can be taken into account in the forward modeling of frequency domain responses. The user should take care when using this option that Tx and Rx wires do not cross themselves or each other.

All grounded wire configurations, except the GSA, allows for multiple input of the configuration parameters such as A-spacing and N-spacing. Combined with the option to spline interpolate the wire integrations, this allows for fast calculation of the response of many configurations in one batch.

**Table C.1:** Configurations available in CR1Dmod.

Config.	Calc. type		
	DC	FD	TD
Wenner	x		
Schlumberger	x		
Dipole-dipole	x	x	(o)
GSA	x	x	(o)
TEM central loop		x	x
Sq. Tx loop + m. dip.		(x)	(x)
HCP FDEM (HLEM)		x	

(x): method is implemented in modeling routine but not in GUI.

(o): method is planned for a future version.

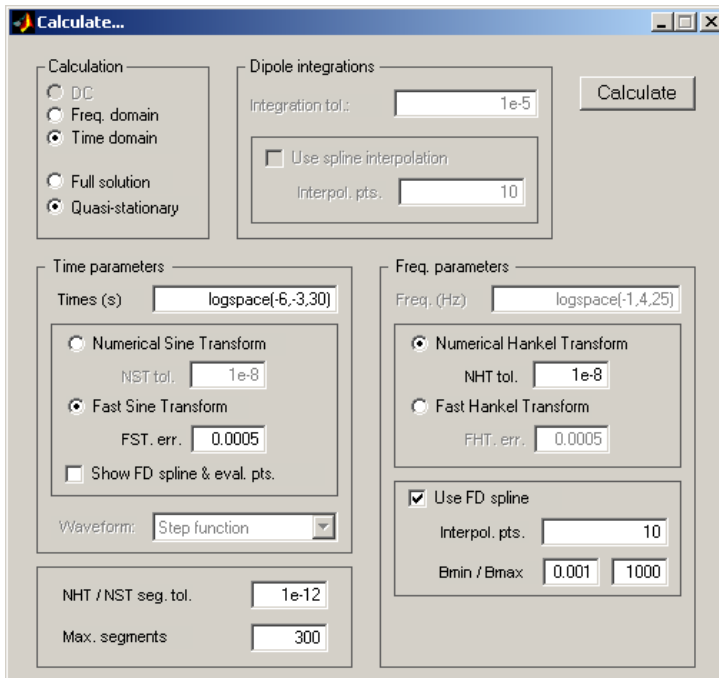


**Figure C.3:** The calculation window of CR1Dmod gives the user control over calculation domain, transform types, tolerances and spline interpolations.

In the calculation window (Fig. C.3), parameters specific to the type of calculation can be adjusted prior to calling the computational routines. For configurations allowing a choice (table C.1), the domain of calculation is selected (DC, FD, TD) as well as the "Full" or "Quasi-static" modes. In full mode, CR1Dmod selects either the full solution or the non-magnetic first layer solution depending on the magnetic susceptibility specified for the first layer. In quasi-static mode, the program assumes both non-magnetic and quasi-static approximations regardless of the specified susceptibility.

Most input fields in this window accept any regular Matlab expression. For instance, the expression `logspace(-6,-3,30)` in the Times input field will result in 30 logarithmically spaced times from one microsecond to one millisecond.

The forward modeling routines are coded in separate functions:

- *emgsafwd.m* calculates frequency domain response of the grounded wire configurations.
- *temmfwd.m* calculates frequency and time domain responses of the central loop configuration. It also has the capability of calculating the response of a square transmitter loop and a magnetic dipole receiver located at the center, but this option has not been implemented in the GUI yet.
- *fdemfwd.m* calculates frequency domain response of the HCP loop-loop configuration.
- *dcgsafwd.m* calculates DC response of grounded wire configurations.

These functions set up the needed parameters, including pointers to the kernel functions, and pass this information to either the NHT or FHT routines, which perform the actual transforms.

After the calculations have ended, the results are saved to a binary Matlab file along with the model, configuration and calculation parameters. Finally, the calculated response is plotted to the screen. In the plots, the impedances of grounded wires are multiplied by a geometric factor to yield the apparent resistivities.

The Cole-Cole resistivity dispersion model used by CR1Dmod may not be applicable to all problems. Therefore the computation of the complex conductivities used by the forward modeling routines has been implemented in a separate function (*Z\_cr.m*). The user is free to change this function to accommodate different models or perhaps to interpolate between data points of laboratory CR measurements.

## C.7 Conclusion

We have developed a Matlab application, CR1Dmod, capable of forward modeling of the response of several commonly used electrical and electromagnetic

methods in a 1D environment. We have obtained results in agreement with other authors (Kauahikaua & Anderson, 1979; Anderson, 1981; Christensen & Auken, 1992; Auken et al., 2001), but the time of computation is not as efficient as other routines. Nevertheless, our code handles complex resistivities defined by a Cole-Cole resistivity dispersion model, and offers solutions based on the full EM equations as well as the quasi-static approximation. As a result, it is also possible to model effects due to changes in the magnetic permeability and permittivity of subsurface layers, and a better understanding of the physical processes can be obtained.

The graphical user-interface of CR1Dmod gives an easy way to build and modify layered models, and offers intimate control of calculation parameters. The Hankel transforms can be calculated either as numerical integrations between the zeros of the Bessel function, or by means of the fast Hankel transform technique. The forward modeling routines and the Hankel transform functions are separate units that can be incorporated into other applications.

With Matlab being the preferred language of numerical computing for geophysical applications at many universities, we hope that this freely distributed code will be found useful for both research and educational purposes.

## C.8 Acknowledgements

We wish to thank Mr. Niels Bøje Christensen for making his Hankel transform codes available to us.

## References

- Anderson, W. (1974). *Electromagnetic Fields About a Finite Electric Wire Source*. USGS-GD 74-041, U.S. Geological Survey.
- Anderson, W. L. (1979). Computer program: Numerical integration of related Hankel transforms of orders 0 and 1 by adaptive digital filtering. *Geophysics*, 44(7), 1287–1305.
- Anderson, W. L. (1981). *Calculation of Transient Soundings for a Central Induction Loop System (Program TCILoop)*. Open-File Report 81-1309, U.S. Geological Survey.
- Auken, E., Breiner, M., Nebel, L., Pellerin, L., Thomsen, P., & Sørensen, K. I. (2001). EMMA - electromagnetic modeling and analysis. In *EEGS Birmingham Proceedings* (pp. 114–115). Birmingham, U.K.: EEGS.
- Chave, A. D. (1983). Numerical integration of related hankel transforms by quadrature and continued fractions expansions. *Geophysics*, 48(12), 1671–1686.
- Christensen, N. B. (1990). Optimized Fast Hankel Transform filters. *Geophysical Prospecting*, 38(5), 545–568.
- Christensen, N. B. & Auken, E. (1992). SELMA - simultaneous electromagnetic layered

- modelling and analysis. In: *Proceedings of Interdisciplinary Inversion Workshop 1 Aarhus 1992, Methodology and Applications within Geophysics, Astronomy, and Geodesy* (ed. B. H. Jacobsen), volume 41 of *Geoskrifter* (pp. 49–56). Aarhus University.
- Christensen, N. B. & Jacobsen, B. H. (2000). *Simultaneous Electromagnetic Layered Modeling and Analysis - Manual for the Electromagnetic Inversion Program SELMA2K*. Department of Earth Sciences, University of Aarhus.
- Cole, K. S. & Cole, R. H. (1941). Dispersion and absorption in dielectrics, I. Alternating current fields. *The Journal of Chemical Physics*, 9(4), 341–351.
- Descloitres, M., Guérin, R., Albouy, Y., Tabbagh, A., & Ritz, M. (2000). Improvement in TDEM sounding interpretation in presence of induced polarization. A case study in resistive rocks of the Fogo volcano, Cape Verde Islands. *Journal of Applied Geophysics*, 45, 1–18.
- Dey, A. & Ward, S. H. (1970). Inductive sounding of a layered earth with a horizontal magnetic dipole. *Geophysics*, 35(4), 660–703.
- Frischknecht, F. C. (1967). Fields about an oscillating magnetic dipole over a two-layer earth, and application to ground and airborne electromagnetic surveys. *Quarterly of the Colorado School of Mines*, 62(1), 326.
- Gosh, D. P. (1971). The application of linear filter theory to the direct interpretation of geoelectrical resistivity sounding measurements. *Geophysical Prospecting*, 19(2), 192–217.
- Hohmann, G. W., Kintzinger, P. R., Van Voorhis, G. D., & Ward, S. H. (1970). Evaluation of the measurement of induced electrical polarization with an inductive system. *Geophysics*, 35(5), 901–915.
- Itoh, T., Ed. (1989). *Numerical Techniques for Microwave and Millimeter-Wave Passive Structures*. New York: Wiley.
- Johansen, H. K. & Sørensen, K. (1979). Fast Hankel Transforms. *Geophysical Prospecting*, 27, 876–901.
- Kauahikaua, J. & Anderson, W. L. (1979). *Programs EMCUPL and SCHCOPL: Computation of Electromagnetic Coupling on a Layered Halfspace with Complex Conductivities*. Open-File Report 79-1430, U.S. Geological Survey.
- Koefoed, O. (1979). *Geosounding Principles, 1*, volume 14A of *Methods in Geochemistry and Geophysics*. Elsevier.
- Marshall, D. J. & Madden, T. R. (1959). Induced polarization, a study of its causes. *Geophysics*, 24(4), 790–816.
- Pelton, S. H., Ward, S. H., Hallof, P. G., Sill, W. R., & Nelson, P. H. (1978). Mineral discrimination and removal of inductive coupling with multifrequency IP. *Geophysics*, 43, 588–609.
- Press, W. H., Flannery, B. P., Teukolsky, S. A., & Vetterling, W. T. (1986). *Numerical Recipes, The Art of Numerical Computing*. Cambridge University Press.

- Ryu, J., Morrison, F., & Ward, S. H. (1970). Electromagnetic fields about a loop source of current. *Geophysics*, 35(5), 862–896.
- Sunde, E. D. (1968). *Earth Conduction Effects in Transmission Systems*. New York: Dover.
- Vanhalala, H., Soininen, H., & Kukkonen, I. (1992). Detecting organic chemical contaminants by spectral-induced polarization method in glacial till environment. *Geophysics*, 57(8), 1014–1017.
- Wait, J. R. (1952). Current-carrying wire loops in a simple inhomogeneous region. *Journal of Applied Physics*, 23(4), 497–498.
- Ward, S. H. & Hohmann, G. W. (1988). Electromagnetic theory for geophysical applications. In M. N. Nabighian (Ed.), *Electromagnetic Methods in Applied Geophysics*, volume 1 chapter 4, (pp. 131–311). Society of Exploration Geophysicists.
- Wong, J. (1979). An electrochemical model of the induced-polarization phenomenon in disseminated sulfide ores. *Geophysics*, 44(7), 1245–1265.
- Zonge, K. L. (1972). *Electrical Properties of Rocks as Applied to Geophysical Prospecting*. PhD thesis, The University of Arizona.

## APPENDIX D

# **Error sources relating to CR measurements over a wide frequency bandwidth**

---

This appendix contains a paper concerned with error sources in wide frequency bandwidth CR measurements.

Not submitted.



# Error sources relating to CR measurements over a wide frequency bandwidth

Thomas Ingeman-Nielsen

Arctic Technology Centre, BYG•DTU, Technical University of Denmark,  
DK-2800 Kgs. Lyngby, Denmark.

Phone: (+45) 45252251, Fax: (+45) 45885935, E-mail address: tin@byg.dtu.dk.

## D.1 Introduction

Since Pelton et al. (1978) published their classic paper on the application of the Cole-Cole model (Cole & Cole, 1941) to Complex Resistivity (CR) measurements, there has been a growing interest in wide frequency bandwidth CR measurements.

In the laboratory, Vinegar & Waxman (1984) studied induced polarization of shaly sands, including CR responses up to 1 kHz and Olhoeft (1984) studied clay organic reactions at frequencies up to 1 MHz. Vanhala & Peltoniemi (1992) studied the CR response of finish ore prospects at frequencies up to 1 kHz and Vanhala et al. (1992) studied organic contaminants in glacial till up to 1 kHz. Later a laboratory technique for CR measurements over wider frequency ranges (up to 10 kHz) was developed (Vanhala & Soininen, 1995), and subsequently applied to the study of oil contaminated sand and till (Vanhala, 1997).

Field scale measurements over similar frequency ranges are more scarce. The main problem is the discrimination of intrinsic CR response from EM coupling effects occurring in field-scale experiments. A number of papers have been published dealing with different ways of decoupling low frequency CR data. One approach is to assume that the CR phase is constant or a linear function of the logarithm of the frequency, and that EM coupling can be represented by the first few terms of a power-series (Hallof, 1974; Coggon, 1984; Song, 1984). Thus, the zeroth power coefficient is then taken as the decoupled phase value.

A different approach was introduced by Pelton et al. (1978) who suggested a multiplication of two Cole-Cole models where one is used to fit the low frequency dispersion and the other the EM coupling response. Major & Silic (1981) pointed out that an addition of the two models is theoretically preferable, and studied the limitations of this model. They concluded that the EM coupling response was generally more complex than what could be described by the Cole-Cole model. Brown (1985) proceeded by developing a model for the EM coupling term, based on the equivalent circuit theory often used in coil-coil FDEM theory, which substituted the second Cole-Cole model.

Yet another approach involves the computation of the EM coupling based on 1D models and subsequent subtraction from the field response. Wynn & Zonge

(1975, 1977) use a proprietary algorithm to curve-match EM coupling responses to the CR spectra and extract the field data. Wait & Gruszka (1986a,b), who studied the complex homogeneous half-space EM coupling response and subtracted the normal EM coupling response, point out that the technique fails to give the correct dispersion for frequencies above 10–100 Hz. Meyer (1990) uses a regular inversion technique to fit a two layer model to the observed data, and treat the residual as the CR effect.

Routh & Oldenburg (2001) showed that the observed response could be approximately described by the DC-resistivity based EM coupling, multiplied by a complex and frequency dependent function describing the CR frequency dispersion. This model allows for decoupling of the phase spectrum, but not the amplitude.

Finally, the most complex and time consuming technique is to include the intrinsic CR effect in the EM coupling calculations (Luo & Zhang, 1998).

The multitude of presented models is sharply contrasted by the lack of published wide frequency bandwidth CR data. Therefore, the presentation of high quality field scale CR measurements would shed light on the relationship between EM coupling and CR effects and give a more solid background for understanding the physical basis of the CR effects.

Here, practical results and problems encountered in relation to our attempts at collecting CR data over wide frequency bands are presented, together with theoretical studies of some possible error sources.

## D.2 Data acquisition

### D.2.1 Equipment and layout

The equipment applied for this project was a system manufactured by Zonge Engineering and Research Organization and consists of an eight channel GDP 32<sup>II</sup> multipurpose geophysical receiver and a GGT3 transmitter. The two units are synchronized with stable crystals clocks in each unit. Furthermore, one receiver channel is dedicated to measuring a current reference signal supplied from the transmitter through a 610 m twisted pair signal cable. The current reference signal is galvanically isolated from the transmitter by means of an isolation amplifier, refer to Figure D.1. For currents up to 2 A, the reference signal is measured across a 0.1  $\Omega$  and 0.909  $\Omega$  low inductance wire-wound shunt resistor connected in series. For higher currents, the 0.909  $\Omega$  resistor is shorted out.

The system allows for up to 9 stainless steel electrodes connected simultaneously to the transmitter system. The pair of electrodes used for transmitting is chosen by the operator by means of a manual switch box. The receiver electrodes in use were non-polarizable electrodes, consisting of a copper electrode injected in a saturated  $\text{CuSO}_4$  solution in a pot of porous ceramic. This type of electrodes is used in order to ensure stable potentials at low frequencies.

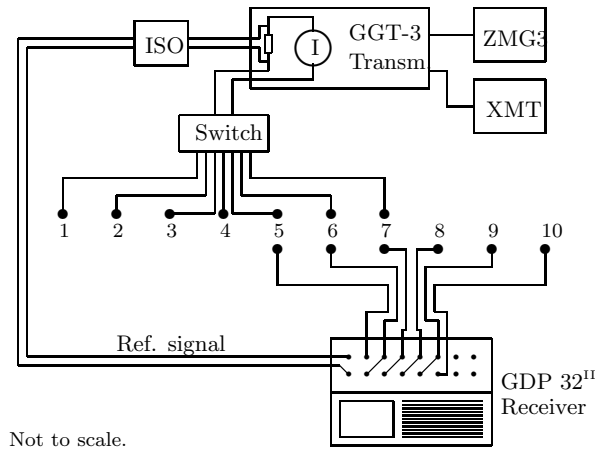


**Figure D.1:** Schematic diagram of the typical layout used for CR measurements in this study. ZMG3 is a motor generator supplying power to the transmitter, and XMT is the unit controlling waveform and frequency of the transmitted signal.

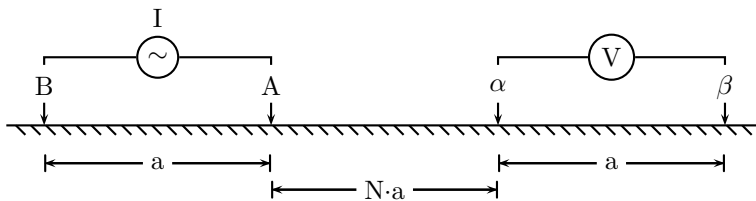


**Figure D.2:** The general collinear dipole-dipole electrode configuration.  $N$  is the dipole separation factor called the  $N$ -spacing, and  $a$  is the dipole size in meters.

The general setup applied is a dipole-dipole configuration (Figure D.2), however to increase the speed of data acquisition the setup is enlarged as shown in Figure D.1. For each pair of transmitter electrodes, several channels of the receiver will be collecting data. The smallest  $N$ -spacing of any active channel must be at least 1, in order to avoid excessive EM coupling and to protect the receiver channels from high voltages. The cables are laid out so that — wherever possible — the distance between two parallel cables is at least 1 m. This is done in order to reduce capacitive coupling between cables.

After completion of one spread, the receiver electrodes can be moved to new locations to the left of the center of the layout, where a new set of measurements is collected. A two-spread profile results in the measurement profile shown in Figure D.3, where normal plotting conventions are followed (Bertin & Loeb, 1976), and it is observed that several data points from the two spreads overlap. These data points can be used as a check of the data quality.

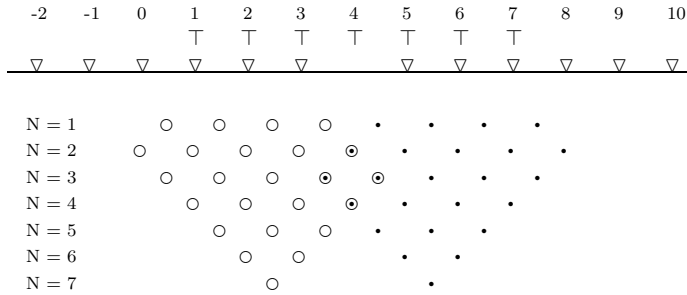


**Figure D.3:** Measurement locations (O, •) plotted using the standard profile plotting conventions. The position of receiver electrodes on the ground surface are indicated by (∇), transmitting electrodes by (T).

## D.2.2 Frequency domain measurements

In practice, the transmitter transmits a 100% duty-cycle square wave current. The potential measured by the receiver is this square wave-form convolved with the ground transfer impedance.

According to standard Fourier analysis any single-valued, bounded and periodic function, which is continuous except for a finite number of discontinuities and has a finite number of maxima and minima, can be completely described by an infinite series of sinusoidal waves of the form

$$f(t, \omega) = \frac{a_0}{2} + \sum_{n=1}^{\infty} (a_n \cos n\omega t + b_n \sin n\omega t) \quad (\text{D.1})$$

In this equation,  $a$  and  $b$  are the fourier coefficients,  $\omega$  is the angular frequency, and  $t$  is the time. For a square wave as used in CR surveying the coefficients are given by:

$$a_0 = 0, \quad a_n = 0 \quad (\text{D.2})$$

$$b_n = \begin{cases} 0 & \text{for } n \text{ even,} \\ \frac{4}{n\pi} & \text{for } n \text{ odd.} \end{cases} \quad (\text{D.3})$$

and the sum becomes

$$f(t, \omega) = \frac{4}{\pi} \sum_{n=1}^{\infty} \left( \frac{1}{n} \sin n\omega t \right) \quad (\text{D.4})$$

By applying a square wave current at a specific fundamental frequency, potential data can be obtained for the corresponding harmonic waveform and a number of odd harmonics. Since the amplitude and power of the harmonics fall off as  $1/n$  and  $1/n^2$  respectively, the number of harmonics analyzed in practice is limited to the first 5 odd harmonics. The harmonic properties of the square wave are illustrated in Figure D.4.

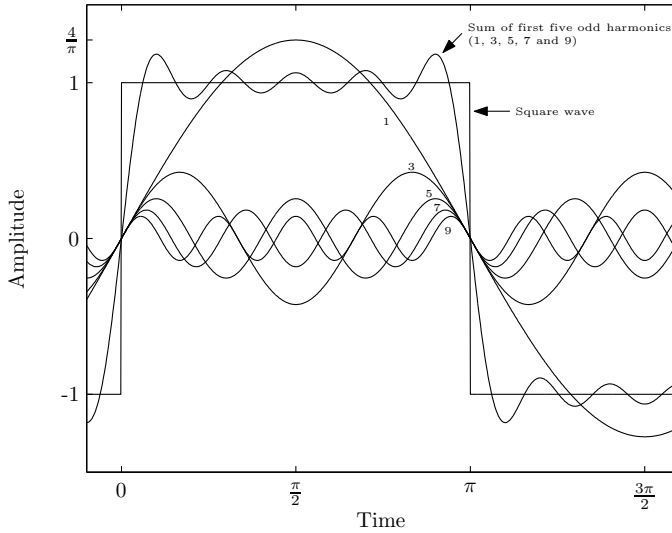


**Figure D.4:** Illustration of the 100% duty cycle square wave, and its first five odd harmonic components (Modified from Zonge & Hughes, 1980).

The GDP 32<sup>II</sup> performs the Fourier analysis by application of the Fast Fourier Transform (FFT) to the data collected at each channel. The result is amplitude and phase data for each of the five harmonics analyzed.

At this point, the measured ground potentials are deconvolved by the current waveform (the reference signal) at each frequency to give the ground impedance:

$$I_{\text{ref}} = \frac{V_{\text{ref}}}{R_s} e^{i\phi_{\text{ref}}} e^{i\omega t} \quad (\text{D.5})$$

$$U = V e^{i\phi} e^{i\omega t} \quad (\text{D.6})$$

$$Z = \frac{U}{I_{\text{ref}}} = \frac{V e^{i\phi}}{\frac{V_{\text{ref}}}{R_s} e^{i\phi_{\text{ref}}}} = \frac{V \cdot R_s}{V_{\text{ref}}} e^{i(\phi - \phi_{\text{ref}})} \quad (\text{D.7})$$

where  $R_s$  is the resistance of the shunt resistor used to generate the reference signal,  $V_{\text{ref}}$  and  $\phi_{\text{ref}}$  are the amplitude and phase of the frequency component of the reference voltage at a specific angular frequency,  $\omega$ , and  $I_{\text{ref}}$  is the corresponding reference current. Similarly,  $V$  and  $\phi$  are the amplitude and phase of the same frequency component of the ground potential difference measured on the input channel, and  $Z$  is the calculated complex impedance. This procedure compensates for deviations between the ideal square waveform and the actual current waveform.

The Zonge instruments allow for integer power-of-2 fundamental frequencies

in the interval 0.016 to 1024 Hz, and measure the 3<sup>rd</sup>, 5<sup>th</sup>, 7<sup>th</sup> and 9<sup>th</sup> harmonics in addition to the fundamental. Thus the highest frequency measurable by this system is 9216 Hz. In practice, the collected frequencies are chosen so that the fundamental frequency (n+1) falls between the 7<sup>th</sup> and 9<sup>th</sup> harmonic of the fundamental frequency (n). This ensures overlap between each section of collected data, and thus inconsistencies are more easily identified and corrected.

The measured impedances may be converted to apparent complex resistivities using the geometric factor known from DC-prospecting:

$$\rho_a^* = Z \cdot K = Z \cdot 2\pi \left[ \frac{1}{|A\alpha|} - \frac{1}{|B\alpha|} - \frac{1}{|A\beta|} + \frac{1}{|B\beta|} \right]^{-1} \quad (\text{D.8})$$

where  $\rho_a^*$  is the apparent complex resistivity and  $K$  is the geometric factor.

### D.2.3 System calibration

Each of the channels in the GDP 32<sup>II</sup> are in theory identical. Nevertheless, small differences may occur due to slightly different properties of the electronic components. With the GDP 32<sup>II</sup> it is possible to record a system calibration to eliminate these effects from the measured data. A stable square wave calibration signal with an amplitude of 1 V is passed to each channel. The measured amplitudes and phases are stored in special calibrate records in the instrument and used to normalize the collected data before deconvolution. System calibration can be performed either internally, where the signal is passed directly to the input of each channel, or externally where the signal must be routed manually to the input terminals of each channel. The latter method allows the operator to include external equipment and wiring — such as the isolation amplifier and communication wire — in the calibration. A systems check function allows the operator to check the current calibration in a similar way.

## D.3 Identifying unexpected effects in the collected data

A number of unexpected effects were observed in the CR field data collected in Greenland and Denmark during the summer of 2003. Very large phase responses (positive or negative) were found in most of the spectra at higher frequencies, and the corresponding apparent resistivities also showed unexpectedly large decreases in magnitude. The responses are of a type, size and shape that would not be expected from natural polarization phenomena in the ground. Figure D.5 shows four measurements from different locations, and illustrates the types of effects encountered. Three of the data sets were collected with dipole sizes of 10 m and N-spacings ranging from 1 to 5. The last data set was collected with a dipole size of 1 m and an N-spacing of four. In contrast to what would be expected

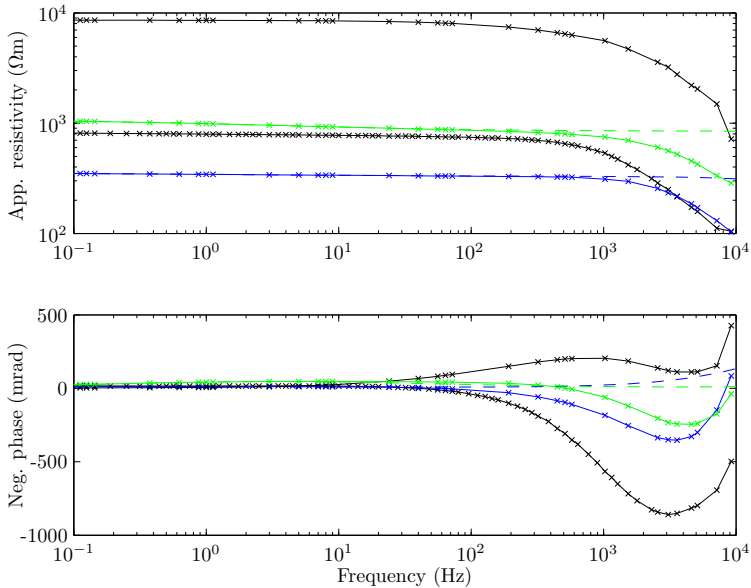


**Figure D.5:** Examples of typical field data curves. Data presented with solid lines are collected using 10 m dipoles and N-spacings from 1 to 5. The last data set (dots) was collected with 1 m dipoles and an N-spacing of 4. Homogeneous half-space models (dashed) have been fitted to the low frequency part of two of the data sets (blue and green).

from normal EM coupling behaviour, this data set is showing the largest phase excursion ( $\sim 850$  mrad). The data are plotted with the sign of the phases reversed, following common practice (Pelton et al., 1978).

Homogenous half-space models incorporating EM and CR effects have been manually fitted to the low frequency part of two of the data sets (blue and green) using the CR1Dmod software (Paper C). It is observed that these simple models are grossly inadequate in describing the observed data.

Figure D.6 gives one example of data sets from the overlapping part of two spreads. Under ideal conditions, these data should be identical. However, in most cases, large differences were observed. The presented example is an extreme case, where phase differences are significant at frequencies as low as 10 Hz.

Comparison has been made with different homogeneous half-space, 2 and 3 layer forward models calculated by CR1Dmod. Although negative coupling at high frequencies can occur in extreme situations in a high/low resistivity environment (Tripp et al., 1990), in many cases, the observed responses have shapes that cannot be explained by any of the 1D models applied.

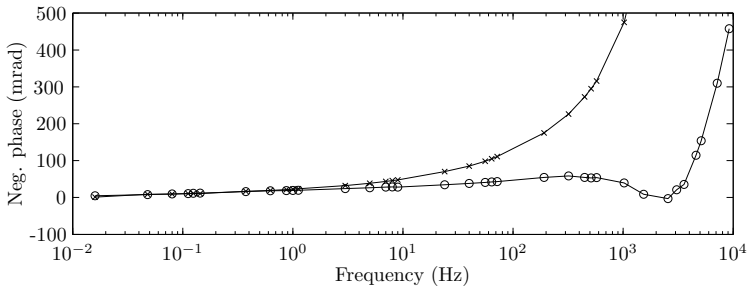


**Figure D.6:** Example of the negative phase of the apparent resistivity for two overlapping measurements of two spreads from a profile collected near the village of Kangerluk (on Disko Island, West Greenland) using 40 m dipoles and an N-spacing of 4.

## D.4 Causes for the observed effects

A number of possible causes for the effects observed in the collected data have been identified and studied:

- a) Deviation from 1D earth model
- b) Layout effects
- c) Capacitive coupling effects
- d) Equipment related challenges

In the following sections, each of these points will be discussed.

### D.4.1 Deviation from 1D earth model

Several studies of 2D and 3D CR effects have been reported (Weller et al., 2000; Hallof & Yamashita, 1990; Hohmann, 1990). Most of these are concerned only with the static approximation, where the time varying properties of the EM fields, and thus the EM coupling, are neglected, or the results are presented only as PFE's at a few frequencies.

An exception is Hohmann (1975), who studied 3D modeling of CR effects and EM coupling by means of an integral equations solution. Also Luo & Zhang (1998) have studied the combined effect of complex resistivity and EM coupling for 3D bodies submerged in a layered half-space. Luo & Zhang did in some cases observe phase reversals in similar frequency ranges as the anomalous Greenlandic field data.

The lack of published wide frequency bandwidth field data and the scarcity of literature on the field of modeling combined CR and EM coupling effects, hinder reasonable estimates of the effects of deviations from a 1D earth model. As 3D modeling tools have not been available, it can only be concluded that responses of the types observed could possibly be generated in situations where 3D effects are significant.

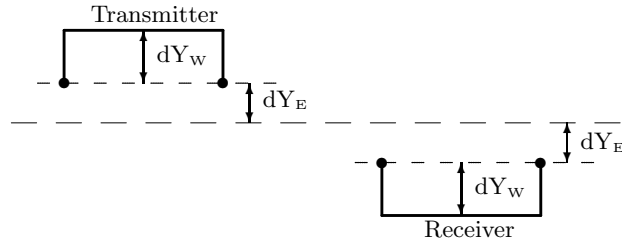


**Figure D.7:** Definition of the layout used in the modeling.  $dY_E$  is the electrode offset from the nominal collinear location and  $dY_W$  is the additional wire offset relative to the electrode positions

Nevertheless, as this type of behavior was observed in an increasing number of measurements, including measurements in areas with relatively simple geology, it seems plausible that the cause should be found elsewhere.

## D.4.2 Layout effects

Several studies deal with the nominal EM coupling response in common CR and IP arrays (most often the dipole-dipole configuration) in the homogeneous half-space situation or over a 1D layered half-space and present modeling results (Millett, 1967; Dey & Morrison, 1973; Hohmann, 1973; Wynn & Zonge, 1977; Ramachandrian & Sanyal, 1980).

In practice however, the layout of electrodes and cables for CR surveys often differ from the ideal dipole-dipole configuration. As indicated in Figure D.1, transmitting and receiving electrodes are separated perpendicular to the profiling direction. Cabling will usually also deviate from the ideal configuration, in order to allow measurements on several dipoles simultaneously, and to avoid moving the transmitter or receiver instrumentation for every dipole combination.

The theory concerning arbitrarily oriented electrode and wire layouts was presented by Sunde (1968). An option for this type of calculations has been incorporated in the CR1Dmod software (Paper C), and has been used to analyze the effects of different deviations from an ideal dipole-dipole configuration.

### D.4.2.1 Modeling the layout effects

The setup applied in the modeling is illustrated schematically in Figure D.7, where  $dY_E$  is the electrode offset from the profile center line, and  $dY_W$  is the receiver and transmitter wire offset relative to the electrode positions. Additional wiring in the situations where the receiver or transmitter are offset compared to the dipole centers have been neglected.

A series of calculations have been performed using a non-dispersive homoge-

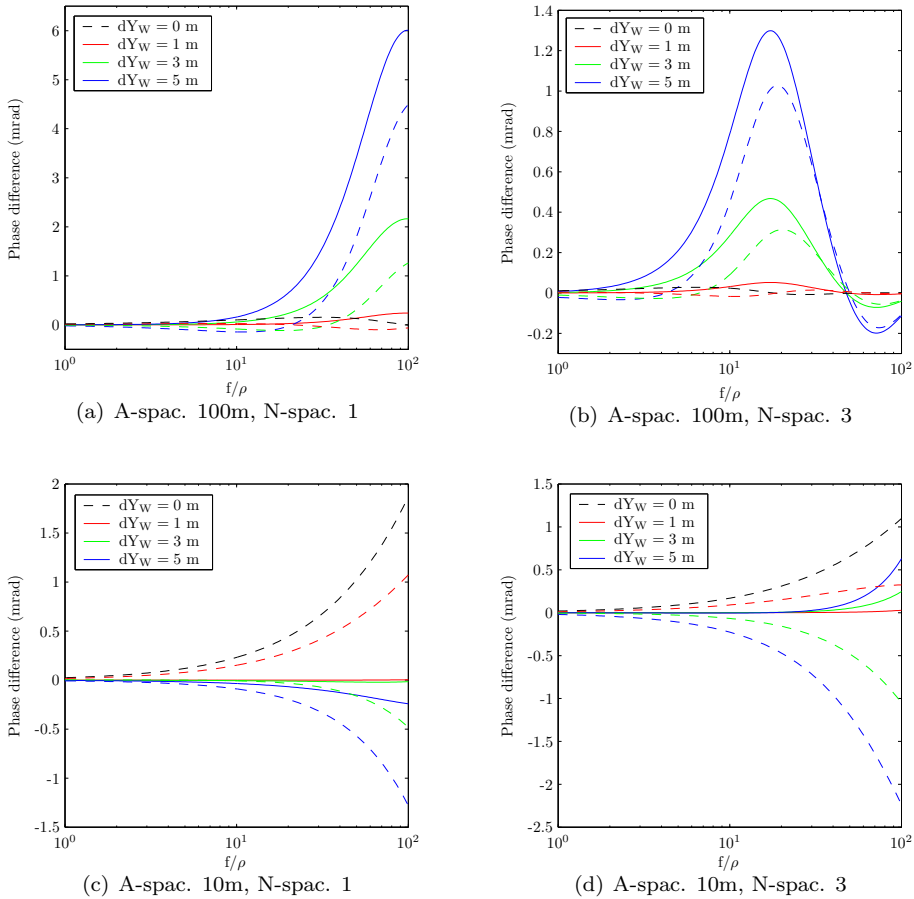


**Figure D.8:** Effect of changing the location of electrodes and wire layout. Solid lines have the electrodes in the original, inline positions ( $dY_E = 0$  m), and only the wire layout is changed. Dashed lines have transmitter and receiver electrodes offset by 2 m ( $dY_E = 1$  m). The effect on the field data is such that positive values of the phase difference results in an increase of the observed negative phase value.

neous half-space model with a resistivity of  $100 \Omega\text{m}$ . Calculations have been done for dipole sizes of 10 m and 100 m, and N-spacings of 1 and 3. Electrode offsets ( $dY_E$ ) were 0 m and 1 m, and  $dY_W$  varied between 0 m and 5 m.

The results of the analysis show that effects of changes to the ideal layout are small, and only high frequencies ( $> 100$  Hz) are affected.

Figure D.8 shows the differences in phase between the ideal response of the inline configuration and the responses of offset configurations ( $d\phi = \phi_{\text{ideal}} - \phi_{\text{offset}}$ ) in four different situations. Modeling has shown that the effect of changing half-

space resistivity is a translation along the frequency axis (this is not the case for changes in the dipole length, unlike the nominal dipole-dipole configuration). Therefore, the modeling results are presented in terms of the parameter  $f/\rho$ .

The largest phase change occurs in the case of 100 m dipoles at N-spacing 1, and amounts to approximately 6 mrad. The remaining configurations all result in phase differences less than  $\pm 2.5$  mrad. In the case of the 10 m dipoles, offsetting the wires have only little effect when the electrodes are in the nominal positions ( $dY_E = 0$  m). An offset of the electrodes, however, does affect the response. This corresponds well with Wait (1951), who found that the grounding term dominates the response at low frequencies and small lengths. It is therefore interesting to see that when electrodes are offset, the cable paths have a much larger influence on the response.

In the case of 100 m dipoles on the other hand, offsetting the electrodes has only little effect on the overall response. The main contribution comes from changes in the cable paths. Again, this is expected, since coupling dominates over grounding response when longer distances or higher frequencies are involved. For 100 m dipoles there is an inverse relationship between N-spacing and the modelled absolute phase differences, whereas such a relationship is not evident for the shorter dipoles.

### D.4.3 Capacitive coupling effects

Some of the collected data sets show high frequency effects that resemble what could be expected from capacitive coupling effects (Zonge, 2004, priv. comm.). Very little information has been published on the effect of capacitive coupling on CR measurements. Wait (1951) studied the effect of capacitive coupling between transmitter and receiver wires in borehole CR measurements. Madden & Cantwell (1967) studied current leakage from the transmitting wire in surface measurements and how the subsequent change in the potential field influences the measured responses in terms of PFE values. Madden & Cantwell conclude that although an effect may be measurable, it will generally not be a significant increase over background values. Their calculations were done under the static approximation and are therefore only valid at very low frequencies.

Zonge & Hughes (1985) studied the effect of Electrode Contact Resistance (ECR) on the measured receiver voltage in CSAMT surveys, taking into account the wire to ground capacitive coupling. They present an equivalent circuit of half the receiver dipole response, and give theoretical and field results that fit the model. They show that for an ideally grounded circuit,  $R_c = 0 \Omega$ , the capacitive effect is effectively shorted out, and does not affect the measurements. At the other limit, for infinite  $R_c$ , the measured effect corresponds to an ungrounded receiver. They present a rule of thumb that when the product of receiver length [km], frequency [kHz] and electrode contact resistance [ $k\Omega$ ] exceeds 2.0, the ECR effect may be appreciable. However, in their calculations Zonge & Hughes assume that the fields are constant over the length of the receiver dipole. In CR surveys

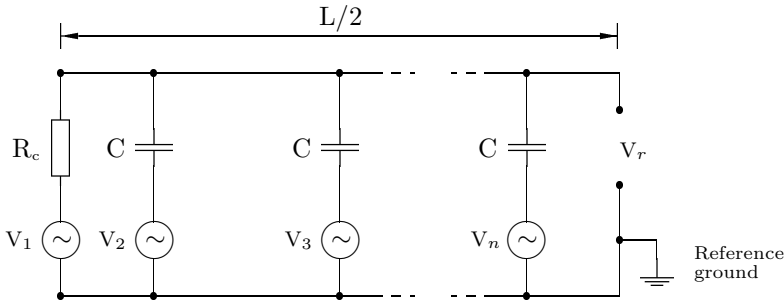


**Figure D.9:** Equivalent circuit for the ECR and capacitive coupling model for half of a receiver dipole.  $V_r$  is the measured potential difference, whereas  $V_i$  is the potential difference between location  $i$  and the common reference ground.

this is not the case. Furthermore, they study only the effect on the magnitude of the received voltage. Therefore, the presented results cannot be directly applied to CR measurements.

### Extending the model for the receiver dipole

(Please see Errata for this section, page 179)

The model presented by Zonge & Hughes (1985) has been extended to allow calculation of the ECR effect and capacitive wire to ground coupling for a receiver dipole in a typical CR setup. The equivalent circuit model for one half of a differential input system is shown in Figure D.9, and the potential difference measured at the receiver is given by:

$$V_r = \frac{X_c}{X_c - (n-1)R_c} V_1 - \frac{R_c}{X_c - (n-1)R_c} \sum_{i=2}^n V_i \quad (\text{D.9})$$

where

$$X_c = \frac{1}{i\omega CL/(2n-2)}$$

is the capacitive reactance of the wire to ground capacitance.  $L$  [m] is the dipole size,  $C$  [F/m] is the distributed wire to ground capacitance,  $R_c$  [ $\Omega$ ] is the electrode contact resistance,  $V_r$  is the potential difference measured in the receiver, and  $V_i$  is the potential difference between location  $i$  along the dipole and the common ground, which is usually defined by an electrode at the center of the receiving dipole.

In this model, the wire resistance and inductance have been neglected as well as the input impedance of the receiver. The values of  $V_i$  are calculated using the normal EM coupling equations for electrode arrays on the surface of a conductive half-space (refer to Paper B or Paper C). Calculations are performed

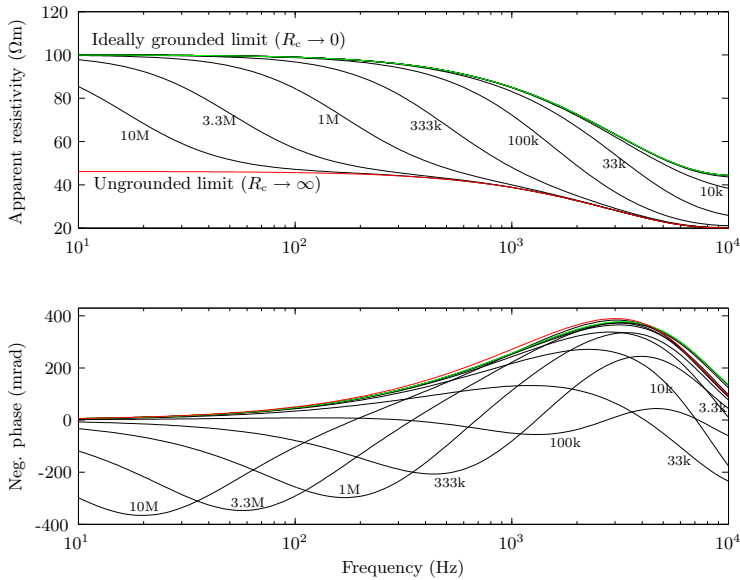


**Figure D.10:** EM coupling response for a 100 m dipole-dipole configuration with N-spacing 1, over a 100 Ωm half-space for different values of the electrode contact resistance,  $R_c$  [Ω].

for the two half dipoles separately, each divided into  $n - 1$  segments. The number of segments is increased until the relative change in both amplitude and phase of the total received voltage between two consecutive iterations is less than a specified maximum error at all frequencies.

The model has been used to calculate the ECR effect on the dipole-dipole configuration for a number of dipole sizes in the range from 10 m to 300 m over homogeneous half-spaces with resistivities of 100, 1000 and 5000 Ωm. A distributed wire to ground capacitance of 23 pF/m (Zonge & Hughes, 1985) and electrode contact resistances in the range from 100 Ω to 10 MΩ were used.

Figure D.10 gives an example of the resulting magnitude and phase responses. The figure includes the ideally grounded limit (green) and the ungrounded limit (red). The amplitude shows same type of response as observed by Zonge & Hughes, where the grounded limit is the low-frequency asymptote and the ungrounded limit the high-frequency asymptote. The phase response has similar asymptotic behavior, but in the transition zone, very large phase excursions are observed.

From the entire sequence of models, the following main observations were made, relating to the phase changes:

- 1) Increasing effect with increasing dipole length,
- 2) slightly decreasing effect with increasing N-spacing,
- 3) complex dependence on the half-space resistivity.

The overall effect is an increase in the measured phase response, and for short dipoles with  $R_c$  less than approximately 30 k $\Omega$ , the size of phase effect is monotonously increasing with frequency (to above 10 kHz). The resistivity dependence is insignificant in relation to these configurations.

For longer dipoles (in the 100 m range) and shorter dipoles for very high  $R_c$  the difference in phase between the nominal and the ECR phase response has a peak at a frequency, which depends inversely on dipole size. Approaching and beyond this frequency, the dependency on N-spacing becomes more complex.

The main conclusion to be drawn from the modeling is that even for short dipoles, phase effects are apparent at high frequencies when the electrode contact resistance is significant.

The model suggests a constant relation between the error in phase and the product of the dipole size, contact resistance and frequency:

$$\Delta\phi \approx K \cdot a \cdot f \cdot R_c \quad (\text{D.10})$$

where  $\Delta\phi$  is the decrease in the observed negative phase angle [mrad],  $a$  is the dipole size [km],  $f$  is the frequency [kHz] and  $R_c$  is the contact resistance [k $\Omega$ ].  $K$  is the proportionality constant, which takes the values 38.6, 36.3 and 35.9 for N-spacings 1, 3 and 5 respectively. These relations are accurate to within a few mrad, for errors up to 100 mrad.

### Suggesting a model for the transmitter dipole

Capacitive coupling between the transmitting cable and the ground have two main effects:

- 1) Current leaks to the ground along the full length of the cable, not only at the grounding points,
- 2) The amplitude of the current flowing in the cable is reduced as a function of distance from the transmitter, and the phase angle changes.

Knowledge of the variation of the current amplitude and phase along the wire is therefore essential in calculating the EM coupling response.

Here it is suggested that the current as a function distance from the transmitter (the current waveform generator) is approximated separately by means of a simple transmission line model. The general EM coupling model is then adapted to include the current function instead of a constant current. In this model, the transmitter is assumed to be located at one end of the transmitter wire. The wire is assumed to have no resistance, any inductance in the system is neglected, and it is assumed that there is no contact resistance at either end. The ground is described as having a constant resistance per unit length. Under these assumptions, the model can be treated as a transmission line with a short circuit termination. Figure D.11 shows the equivalent circuit model.

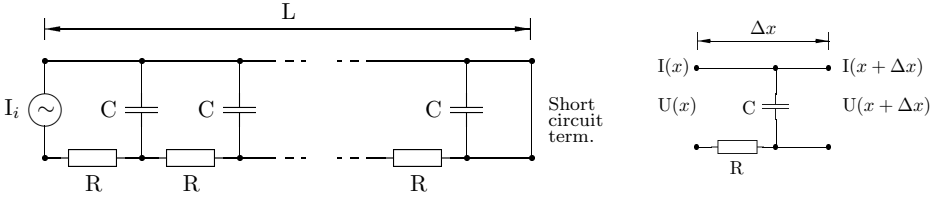


**Figure D.11:** Equivalent circuit of transmission line model of capacitive coupling between ground and wire, and a differential element of the transmission line.

Following general transmission line theory (i.e. Cheng, 1989) the solution to the governing differential equations can be expressed in terms of the current at any point,  $x$ :

$$I(x) = \frac{I_i}{2Z_0} ((Z_i + Z_0)e^{-\gamma x} - (Z_i - Z_0)e^{\gamma x}) \quad (D.11)$$

$$Z_i = Z_0 \frac{Z_L + Z_0 \tanh(\gamma L)}{Z_0 + Z_L \tanh(\gamma L)} = Z_0 \tanh(\gamma L) \quad (D.12)$$

$$Z_0 = \sqrt{\frac{R}{i\omega C}} \quad (D.13)$$

where  $I_i$  [A] is the current supplied by the transmitter,  $L$  [m] is the total length of the wire,  $C$  [F/m] is the distributed wire to ground capacitance,  $R$  [ $\Omega$ /m] is the equivalent ground resistance, and  $Z_L$  is the termination impedance. In this model,  $Z_L$  is assumed to be zero corresponding to no contact resistance. The propagation constant,  $\gamma$ , is  $\sqrt{i\omega RC}$ .

The general formulation of the EM coupling equations assumes a constant current function (Sunde, 1968; Dey & Morrison, 1973). In order to allow for current variation along the length of the transmitter wire, the grounding function, which is normally analytically integrated, must be included in the numerical integration, along with the current function.

In the case of a homogeneous, non-magnetic half-space under the quasi-static approximation ( $k_0 \approx 0$ ), analytical solutions exist to the Hankel transforms, and the mutual impedance for the dipole-dipole configuration is given by:

$$Z = \frac{\hat{z}_0}{2\pi I_i} \int_A^B \int_\alpha^\beta \left[ \frac{I(x)}{k_1^2 r^3} ((ik_1 r + 1)e^{-ik_1 r} - 1) + \frac{2I(x)}{k_1^2 r^3} \right] ds dS \quad (D.14)$$

where  $(A, B)$  and  $(\alpha, \beta)$  are the grounding points of the transmitter and receiver,  $dS$  and  $ds$  are the respective infinitesimal wire elements and  $r$  is distance between them.  $\hat{z}_0 = i\omega\mu_0$  where  $\mu_0$  is the magnetic permeability of free space,  $k_1$  is given by  $\sqrt{-i\omega\mu_0\sigma_1}$ , and  $I_i$  is the current supplied by the current generator.

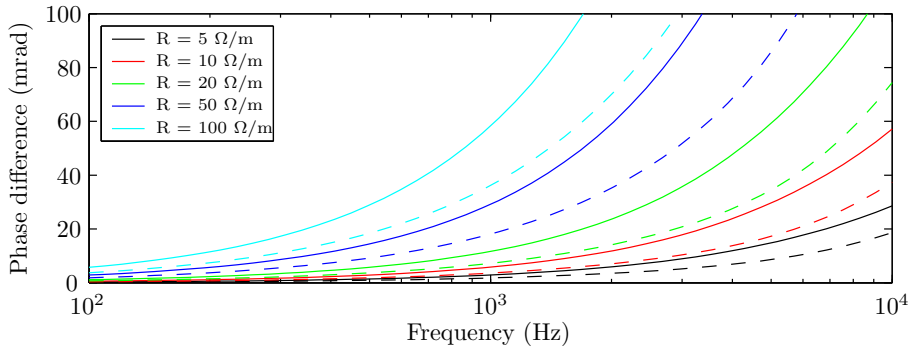


**Figure D.12:** The difference in phase response between the nominal and the capacitively coupled apparent resistivity, as predicted by the presented model. Data for the transmitter placed at electrode A (solid) and electrode B (dashed) are shown.

In the application of this model, the main challenge is to estimate the ground resistance,  $R$ . In fact, it is nonsense to discuss ground resistance, since resistance is not a property of the ground but related to the current path, which in turn depends on the ground resistivity, location of the current electrodes, etc. In the application of the transmission line model, a range of values of  $R$  have been applied, independently of the parameters of the coupling model. As with the model of the receiver dipole a value of 23 pF/m has been used for the wire to ground capacitance.

Figure D.12 shows the phase effects of the coupling model subtracted from the nominal response for 100 m dipoles at N-spacing 1, over a 100  $\Omega$ m half-space for equivalent ground resistances between 5 and 100  $\Omega$ /m.

The model predicts the phase effects to be larger when the transmitter is located at electrode A (furthest from the receiver dipole) than when located at electrode B. The difference between the two situations decreases with increasing N-spacing. The phase effects increase with the a-spacing and with increasing equivalent ground resistance. The model predicts that the phase differences are always positive, corresponding to an increase of the measured negative phase values (values become more negative). Effects on the amplitude of the calculated apparent resistivities should be insignificant (less than 1%) at frequencies less than approximately 1 kHz, rising to more than 15% at the highest frequency.

The presented model is a primitive attempt to describe the capacitive coupling effects arising from the transmitter. The model suffers from the inherent difficulties of establishing the equivalent ground resistance. An estimate can be obtained from a two-electrode resistance measurement with a simple ohm-meter. Such a measurement will include the electrode contact resistance and will therefore be an approximate upper bound on the resistance.

In order to be of practical use, the model should be changed to allow for a transmitter located at the center of the grounded wire, instead of at the end points. It seems also necessary to include the effect of electrode contact resistance.

In spite of these obvious shortcomings of the model, it is interesting to observe that it predicts phase effects that are generally opposite those predicted from the model of the receiver dipole. Although the frequency dependence of the two effects are different, this indicates that they may to some extent cancel each other out.

#### D.4.4 Equipment related challenges

A study of the reference channel phases in a number of the collected field data sets revealed large differences of up to  $\pi$  radians between the largest and smallest phases observed at high frequencies among the data sets. In some cases, the resulting impedance phases seemed to be mirror images of the phases measured on the reference channel, indicating that the measured reference phases did not correspond to the phases of the actual transmitted current. Therefore the isolation amplifier and the signal cables were studied.

##### D.4.4.1 The isolation amplifier

Tests performed at Zonge Engineering and Research Organization in the summer of 2004 (Ingeman-Nielsen & Szidarovszky, 2004) relating to their laboratory setup for testing rock samples have shown problems relating to electronic filters in the design of the isolation amplifier.

The isolation amplifiers manufactured by Zonge contain an AD210 optical isolation amplifier unit. It has a low pass filter (LPF) on both input and output side and an internal power supply. According to the manufacturers specifications for the AD210 the filter on the output may be needed to reduce ripples created by the carrier signal from the optical unit.

In the laboratory setup, the receiver is operated with isolation amplifiers on both reference channel and measurement channel. The electronic components of the filters had to be closely matched to ensure acceptable measurements at high frequencies. Pushing the cutoff frequency (the -3 dB point) of the filter on the output side also improved the performance. These results indicate that the isolation amplifiers have a transfer function which affect the data quality at high frequencies. Furthermore, indications were found that the transfer function depends on the impedance across which the unit is connected.

##### Transfer function of the isolation amplifier

The transfer function of the isolation amplifier has been studied for a number of different filter combinations. Table D.1 lists the electronic components used for the low pass filter on the output, as well as the cutoff frequency for the

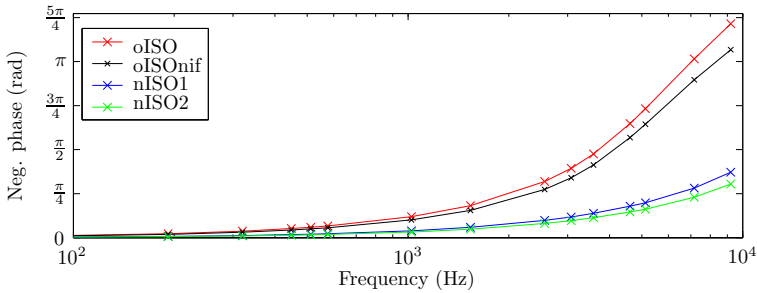


**Figure D.13:** The phase of the isolation amplifier transfer functions for the different filter configurations.

input and output filters. Component numbers refer to the schematics included in Appendix E

Figure D.13 shows the phase response of the different configurations of filters in the isolation amplifier. The data were collected with the GDP 32<sup>II</sup> in system check mode, using an internal calibration.

It is observed that the original isolation amplifier (designated oISO) and the isolation amplifier with the input filter removed (designated oISONif) cause very large negative phases, and that removal of the filter on the input side somewhat decreases the phase response. The isolation amplifiers with the cutoff frequency of the output filter pushed towards higher frequencies (designated nISO1 and nISO2) show large reductions in the phase response, but responses of more than  $\pi/4$  radians still remain. The fact that the response changes only slightly between nISO1 and nISO2 suggests that most of the remaining phase response originates from the AD210 unit itself.

**Table D.1:** Properties of the low pass filters for different configurations of the isolation amplifier.

ISOamp	LPF <sub>in</sub>	LPF <sub>out</sub>	LPF <sub>out</sub> components			
	f <sub>c</sub>	f <sub>c</sub>	R1	R2	C9	C10
oISO	1.5kHz	10kHz	4.3kΩ	18kΩ	3.3nF	1nF
oISONif	n/i	10kHz	4.3kΩ	18kΩ	3.3nF	1nF
nISO1	n/i	56kHz	10kΩ	10kΩ	0.4nF	0.2nF
nISO2	n/i	450kHz	10kΩ	10kΩ	47pF	27pF

LPF: Low-pass Filter. f<sub>c</sub>: Cutoff freq. (-3dB) n/i: Not installed.

### Alternative current reference: The Hall device

Since the tests at Zonge's suggested a dependency of the isolation amplifiers response on the shunt resistance, it is desirable to have a current reference method independent of the shunt resistance as an alternative to the isolation amplifier. A Hall device of the type LA-25NP was applied for this purpose. The operational principle of the Hall device is that a current carrying cable generates a magnetic field proportional to the current. This magnetic field in turn induces a current in a coil in the Hall device; the current is passed through a metal film resistor to generate a potential difference, which is measurable by the GDP 32<sup>II</sup>. In the configuration applied, the secondary current induced in the Hall device equals 1/1000 of the primary current, and a 241.7  $\Omega$  metal film resistor was used to generate the voltage difference.

### Test of current reference methods

Two tests were designed to identify the differences in responses of the reference methods. For the first test, the R-test, a load was constructed from a 2  $\Omega$  and a 1  $\Omega$  resistance in series. For the second test, the RC-test, a total capacitance of 40  $\mu\text{F}$  was connected in parallel with the 2  $\Omega$  resistor. The transmitter was an NT20 transmitter from Zonge running in ZeroTEM mode, and transmitting a 100% duty-cycle square waveform at 1.10 A. The GDP 32<sup>II</sup> was operated with three channels in use. One channel was measuring the potential difference across the load, the second measuring the Hall device current reference and the last channel the current reference output of the transmitter. Measurements were collected using the three filter combinations oISO, oISONif and nISO2 in the isolation amplifier. Finally, measurements were done directly on the shunt resistor, without isolation.

The ideal response would be a resistance of 3  $\Omega$  and a phase of 0 mrad over the entire frequency band for the R-test. For the RC-test, the ideal response is given by the impedance function:

$$Z = \left( \frac{1}{R_1} + i\omega C \right)^{-1} + R_2 \quad (\text{D.15})$$

where  $R_1 = 2 \Omega$ ,  $R_2 = 1 \Omega$  and  $C = 40 \mu\text{F}$ .

The NT20 transmitter has an option of using either a 0.1  $\Omega$  or a 1  $\Omega$  low-inductance wire-wound resistor for current reference (similar to the GGT3 field transmitter), and measurements were made for both resistors.

### Results of the tests

Data from the two tests are only presented from 1 kHz to 10 kHz, because responses and differences in responses from the isolation amplifier are small at lower frequencies, and asymptote to 0 mrad for very low frequencies. This is an important result by itself.

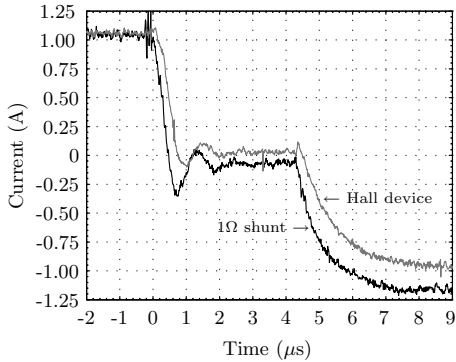


**Figure D.14:** The waveform of the NT20 transmitter when connected across a  $3\ \Omega$  load. The black line represents the current waveform as measured by an oscilloscope connected across the  $1\ \Omega$  shunt resistor in the NT20, whereas the grey line is the waveform calculated from the Hall device output.

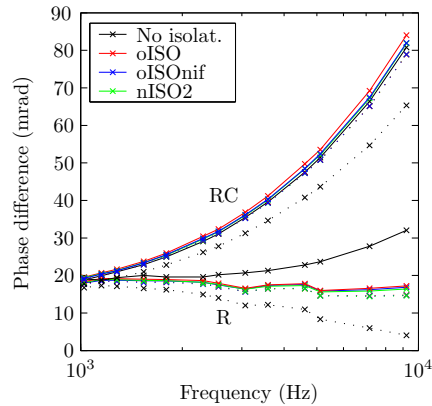


**Figure D.15:** Impedances calculated based on the Hall device current reference and subtracted from the model response. The data sets relate to different filter settings and shunt resistances: solid lines for  $0.1\ \Omega$  and dots for  $1\ \Omega$ .

Figure D.15 shows the impedances calculated using the Hall device current reference. The data are presented as measured phase data subtracted from the model data. The phases are seen to be as high as 20 mrad at 1 kHz, and either remain fairly constant (R-test) or continually increase (RC-test) towards the highest frequency. Figure D.14 shows a part of the 1 Hz current waveform transmitted with the NT20, as the waveform changes polarity. It shows the signal across the  $1\ \Omega$  shunt resistor and the output of the Hall device, while transmitting through the  $3\ \Omega$  resistive load. The waveform is not an ideal 100% duty cycle square wave, but has a segment which is close to zero for approximately  $3\ \mu\text{s}$ . The Hall device response is seen to lag behind the signal measured across the shunt.

The differences between the phase responses of the two tests are attributed to changes in the current waveform due to the change in impedance of the load and to inadequate ability of the Hall device to follow the waveform. The resistance of the shunt resistor has only little effect on the responses in Figure D.15, except when channel 2 is connected to the shunt without isolation. This indicates that common-mode problems could also play an important role.

Figure D.16 shows the phase deviation of the calculated impedances when the isolation amplifier response is used as current reference. It is evident that differences exist between the use of  $0.1\ \Omega$  and  $1\ \Omega$  shunt resistance. Differences are most evident in the RC-test, where also the direct measurements show large differences. The measurements using the nISO2 filter configuration corresponds best with the direct measurements, except for the  $1\ \Omega$  case in the R-test.

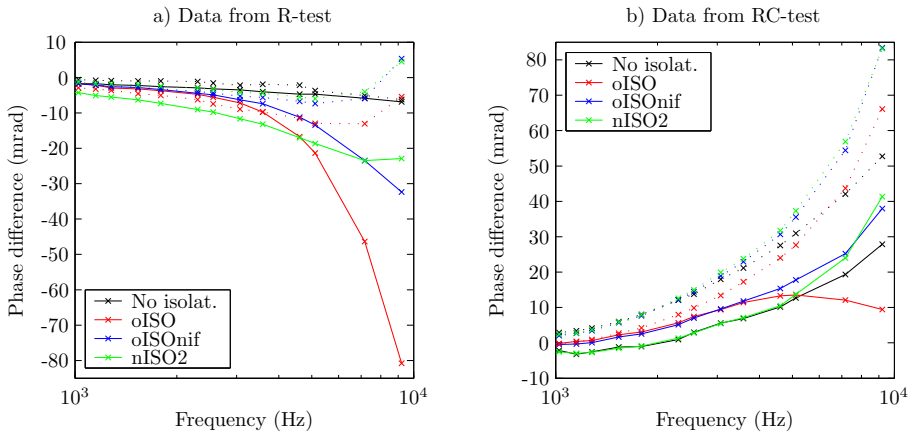


**Figure D.16:** The phase of the impedances from the shunt based current reference (with and without isolation amplifier) subtracted from the model response. Solid lines represent measurements using the  $0.1 \Omega$  shunt, dots the  $1 \Omega$  shunt.

The most important result is that the responses of all filter configurations seem to be good and well calibrated (within 5 mrad) up to 1 kHz. The test has shown that for frequencies higher than 1 kHz, the applied calibration procedure does not ensure measurement of the correct responses. The calibration procedure does not take into account the differences that seem to occur due to changing the shunt resistor. Furthermore, the effect of the low pass filtering in the isolation amplifier is not completely calibrated out with the current procedure. Of the filter combinations tested, the nISO2 filter seems to give the better results in most cases.

#### D.4.4.2 Communication wire

The signal cable used to connect the GDP 32<sup>II</sup> to the transmitter is a 610 m twisted pair cable. For dipole sizes of 40 m, no more than approximately 150 m cable is needed to connect the receiver and transmitter in normal field operation. The rest of the cable is usually kept rolled on a cable reel for convenience.

The cable has been tested for effects relating to the cable construction as well as effects related to having the cable rolled up. The measurements were carried out as an external systems check with an internal calibration. The calibration output was passed to the isolation amplifier and from there through the signal cable back to the receiver. A second channel measured the calibration signal directly and was used as reference. The test was repeated with different lengths of cable rolled out. The response of the isolation amplifier with no signal cable connected has been subtracted from the data, and the resulting phases are presented

in Table D.2.

Large phase responses are observed as a result of using the twisted pair signal cable. As the signal cable is included in the normal external calibration procedure, the main interest is in the difference between having the cable rolled up or rolled out. The last row of the table lists the phase differences observed between the two extremes. It is seen to result in differences of up to 44 mrad at the highest frequency. When 150 m of the cable is rolled out, the difference amounts to 11 mrad.

A field test was conducted to elucidate the possible effects of having the communication wire wound like a coil and placed in the field of the transmitting dipole. A dipole-dipole configuration of a-spacing 30 m and N-spacing 2 was used. Measurements were conducted with approximately 400 m of the communication wire wound on the reel, and 90 m laid out to connect transmitter and receiver. The observed data suffered from the effect described above, originating from calibration with all the wire wound on the reel. Changing the orientation of the reel from being parallel to the dipole-dipole axis to being perpendicular to it, resulted in small phase changes of up to 4 mrad at the highest frequencies.

Although insignificant in this configuration, the effect may increase to significant levels when smaller N-spacings and shorter dipoles are used. In these cases more of the communication wire will be wound on the reel, and the field will be stronger, as the distance from the transmitting dipole is shorter.

#### D.4.5 Discussion of error sources

A number of possible causes have been studied in order to explain the anomalous field-data collected in Greenland. The observed effects cannot be attributed to a single error source, but rather to a combination of sources. The most significant problems seem to relate to the reference signal and possibly capacitive coupling.

Although the normal external calibration procedure is expected to remove

**Table D.2:** Phase responses observed due to the twisted pair communication wire. The row labels are the lengths of wire unrolled from the cable reel, i.e. 0 m corresponds to all the wire being on the reel, 610 m to the wire totally rolled out. All values in mrad.

	64 Hz	1024 Hz	2560 Hz	3584 Hz	5120 Hz	9216 Hz
0 m	-2.3	-34.9	-86.5	-121.3	-176.7	-339.2
50 m	-2.3	-34.6	-85.8	-120.3	-175.4	-336.8
100 m	-2.3	-34.3	-84.9	-119.0	-173.3	-332.0
150 m	-2.3	-33.8	-83.7	-117.3	-171.0	-328.3
200 m	-2.3	-33.5	-83.1	-116.5	-169.7	-325.5
610 m	-2.1	-30.6	-75.4	-105.5	-153.8	-295.3
$\Delta_{\max}$	0.2	4.3	11.1	15.8	22.9	43.9

any effects introduced in the reference channel, the presented results show that this is not the case at high frequencies. A residual response from the isolation amplifier is present and depends on the resistance of the shunt resistor in use.

An alternative current reference method, based on a Hall device was tested. The device does not follow the current waveform well enough. This could be related to the fact that the waveform supplied by the NT20 transmitter is not a perfect square wave.

The transmitter used for the test measurements is different from the one used for field measurements. Due to voltage and common mode considerations, it was not possible to perform the tests using the field transmitter, and thus the effects in actual field data have not been assessed. Since the waveform of the actually transmitted current seems to be one of the parameters influencing the data, it is possible that the isolation amplifier and Hall device responses behave slightly different when applied in the field setup.

In order to obtain better reference signals, it is suggested that a Hall device of the type LTS-15NP from LEM Components be tested. According to the specifications, it should have a delay time better than 50 ns, corresponding to less than 3 mrad at 9216 Hz.

Also, the signal cable used to supply the current reference signal to the receiver has been proven to have a residual response. As the calibration is usually done with the signal cable rolled on the cable reel, the size of the residual response is related how much of the cable is rolled out during the field measurements. Reducing the length of the reference cable to an absolute minimum should minimize this effect.

Capacitive coupling between the receiver wire and the ground may have a significant influence on the measurements when the contact resistance is high. This may occur due to bad placement of the electrodes, or when electrodes have to be placed in very dry materials. Using the derived approximate relation for the phase error and expected worst case parameters for the measurements collected in relation to this project, maximum phase effects may amount to 75 mrad.

The development of the capacitive coupling model is purely theoretical. An evaluation of the actual effect on field data would be of great interest. Assuming that other error sources have been eliminated, such data could be collected by inserting resistors between the electrodes and the receiver wire, as described by Zonge & Hughes (1985).

In order to minimize the effects on field measurements using the currently available equipment the following list of precautions are suggested in order of increasing importance:

1. The operator should ensure low contact resistance by careful placement of the pot-electrodes and possibly by using several pots in parallel at each location. Contact resistance should be checked regularly, as it may change during the course of a day.

2. The nISO2 filter configuration should be used in the isolation amplifier.
3. The signal cable used to connect the receiver to the isolation amplifier, should be cut to lengths as short as possible.

Furthermore, it is suggested that the operator makes an internal calibration previous to an external calibration, and dumps both calibrates to a computer. In case of problems, the internal calibration can be applied to the data, which may help in locating the cause.

Even when these precautions are followed, effects may still be present in the high-frequency part of the data. In order to further reduce these effects, the following initiatives are suggested:

1. Development of a different current reference method, possibly based on a Hall device with better response characteristics.
2. Development of an optical cable solution for supplying current reference information to the receiver.
3. The use of shielded cables for the receiver dipole should be tested, in order to reduce capacitive coupling.

## D.5 Field test

A field test of the system has been conducted at a site in Mårum, in the northern part of Zealand, Denmark. In the choice of test location, a thick, homogenous sequence of clays was preferred. First of all, a relatively homogeneous subsurface would greatly facilitate interpretation of the test data. Secondly, the relatively low resistivity of clays ensures an EM coupling response even at moderate dipole-lengths. Last but not least, massive clay deposits are known to show only small IP and CR responses (Marshall & Madden, 1959; Anderson & Keller, 1964), and thus the discussion of how to include the CR response in the EM model, would be of little importance in relation to the collected data. The site at Mårum was chosen based on the geological basis-data maps from the Geological Survey of Denmark and Greenland (Søndergaard, 1979), showing a sequence of clays of more than 100 m in thickness. It is located in a forrest in an area with level topography. Thus topographic effects as well as anthropogenic noise sources should be minimal.

### D.5.1 Equipment and setups applied

A 400 m 2D profile of resistivity data were collected at the site using the ABEM SAS4000 terrameter in conjunction with the LUND Imaging system. The Wenner electrode configuration was applied with a minimum electrode spacing of 5 m. This MEP profile was collected in order to get a general impression of the subsurface resistivity distribution.

Complex resistivity measurements were performed using a simplified setup. The configuration applied was the dipole-dipole configuration, with a dipole size of 30 m. Only one transmitting dipole was used, and thus the switching circuitry and additional cables could be avoided. The transmitter was positioned at the center between the two transmitting electrodes.

Three receiver dipoles were applied, with N-spacings of 1, 2 and 3 (designated dipole R1, R2 and R3, respectively). For the basic testing, only one dipole was connected to the receiver at a time, with the receiver placed at the center of the dipole. In this configuration, all transmitter and receiver electrodes and wiring are in a co-linear orientation. Along with the ground potential, current reference was collected using both Hall device and isolation amplifier in the nISO2 configuration. For the R3 dipole, measurements were collected using only the Hall device for current reference. The signal cables used to connect the receiver with the reference devices were the original signal cables cut in lengths to fit the transmitter-receiver separation distance. Data were collected at six fundamental frequencies in the range from 0.125 Hz to 1024 Hz. Three repetitions (stacks) were collected for each fundamental frequency in order to estimate the accuracy of the measurements.

A second test was performed in order to evaluate the effect of using several receiver dipoles. All three dipoles were connected simultaneously to the receiver, which was positioned first at the center of dipole R1 and thereafter at the center of dipole R2. The electrodes were connected in the usual manner, refer to the receiver part of Figure D.1.

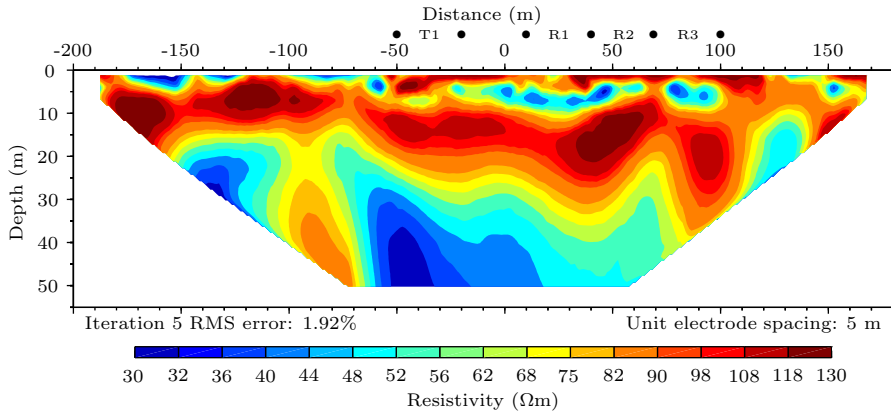
## D.5.2 Results and discussion

Figure D.17 shows the resistivity profile inverted using the Res2Dinv inversion package (Loke, 2000). Although resistivities are generally low, considerable variation in resistivities are also observed. Instead of the homogeneous environment expected, this area is better described by a high/low or high/low/high/low type resistivity environment. Especially an area of higher resistivity should be noticed, located at 50m directly below the R2 dipole location, at a depth of approximately 10 to 25 m below ground level.

The responses measured in the single dipole tests are given in Figure D.18. All the collected data are seen to be within normal ranges, and appear to be well behaved. Standard deviations between the three stacks have been calculated for every frequency, according to the definition

$$std = \sqrt{\frac{1}{n} \sum_{i=1}^n (x_i - \bar{x})^2} \quad , \quad \bar{x} = \frac{1}{n} \sum_{i=1}^n x_i \quad (D.16)$$

With few exceptions, the calculated standard deviations were less than 1 mrad for the phase and less than 0.1  $\Omega\text{m}$  for the apparent resistivity at all frequencies. Higher standard deviations occur occasionally, especially for the harmonics of the



**Figure D.17:** MEP resistivity profile collected at Måarum. The vertical exaggeration is 2:1. Electrode locations of the CR measurements are indicated above the  $x$ -axis ( $\bullet$ ), as well as the dipole designations for the transmitter (T1) and receiver dipoles (R1, R2 and R3).

highest fundamental frequencies (a maximum standard deviation of 9 mrad was observed).

In the phase spectra, the high-frequency phase peak moves towards lower frequencies with increasing N-spacing, as expected for a dipole-dipole configuration on a layered half-space. Nevertheless, there are indications that the data are affected by inhomogeneities in the subsurface. The low frequency apparent resistivity of the R2 measurement is somewhat higher than the others, and indicate that measurements made with this dipole are especially affected by the area of higher resistivity observed in the MEP profile.

Despite the observed non-1D effects, an attempt has been made at an interpretation using 1D modeling. Models of increasing complexity were calculated and manually fitted to the field data using the CR1Dmod forward modeling software (Paper C). The properties of the final models are given in Table D.3, and the model responses are included in Figure D.18. At frequencies less than 10 Hz, the impedances calculated based on the isolation amplifier and Hall device current references give identical results, and the models all fit the data well. The figure therefore shows only frequencies above 10 Hz. At frequencies between 10 Hz and 2 kHz, the nISO2 data give slightly higher phases, whereas the Hall device results in higher phases above 2 kHz. The nISO2 data give abnormal responses for the highest frequencies (most apparent in the R2 data).

The model fitting was manual and trial and error based, and was started with a 2 layer model of the high/low type. Small phase responses at low frequencies indicated that CR effects were present, and these were always attributed to the high resistivity layer. For the R3 case, Figure D.18 shows two models, a two layer model (blue) and a three layer model (red). The three layer model fits the phase peak better at the cost of a poorer fit of the up-slope. In general, the calculated models lie above the Hall device data at lower frequencies. This fits

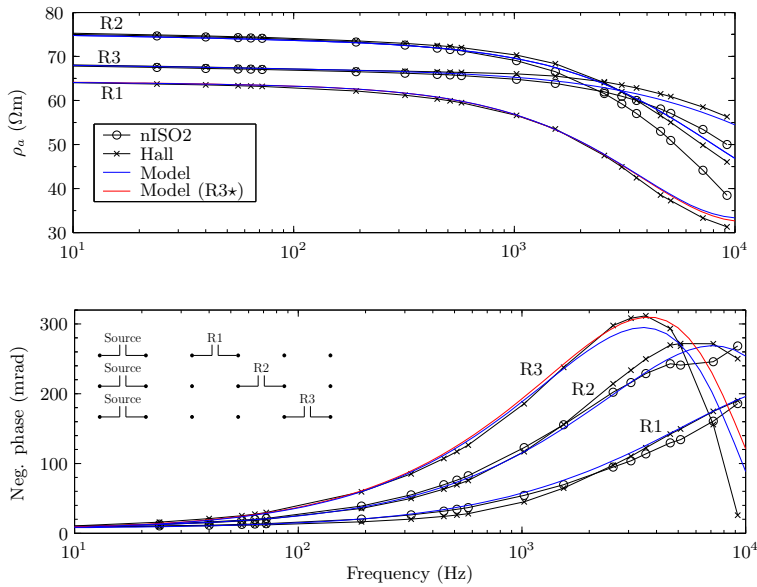
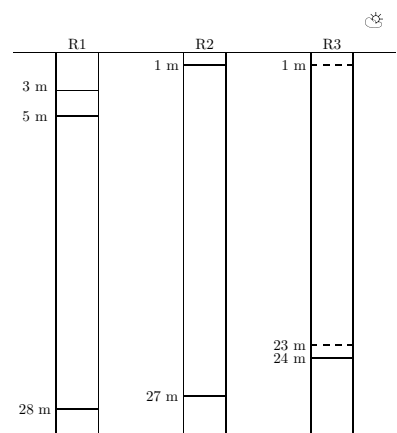


**Figure D.18:** Responses measured using only one receiver dipole at a time. Blue and red lines are the responses of 1D models manually fitted to the collected data.

**Table D.3:** Layer parameters obtained by manually fitting models to the three data sets collected at Mårum.

	$h$	$\rho_0$	$m$	$\tau$	$c$
<b>R1</b>					
L 1	3 m	1 kΩm			
L 2	2 m	46 Ωm			
L 3	23 m	76 Ωm	0.1	0.001	0.22
L 4		30 Ωm			
<b>R2</b>					
L 1	1 m	1 kΩm			
L 2	26 m	93 Ωm	0.12	0.001	0.3
L 3		55 Ωm			
<b>R3a</b>					
L 1	24 m	90 Ωm	0.12	0.01	0.3
L 2		55 Ωm			
<b>R3*</b>					
L 1	1 m	65 Ωm			
L 2	22 m	89 Ωm	0.12	0.01	0.3
L 3		55 Ωm			



the observations from the laboratory tests.

As the N-spacings become smaller, more complex models are needed in order to get a decent fit with the data. The R1 measurements are very sensitive to the shallow layering, and all four layers observed in the MEP profile were needed in order to fit the data. The R2 and R3 measurements can be fitted fairly well with three layer models. The higher resistivity of layer two in R2 and R3, is believed to be the manifestation of the high-resistive area observed on the MEP profile. The highly resistive top layer was needed in order to fit the high-frequency part of the response.

None of the models fit the data perfectly over the entire frequency spectrum. Especially the very high frequency data have been difficult to fit. It is likely, that an automated inversion algorithm would be able to fit the data better, but none is available at present. Nevertheless, it seems evident that some problems with data quality at the highest frequencies still remain. This is in agreement with the laboratory tests, that showed deviations from the expected results at very high frequencies.

The fact that the measurements can be reasonably fitted by hand, by models that make physical sense for the environment in which the data were obtained, shows that the equipment should be capable of making good measurements over a wide range of frequencies. With some more work relating to the current reference methods, good data should be obtainable over the entire frequency range.

Data from the test of multiple receiver dipoles are shown in Figure D.19. Magnitude effects were limited to a few  $\Omega\text{m}$ , and therefore only the phase data are presented. Solid lines represent phase changes observed when connecting multiple dipoles simultaneously, compared to the response observed with only one dipole connected. The data are presented as the response measured in situations R1a and R1B subtracted from the responses of R1 and R2, respectively, and show that the measured negative phase response of a specific channel is reduced (it becomes less negative) when more channels are connected. A larger effect is observed for R2 than for R1. The channel measuring R2 is connected to the channel measuring R1 on one terminal and the channel measuring R3 on the other terminal (refer to Figure D.1). The channel measuring R1 is only connected to another channel on one terminal. This is believed to be the cause of the difference in response change. Since no other parameters relating to the layout for the channel in question are changed, the observed differences must relate solely to the fact that more channels are connected.

The effect of having the receiver offset away from the center of the measured dipole is shown with dotted lines in Figure D.19. For the R1b measurement, the receiver was located at the center of the R2 dipole, and vice versa for R2a. The R3b and R3a situations have the receiver offset by one and two dipole spacings. For these data sets the wire layout for the individual channels are changed depending on the situation, and thus both capacitive and EM coupling come into play. Furthermore, the data were collected for several dipoles simultaneously, so

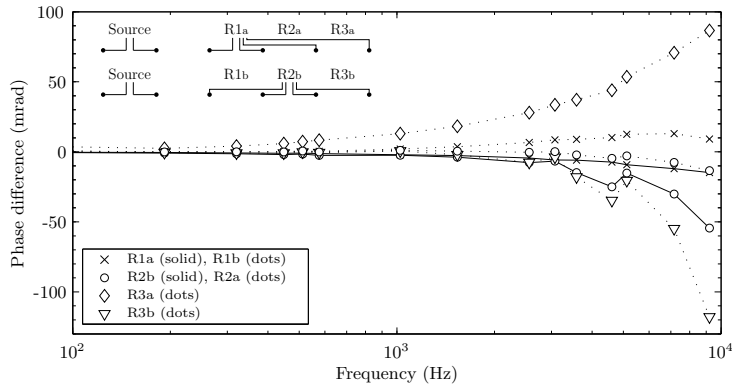


**Figure D.19:** Phase differences between responses when only one channel is connected and the response when multiple channels are connected simultaneously. Data for the receiver at the center of the same dipole (solid) and offset one or two dipole lengths (dots) are presented.

the multi-channel effect is included in the observed differences as well.

The data sets exhibit much larger phase effects than what was predicted from the layout modeling. In the modeling, the extra cable length connecting the offset receiver to the dipoles was neglected. The presented data suggests that this simplified representation is not adequate. Additional capacitive coupling due to the extra cable lengths should also be considered. However, since the contact resistance was observed to be less than 600  $\Omega$ , this effect is likely to be of minor importance.

## D.6 Conclusions

After identification of problems relating to the high-frequency part of collected CR data, a theoretical and practical study of possible error sources was conducted.

The effects of offsetting the electrodes and cables from the ideal collinear locations were modelled and proved to be of minor importance. The effect of not having the receiver located at the center of the dipole, and thus the need for additional cabling, was neglected. A subsequent field test has shown that the neglected part of the setup may result in appreciative errors, and that receiver offset should be kept at a minimum.

A model of ECR effect for receiver dipoles in CSAMT surveys (Zonge & Hughes, 1985) was extended to cover the collinear dipole-dipole configuration used in CR surveys. The ECR and capacitive coupling effect was shown to be significant. An approximate relation of the the decrease in the negative phase angles to the product of the dipole size ( $a$ , [km]), the frequency ( $f$ , [kHz]) and the contact resistance ( $R_c$ , [k $\Omega$ ]) was developed and is given by

$$\Delta\phi \approx K \cdot a \cdot f \cdot R_c \quad (\text{D.10})$$

where  $K$  is the proportionality constant, which takes the values 38.6, 36.3 and 35.9 for N-spacings 1, 3 and 5. Applying these relations it was found that the capacitive coupling effects in measurements obtained in Greenland in relation to this study, may result in phase reductions of up to 75 mrad.

A simple model for the capacitive coupling between the transmitter dipole and the ground was developed based on a transmission line model. The model predicts phase effects that are opposite in sign than those arising from the receiver dipole model. The model however needs improvement to be of any practical use.

Equipment related issues were addressed as well. The isolation amplifier used to galvanically isolate the current reference signal, and the signal cable passing the reference signal to the receiver, proved to have residual responses that were not effectively calibrated out at high frequencies. In order to reduce these effects, changes were made to the design of the lowpass filters in the isolation amplifier, and the signal cable was reduced to the minimum length required.

A subsequent field test showed that measurements collected with the modified instrumentation applied in the nominal collinear dipole-dipole configuration resulted in data that could be fitted reasonably well by geologically sensible 1D models. The test also showed that the application of multiple channels to measuring an extended number of receiver dipoles simultaneously (as is the normal practice), resulted responses different from those obtained when the dipoles were measured independently. These changes were related to EM and capacitive coupling effects of the extra cabling from the distant dipoles to the receiver, but also simply to connecting the extra channels.

It is suggested, that additional work is put into developing a better current reference technique, to further improve the data quality. This new system should be tested in a homogeneous half-space environment with limited CR effects in order to determine its accuracy. It would also be of great interest to prove the validity of the receiver dipole capacitive coupling model through field tests.

APPENDIX E

# Schematics of the isolation amplifier

---



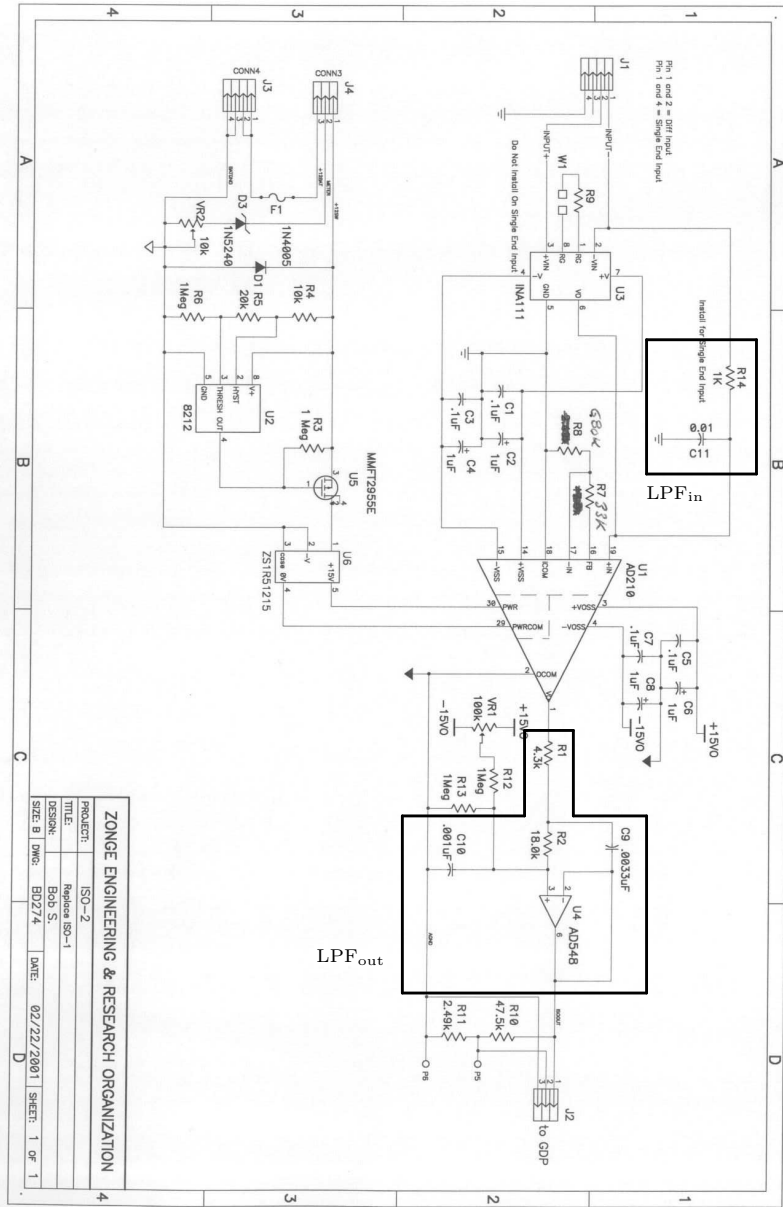


**Figure E.1:** Schematics of the isolation amplifier.  $LPF_{in}$  is the low pass filter on the input side,  $LPF_{out}$  is the low pass filter on the output side.



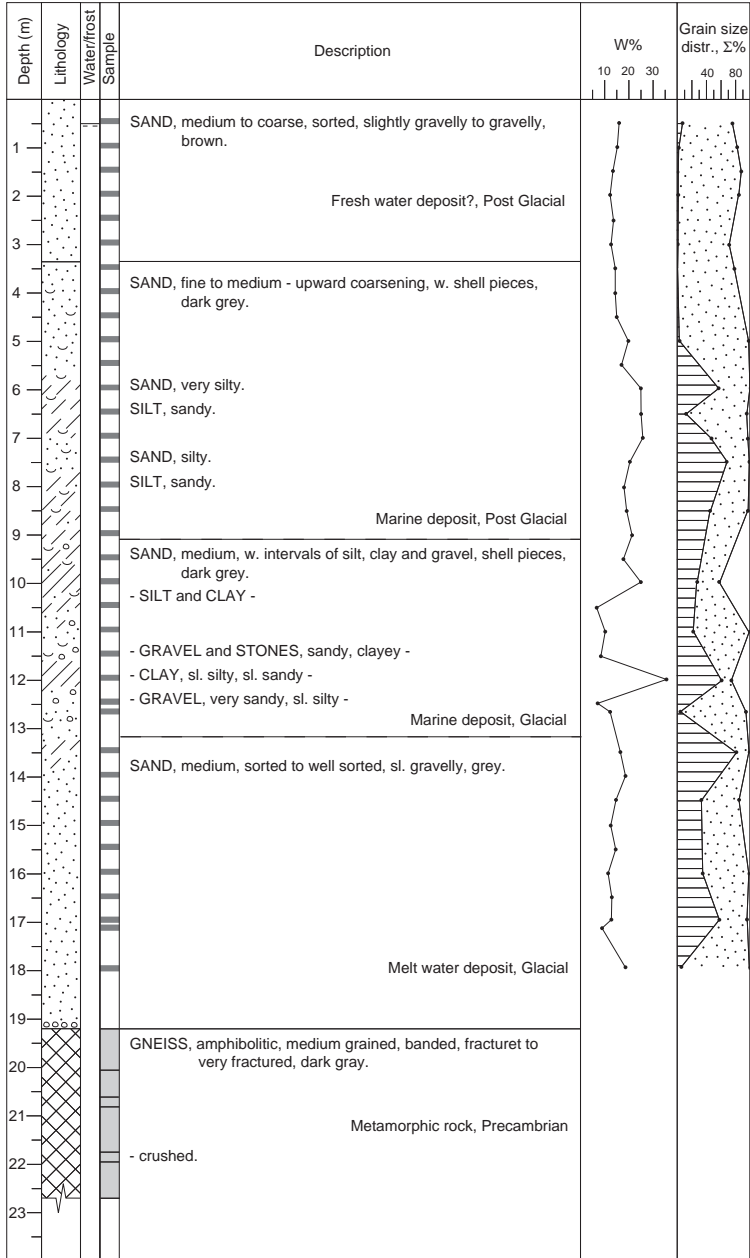
## Borehole logs

This appendix contains lithological logs, water content and grain-size information for the four boreholes conducted in August 2003. The graphed water content is the geotechnical water content, defined as the weight percentage of water to soil matrix, and may thus be greater than 100%, especially when samples have a large ice content. The logs have been compiled and kindly supplied by Clausen (2005).

SOIL SIGNS		GRAIN SIZE	
	Cobbles and Gravel		Gravel (> 2 mm)
	Sand		Sand (0,75 - 2 mm)
	Silt		< 0,75 mm
	Clay		
	Rock		
	Shells		
	Organic soils		
	Sample		
	Core		
	Frost table		
	Water table		

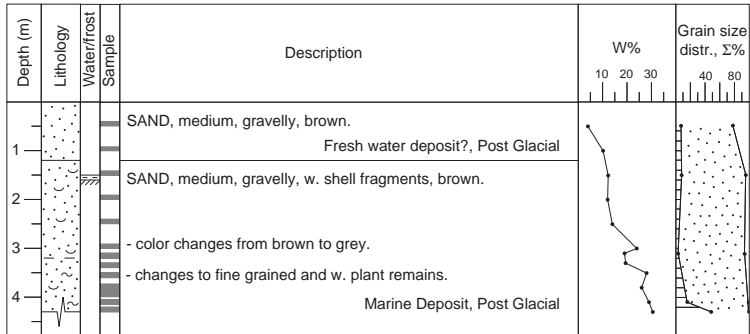
Legend for borehole logs.

### F.1 Borehole 2003-4



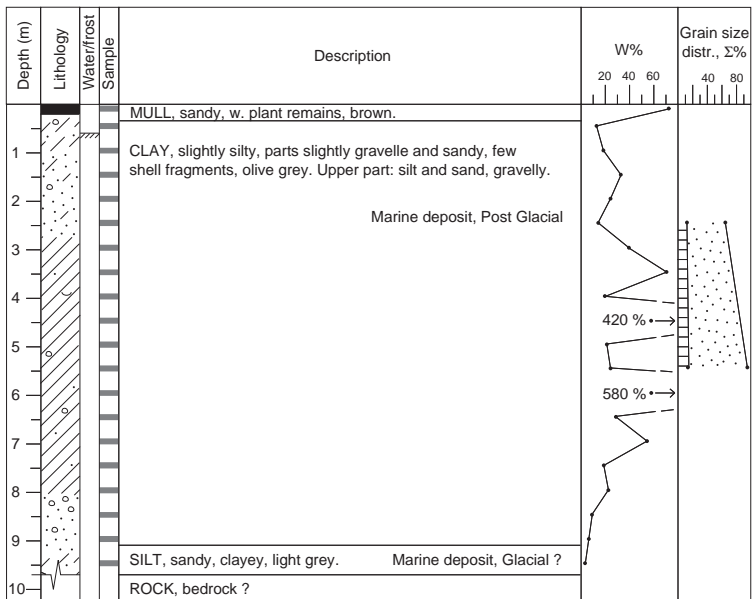
Borehole log supplied by Clausen (2005, priv. comm.).

## F.2 Borehole 2003-5



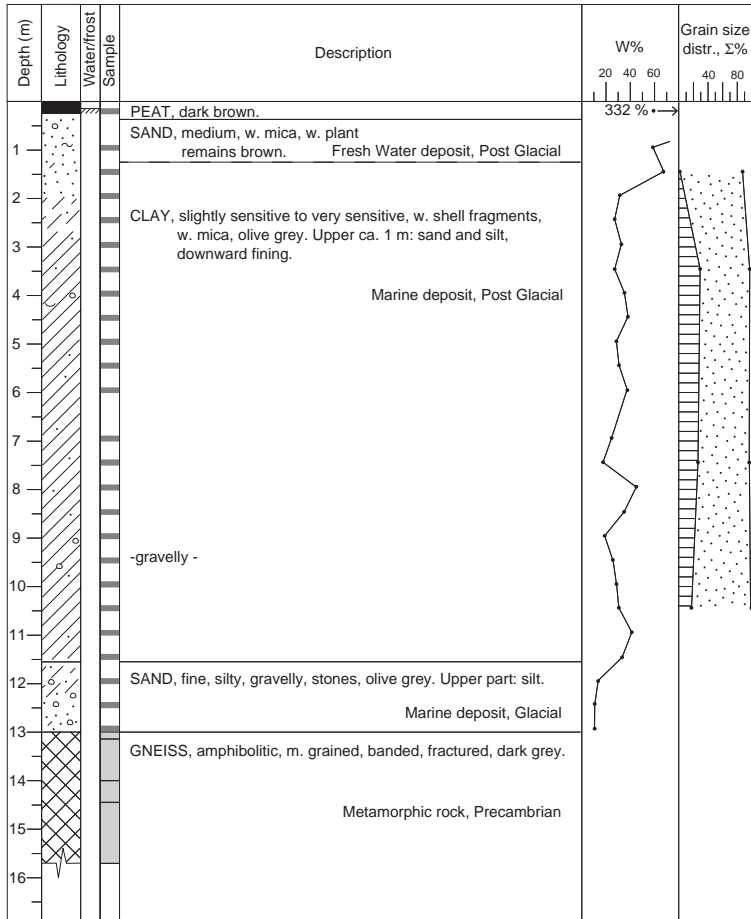
Borehole log supplied by Clausen (2005, priv. comm.).

## F.3 Borehole 2003-6



Borehole log supplied by Clausen (2005, priv. comm.).

### F.4 Borehole 2003-7



Borehole log supplied by Clausen (2005, priv. comm.).

# Bibliography

---

- ABEM (1999). *Instruction Manual — Terrameter SAS 4000 / SAS 1000*. ABEM Instruments AB.
- Andersen, M. L., Jacobsen, J. R. G., Jensen, C. B., & Olufsen, K. A. (2001). Kortlægning af permafrost med georadar og MEP. The Arctic Technology Centre, BYG•DTU, Technical University of Denmark. Unpublished student report.
- Anderson, D. M. & Morgenstern, N. R. (1973). Physics, chemistry, and mechanics of frozen ground: a review. In *North American Contribution, Second International Conference on Permafrost, Yakutsk, USSR* (pp. 257–288). Washington DC: National Academy of Sciences.
- Anderson, D. M., Tice, A. R., & McKim, H. L. (1973). The unfrozen water and apparent specific heat capacity of frozen soils. In *North American Contribution, Second International Conference on Permafrost, Yakutsk, USSR* (pp. 289–295). Washington DC: National Academy of Sciences.
- Anderson, L. A. & Keller, G. V. (1964). A study in induced polarization. *Geophysics*, 29(5), 848–864.
- Anderson, W. (1974). *Electromagnetic Fields About a Finite Electric Wire Source*. USGS-GD 74-041, U.S. Geological Survey.
- Anderson, W. L. (1979). Computer program: Numerical integration of related Hankel transforms of orders 0 and 1 by adaptive digital filtering. *Geophysics*, 44(7), 1287–1305.
- Anderson, W. L. (1981). *Calculation of Transient Soundings for a Central Induction Loop System (Program TCILoop)*. Open-File Report 81-1309, U.S. Geological Survey.
- Angoran, Y. & Madden, T. R. (1977). Induced polarization: A preliminary study of its chemical basis. *Geophysics*, 42(4), 788–803.
- Annan, A. P. & Davis, J. L. (1976). Impulse radar sounding in permafrost. *Radio Science*, 2(4), 383–394.
- Arcone, S. A., Brockett, B. E., Lawson, D. E., & Chacho, E. F. (1987). *Evaluation of the Magnetic Induction Conductivity Method for Detecting Frazil Ice Deposits*. Report 87-17, U.S. Army CRREL.
- Auken, E., Breiner, M., Nebel, L., Pellerin, L., Thomsen, P., & Sørensen, K. I. (2001). EMMA - electromagnetic modelling and analysis. In *EEGS Birmingham Proceedings* (pp. 114–115). Birmingham, U.K.: EEGS.

- Baumgartner, F. (2003). The Arctic Technology Centre, BYG•DTU, Technical University of Denmark. Private communication.
- Beamish, D. (2002). An assessment of inversion methods for AEM data applied to environmental studies. *Journal of Applied Geophysics*, 51, 75–96.
- Beard, L. P. (2000). Comparison of methods for estimating earth resistivity from airborne electromagnetic measurements. *Journal of Applied Geophysics*, 45, 239–259.
- Bertin, J. & Loeb, J. (1976). *Experimental and Theoretical Aspects of Induced Polarization*, volume 1. Gebruder Bomtraege.
- Börner, F., Gruhne, M., & Schön, J. (1993). Contamination indications derived from electrical properties in the low frequency range. *Geophysical Prospecting*, 41(1), 83–98.
- Brown, R. J. (1984). Corrections to Millett's table of electromagnetic coupling phase angles. *Geophysics*, 49(9), 1554–1555.
- Brown, R. J. (1985). EM coupling in multifrequency IP and a generalization of the Cole-Cole impedance model. *Geophysical Prospecting*, 33(2), 282–302.
- Chave, A. D. (1983). Numerical integration of related hankel transforms by quadrature and continued fractions expansions. *Geophysics*, 48(12), 1671–1686.
- Cheng, D. K. (1989). *Field and Wave Electromagnetics*. Reading, Massachusetts: Addison-Wesley Publishing Company.
- Chew, W. C. & Sen, P. N. (1982). Dielectric enhancement due to electrochemical double layer: Thin double layer approximation. *Journal of Chemical Physics*, 77(9), 4683–4692.
- Christensen, N. B. (1990). Optimized Fast Hankel Transform filters. *Geophysical Prospecting*, 38(5), 545–568.
- Christensen, N. B. & Auken, E. (1992). SELMA - Simultaneous electromagnetic layered modelling and analysis. In B. H. Jackobsen (Ed.), *Proceedings of Interdisciplinary Inversion Workshop 1 Aarhus 1992, Methodology and Applications within Geophysics, Astronomy, and Geodesy*, volume 41 of *Geoskrifter* (pp. 49–56). Aarhus University.
- Christensen, T. R., Johansson, T., Akerman, H. J., Mastepanov, M., Malmer, N., Friberg, T., Crill, P., & Svensson, B. H. (2004). Thawing sub-arctic permafrost: Effects on vegetation and methane emissions. *Geophysical Research Letters*, 31(4), L04501. doi:10.1029/2003GL018680.
- Christiansen, H. H. & Humlum, O. (2000). Permafrost. In B. H. Jakobsen, J. Böcher, N. Nielsen, R. Guttesen, O. Humlum, & E. Jensen (Eds.), *Topografisk Atlas Grønland* (pp. 32–35). Det Kongelige Danske Geografiske Selskab og Kort & Matrikelstyrelsen.
- Clausen, H. (2005). The Arctic Technology Centre, BYG•DTU, Technical University of Denmark. Private communication.
- Coggon, J. H. (1984). New three-point formulas for inductive coupling removal in induced polarization. *Geophysics*, 49(3), 307–309. See erratum: *Geophysics* (1984) Vol. 49, p. 1395.

- 
- Cole, K. S. & Cole, R. H. (1941). Dispersion and absorption in dielectrics, I. Alternating current fields. *The Journal of Chemical Physics*, 9(4), 341–351.
- Collett, L. S. (1959). Laboratory investigation of overvoltage. In J. R. Wait (Ed.), *Overvoltage Research and Geophysical Applications* chapter 5, (pp. 50–70). London: Pergamon Press.
- Cummings, D. (1979). Determination of depths to an irregular interface in shallow seismic refraction surveys using a pocket calculator. *Geophysics*, 44(12), 1987–1988.
- Dahlin, T., Leroux, V., & Nissen, J. (2002). Measuring techniques in induced polarization imaging. *Journal of Applied Geophysics*, 50(3), 279–298.
- Daniels, J. J., Keller, G. V., & Jacobson, J. J. (1976). Computer-assisted interpretation of electromagnetic soundings over a permafrost section. *Geophysics*, 41(4), 752–765.
- Das, U. C. (1995). Apparent resistivity curves in controlled-source electromagnetic sounding directly reflecting true resistivities in a layered earth. *Geophysics*, 60, 53–60.
- Das, U. C. (1997). Multiseparation, multisystem electromagnetic depth sounding - an extension for unification. *Geophysics*, 62(1), 56–62.
- Delapierre, A. (2003). The Arctic Technology Centre, BYG•DTU, Technical University of Denmark. Private communication.
- Descloitres, M., Guérin, R., Albouy, Y., Tabbagh, A., & Ritz, M. (2000). Improvement in TDEM sounding interpretation in presence of induced polarization. A case study in resistive rocks of the Fogo volcano, Cape Verde Islands. *Journal of Applied Geophysics*, 45, 1–18.
- Dey, A. & Morrison, F. (1973). Electromagnetic coupling in frequency and time-domain induced-polarization surveys over a multilayered earth. *Geophysics*, 38(2), 380–405.
- Dey, A. & Ward, S. H. (1970). Inductive sounding of a layered earth with a horizontal magnetic dipole. *Geophysics*, 35(4), 660–703.
- Dias, C. A. (2000). Developments in a model to describe low-frequency electrical polarization of rocks. *Geophysics*, 65(2), 437–451.
- Dieter, K., Paterson, N. R., & Grant, F. S. (1969). IP and resistivity type curves for three-dimensional bodies. *Geophysics*, 34(4), 615–632.
- DMI (2005). Temperature data for Sisimiut, Greenland. Danish Meteorological Institute. <http://www.dmi.dk>.
- Escher, A., Sørensen, K., & Zeck, H. P. (1976). Nagsugtoquidian Mobile Belt in West Greenland. In A. Escher & W. S. Watt (Eds.), *Geology of Greenland* (pp. 76–95). Copenhagen: Denmark: The Geological Survey of Greenland.
- Farquharson, C. (2002). Department of Earth & Ocean Sciences, University of British Columbia. Private communication.
- Fitterman, D. V. & Yin, C. (2004). Effect of bird maneuver on frequency-domain helicopter EM response. *Geophysics*, 69(5), 1203–1215.
-

- Foged, N. (1979). *Engineering Geological Investigations of Quaternary Marine Clay Deposits in West Greenland*. PhD thesis, Technical University of Denmark. In Danish.
- Foged, N. & Clausen, H. (2003). Engineering geology and geotechnical engineering in West Greenland — Permafrost related features in Sisimiut. In *Proceedings of 14 Tagung für Ingenieurgeologie*.
- Frischknecht, F. C. (1967). Fields about an oscillating magnetic dipole over a two-layer earth, and application to ground and airborne electromagnetic surveys. *Quarterly of the Colorado School of Mines*, 62(1), 326.
- Frischknecht, F. C., Labson, V. F., Spies, B. R., & Anderson, W. L. (1991). Profiling methods using small sources. In M. N. Nabighian (Ed.), *Electromagnetic Methods in Applied Geophysics*, volume 2 chapter 3, (pp. 105–270). Society of Exploration Geophysicists.
- Fuller, B. D. & Ward, S. H. (1970). Linear system description of the electrical parameters of rocks. *IEEE Transactions on Geoscience Electronics*, GE-8(1), 7–18.
- Garnett, J. C. M. (1904). Colours in metal glasses and in metallic films. *Philosophical Transactions of the Royal Society of London. Series A*, 203, 385–420.
- Geonics (1979). *Operating Manual for EM16R VLF Resistivity Meter*. Geonics Limited.
- Gorham, E. (1991). Northern peatlands: Role in the carbon cycle and probable responses to climatic warming. *Ecological Applications*, 1(2), 182–195.
- Gosh, D. P. (1971). The application of linear filter theory to the direct interpretation of geoelectrical resistivity sounding measurements. *Geophysical Prospecting*, 19(2), 192–217.
- Grahame, D. C. (1947). The electrical double layer and the theory of electrocapillarity. *Chemical Reviews*, 41, 441–501.
- Hagedoorn, J. G. (1959). The plus-minus method of interpreting seismic refraction sections. *Geophysical Prospecting*, 7, 158–181.
- Hallof, P. G. (1974). The IP phase measurement and inductive coupling. *Geophysics*, 39(5), 650–665.
- Hallof, P. G. & Yamashita, M. (1990). The use of the IP method to locate gold-bearing sulfide mineralization. In J. B. Fink, E. O. McAlister, B. K. Sternberg, W. G. Wielduwilt, & S. H. Ward (Eds.), *Induced Polarization: Applications and Case Histories*, volume 4 of *Investigations in Geophysics* chapter 3, (pp. 227–279). Society of Exploration Geophysicists.
- Hoekstra, P. (1978). Electromagnetic methods for mapping shallow permafrost. *Geophysics*, 43(4), 782–787.
- Hoekstra, P. & Delaney, A. (1974). Dielectric properties of soils at UHF and microwave frequencies. *Journal of Geophysical Research* *Journal of Geophysical Research*, 79(11), 1699–1708.
- Hoekstra, P. & McNeill, D. (1973). Electromagnetic probing of permafrost. In *North American Contribution, Second International Conference on Permafrost, Yakutsk, USSR* (pp. 517–526). Washington DC: National Academy of Sciences.

- Hoekstra, P., Sellmann, P. V., & Delaney, A. (1975). Ground and airborne resistivity surveys of permafrost near Fairbanks, Alaska. *Geophysics*, 40(4), 641–656.
- Hohmann, G. W. (1973). Electromagnetic coupling between grounded wires at the surface of a two-layer earth. *Geophysics*, 38(5), 854–863.
- Hohmann, G. W. (1975). Three-dimensional induced polarization and electromagnetic modeling. *Geophysics*, 40(2), 309–324.
- Hohmann, G. W. (1990). Three dimensional IP models. In J. B. Fink, E. O. McAlister, B. K. Sternberg, W. G. Wielduwilt, & S. H. Ward (Eds.), *Induced Polarization: Applications and Case Histories*, volume 4 of *Investigations in Geophysics* chapter 3, (pp. 150–178). Society of Exploration Geophysicists.
- Hohmann, G. W., Kintzinger, P. R., Van Voorhis, G. D., & Ward, S. H. (1970). Evaluation of the measurement of induced electrical polarization with an inductive system. *Geophysics*, 35(5), 901–915.
- Huang, H. & Fraser, D. C. (2002). The use of quad-quad resistivity in helicopter electromagnetic mapping. *Geophysics*, 67(2), 459–467.
- Ingeman-Nielsen, T. (2001). Geophysical investigation for groundwater at Kangerluk. Master's thesis, The Arctic Technology Centre, BYG•DTU, Technical University of Denmark.
- Ingeman-Nielsen, T. & Szidarovszky, A. (2004). *High Frequency Labrocks Measurements*. Technical report, Zonge Engineering and Research Organization. Unpublished.
- Itoh, T., Ed. (1989). *Numerical Techniques for Microwave and Millimeter-Wave Passive Structures*. New York: Wiley.
- Jacobi, O. (2000). Koordtrans, a spread sheet for coordinate conversion between different systems used in Greenland. The Arctic Technology Centre, BYG•DTU, Technical University of Denmark.
- Johansen, H. K. & Sørensen, K. (1979). Fast Hankel Transforms. *Geophysical Prospecting*, 27, 876–901.
- Kane, D. L. & Chacho, E. F. (1990). Frozen ground effects on infiltration and runoff. In *Cold Regions Hydrology and Hydraulics* (pp. 259–300). American Society of Civil Engineers.
- Kauahikaua, J. & Anderson, W. L. (1979). *Programs EMCUPL and SCHCOPL: Computation of Electromagnetic Coupling on a Layered Halfspace with Complex Conductivities*. Open-File Report 79-1430, U.S. Geological Survey.
- Kawasaki, K., Osterkamp, T. E., Jurick, R. W., & Kienle, J. (1982). Gravity measurements in permafrost terrain containing massive ground ice. *Annals of Glaciology*, 4, 133–140.
- Kay, A. & Duckworth, K. (1983). The effect of permafrost on the IP response of lead zinc ores. *Journal of the Canadian Society of Exploration Geophysicists*, 19(1), 75–83.
- Keevil, N. B. & Ward, S. H. (1962). Electrolyte activity: Its effect on induced polarization. *Geophysics*, 27(5), 677–690.

- Keller, G. V. (1959). Analysis of some electrical transient measurements on igneous, sedimentary and metamorphic rocks. In J. R. Wait (Ed.), *Overvoltage Research and Geophysical Applications* chapter 7, (pp. 93–111). London: Pergamon Press.
- Keller, G. V. & Frischknecht, F. C. (1966). *Electrical Methods in Geophysical Prospecting*. Oxford: Pergamon Press.
- King, M. S. (1984). The influence of clay-sized particles on seismic velocity for Canadian Arctic Permafrost. *Canadian Journal of Earth Sciences*, 21(1), 19–24.
- King, M. S., Zimmerman, R. W., & Corwin, R. F. (1988). Seismic and electrical properties of unconsolidated permafrost. *Geophysical Prospecting*, 36(4), 349–364.
- Klein, J. D., Biegler, T., & Horne, M. D. (1984). Mineral interfacial processes in the method of induced polarization. *Geophysics*, 49(7), 1105–1114.
- Kleinberg, R. & Griffin, D. (2005). NMR measurements of permafrost: Unfrozen water assay, pore-scale distribution of ice, and hydraulic permeability of sediments. *Cold Regions Science and Technology*, 42(1), 63–77.
- Koefoed, O. (1979). *Geosounding Principles, 1*, volume 14A of *Methods in Geochemistry and Geophysics*. Elsevier.
- Kong, F.-N. & By, T. L. (1995). Performance of a GPR system which uses step frequency signals. *Journal of Applied Geophysics*, 33, 15–26.
- Leung, T. M. (2003). Controls of travelttime data and problems of the generalized reciprocal method. *Geophysics*, 68(5), 1626–1632.
- Lima, O. A. L. & Sharma, M. M. (1990). A grain conductivity approach to shaly sandstones. *Geophysics*, 55(10), 1347–1356.
- Lima, O. A. L. & Sharma, M. M. (1992). A generalized Maxwell-Wagner theory for membrane polarization in shaly sands. *Geophysics*, 57(3), 431–440.
- Loke, M. H. (1999). *RES2DMOD Ver. 2.2, Rapid 2D Resistivity Forward Modelling Using Finite-Difference and Finite-Element Methods*.
- Loke, M. H. (2000). *RES2DINV Ver.3.44 for Windows 95/98 and NT. Rapid 2-D Resistivity & IP Inversion Using the Least-Squares Method*. Abem Instruments AB. Software manual.
- Lunardini, V. J. (1981). *Heat Transfer in Cold Climates*. New York: Van Nostrand Reinhold Company.
- Luo, Y. & Zhang, G. (1998). *Theory and Application of Spectral Induced Polarization*. Number 8 in Geophysical Monograph Series. Society of Exploration Geophysicists.
- MacInnes, S. (2000). *CCINV - CR to Cole-Cole Inversion Program*. Zonge Engineering and Research Organization Inc., Tucson, Arizona.
- Madden, T. R. & Cantwell, T. (1967). Induced polarization, a review. In D. A. Hansen, W. E. Heinrichs, R. C. Holmer, R. E. MacDougall, G. R. Rogers, J. S. Sumner, & S. H. Ward (Eds.), *Mining Geophysics*, volume 2 chapter 2, (pp. 373–400). The Society of Exploration Geophysicists.
- Maillet, R. (1947). The fundamental equations of electrical prospecting. *Geophysics*, 12(4), 529–555.

- Major, J. & Silic, J. (1981). Restrictions on the use of Cole-Cole dispersion models in complex resistivity interpretation. *Geophysics*, 41(6), 916–931.
- Marshall, D. J. & Madden, T. R. (1959). Induced polarization, a study of its causes. *Geophysics*, 24(4), 790–816.
- McNeill, J. D. (1980). *Electromagnetic Terrain Conductivity Measurement at Low Induction Numbers*. Technical Note TN-6, Geonics Limited.
- McNeill, J. D. & Labson, V. F. (1991). Geological mapping using VLF radio fields. In M. N. Nabighian (Ed.), *Electromagnetic Methods in Applied Geophysics*, volume 2 chapter 7, (pp. 521–640). Society of Exploration Geophysicists.
- Meyer, W. H. (1990). EM inversion of spectral IP data. In J. B. Fink, E. O. McAlister, B. K. Sternberg, W. G. Wielduwilt, & S. H. Ward (Eds.), *Induced Polarization: Applications and Case Histories*, volume 4 of *Investigations in Geophysics* chapter 2, (pp. 104–127). Society of Exploration Geophysicists.
- Millett, F. B. (1967). Electromagnetic coupling of collinear dipoles on a uniform half-space. In D. A. Hansen, W. E. Heinrichs, R. C. Holmer, R. E. MacDougall, G. R. Rogers, J. S. Sumner, & S. H. Ward (Eds.), *Mining Geophysics*, volume 2 chapter 2, (pp. 401–419). The Society of Exploration Geophysicists.
- Mitchel, J. K. (1993). *Fundamentals of Soil Behavior*. John Wiley & Sons.
- Mortensen, H. (2004). Geotechnical properties of permafrozen soil - literature review and determination of geotechnical properties. The Arctic Technology Centre, BYG•DTU, Technical University of Denmark. Unpublished student report.
- Murmann, R. P. (1973). Ionic mobility in permafrost. In *North American Contribution, Second International Conference on Permafrost, Yakutsk, USSR* (pp. 352–359). Washington DC: National Academy of Sciences.
- Nabighian, M. N. & Elliot, C. L. (1976). Negative induced-polarization effects from layered media. *Geophysics*, 41(6A), 1236–1255.
- Nair, M. R. & Sanyal, N. (1980). Electromagnetic coupling in IP measurements using some common electrode arrays over a uniform half-space. *Geoexploration*, 18(2), 97–109.
- Olhoeft, G. R. (1974). Electrical properties of rocks. In R. G. J. Strens (Ed.), *Physics and Chemistry of Minerals and Rocks* (pp. 261–278). London: Wiley.
- Olhoeft, G. R. (1977). Electrical properties of natural clay permafrost. *Canadian Journal of Earth Sciences*, 14(1), 16–24.
- Olhoeft, G. R. (1982). Warburg impedances at single water-mineral interfaces. 52<sup>nd</sup> SEG meeting, Expanded Abstracts, 516–518.
- Olhoeft, G. R. (1984). Clay organic reactions measured with complex resistivity. 54<sup>th</sup> SEG meeting, Expanded Abstracts, 356–358.
- Olhoeft, G. R. (1985). Low-frequency electrical properties. *Geophysics*, 50(12), 2492–2503.
- Osterkamp, T. E., Jurick, R. W., Gislason, G. A., & Akasofu, S.-I. (1980). Electrical resistivity measurements in permafrost terrain at the Engineering Creek road cut, Fairbanks, Alaska. *Cold Regions Science and Technology*, 3, 277–286.

- Palacky, G. J. & Stephens, L. E. (1992). Detection of subbottom ice-bonded permafrost on the Canadian Beaufort Shelf by ground electromagnetic methods. *Geophysics*, 57(11), 1419–1427.
- Paterson, N. R. & Ronka, V. (1971). Five years of surveying with the very low frequency - electro magnetics method. *Geoexploration*, 9, 7–26.
- Pelton, S. H., Ward, S. H., Hallof, P. G., Sill, W. R., & Nelson, P. H. (1978). Mineral discrimination and removal of inductive coupling with multifrequency IP. *Geophysics*, 43, 588–609.
- Pelton, W. H., Sill, W. R., & Smith, B. D. (1983). Interpretation of complex resistivity and dielectric data. part I. *Geofizikai Kozlemlenyek*, 29(4), 297–330.
- Press, W. H., Flannery, B. P., Teukolsky, S. A., & Vetterling, W. T. (1986). *Numerical Recipes, The Art of Numerical Computing*. Cambridge University Press.
- Ramachandrian, N. & Sanyal, N. (1980). Electromagnetic coupling in IP measurements using some common electrode arrays over a uniform half-space. *Geoexploration*, (18), 97–109.
- Rivkina, E. M., Laurinavichus, K. S., Gilichinsky, D. A., & Shcherbakova, V. A. (2002). Methane generation in permafrost sediments. *Doklady Biological Sciences*, 383(6), 179–181.
- Roethlisberger, H. (1961). *The Applicability of Seismic Refraction Soundings in Permafrost Near Thule, Greenland*. Technical Report 81, U.S. Army CRREL.
- Routh, P. S. & Oldenburg, D. W. (2000a). Complex conductivity inversion from EM coupling contaminated frequency domain IP data. 70<sup>th</sup> SEG meeting, Expanded Abstracts, 1089–1092.
- Routh, P. S. & Oldenburg, D. W. (2000b). Electromagnetic coupling in frequency-domain induced polarization data: A method for removal. 70<sup>th</sup> SEG Meeting, Expanded Abstracts, 1081–1084.
- Routh, P. S. & Oldenburg, D. W. (2001). Electromagnetic coupling in frequency-domain induced polarization data: A method for removal. *Geophysical Journal International*, 145(1), 59–76.
- Rubinstein, I. (1995). *Fundamentals of Physical Electrochemistry*, chapter 1, (pp. 1–25). Marcel Dekker.
- Ryu, J., Morrison, F., & Ward, S. H. (1970). Electromagnetic fields about a loop source of current. *Geophysics*, 35(5), 862–896.
- Saint-Amant, M. & Strangway, D. W. (1970). Dielectric properties of dry, geologic materials. *Geophysics*, 35(4), 624–645.
- Saloheimo, K. (1990). Model studies on spectral induced polarization. *Acta Polytechnica Scandinavica, Applied Physics Series*, Ph167, 1–114.
- Scheider, W. (1975). Theory of the frequency dispersion of electrode polarization. topology of networks with fractional power frequency dependence. *Journal of Physical Chemistry*, 79(2), 127–136.
- Scott, W. J. & Hunter, J. A. (1977). Application of geophysical techniques in permafrost regions. *Canadian Journal of Earth Sciences*, 14(1), 117–127.

- Scott, W. J., Sellmann, P. V., & Hunter, J. A. (1990). Geophysics in the study of permafrost. In S. H. Ward (Ed.), *Geotechnical and Environmental Geophysics, Volume I: Review and Tutorial* (pp. 355–384). Tulsa, Oklahoma: Society of Exploration Geophysicists.
- Seigel, H. O. (1959). Mathematical formulation and type curves for induced polarization. *Geophysics*, 24, 547–565.
- Shuey, R. T. & Johnson, M. (1973). On the phenomenology of electrical relaxation in rocks. *Geophysics*, 38(1), 37–48.
- Simon, B. (2001). Improved and new resistivity-depth profiles for helicopter electromagnetic data. *Journal of Applied Geophysics*, 46, 65–76.
- Sihvola, A. (1999). *Electromagnetic Mixing Formulas and Applications*, volume 47 of *Electromagnetic Waves Series*. The Institution of Electrical Engineers.
- Sinha, A. K. (1980). A study of topographic and misorientation effects in multifrequency electromagnetic soundings. *Geoexploration*, 18, 111–133.
- Sinha, A. K. & Stephens, L. E. (1983a). Deep electromagnetic sounding over the permafrost terrain in the Mackenzie Delta, N.W.T., Canada. In *Proceedings of the Fourth International Conference on Permafrost* (pp. 1166–1171).
- Sinha, A. K. & Stephens, L. E. (1983b). *Permafrost Mapping over a Drained Lake by Electromagnetic Induction Methods*. Paper 83-1, Geological Survey of Canada.
- Slater, L. & Lesmes, D. (2002). IP interpretation in environmental investigations. *Geophysics*, 67(1), 77–88.
- Søndergaard, B. (1979). Geologisk basisdatakort, 1514 I, Helsingør. Danmarks Geologiske Undersøgelse.
- Song, L. (1984). A new IP decoupling scheme. *Exploration Geophysics*, 15, 99–112.
- Spies, B. R. & Eggers, D. E. (1986). The use and misuse of apparent resistivity in electromagnetic methods. *Geophysics*, 51(7), 1462–1471.
- Stähli, M. & Stadler, D. (1997). Measurement of water and solute dynamics in freezing soil columns with time domain reflectometry. *Journal of Hydrology*, 195, 352–369.
- Sunde, E. D. (1968). *Earth Conduction Effects in Transmission Systems*. New York: Dover.
- Telford, W. M., Geldart, L. P., & Sheriff, R. E. (1990). *Applied Geophysics*. Cambridge University Press, 2nd edition.
- Timur, A. (1968). Velocity of compressional waves in porous media at permafrost temperatures. *Geophysics*, 33(4), 584–595.
- Tripp, A. C., Klein, J. D., Halverson, M. O., Kingman, J., & Grant, T. W. (1990). Induced-polarization spectral interpretation including electromagnetic coupling data — a field example. In J. B. Fink, E. O. McAlister, B. K. Sternberg, W. G. Wielduwilt, & S. H. Ward (Eds.), *Induced Polarization: Applications and Case Histories*, volume 4 of *Investigations in Geophysics* chapter 2, (pp. 179–198). Society of Exploration Geophysicists.
- Van der Kruk, J., Meekes, J. A. C., Van Den Berg, P. M., & Fokkema, J. T. (2000). An apparent-resistivity concept for low-frequency electromagnetic sounding techniques. *Geophysical Prospecting*, 48, 1033–1052.

- Van Voorhis, G. D., Nelson, P. H., & Drake, T. L. (1973). Complex resistivity spectra of porphyry copper mineralization. *Geophysics*, 38(1), 49–60.
- Vanhala, H. (1997). Mapping oil-contaminated sand and till with the spectral induced polarization (SIP) method. *Geophysical Prospecting*, 45(2), 303–326.
- Vanhala, H. & Peltoniemi, M. (1992). Spectral IP studies of Finnish ore prospects. *Geophysics*, 57(12), 1545–1555.
- Vanhala, H. & Soininen, H. (1995). Laboratory technique for measurement of spectral induced polarization response of soil samples. *Geophysical Prospecting*, 43(5), 655–676.
- Vanhala, H., Soininen, H., & Kukkonen, I. (1992). Detecting organic chemical contaminants by spectral-induced polarization method in glacial till environment. *Geophysics*, 57(8), 1014–1017.
- Verma, R. K. (1973). Topographic effects on electromagnetic depth sounding systems. *Geophysical Prospecting*, 21(1), 1–25.
- Vinegar, H. J. & Waxman, M. H. (1984). Induced polarization of shaly sands. *Geophysics*, 49(8), 1267–1287.
- Wait, J. R. (1951). *Basis of Electrical Prospecting Methods Employing Time Varying Fields*. PhD thesis, University of Toronto.
- Wait, J. R. (1952). Current-carrying wire loops in a simple inhomogeneous region. *Journal of Applied Physics*, 23(4), 497–498.
- Wait, J. R. (1955). Mutual electromagnetic coupling of loops over a homogeneous ground. *Geophysics*, 20(3), 630–637.
- Wait, J. R. (1982). Electromagnetic response of a medium loaded with coated conductive particles. *IEEE Transactions on Geoscience and Remote Sensing*, GE-20(4), 500–504.
- Wait, J. R. (1989). Complex resistivity of the earth. In J. A. Kong (Ed.), *Progress in Electromagnetics Research I* chapter 1, (pp. 1–173). Elsevier.
- Wait, J. R. & Gruszka, T. P. (1986a). Interaction of electromagnetic and electrochemical effects in geophysical probing. *Electronics Letters*, 22(7), 393–394.
- Wait, J. R. & Gruszka, T. P. (1986b). On electromagnetic coupling removal from induced polarization surveys. *Geoexploration*, 24(1), 21–27.
- Ward, S. H. & Fraser, D. C. (1967). Conduction of electricity in rocks. In D. A. Hansen, W. E. Heinrichs, R. C. Holmer, R. E. MacDougall, G. R. Rogers, J. S. Sumner, & S. H. Ward (Eds.), *Mining Geophysics*, volume 2 chapter 2, (pp. 197–223). The Society of Exploration Geophysicists.
- Ward, S. H. & Hohmann, G. W. (1988). Electromagnetic theory for geophysical applications. In M. N. Nabighian (Ed.), *Electromagnetic Methods in Applied Geophysics*, volume 1 chapter 4, (pp. 131–311). Society of Exploration Geophysicists.
- Washburn, A. L. (1979). *Geocryology - A survey of periglacial processes and environments*. University of Washington.
- Weidick, A. (1976). Glaciation and the Quaternary of Greenland. In A. Escher & W. S. Watt (Eds.), *Geology of Greenland* (pp. 430–458). Copenhagen: Denmark: The Geological Survey of Greenland.

- 
- Weller, A., Frangos, W., & Seichter, M. (2000). Three-dimensional inversion of induced polarization data from simulated waste. *Journal of Applied Geophysics*, 44, 67–83.
- Wescott, E. M. (1982). *Evaluation of Geophysical Methods in the Fairbanks Mining District*. Open-file Report 171, Alaska Division of Geological and Geophysical Surveys.
- West, S. S. (1943). The mutual impedance of collinear grounded wires. *Geophysics*, 8(2), 157–164.
- Wilt, M. & Stark, M. (1982). A simple method for calculating apparent resistivity from electromagnetic sounding data. *Geophysics*, 47(7), 1100–1105.
- Wong, J. (1979). An electrochemical model of the induced-polarization phenomenon in disseminated sulfide ores. *Geophysics*, 44(7), 1245–1265.
- Wong, J. & Strangway, D. W. (1981). Induced polarization in disseminated sulfide ores containing elongated mineralization. *Geophysics*, 46(9), 1258–1268.
- Wynn, J. C. & Zonge, K. L. (1975). EM coupling, its intrinsic value, its removal and the cultural coupling problem. *Geophysics*, 40(5), 831–850.
- Wynn, J. C. & Zonge, K. L. (1977). Electromagnetic coupling. *Geophysical Prospecting*, 25(1), 29–51.
- Yin, C. & Fraser, D. C. (2004). Attitude corrections of helicopter EM data using a superposed dipole model. *Geophysics*, 69(2), 431–439.
- Zonge, K. L. (1972). *Electrical Properties of Rocks as Applied to Geophysical Prospecting*. PhD thesis, The University of Arizona.
- Zonge, K. L. (2004). Zonge Engineering and Research Organization, Tucson, Arizona. Private communication.
- Zonge, K. L. & Hughes, L. J. (1980). The complex resistivity method. Unpublished report.
- Zonge, K. L. & Hughes, L. J. (1985). The effect of electrode contact resistance on electric field measurements. 55<sup>th</sup> SEG meeting, Expanded Abstracts, 231–234.



# Errata

---

## Capacitive coupling effects

Please notice that there is an error of sign in the equation D.9 on page 140. The correct equation should read:

$$V_r = \frac{X_c}{X_c + (n-1)R_c} V_1 + \frac{R_c}{X_c + (n-1)R_c} \sum_{i=2}^n V_i \quad (\text{D.9})$$

This has implications on the results presented especially in figure D.10 and the values of the constants of proportionality in equation (D.10). The phase effect of the capacitive coupling is not positive as stated on page 142, but a negative response instead. The response is similar in polarity and shape to the Cole-Cole CR and EM coupling responses. The conclusions related to which parameters affect the response remains valid.

The correct model with some extensions as well as modelling results were presented at the SEG meeting in 2006:

Ingeman-Nielsen, T. (2006). The effect of electrode contact resistance and capacitive coupling on complex resistivity measurements. 76<sup>th</sup> Annual International Meeting, SEG Expanded Abstracts 25, 1376–1380.

Thomas Ingeman-Nielsen



Report no R-123  
ISSN 1602-2917  
ISBN 87-7877-192-7